The Role of Neuroplastin and Otoferlin in Hearing

By: Fanbo Kong

For PhD

The University of Sheffield

Faculty of Science

School of Biosciences

Acknowledgements

Abstract

Sound transduction occurring at cochlear hair cells is important for analysing acoustic information from the outside world. The project of the PhD is to investigate cochlear hair cell basal lateral current profile and the exocytosis of mammalian cochlear hair cells. Here, we investigated two proteins. One is neuroplastin, a cell adhesion molecule which belongs to Basigin family and have been found to be essential for normal development and maintenance of OHC stereocilia. However, we still have a limited understanding on the role of neuroplastin in cochlear hair cells. The other protein is otoferlin, the primary Ca^{2+} sensor expressed in cochlear hair cell which has an essential role in Ca^{2+}-dependent exocytosis and endocytosis when using constitutive knock-out mouse models. It is unclear whether otoferlin plays a key role in the maintenance of Ca^{2+}-dependent exocytotic function in adult IHCs.

Our research showed neuroplastin is found in OHC stereocilia and IHC basolateral membrane. Single-cell patch clamping experiments showed that mature *Nptn*-knockout mouse OHCs have significantly decreased MET currents and MET channel open probabilities, indicating neuroplastin is essential for hair cell mechanoelectrical transduction and Ca^{2+} homeostasis. In addition, both OHCs and IHCs of *Nptn*-knockout mice failed to acquire basolateral current profile, suggesting neuroplastin is important for the acquisition of mature basolateral K^+ currents in IHCs.

As for otoferlin, after trying different conditional knock-out model, we investigated the Otoferlin$^{tm1c/tm1c}$ X Myo15-Cre$^{+/-}$ mouse model. The capacitance measurement experiments showed that Otoferlin$^{tm1c/tm1c}$ X Myo15-Cre$^{+/-}$ mouse IHCs had significantly reduced exocytosis from P10 onwards, which indicates that otoferlin plays an important role in Ca^{2+} sensing in cochlear hair cell also in late pre-mature and mature age.

Table of contents

List of Figures

List of Tables

Abbreviations

ΔC_m	Capacitance difference
4-AP	4-Aminopyridine
ABR	Auditory brainstem response
Barhl1	BarH Like Homeobox 1
BK	Big Potassium Channel
CAM	Cell Adhesion Molecule
DPOAE	Distortion Product Otoacoustic Emissions
I_{Ca}	Calcium current
I_K	Potaasium current
$I_{K,f}$	Fast potassium current
$I_{K,n}$	Negatively activating potassium current
I_{K1}	Inward rectifier current
$I_{K,DR}$	Delayed rectifier K current
IHC	Inner Hair Cell
I-V	current-voltage
LOC	Lateral olivary complex
OHC	Outer Hair Cell
MET	Mechano Electrical Transduction
MOC	Medial olivary complex
Myo7a	Myosin 7a

Myo15	Myosin 15
PBS	Phospho-buffered saline
RRP	Readily releasable pool
SGN	Spiral ganglion neuron
SK2	Small conductance Ca^{2+}-acitvated K^+ channels
SRP	Secondary releasable pool
Syt	Synaptotagmin
TEA	Tetraethylammonium ions
Vglut3	Vesicular Glutamate Transporter Type 3

1 Introduction

Analyzing information from the outside world is crucial for the survival of mammals. Hearing is one of the most versatile and important senses of our conscious experience. It allows human to detect external stimuli in the environment with capability of analyzing their nature and localization. In this chapter, I will illustrate the pathway of sound transmission and transduction.

In nature, periodic longitudinal waves of high pressure (compressions) and low pressure (rarefactions) generates a perceptual phenomenon, sound. The travelling speed of sound in air is about 340 m/s. Two important features of sound are intensity and frequency. The nature of sound intensity is the amplitude of the longitudinal wave, for audible sounds, and it is expressed in decibel sound pressure level (dB SPL). The frequencies of sound are measured in hertz (Hz). In clinical practice, pure-tone audiogram is used to determine the hearing thresholds.

The human auditory system is specialized to discriminate the frequency, intensity and direction of sounds. Figure 1.1 shows the anatomy of the human auditory system. There are three parts of the ear: outer, middle and inner ear. Outer ear contains pinna, tragus, outer ear canal (external auditory canal) and ear drum (tympanic membrane). The pinna and the tragus gather the sound waves into the external auditory canal that is embedded 2.5cm deep into the temporal bone. The funnel shape of the outer ear focuses the sound waves onto the ear drum, causing it to vibrate. In the vertical plane, the outer ear is important for sound localization (Boron and Boulpaep, 2012).

Between the ear drum and the oval window, there is an air-filled chamber which is the middle ear. The air pressure is equalized between the outside and inside of the ear drum by eustachian tube (Figure 1.1), which is connected to the nasopharynx. The three ossicles in the middle ear (Incus, Malleus and Stapes) transfer ear drum vibrations to the oval window, which leads to the movement of the cochlea fluid. The middle ear plays an important role in matching the different acoustic impedance

between air and water. The ear drum is about 20-folds larger than the oval window, amplifying the pressure wave from the air side to the water side. At the same time, the malleus and incus form a lever system, amplifying the pressure wave to stop most of the sound energy from being reflected when it reaches the cochlea fluid (Boron and Boulpaep, 2012).

The inner ear contains several chambers and tubes that are connected to each other, which are called membranous labyrinth. There are mainly two parts of the labyrinth: the vestibular system and the cochlea, the auditory portion of the labyrinth. The sensory organs in the vestibule detect the orientation and linear acceleration of the head, while the semicircular canals detect the angular acceleration of the head. Lying inside the temporal bone of the skull, together with vestibular apparatus is the cochlea. The snail-shaped cochlea is the analyzer of the frequency and amplitude of the sound. The sensory hair cells in the cochlea transduces the physical sound signals into electrical signals. As a result, the hair cells release neurotransmitter to the auditory neurons, triggering the neuron firing and the information of sound is finally conveyed to central brain (Boron and Boulpaep, 2012). The different steps in sound transduction will be described in the following content.
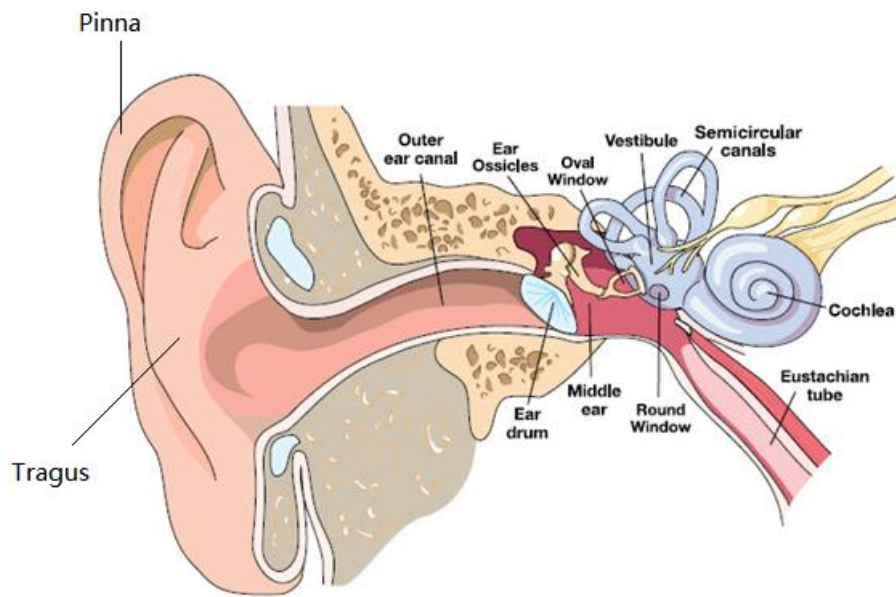
Figure 1.1：Anatomy of the human auditory system

Sound is collected by outer structures (outer auditory canal). The middle ear consists of the eardrum (tympanic membrane), ossicles. The inner ear is composed of the vestibule and the sensory organ- cochlea. The sound signal finally goes to higher cognitive centres in the brain through nerve fibres and synapses(modified from Denoble & Chimiak, https://www.diversalertnetwork.org/health/ears/anatomy-of-the-ear)

1.1 The structure of the mammalian cochlea

The cochlea is a mechano-sensory organ responsible to convert sound into an electrical signal and relaying it to the brain. It is a coiled bone structure which has about 2.5 turns in human and mouse (Elliott & Shera, 2012) (Figure 1.2)and consists of three fluid filled chambers called scala vestibuli, scala media and scala tympani. The outer chamber scala vestibuli is separated from the scala media by Reissner's membrane (RM) and the scala tympani below scala media is partitioned from it by basilar membrane (BM) (FIGURE 1.2). The three separated chambers run along the entire length of the cochlea until the scala vestibuli and the scala tympani joined together at the apex of the cochlea by an opening called helicotrema (Hudspeth, 2014).
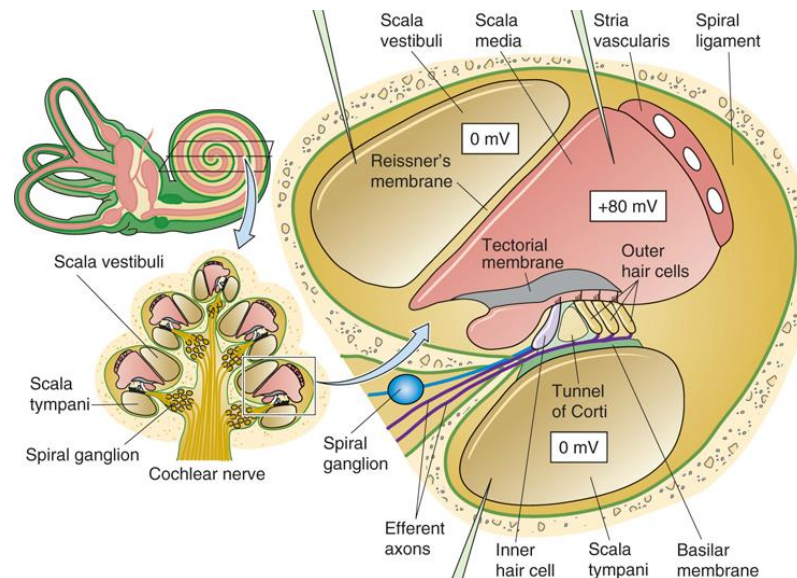
Figure 1.2: Structure of the cochlea

The cochlea is a coiled structure lying in the inner ear, together with the vestibular apparatus, which includes vestibule and semicircular cannals. (b) The cross section of the fluid-filled cochlea. The chambers which are called scalae are separated by the Reissner's membrane and Basilar membrane. The fluid which fills the scala vestibuli and scala tympani is called perilymph and the fluid contained in scala media is called endolymph. The auditory endolymph has a voltage of +80mV relative to perilymph, generating endocochlear potential (modified from Boron and Boulpaep, 2012).

As illustrated in Figure 1.2, the fluid contained in the scala vestibuli and the scala tympani is called perilymph, the content of which is like ordinary extracellular fluid in other body parts. The scala media contains endolymph, a special extracellular fluid which has different ion composition compared to perilymph. The composition of these extracellular fluids is listed in TABLE 1. As shown in TABLE 1, endolymph has a different composition from ordinary extracellular fluid. It has high K^+ and low Na^+ concentration (which is about 157mM and 1.3mM, respectively) and its Ca^{2+} concentration is very low (20-40μM), which is very important for sensory transduction in the cochlea. Perilymph contains much lower concentration of K^+ (between 4 and 6mM) but higher Na^+ (140-150mM) and Ca^{2+} concentration (0.6-1.3mM) (Wangemann, 2006). The transepithelial voltage present between the scalae media and tympani is called endocochlear potential, it gives a big driving force for sensory transduction in hair cells of the organ of Corti (being mentioned in the next paragraph).

Table 1.1 Composition of cochlear fluids (modified from Wangemann, 2006)

Component	Unit	Endolymph Scala media	Perilymph scala vestibuli	Perilymph Scala tympani
Na^+	(mM)	1.3	141	148
K^+	(mM)	157	6.0	4.2
Ca^{2+}	(mM)	0.023	0.6	1.3
Cl^-	(mM)	132	121	119
HCO_3^-	(mM)	31	18	21
Glucose	(mM)	0.6	3.8	3.6
pH	(pH units)	7.4	7.3	7.3
Protein	(mg dl^{-1})	38	242	178

The mechano-sensory organ of the cochlea is called the organ of Corti, which lies on top of the BM.The human organ of Corti has about 15,000 HCs in each ear (Úlehlová et al., 1987). It has one row of Inner hair cells (IHC), three rows of outer hair cells (OHC) and many types of non-sensory cells. For example, the rod-like pillar cells form an arch within the organ of Corti, creating the tunnel of Corti, which keeps the structural rigidity inside the organ of Corti. Inner phalangeal cells surround the IHCs on the modiolar side and Deiter's cells dock the base of each OHCs, forming a cup-like structure. There are also other kind of supporting cells, such as Claudius' cells, Hensen's cells and so on (Raphael & Altschuler, 2003).The Cross section views the organ of Corti is presented in FIGURE 1.3
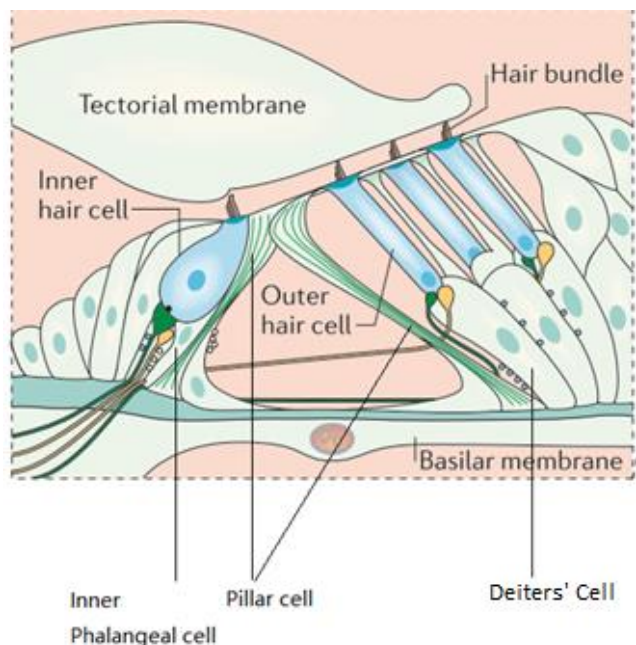
Figure 1.3:The cross section of the organ of Corti

The organ of Corti lies on the top of BM. It has a single line of IHC and three lines of OHC. The hair bundles lie on the apical side of the HCs and there is a layer of tectorial membrane lying on top of the hair bundles.

The HCs are important for the perception and transduction of auditory stimuli. As shown in Figure 1.3, the IHCs have a shape of a flask. In rodents like chinchilla, they can grow into about 35μm long and about 10μm wide at the widest point. The nucleus of IHCs normally locates at the centre of the cell and most of the organelles locate at the apical side. The OHCs are cylindrical in shape and their size varies along the cochlea, for example, in guinea pig, they grow into 20μm to 100μm long (referring apex to base). Being different from the IHCs, the nucleus of OHCs lies on the basal side (Figure 1.3) (Pujol et al, 1998).

Rows of mechano-receptive hair bundles lie on the apical side of the HCs. There is a tectorial membrane lying on the top of the hair cells and it makes contacts with the highest stereocilia tips of the OHCs. The hair bundles are formed by actin-filled stereocilia, the further the rows are from the edge of the array, the stereocilia rows becomes shorter, forming a stair-case bundle structure. The rows of the stereocilia are connected by a filamentous structure, tip links, which connects the upper end of the stereocilia to the nearest taller stereocilia (Figure 1.4) (Pickles et al., 1984). The hair bundles play an important role in sound signal transduction, which will be discussed in more details below.

Another important structure of the HCs are the ribbon synapses. The synaptic ribbon (or called dense body) is anchored to the presynaptic plasma membrane and tethered to a lot of synaptic vesicles. The dense structure lie on the base of the HCs and faces towards the postsynaptic density (PSD) of the auditory nerve fibres (R. Nouvian et al., 2006). The ribbon synapses release glutamate to excite the afferent nerve, which then send the information to the brain (Figure 1.4) (Matsubara et al., 1996).
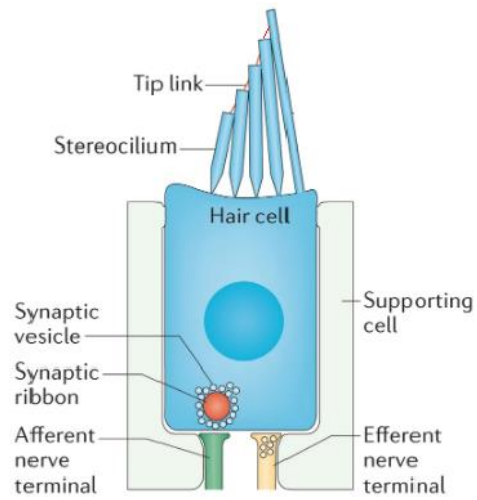
Figure 1.4:A simplified drawing of hair cell structure.

The stereocilia on the apical side form a stair-case structure and linked by tip links. The synaptic ribbon is anchored to the basal presynaptic plasma membrane and faces the postsynaptic density, forming a ribbon synapse with afferent nerve terminal (modified from Hudspeth, 2014).

1.2 Sound reception and interpretation

1.2.1 Stapes movement and Basilar membrane movement

Being briefly introduced by the general introduction part, middle ear primarily transfers the ear drum vibration (caused by sounds) towards the oval window. The key component of the transfer is accomplished by the ossicles. As illustrated in Figure 1.5, during the compression phase of a sound wave, the tympanic membrane is pushed towards the oval window, causing the stapes to move inward and push the oval window, pressing the cochlea fluid in scala vestibuli inward. Because the scala vestibuli and the scala tympani are joined together at the helicotrema, the inward movement of the perilymph in scala vestibuli leads to an opposite movement of scala tympani perilymph, hence the round window (moving outward). During the rarefaction phase, the movement of the stapes is reversed, so are the rest of the structure (Boron and Boulpaep, 2012).
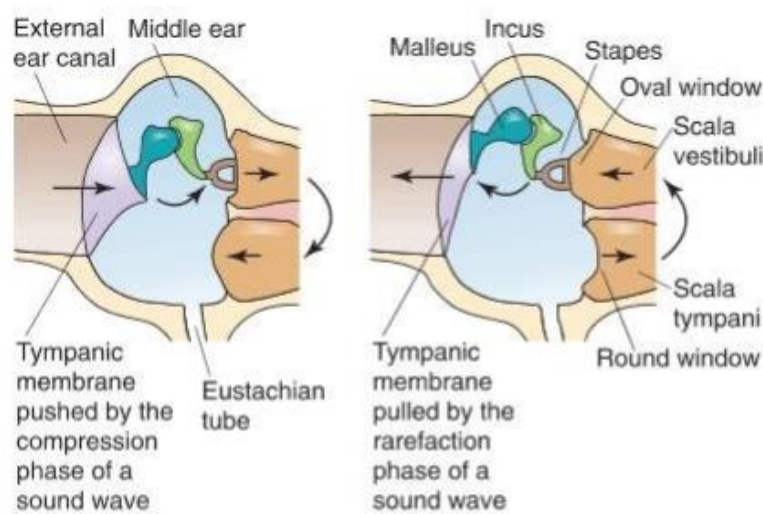
Figure 1.5:The transfer of the vibration and stapes movement.

The displacement of ear drum causes displacement of stapes and the oval window. The displacement then causes fluid movement in the scala vestibuli. In response to the movement, the fluid in the scala tympani and the round window moves towards the opposite direction (modified from Boron and Boulpaep, 2012).

Although there are two kinds of membranes that run along the cochlea and separate the cochlea chambers, the Reissner's membrane is very thin and flexible. It means that the scala media is almost incompressible. So, during the compression phase, the scala vestibuli pressure increases and becomes higher than scala tympani pressure, pushing Basilar membrane to bend downward. In the rarefaction phase, the stapes pulls outward, in sequence causing the scala vestibuli pressure decreases below scala tympani pressure, leading to downward movement of BM. In this way, the fluid movement drives BM oscillation in a wave-like form, which will later stimulate the auditory hair cells (details will be discussed below). The simplified movement of BM by stapes movement is illustrated in Figure 1.6, in which the green line represents the BM (Kandel, 2000).
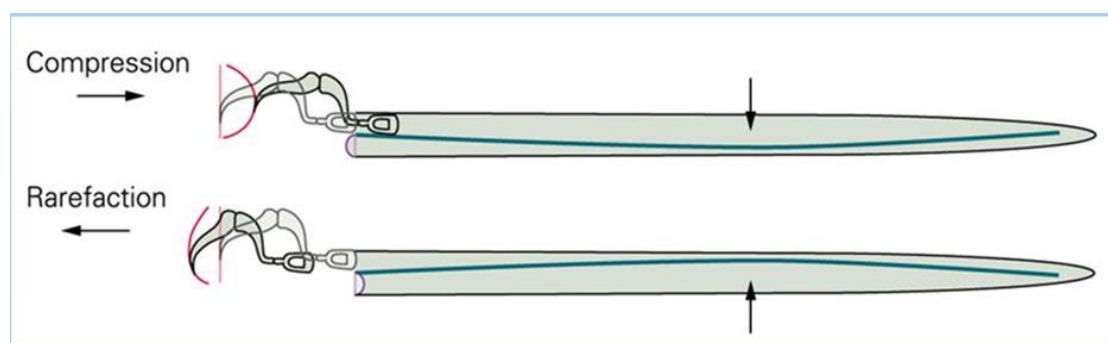
Figure 1.6:The stapes and basilar membrane movement during sound transfer.

In compression phase, the stapes moves inward, causing scala vestibuli pressure increases above scala tympani pressure, as a result, the BM bows downward. In rarefaction phase, the stapes is pulled outward, which makes scala vestibuli pressure falls below the scala tympani pressure, causing the BM bows upward. Such movement generates a wave-form of BM oscillation during sound stimuli(modified from Kandel, 2000)

Simple transfer of sound wave is not enough for optimal sound detection. In order to increase the sensitivity to sound perception, basilar membrane has evolved into a specific structure with its apical side being broad, heavy and flaccid, and gradually changing into a narrow, light and taut texture towards the base of the cochlea (Békésy., 1961; Olson et al, 2012; Teudt and Richter, 2014). The smooth variation of the basilar membrane gives a feature of a continuously varying medium for the pressure waves in the cochlea. As a result, the BM responds to the sound stimuli with vibration and it is tonotopically organised. The basilar membrane near the base part of the cochlea is displaced by higher sound frequencies and the lower frequencies displace the apex. This resonance phenomenon progresses along the cochlea, which grows in amplitude and decreases in wavelength until it reach its particular frequency (FIGURE 1.7) (Hudspeth, 2014). Due to the tonotopical organisation, different sound frequencies will only activate the corresponding region along the basilar membrane, which gives Human capability to resolve sound from 20Hz (excite the apex) to 20kHz (excite the base) differing in frequency by 0.2% (Spiegel & Watson, 1984).
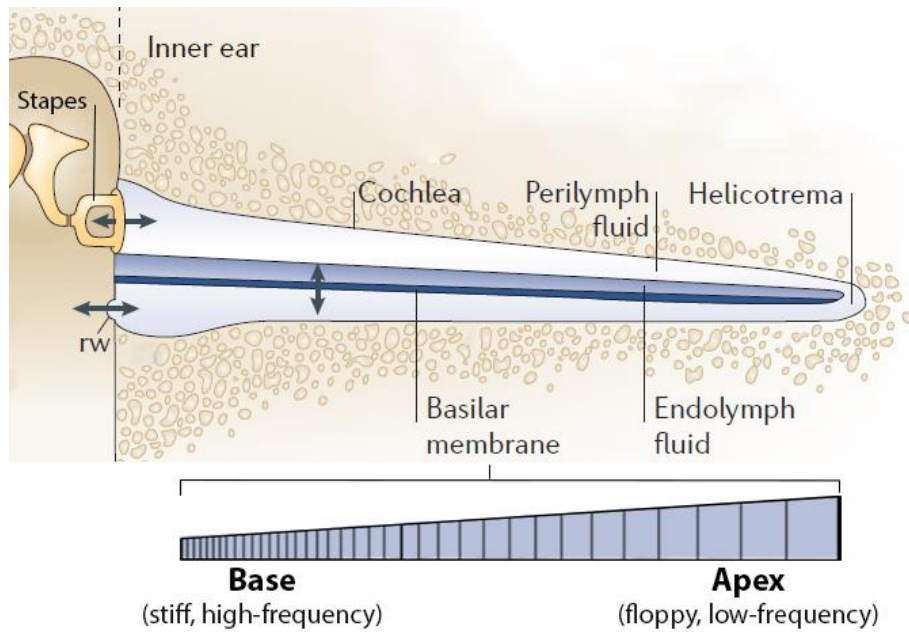
Figure 1.7:The unrolled mammalian cochlea

The sound vibrations conduct through the stapes, causing pressure waves in the cochlea fluids. The pressure waves travel through the helicotrema and finally relieved at the round window (rw) of the cochlea. The basilar membrane, which is narrow and taut at the base and smoothly becomes wide and floppy at the apex, is displaced by the pressure wave. The basal part basilar membrane is activated by high-frequency sound and the apex is displaced by low-frequency sounds modified from (Fettiplace & Hackney, 2006).

1.2.2 Amplification of the sound signal by outer hair cells and mechano-electrical transduction

In addition to the mechanisms responsible to convert air pressure waves entering the outer ear into travelling water-pressure waves in the cochlea, another important process is required to stimulate the sensory hair cells, called mechanoelectrical transduction (MET).

The stereociliary bundles on the apical side of the HCs are crucial for MET. They lie on the cuticular plate of the HCs and each stereocilia connect to the adjacent taller stereocilia via a structure called tip links, which are present in both lower vertebrates and mammals (Pickles et al., 1984; Furness, Richardson and Russell, 1989; Evans, 2020). During a travelling wave, the fluid pressure inside the cochlear partition pulls the incompressible scala media up or pushes it down, which causes the organ of Corti to shear towards or move away from the hinge of TM. For OHCs, the taller row of hair bundles is in contact with the TM. As a result, they are moved by the sound-evoked shearing between the reticular plate and the TM.

As shown in Figure 1.8a, when the organ of Corti shears toward the hinge of tectorial membrane, the hair bundles of OHCs are displaced toward their longer stereocilia, increasing the tip link tension (Pickles et al 1984). As a result, the opening of cation MET channels localized at the top of the shorter rows of stereocilia is increased (Shotwell et al., 1981). About 10% of IHC MET current is available at rest because the channels are partially open in the absence of external stimuli. This resting open probability of the MET channels can reach 50% in the presence of endolymphatic Ca^{2+} concentrations (Crawford et al, 1991; Corns et al. 2014). As mentioned before, there is a high endocochlear potential (+80mV). While the MET channels opening increases, the big electrical driving force for K^+ and Ca^{2+} influx causes an inward depolarizing current in HCs.

In OHCs, the receptor potential generated by the MET current cause the activation of the motor protein prestin, which is enriched in lateral wall of OHCs. Prestin is in a tetramer structure and it has Cl⁻ binding sites (Hallworth & Nichols, 2012). The binding affinity of prestin to Cl⁻ decreases during OHC depolarization, causing a conformational change. As a result, the OHC contract in response to the depolarization and elongation in response to hyperpolarization (Figure 1.8b); such a movement is called electromotility (Brownell *et al.*, 1985; Ashmore 1985) (Figure 1.8c). OHC electromotility accentuates the upward and downward movement of basilar membrane up to about 1000 fold, hence increasing the sensitivity of the cochlea to sound (Okoruwa et al., 2008).

A
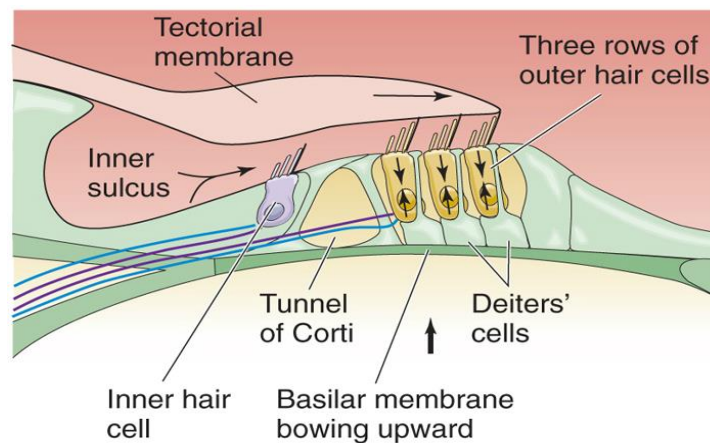
B
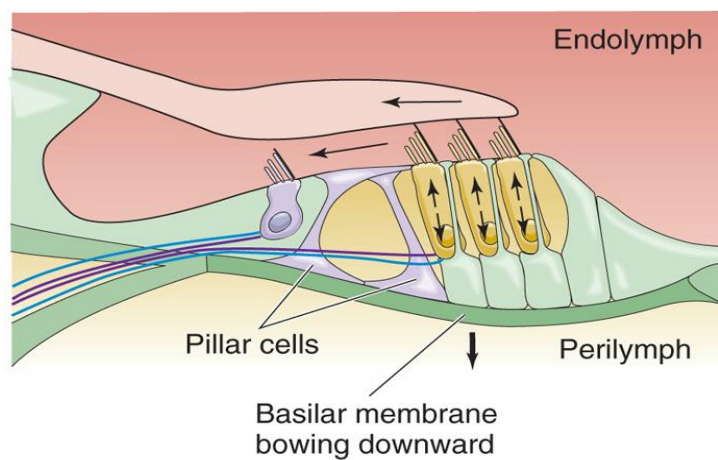
C
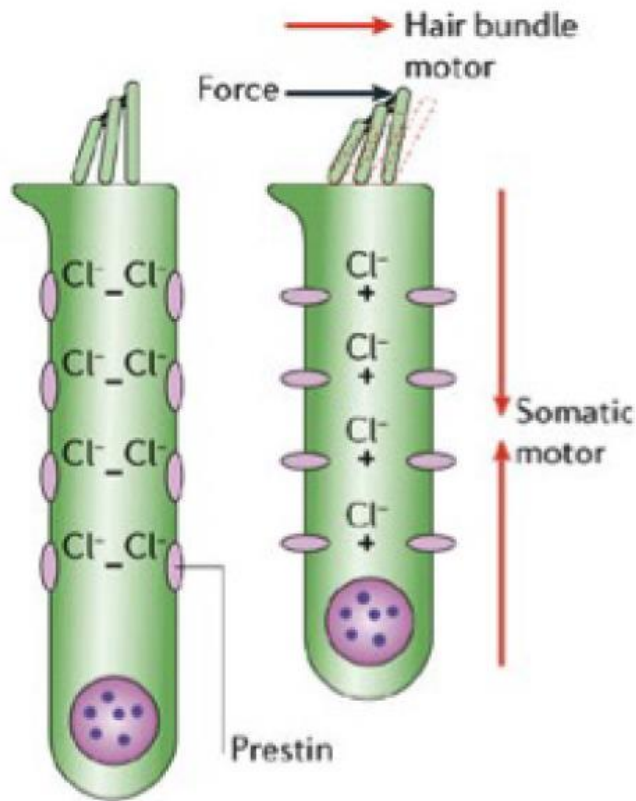
Figure 1.8:Movement of tectorial membrane and hair cells，electromotility of OHCs

(A) Upward movement of TM tilts hair bundles of the HCs towards the longer row of stereocilia, opening the MET channels and in sequence causing depolarization of the HCs. In response, the OHCs contract and (B) downwards movement of TM moves the hair bundles away from the longer row and hyperpolarize the HCs, causing elongation of OHCs. (C) Schematic diagram of the electromotility of OHCs. Prestin changes its binding affinity to Cl^- during depolarization and hyperpolarization, causing the OHCs to contract or elongate respectively. Electromotiliy helps to amplify the sound signal (pictures modified from Fettiplace and Hackney, 2006; Boron and Boulpaep, 2012).

The movement of the endolymph between the TM and the organ of Corti during sound amplification cause the displacement of the free-floating IHC hair bundles, leading to the opening of their MET channels. In IHCs, the receptor potential causes the opening of L-type (Ca$_v$1.3) voltage-gated Ca^{2+} channels localized at the presynaptic site. Ca$_v$1.3 channels contribute to more than 90% of all Ca^{2+} channels in HCs (Platzer et al., 2000). The inward Ca^{2+} current triggers the exocytosis of vesicles around the synaptic ribbon, leading to the glutamate release from the presynaptic region and then activation of AMPA receptors at the postsynaptic afferent terminals. Then, the activated afferent nerve fibers send the information to the brain (Matsubara et al., 1996). In a cochlea, the IHCs play as major sound transducers.

1.3 Initial development of cochlea

Starting from embryonic day 7 or 8 (E7-8), a group of ectodermal embryonic cells called otic placode start to develop into a neurosensory structure. During such development, the head surface ecotderm induces otic placode, which then invaginates, forming a cup structure called otic cup. By E9 to E10, the otic cup closes, forming a transient structure named as otocyst or otic vesicle. The cells from otocyst can differentiate into most cell types of the adult inner ear(Bissonnette and Fekete, 1996; Sanchez-Calderon et al., 2007). There are many factors contributing the cardinal axes of the otocyst. The anterior-posterior (A-P) axis formation fixes first and retinoic acid (RA) produced by ecodermal cells were found to be the determining factor for the establishment (Bok et al., 2011).The A-P polarity of otocyst is also defined by many other gene expression. For example, there is an asymmetrical expression pattern in A-P axis of otocyst. Fgf10, Neurogenin1 (Alsina et al., 2004; Pauley et al., 2003) is more expressed in the anterior part, while Otx1 and Otx2 (Morsli et al., 1999) are expressed posteriorly. The Dorsal-ventral (D-V) axis development is thought to be induced by the hindbrain and notochord(Bok, et al. 2005). The ventral development of the otocyst requires Shh and Wnt signalling (Bok et al., 2005) but there can be other pathways contributing. Eventually, the dorsal part of the otocyst will develop into vestibular

system while the ventral part will form the cochlear duct. The medial-lateral axis (M-L) development starts at about the same time as A-P polarity formation(Wu et al., 1998), and it shows a gradient expression of Wnt and Fgf3 (Deol, 1964). The simplified expression pattern of the otocyst three axis formation is illustrated in Figure 1.9.
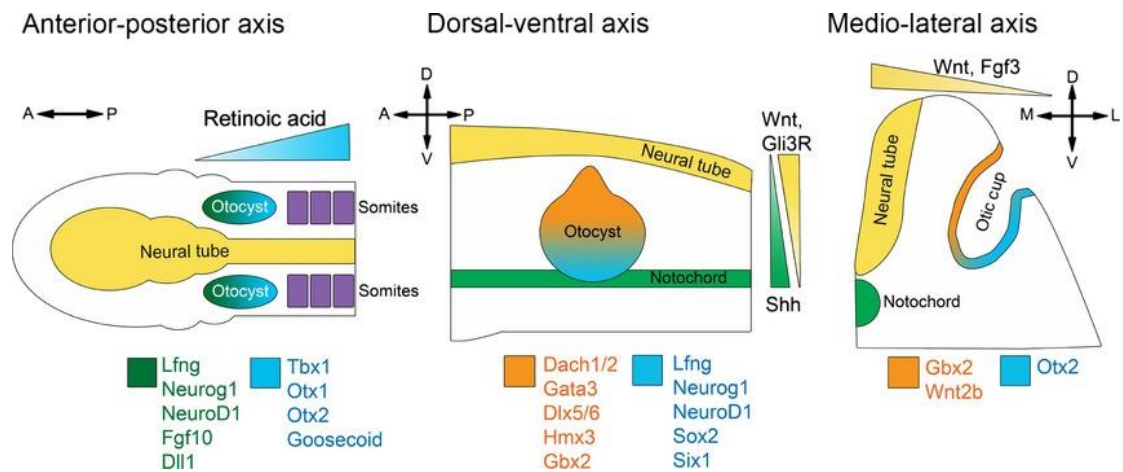
Figure 1.9:Determination of otocyst polarity.

The first established axis is A-P and M-L axis. The D-V axis determination happens after. The Retinoic acid gradient expression determines the A-P polarity, while the notochord provides Shh to form ventral part of the otocyst. In addition, the Wnt and Fgf3 from neural tube help with the M-L polarity formation(modified from Basch et al., 2016).

After otocyst axis determination, cochlea starts to grow. From ventral otocyst, there is a group of cell protrudes around E11, forming the starting part of the cochlear duct and the elongation of the protrusion continues for about 5 days (Van De Water and Ruben, 1978). During these days, the cell of the otocyst undergoes a series of changes, including termination of mitosis and differentiation, finally forming a proper functioning cochlea. The simplified timeline is illustrated in Figure 1.110 and more details of the hair cell development will be described in later parts.
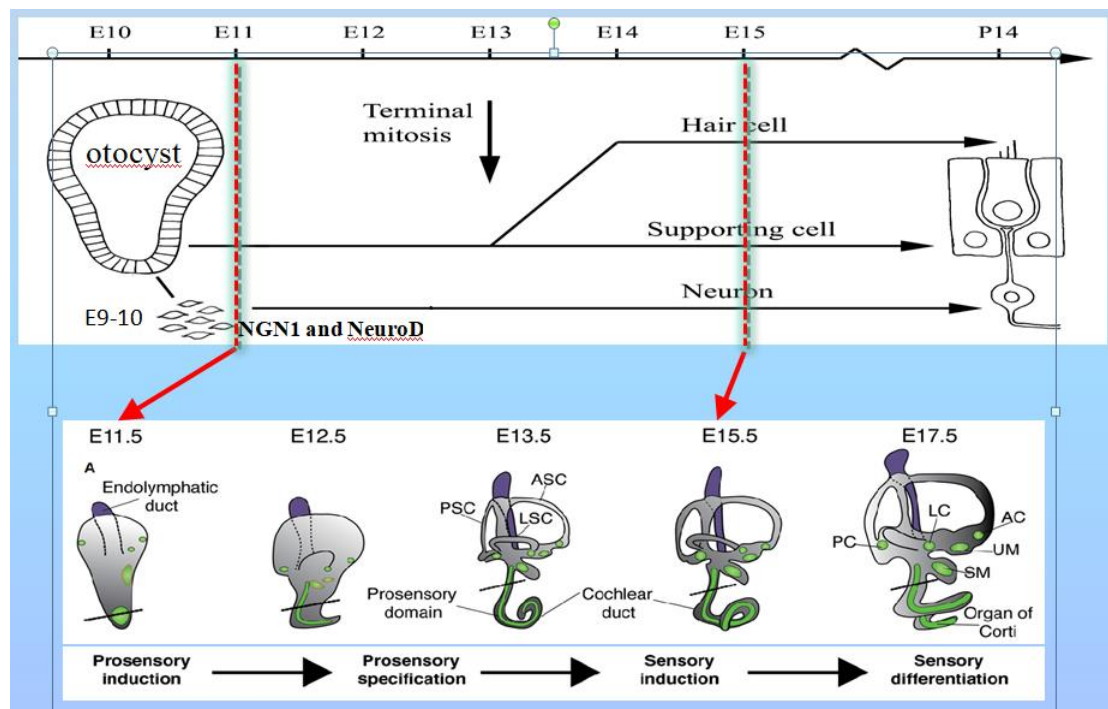
Figure 1.10:Simplified timeline of cochlea development.

After the otocyst formation (E10), the protrusion from ventral otocyst starts to elongate for about 5 days, forming the cochlear duct. The dorsal part of the otocyst finally develops into vestibular system. During this time, the neurosensory development also happens, resulting in different functioning cells such as hair cells, suppporting cells and neurons(modified from Basch et al., 2016).

1.4 Cell fate decision in cochlea development

As described before, there are three rows of OHCs and one row of IHCs in the organ of Corti, which are surrounded by different types of non-sensory cells. While inner phalangeal and border cells are found next to the IHCs, the Deiter's Cells surround the OHCs. The tunnel of Corti is formed by two pillar cells. This very precise cellular arrangement requires a precise control over cell fate and number. As illustrated in Figure 1.10, the protrusion from ventral otocyst start to elongate from about E11.5 and finally form the organ of Corti by E17.5 The protrusion contains the cell progenitors, which will finally form the sensory and non-sensory cells in organ of Corti. After the initial proliferation period, the cell progenitors undergo terminate mitosis by about E12.5 starting from the apex of the cochlear duct (Ruben, 1967).

The cell cycle exit of the progenitor cells is finely controlled by many factors. The prosensory progenitors in the ventral otocyst protrusion express a Notch signalling ligand, *jagged-1*(*Jag1*) and the expression is normally identified by *Sox2* expression (Brooker et al., 2006).Starting around E12, a morphogenetic wave of cyclin-dependent kinase inhibitor *p27^{Kip1}* transcription is generated. Cyclin-dependent kinases (CDKs) act with their co-factor, cyclins. The cyclin/CDK complexes are usually found to play an important role in regulating cell cycle progression (Sherr & Roberts, 1999). CDK inhibitor proteins (CKIs) regulate the activity of cyclin/CDK complexes. *P27^{Kip1}* is from the Cip/Kip CDK inhibitor protein family and was shown to play a role in timely cell cycle exit in other tissues in mice (Kiyokawa et al., 1996). In mouse cochlear duct, there is a transient progression of *p27^{Kip1}* expression from apex to base. The wave of *p27^{Kip1}* expression guides the cell cycle exit and is thought to help defining prosensory domain of the cochlea (Chen & Segil, 1999). In addition, *p27^{Kip1}* expression enforces the cell cycle to be temporally separated from cell differentiation in the cochlea, which means there is a fixed number of postmitotic progenitors generated first, before those cells

going into differentiation. The cell-type specific patterns of $p27^{Kip1}$ transcriptional regulation is also found in the mature organ of Corti, suggesting that it also helps with postmitotic differential regulation (Lee et al., 2006).

After cell cycle exit period (E12-E13.5), the cochlea prosensory hair cells start to differentiate on a base-to-apex gradient. During this stage, the basic helix-loop-helix (bHLH) transcription factor *Atoh1* plays a key role in cell fate determination. Previous research shows that only *Atoh1* positive cells later differentiate into sensory hair cells (Jarman et al., 1993; Driver et al., 2013). Conditional deletion experiments showed that *Atoh1* also helps with cell survival after differentiation; its expression is also required for stereocilia development (Cai et al., 2013). *Atoh1* expression is regulated by several signaling pathways, one is the Notch signalling pathway. The Notch signalling controls hair cell fate decision through lateral inhibition. Developing hair cells express *Atoh1* with Notch ligands, which bind to Notch1 in adjacent cells then induce the release of Notch intracellular domain (NICD) from such adjacent cell membranes. When there is an increase in NICD, inhibitory bHLH transcription factors such as *Hes1* and *Hes5* follows, leading to a block of *Atoh1* expression then the hair cell fate is inhibited and the supporting cell fate is promoted instead(Atkinson et al., 2015). Wnt signalling plays pattern the extent of the sensory and non-sensory domains of the cochlea. The way it works is called Wnt/β-catenin signalling. After binding to Wnt receptors, the destruction complex within the cell is disrupted, which stops β-catenin from being degraded in the cytoplasm. Then β-catenin translocates into cell nucleus to drive Wnt target genes. β-catenin can interact with 3'-enhancer of *Atoh1* gene (Shi, et al., 2010) and knock-out of β-catenin inhibits hair cell formation from sensory progenitors (Shi et al., 2014). The Notch and Wnt signalling in the cochlea also interact with each other. Inhibition of Notch signalling increases β-catenin expression, while 3'-enhancer of *Atoh1* gene leads to Notch inhibition (Shi et al., 2010) and a combination of Notch inhibition and Wnt signalling activation help with supporting

cell proliferation in the neonatal cochlea (Ni et al., 2016). A simplified picture of cell fate decision and differentiation is illustrated in Figure 1.11
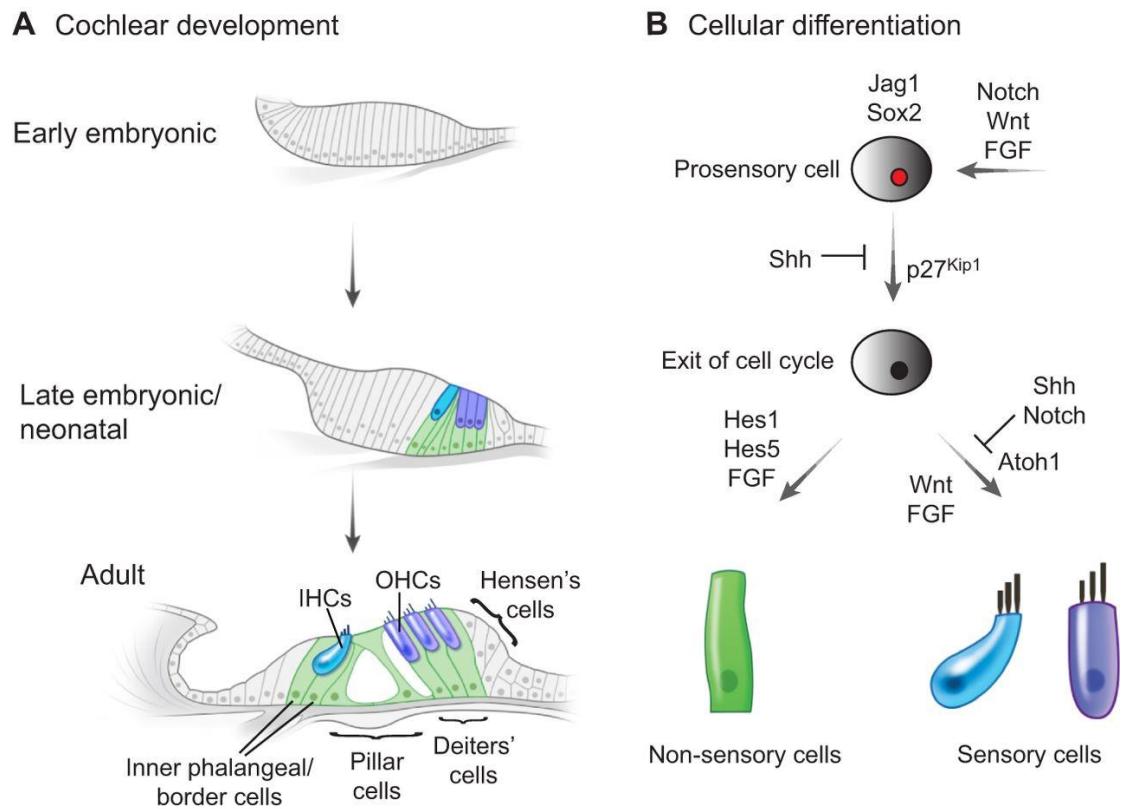
Figure 1.11:Simplified hair cell fate decision process during cochlear development

(A) Cochlear development with sensory and non-sensory cells and their progenitors labelled (IHC-blue, OHC-purple, supporting cells-green). (B) Different gene expression and signalling pathways involved in cellular differentiation. The prosensory cells express *Jag1*, marked by transcription factor Sox2, is under regulation of Notch, Wnt and FGF signalling. At this stage, the cells mainly go through proliferation. Then *p27^{Kip1}* is expressed to induce the cell fate exit and such induction is inhibited by Shh signalling. After mitosis termination, *Atoh1* induces sensory cell fate, which requires Wnt and FGF signalling, while Notch target genes *Hes1* and *Hes2* induces non-sensory cell fate (modified from Atkinson et al., 2015).

Post-transcription regulation is also important in cell differentiation in the cochlear duct. Hair cells and otic neurons express a family of small non-coding RNAs (miRNAs) called miR-183 family which includes miR-183, miR-96 and miR-182 (Weston et al., 2006). A mature miRNA is normally single-stranded and 21-23 nucleotides in length. It binds to the 3' untranslated region of target mRNA then reduce the translation of the target (Kloosterman & Plasterk, 2006). The binding specificity of miRNAs comes from a region called the seed region (nucleotides 2-7)(Lewis et al., 2005). In inner ear, miR-96 has been found to play a role in cell fate decision and development of the cochlea. In diminuendo mouse model, the mouse has a single base change in the miR-96 seed region and in the adult diminuendo mouse hair cells show immature morphology and function. The hair cell state is arrested at around P0. For example, the afferent innervation on mutant cells are disorganized and extended, and the mutant adult IHCs are still presenting ACh receptors, which is associated with direct efferent fibre contact (another embryonic feature of IHCs) (Kuhn et al., 2011).

1.5 Innervation of HCs and its development

There are two types of innervations of HCs in the cochlea: afferent and efferent innervation. The afferent innervation are formed by spiral ganglion neurons (SGN) (Kiang, et al., 1984) and it conveys the information from cochlea to the brainstem. As mentioned before, the cochlea is tonotopically organised, meaning that the HCs in particular region are activated with specific frequencies. The tonotopic map is preserved along the SGNs, then the cochlear nucleus, superior olivary complex then to the cortex (Kandler et al., 2009). The efferent innervation comes from the superior olivary complex (Liberman & Brown, 1986; Strutz, 1981) and it is thought to regulate hair cell activity to help sound perception (Cooper & Guinan, 2006). In the following part, I will describe the innervation and its development in more details.

1.5.1 Afferent innervation

In the inner ear, the SGN form the afferent innervation of the organ of Corti. The soma of the SGNs locate in the Rosenthal's canal, a latticework of bone spirals around in parallel to the cochlea. The peripheral processes of the SGN cell body contact the organ of Corti, while the central processes projects towards the brainstem. On the basis of several factors, such as somatic size and characteristics of the central and peripheral processes, the SGNs are classified into two main groups, the type I and type II SGNs (Kiang, et al., 1984).

Type I SGNs are large and bipolar, their cytoplasm is rich in ribosomes, endoplasmic reticulum (ER) and Golgi bodies (Spoendlin, 1981). The processes of type I SGNs are heavily myelinated (Thomsen, 1967). Type I SGNs' cell bodies in mouse and rat, but not in humans, are myelinated (Ota & Kimura, 1980). Type I SGNs constitute over 90% of the auditory nerve (M. C. Liberman, 1980) and in adult mice, each type I SGNs only innervates one IHC, while each IHC is innervated by many type I SGNs (10-30 in mouse: Liberman et al., 1990). Type II SGNs are relatively small, they are either bipolar or pseudomonopolar and only take 5-10% of the population (Pujol et al., 1995). Unlike type I SGNs, type II SGNs do not have much of usual organelles (Spoendlin, 1973) and they are not myelinated (Spoendlin, 1971). In adult mice, type II SGNs only innervate the OHCs; each type II SGN innervates 3-10 OHC s(Berglund & Ryugo, 1987). The function of type II SGNs is not known for sure. Previous research suggested that type II SGNs are involved in nociception (Brown, 1994) and in the suppression of cochlear amplification signal to protect it from overstimulation (Froud et al., 2015).

1.5.2 Efferent innervation

There are two major branches of the superior olivary complex which form the efferent system to the organ of Corti. One branch originates from the lateral olivary complex (LOC) and one originates from the medial olivary complex (MOC). Efferent neurons

that originate from the lateral olivary complex (LOC) form synapses with type I SGNs on their dendrites (axo-dendritic contacts) rather than forming direct contacts. The function of LOC efferent synapses are thought to modulate type I SGN activities, and help with spatial sound localization (Darrow et al., 2006). Medial olivary complex (MOC) sends their efferent processes towards the OHC, forming direct contacts by large inhibitory synapses. MOC activity reduces the movement of the basilar membrane, making the gain of cochlear amplification smaller and allow the detection of particular signals (such as speech) in background noise (Cooper & Guinan, 2006). Efferent neurons in the cochlea use acetylcholine as the primary neurotransmitter, which activates $\alpha9$ $\alpha10$ nicotinic acetylcholine receptors (nAChRs) coupled with SK2 potassium channels. The function of efferent activation is inhibitory to HCs. In addition, efferent neurons release gamma-aminobutyric acid (GABA), which is likely to inhibit acetylcholine release and to modulate type II SGN afferent input (Thiers et al., 2008; Maison et al., 2013; Wedemeyer et al., 2013). The simplified innervation of the organ of Corti is illustrated in Figure 1.12.
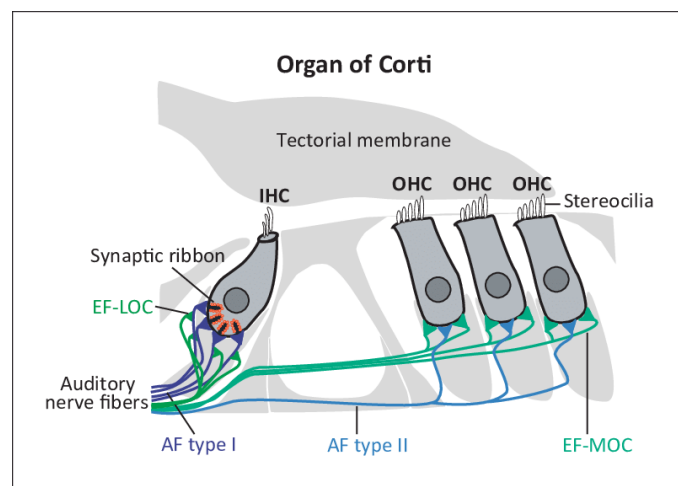
Figure 1.12: The innervation of hair cells.

Afferent fibres innervate both IHCs and OHCs (AF type I for IHCs and AF type II for OHCs); the lateral efferent fibres innervate IHCs (EF-LOC: efferent fibre lateral olivary complex) and the medial efferent fibres innervate OHCs (EF-MOC: efferent fibre medial olivary complex). Modified from Rüttiger et al., 2017.

1.5.3 Development of the afferent and efferent innervation

The innervation of the organ of Corti changes during development. Starting from the mouse embryonic stage (about E12-E13), the extension of statoacoustic ganglion (SAG) neurons begins. The target of the statoacoustic ganglion is immature neurotrophin-3 (NT-3)-positive epithelial cells (Fariñas et al., 2001). Later in development (E17-E18), the guidance cue for afferent neurons becomes into a combination of NT-3 and brain-derived neurotrophic factor (BDNF) to help the afferent neurite outgrowth towards the IHC and OHC regions in the organ of Corti (Pirvola et al., 1992). From E18 to P0, both type I and type II fibres are immature and the innervation on IHCs and OHCs are unorganized. At birth, both the type I and type II SGNs arborize and form contacts with all the HCs (both IHCs and OHCs) (Huang, et al., 2007). From P0 to P3, the afferent innervation undergoes a period of refinements. The type I and type II SGN fibre tracts separate into three bundles under the three rows of OHCs. Type I SGN forms calyceal terminal complexes around the basolateral region of the IHCs and the tracts of which keep staying dorsal to the type II SGN fibre tracts (Huang, et al,. 2007b). From P3 to P6, type I afferent nerve fibres withdrawal from OHCs, together with their nerve terminals are reduced (Sobkowicz et al., 1982). By second postnatal week, type I SGNs no longer innervate the OHCs so they innervate the IHCs only (Huang, et al,. 2007b). Intracellular staining studies suggested that the position of the synapses around the IHC surface also determines the size of the SGNs. The ribbon synapses on the modiolar side are bigger and the connected afferent fibres have a smaller diameter. As being illustrated in Figure 1.19, the afferent fibres also show a higher sensitivity threshold and a lower spontaneous rate. As for the pillar side, the morphology is the opposite (small ribbon with thicker afferent fibres with a lower sensitivity threshold and a higher spontaneous rate (Liberman, 1982).

Type II SGNs' branches form contacts with both IHCs and OHCs at birth but the pruning starts soon after. By P3, all the type II SGN innervation on IHC is gone, while the contacts with OHC keep increasing until P6. After reaching the peak (more than 40

contacts per OHC), the number of type II innervation decreases until there are only a few left when the cells reach their maturity (Sobkowicz *et al.*, 1986; Barclay *et al.*, 2011; Huang *et al.*, 2012). The growth and retraction of type I and type II SGNs is suggested to be separated (Huang et al., 2007a). For efferent neurons, the innervation on immature IHCs are in a form on direct contacts (Simmons, 2002).

As for efferent system, the timing and the innervation pattern is slightly different from afferent innervation. Previous mouse studies showed that on E11, ipsilateral inner ear efferent neurons can be observed in embryonic mouse hindbrain(Karis et al., 2001). Efferent fibres penetrate the sensory neuroepithelia, sending their individual axon branches below hair cells around E14-15(Fritzsch, 1996). Starting from P1, cholinergic efferent synaptic currents can be observed in IHCs, suggesting the beginning of efferent regulation on IHCs. To investigate the expression of nAChR clusters, previous research used Alexa Fluor 488 conjugated α-bungarotoxin (a neurotoxin that reversibly bind to α9-containing nAChR) to label to label the nAChR. By P8, there are about 16 nAChR clusters formed on each immature IHC (Roux et al., 2011). The early onset of cholinergic synaptic inputs are suggested to play a role in maturation of the auditory pathway (Roux et al., 2011). After maturation (P12 for IHCs and P8 for OHCs), the efferent neurons from MOC start to innervate OHC at around P8, while the efferent fibres originated from LOC only form axondendritic contacts with type I SGNs (Darrowet al., 2006). The different innervation pattern in HCs before and after hearing onset is illustrated in Figure 1.13.
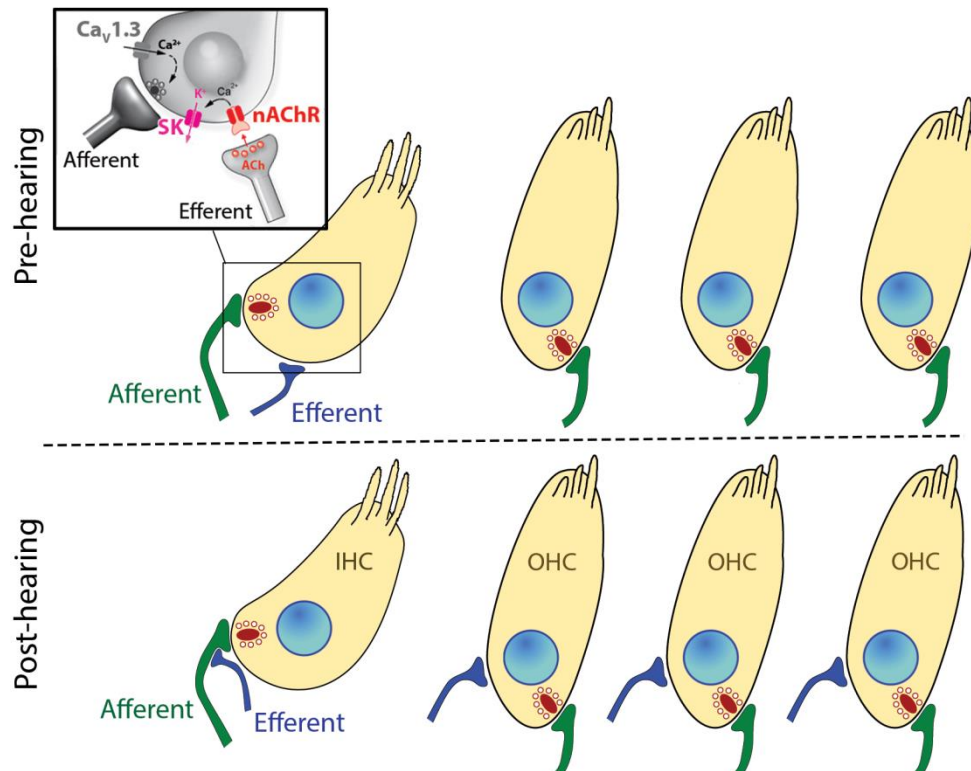
Figure 1.13:Hair cell innervation before and after hearing onset

The afferent fibres contact both immature and mature HCs. The efferent fibres contact immature IHCs directly, but after hearing onset, the efferent only form axodendritic contacts with type I SGNs that contact IHCs. For OHCs, the efferent fibres only start to form contacts after P8, and they form direct contacts with OHCs after hearing onset.

1.6 Morphological maturation of hair cell

After E15, the cell fate of most cells in cochlear duct is decided. The cells start to go through a series of morphological and functional maturation. Hair cells go through maturation during development with a basal to the apex gradient along the cochlea, most of which is completed by postnatal day 18 (P18) (Ehret, 1976).

In terms of surface morphology development, some hair cells start to show surface morphogenesis starting from 18th gestational day (Anniko, 1983). The OHCs membrane area increases during development, at the same time the length of OHCs increases while the width decreases with age (Abe et al., 2007). In contrast, although the IHC number is set before birth, the surface area of IHCs doubles during the development, reaching the peak at P16 (Kaltenbach & Falzarano, 1994).

The hair bundle development is an important maturation process of HCs. The core of the stereocilia is formed by actin filaments. The β- and γ-actin form the actin filaments with plus ends pointing towards the stereocilia tip (Tilney et al., 1992). Espin (ESPN), plastin1 and T-plastin form cross links between the filaments (Daudet and Lebart, 2002; Li et al., 2004). During embryonic stages, the hair bundle development starts with growth of microvilli on the apical side of HCs, marking the initiation of hair bundle development (Lim and Anniko, 1985; Nishida et al., 1998). The actin core treadmilling keeps the core of stereocilia dynamic, as the actin monomers move from the tips to the cell body and the polymerization and depolymerization is well under control (Rzadzinska et al., 2004). The microvilli then grows into stereocilia, some of which elongate themselves along a microtubule-formed structure called kinocilium, forming a staircase structure with 2 to 4 rows (Kaltenbach & Falzarano, 1994; Peng, et al, 2009). After the first elongation period, the stereocilia stop growing in length but increase their width by adding actin filaments. The core part in the centre of the actin filaments extends basally, forming rootlets to link the stereocilia and a specialized actin network called the cuticular plate on the apical surface of the HC, and the basal part of the

filaments is shaped into a taper structure. After this, the elongation of the stereocilia starts again until it reaches the final length. By the end of maturation, the kinocilium degrades and disappears in the mammalian cochlea and the hair bundles form in parallel. The length of hair bundle increases with distance from the base to the apex along the cochlea (Figure 1.14). For human cochlea, the hair bundle length varies roughly from 3-8 μm and the OHC stereocilia is shorter than IHC's (Saunders & Garfinkle, 1981; Wright, 1984).
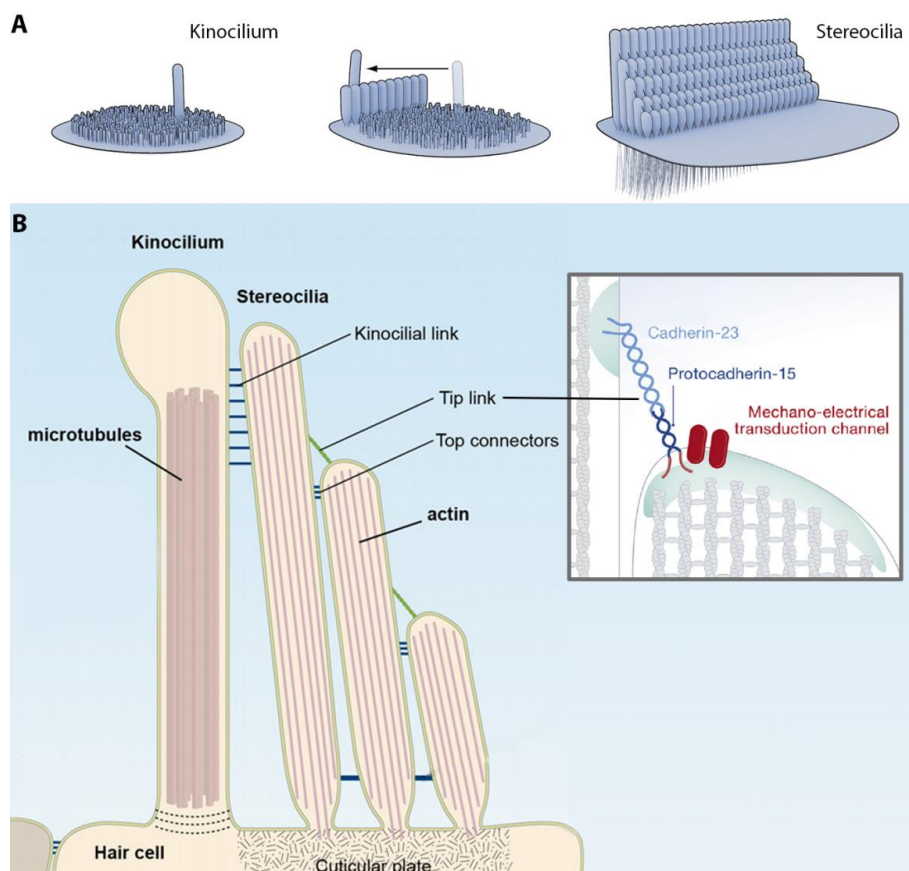
Figure 1.14:Development and structure of hair bundles

(A)Simplified process of hair bundle development, the microvilli grow towards the kinocillium, forming a stair-case structure. The kinocilium moves towards an end of the cuticular plate and eventually disappear, leaving several rows of stereocilia forming stair-case- shape hair bundles. (B) Stereocilia are linked by tip links and top connectors. Cadherin 23 and protocadherin-15, which is associated with MET channels, form the tip links (modified from Schwander et al., 2010b).

The regulation of stereocilia length depends on myosin motor proteins. Myosin 15a (Myo15a) locates at the stereocilia tips and, together with its cargo protein called whirlin, helps to regulate the differential stereocilia growth (Belyantseva et al., 2005). Myosin 3a (Myo3a) binds to ESPN1 and transports ESPN1 to the stereocilia tips to regulate stereocilia width (McGrath et al., 2017). Previous research suggested that myosin 7a (Myo7a) helps to regulate stereocilia growth by restricting actin assembly (Palmgren et al., 2001) and F-actin rearward flow (Figure 1.14) (Prosseret al., 2008).

The taper shape at the base helps the stereocilia to pivot around it, which allows a synchronized movement during mechanical stimulation (Hudspeth and Corey, 1977). Myosin 6a (Myo6a) was reported to retain the protein tyrosine phosphatase receptor Q (PTPRQ) at the stereocilia base (Sakaguchi et al., 2008) to form the taper shape, while PTPRQ were also found to regulate actin remodelling (Takenawa and Itoh, 2001).

Hair bundle development also involves remodelling of stereocilia tip link. During development, the stereocilia of cochlear HCs are interconnected by several transient structures such as lateral links, ankle links and kinociliary links. After hearing onset, the HCs only contains tip links and horizontal top connectors (Figure 1.14) (Goodyear et al., 2005). Transmembrane receptor protein cadherin 23 (Cdh23) and protocadherin 15 (Pcdh15) localize to transient lateral links and kinociliary links in developing hair bundles. In mature HCs, they form the tip-links between rows of stereocilia (Michel et al., 2005; Siemens et al., 2004) and Pcdh15 appears to be closely associated with MET channels. A splice variant of the adaptor protein harmonin is also found in developing hair bundles to bind with Cdh23, Pcdh15, myo7a and F-actin to establish linkage between hair bundles. Mutations in the genes encoding for myo7a lead to severe forms of deaf-blindness, called Usher syndromes (USH1) (Verpy et al., 2000). G protein-coupled receptor 98 (VLGR1), usherin and adaptor protein whirlin can be found at the ankle link region during hair bundle development (Michalski et al., 2007) and mutation in these genes can cause USH2, another form of Usher syndrome

(Schwanderet al., 2010b). A simplified picture of hair bundle length regulation is illustrated in Figure 1.15.
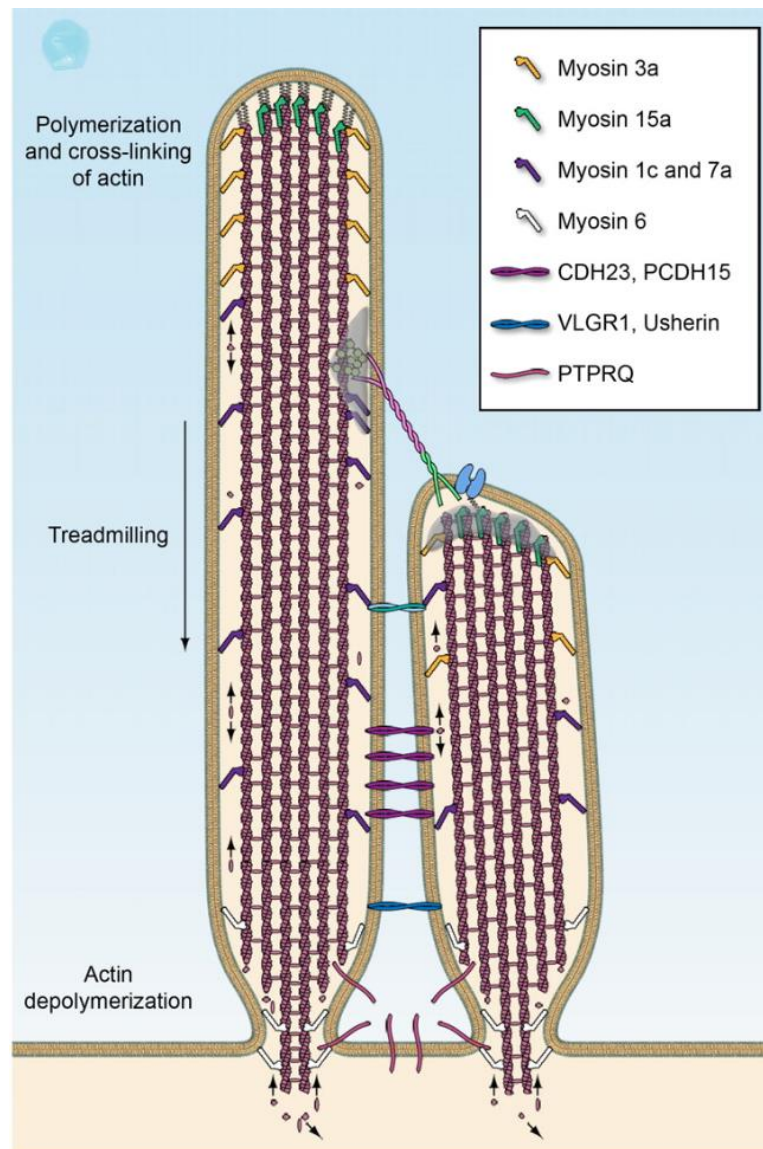
Figure 1.15:Hair bundle proteins and Hair bundle length regulation

A simplified diagram of two stereocilia indicating the distribution of some hair bundle proteins discussed in the text. Cdh23, Pcdh15 with MET channels form the tip link. Myo3a, myo7a and myo15a are mostly found at the tip of stereocilia while myo6 retains PTPRQ at the base. The actin polymerization starts at the tip of the stereocilia and the treadmilling goes towards the base, where the actin filaments become depolymerized (modified from Schwander et al., 2010b).

1.7 Functional maturation of inner hair cells

During HC development, there is a series of physiological changes. The resting membrane potential of immature IHCs (Kros *et al*, 1998; Marcotti *et al.*, 2003a) and OHCs (Helyer, et al., 2005; Jeng et al., 2020) are roughly -60mV. The potassium currents include the outward delayed rectifier K current $I_{K,DR}$ and the inward rectifier K current I_{K1}. The outward $I_{K,DR}$ activates at potential positive to - 40mV, while the inward I_{K1} activates negative to -80mV (Marcotti *et al.*, 1999; Marcotti, *et al.*, 2003a). In previous research, the K channel $K_V2.1$ was suggested to be the carrier of $I_{K,DR}$ but the hypothesis was not verified (Helyer et al., 2007). There is also a calcium current I_{Ca} and a sodium current I_{Na}. I_{Ca} is mainly carried by $Ca_v1.3$ voltage-dependent Ca^{2+} channels (Brandt et al., 2003) and is normally activated at -65mV (near to the membrane resting potential) and peaks at -20mV. I_{Ca} is responsible to generate the spontaneous action potential firing (Marcotti *et al.*, 2003). What's more important, I_{Ca} plays an important role in regulating exocytosis (Johnson, et al, 2005), which will be discussed in more details later of the chapter. I_{Na} is likely to be carried by voltage-gated Na^+ channel $Na_V1.1$ and/or $Na_V1.6$. They activate around -60mV, reaching a peak at -15mV in immature HCs, and are quickly down regulated during maturation. The function of I_{Na} is suggested to help with setting the frequency of spontaneous action potential firing (Marcotti, et al., 2003). There is also a Ca^{2+} activated potassium current I_{SK2}, which is carried by apamin-sensitive small conductance Ca^{2+}-activated K^+ channels (SK2 channels). SK2 channels are Ca^{2+} dependent, causing K^+ efflux following their activation by Ca^{2+}, leading to a HC hyperpolarization (Fuchs, 1996) to reduce OHC responses towards sound stimuli by reducing the BM motion and causing temporal decrease in sensitivity (Guinan, 2006).The activation of SK2 channels can be caused by Ca^{2+} influx through $Ca_v1.3$ and through α9α10 nAChRs, which are highly permeable to Ca^{2+} (Weisstaub et al., 2002) or through purinergic receptors (Johnson et al., 2011b). As mentioned in the HC innervation chapter, the MOC efferent fibres directly contact with OHC basal lateral surface. When MOC efferent fibres are activated, they release

acetylcholine to activate α9α10 ACh receptors, leading to Ca^{2+} influx. There is also evidence suggesting that release of Ca^{2+} from internal store also contributes to the process. I_{SK2} expresses in immature IHCs but they do not express in mature IHCs (Figure 1.16).
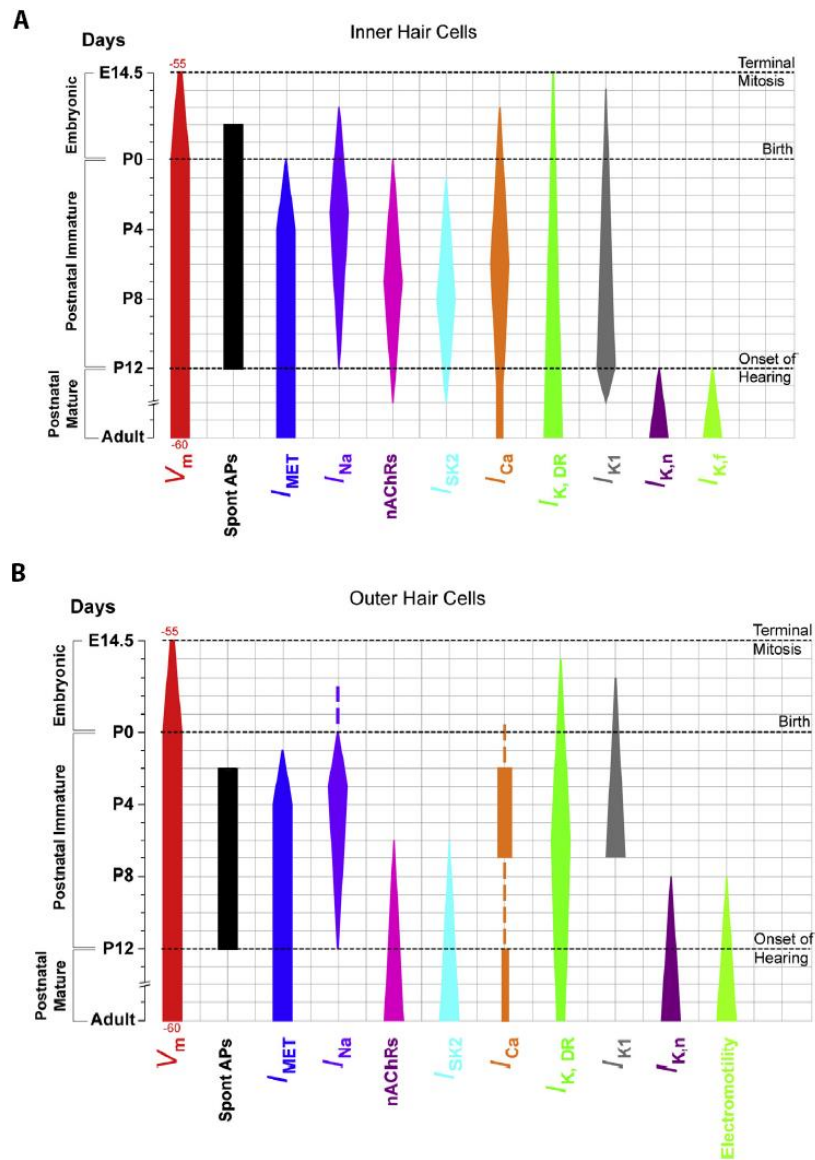
Figure 1.16:Physiological changes in HCs during development

Physiological properties of mouse IHCs (A) and OHCs (B). The vertical bars describe the presence of the currents during development. The width of the bars indicate the scale of the currents. V_m stands for membrane potential, while Spont APs is abbreviation of spontaneous action potentials(modified from Corns *et al.*, 2014).

Immature IHCs were found to fire spontaneous Ca^{2+}-dependent action potentials, which are generated and modulated by several currents (Marcotti et al., 2003b). During resting state, the resting potential of immature IHCs is maintained about -60mV by $I_{K,DR}$ (Marcotti et al., 2003a), I_{K1} (Marcotti et al., 1999), and I_{SK2} activated by Ca^{2+} influx from α9α10 nAChRs ($I_{SK2\,(nAChRs)}$) (Marcotti et al., 2003a) and from purinergic receptors ($I_{SK(P2X)}$)(Johnson et al., 2011b). The key component of the action potential generation is Ca^{2+} influx through $Ca_{v1.3}$ (I_{Ca}) and I_{Na} helps to reduce the time towards the threshold spike (Marcotti et al., 2003b). The delayed rectifier $I_{K,DR}$, together with SK2 currents, repolarize the cell (Marcotti et al., 2004b). The action potential curve is illustrated in Figure 1.17
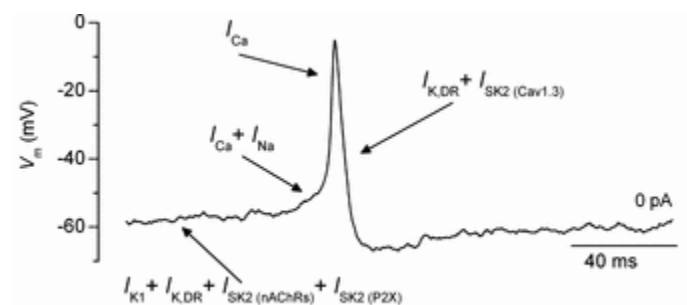
Figure 1.17:Immature IHC spontaneous action potential

The resting membrane potential of immature IHCs is around -60mV, which is maintained by K^+ current I_{K1}, $I_{K,DR}$ and I_{SK2} gated by α9α10 nAChRs and purinergic receptors. The I_{Ca} through Ca^{2+} gated channel $Ca_{v1.3}$ is to generate action potential while the I_{Na} help to boost the spike timing. The repolarization of the immature IHCs are carried by $I_{K,DR}$ and I_{SK2} gated by $Ca_{v1.3}$ (modified from Marcotti, 2012).

In the first postnatal week, along the cochlea coil, immature IHCs show different AP firing pattern. The apical IHC AP firing are bursting like, which means there are gaps between a series of fast AP firing. The basal IHCs fire more regular APs, showing a more stable pattern (Figure 1.18). The explanation of this is that the apical IHCs are more hyperpolarized by I_{SK2}. Being similar to the MOC efferent inhibitory effect on OHCs, immature IHCs receive acetylcholine from efferent fibres and ATP from supporting cells, which activate the SK2 channel opening hence a hyperpolarization (Johnson et al., 2011b). The position-dependent AP firing is thought to affect IHC morphology and biophysical property to tonotopically map the IHCs along the cochlea, fulfilling their function at different places of the cochlea (Johnson et al., 2008). The spontaneous action potential starts from birth until the onset of hearing (P12) (Marcotti et al., 2003a). During the second postnatal week, the expression of I_{K1} increases, this rectifier current hyperpolarize the cell so the IHCs can only fire action potential when there is external stimuli such as purinergic receptor activation (Tritsch et al., 2007).
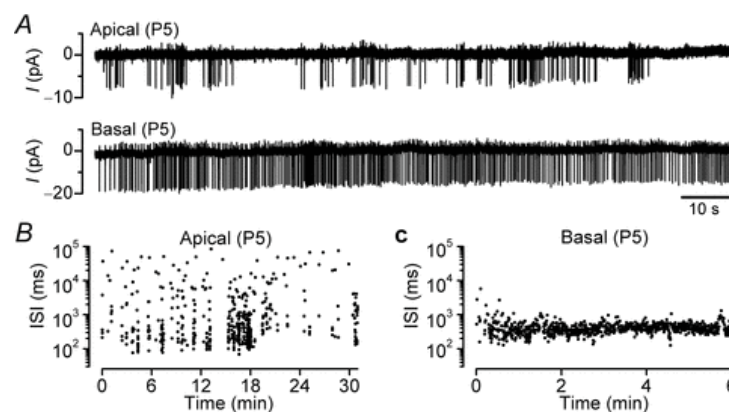
Figure 1.18 :Different AP firing pattern between apical and basal IHCs in the first postnatal week

(A) The cell-attached spontaneous firing activity measurements showed that the apical IHCs show bursting like AP firing pattern, while the basal IHCs AP firing is more regular. (B)(C) Inter-spike intervals (ISI) shows that the spiking rate in apical IHCs is different, while the basal cells fire more continuously (Johnson et al., 2011b).

Mature HCs do not show spontaneous action potential firing anymore and the resting membrane potential of mature HCs is between -70 and -80mV *in vitro*. They still keep $I_{K,DR}$ and I_{Ca} but no longer express I_{K1} and I_{Na}. As mentioned in the innervation chapter, 95% of type I afferent contacts are made with IHCs and convey the sound stimulus information towards the brainstem. To better deliver the signal, the afferent fibres can preserve the periodicity of the sound stimuli by releasing neurotransmitter at the same frequency as the graded potential firing up to several kilohertz so the periodicity of the sound stimuli can be preserved. Such phenomenon is called phase locking. The need of quick release requires fast graded voltage responses towards the stimuli hence the membrane time constant needs to be fast. To achieve this, IHCs express $I_{K,f}$, a fast Ca^{2+} activated K^+ current through large-conductance and voltage-Ca^{2+}-activated K^+ channels (BK channels). $I_{K,f}$ is expressed in mature IHCs and contributes to the fast component of the repolarizing current (Kros et al., 1998). The slow part of the repolarization is contributed by $I_{K,s}$, a classic delayed rectifier K^+ current, and $I_{K,n}$, which is a negatively activating slow rectifier K^+ current (Marcotti et al., 2003a). Potassium channel KCNQ4 contributes to the $I_{K,n}$. It was reported to contribute OHC maturation during development (Marcotti & Kros, 1999). In IHCs, $I_{K,n}$ is already open at around -70mV, which is important to provide an efficient K^+ exit, avoiding K^+ accumulation so it is important to resting membrane potential (Marcotti et al., 2003a). During sound stimulation, the MET channels are opened, leading to the depolarization of the cell, causing Ca^{2+} influx. Being different from immature IHCs, fast activating $I_{K,f}$ prevents the mature IHCs to fire an action potential, it repolarizes the cell with help of $I_{K,s}$ and $I_{K,n}$. So the mature IHCs respond to quick graded receptor potentials (RPs) instead of firing action potentials (Marcotti et al., 2003a), which lead to glutamate release and activation of type I SGNs (Saaid Safieddine et al., 2012). As for OHCs, mature OHCs express $I_{K,n}$, I_{SK2} and starts to show electromotiliy.

Although the exocytosis of both immature and mature IHCs are triggered by Ca^{2+} through $Ca_V 1.3$ Ca^{2+} channels, the Ca^{2+} current in the two stages of development is

different. The Ca^{2+} current of immature IHCs show slower kinetics, stronger inactivation and higher amplitude than those of mature IHCs (Johnson et al., 2008) (Figure 1.19). $Ca_v1.3$ Ca^{2+} channels at mature IHCs were found to have fast gating, which fulfils the requirement of precise temporal coding (Johnson et al., 2011).

Another change in functional maturation of mouse IHCs is the relationship between Ca^{2+} entry and the rate of synaptic exocytosis. IHCs that mainly respond to low frequencies (smaller than 1 kHz), which are located towards the cochlear apex, are phase locked to sound stimulation. They show a phasic component to represent the sound frequency. For IHCs at the base (responding to sounds higher than 1 kHz), the intensity and the duration of the sound is analysed by the IHCs responding to graded and sustained receptor potentials (Palmer et al., 1986). In previous research, the relationship between Ca^{2+} entry and the rate of synaptic exocytosis in acutely isolated mouse cochlea was tested under near-physiological conditions. As shown in the figure 1.19, the relationship between the Ca^{2+} entry (Ca^{2+} current, I_{Ca}) and the rate of vesicle fusion (membrane capacitance change, ΔC_m) can be defined as a transfer function of average ΔC_m against the corresponding I_{Ca}. In immature IHCs, the transfer function is exponential, which indicate a high Ca^{2+} cooperativity in exocytotic process. In mature IHCs, the transfer function is switched to a linear relation (Saaid Safieddine et al., 2012)(Figure 1.19). Such linear exocytotic Ca^{2+} dependence can be also observed in mature OHCs (Johnson et al., 2010).

The switch from a non-linear to a linear relationship indicate that the release efficiency of IHCs increases during the maturation of IHCs (Beutner et al.,2001). One explanation for the increase in release efficiency is that during maturation, extrasynaptic Ca^{2+} channels are removed and only the ones localised at the presynaptic active zones are left. At the same time, the ribbons become larger and their number drops (Wong et al., 2014). The refinements result in a tighter spatial coupling (from micro-domain coupling to nano-domain coupling) between Ca^{2+} channels and synaptic vesicles at the active zones, so a synaptic exocytotic fusion event can be triggered by only one Ca^{2+}

channel opening in mature IHCs instead of needing several Ca$_v$1.3 channels to open. In addition, a developmental change of the molecular composition of the IHC synaptic machinery might also account for the switch of the transfer function (Johnson et al., 2008).
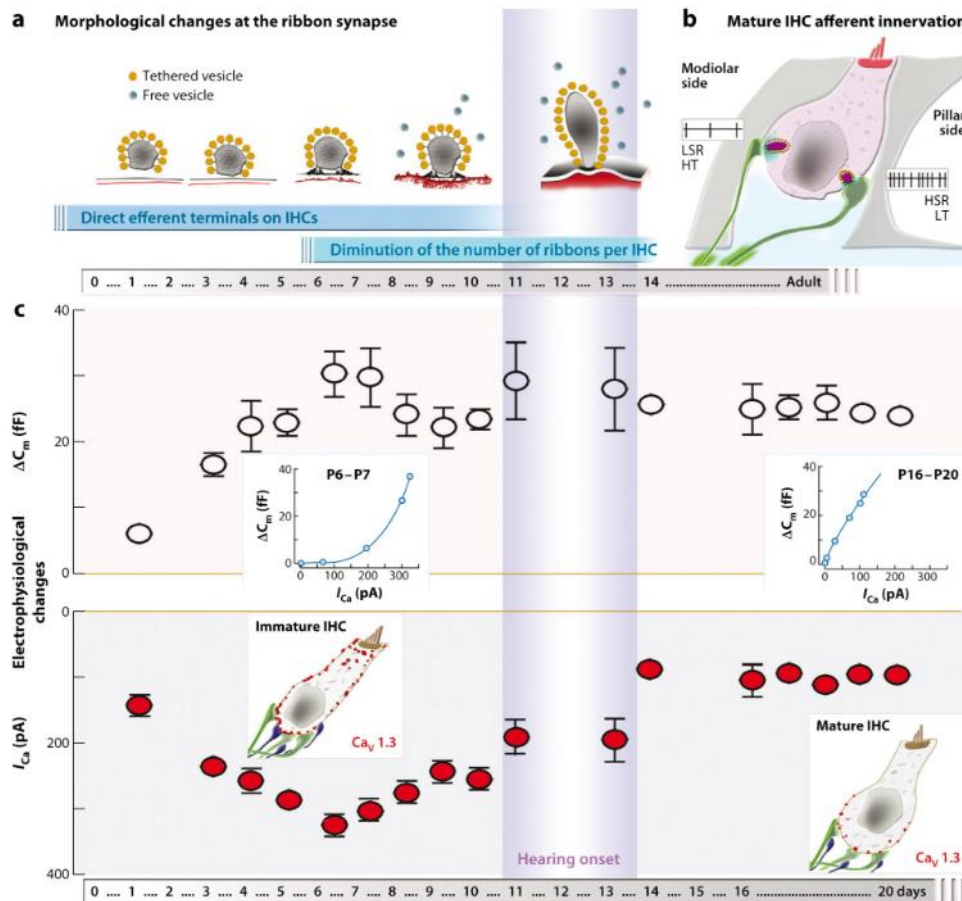
Figure 1.19:Morphological and functional maturation of mouse IHCs.

(a) Morphological changes of mouse IHC ribbon synapse. (b) Afferent innervation of mature IHCs. The modiolar side is innervated by afferent fibres with high threshold sensitivity and low spontaneous rate, the diameter of the fibres is smaller. On the pillar side, the reverse is the case. (c) Functional changes during IHC development: the relationship between the potential difference change($\triangle$C$_m$) and the Ca^{2+} current (I$_{Ca}$) changes from an exponential pattern to a linear pattern. The Ca$_v$ 1.3 voltage gated channels decrease and form nanodomains during the maturation (modified from Safieddine, et al., 2012).

1.8 Calcium Sensors

1.8.1 Ribbon, Calcium sensing and Synaptic vesicle release

In CNS synapses, there are many proteins found to be involved in neurotransmitter release such as synaptophysin (Jahn, et al., 1985; Leube et al., 1987), synapsin (Südhof et al., 1989) and synaptotagmins(Perin et al., 1991). Soluble NSF Attachment Receptor (SNARE) protein complex on the vesicle membrane, which includes synaptobrevin2, syntaxin 1A and synaptic membrane synaptosome-associated protein (SNAP) -25, mediates the membrane fusion (Sollner et al., 1993). The SNARE proteins form the core membrane-fusion machine but the assembly of the complex is not regulated by Ca^{2+}(Roux et al., 2006). On the other hand, the IHC exocytosis is Ca^{2+} driven and it is helped by the specialized structure ribbon synapses.

Ribbon synapses in IHCs are specialized to fast and temporally precise synaptic vesicle release (Parsons et al., 1994). It is an electron-dense structure and there are a lot of vesicles tethered to it (Smith & Sjöstrand, 1961). The major component of the ribbon is protein Ribeye (Khimich et al., 2005). Ribeye contributes to over 65% of the ribbon volume and its major function is to provide structural support to the ribbon (Zenisek et al., 2004). In constitutional ribeye-knock-out mice, more active zones were found from individual synaptic contact while there is also an increase in PSD size and glutamate receptor (GluA3) clusters (Becker et al., 2018; Jean et al., 2018). The developmental compensation of ribeye knockout can reduce the effect of the loss of ribbon-tethered SVs, but there is a limit. The mutants' afferent firing threshold was increased and the adaptation recovery was slowed down, indicating the functions of the ribbon in vesicle replenishments (Jean et al., 2018). Another important protein of the ribbon is piccolo. Its function is to organize presynaptic SV clustering, exocytosis and replenishment together with bassoon (Mukherjee et al., 2010) and Rab3-interacting molecules (RIMs)(Butola et al., 2017) (Figure 1.20a).

The ribbon synapse goes through morphological maturation during development. In mice, hearing onset occurs at about postnatal day 12 (P12). Before P6, mouse IHC ribbon synapses have a spherical electron-dense structure at the presynaptic membrane. At P6, the ribbons form a connection to a membrane structure called the presynaptic thickening by two tubular rootlets (Roux et al., 2009). Later, the presynaptic thickening develops into a presynaptic active zone and the ribbon's structure change from a spherical to a larger olive-type shape. In the meantime, the two rootlets become one arcuate density so the ribbons stay attached to the membrane at around P8 (Safieddine et al., 2012). The postsynaptic density (PSD) formation starts later than the presynaptic structure and the structure is opposed to the presynaptic active zone at around P8 (Friedman et al., 2000). By the onset of hearing, P12, the oval shape of the IHC ribbons become more prevalent, with a single attachment to the presynaptic active zone (Saaid Safieddine et al., 2012) (Figure 1.19).

As mentioned in the functional maturation of IHCs, during the development, the Ca^{2+} channels ($Ca_V1.3$) cluster around the ribbons and the extrasynaptic channels are removed (Wong et al., 2014). The protein being heavily involved in this progress is RIMs and RIM-binding proteins (RIM-BPs). For IHCs, RIM2α/β, are the two major isoforms promoting the clustering of $Ca_v1.3$ Ca^{2+} channels at the active zones. They physically interact with pore-forming α-subunit of the $Ca_v1.3$ Ca^{2+} channels to help them insert into the cell membrane. Previous research found that hair cell with disrupted RIM expression showed smaller Ca^{2+} current and exocytosis (Jung et al., 2015). RIM-BP2 was found in IHCs and t it might act as a linker between RIM, bassoon and $Ca_v1.3$ channels to help with the clustering of Ca^{2+} channels at presynaptic area (Hibino et al., 2002).

The synaptic vesicle pools in the IHCs are defined in the same way as CNS synapse vesicular pools. The fast component of the release is called the readily releasable pool (RRP) and the slow component is slowly releasable pool (SRP). Short depoloarization of the IHCs recruits the RRP. After the first RRP depletion, the SRP contributes to the

continuous replenishment of the ribbon-associated synaptic vesicles (Beutner & Moser, 2001). Morphologically, there are also vesicles docked beneath the ribbon and it is also considered to contribute to the RRP (Goutman & Glowatzki, 2007). When synaptic vesicles at IHC ribbon synapses sense Ca^{2+}, the readily releasable vesicles near the presynaptic active zones fuse with the IHC plasma membrane. The fusion process involves priming and triggering stages. In the priming stage, the synaptic vesicles dock to the plasma membrane, rendering the vesicles to get them ready to be released. During the triggering stage, Ca^{2+} and the presynaptic Ca^{2+} sensors which bind to them help the opening of fusion pores (Chapman, 2002)(Figure 1.20b).

Calcium sensors bind to Ca^{2+} via their C2 domains (Fernández-Chacón et al., 2001; Roux et al., 2006)(Figure 1.19c). The most characterized C2 domains are C2A and C2B domains in synaptotagmin 1 (Syt1). The β-sandwich structures of the C2 domains in synaptotagmins bind to three or two Ca^{2+} ions respectively (Fernandez et al., 2001; Shao et al., 1996; Ubach et al., 1998). For murine otoferlin, there are 6 C2 domains to bind to Ca^{2+}(C2A-C2F).The calcium sensors binding to the Ca^{2+} and make the fusion occurs on a much shorter time scale (Roux et al., 2006).
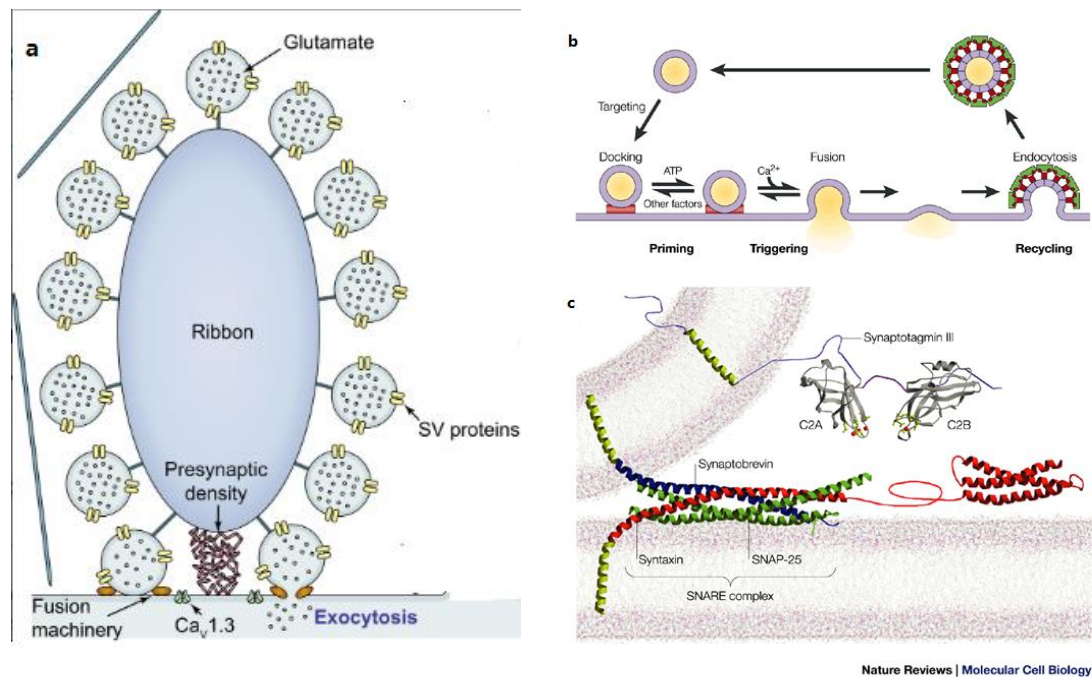
Figure 1.20: Ribbon synapses and synaptotagmin Ca2+ sensing model

(a)Ribbon synapses with a lot of synaptic vesicles (SV) tethered to the ribbon. Voltage gated $Ca_v1.3$ Ca^{2+} channels cluster around the ribbon and the Ca^{2+} current going through them trigger the fusion machinery for exocytosis, resulting in glutamate release. (b)Typical synaptic vesicle release cycle. During priming stage, the neurotransmitter-loaded vesicles dock to the active zones of the plasma membrane. The ATP and other components helps the vesicle become prepared for fusion (Klenchin & Martin, 2000). Then the Ca^{2+} sensing in triggering stage opens a fusion pore between the vesicle and the plasma membrane(Augustine, 2001). After release, clathrin-mediated endocytosis recycle the vesicles for the next round of release (Takei & Haucke, 2001). (c) Synaptotagmin 3-mediated fusion apparatus, the SNARE complex binds to synaptotagmin 3 to help with membrane fusion. Picture modified from (Chapman, 2002; and Pangrsic & Vogl, 2018)

1.8.2 Otoferlin

Being different from conventional synapses, cochlear IHCs do not express SNARE proteins found in central nervous system (CNS) (Régis Nouvian et al., 2011), the immunoreactivity of synaptophysin and synapsin were also not found in cochlear hair cells(Gil-Loyzaga & Pujol, 1988; Safieddine & Wenthold, 1997). It is also debatable whether IHCs express classical Ca^{2+} sensors such as synaptotagmin 1 and 2. According to some research, they do not express classical Ca^{2+} sensors such as synaptotagmin (Syt) 1, 2 and 9 (Pangršič et al., 2012). But in some research immunostaining showed synaptotagmin 1 and 2 expression in HCs (Johnson et al., 2010). The primary Ca^{2+} sensor of cochlear IHCs is otoferlin, which belongs to the ferlin family and is located in the IHC synaptic vesicle membrane. Ferlin family has been shown to be involved in membrane fusion events (McNeil & Kirchhausen, 2005).

Unlike synaptotagmins, which only has 2 C2 domains, otoferlin has 6 C2 domains. Fluorescence spectra research showed that 5 out of 6 C2 domains of otoferlin binds to Ca^{2+} ($[Ca^{2+}]_{1/2}$=~15-25µM) and the titration experiments with Mg^{2+} indicated that the binding was Ca^{2+} specific. The otoferlin-liposome samples show a leftward shift in $[Ca^{2+}]_{1/2}$ ($[Ca^{2+}]_{1/2}$=~2-10µM, Table 1.2), indicating that membrane can induce otoferlin Ca^{2+} binding affinity(C. P. Johnson & Chapman, 2010). Otoferlin has the ability to interact with the t-SNARE proteins syntaxin1 and SNAP25 in a Ca^{2+} dependent manner despite the fact that IHCs do not express neuronal SNAREs (Roux et al., 2006). When Ca^{2+} is present, otoferlin can also stimulate SNARE-mediated membrane fusion in vitro studies (Johnson et al., 2010). The discrepancies described above and the vesicle fusion machinery at IHC ribbon synapses is still waiting to be clarified.

C2 domain	– Liposomes $[Ca^{2+}]_{1/2}$	+ Liposomes $[Ca^{2+}]_{1/2}$
	μM	μM
C2A	ND	ND
C2B	21.1 ± 1.1	6.7 ± 0.3
C2C	15.1 ± 2.0	5.4 ± 0.1
C2D	17.0 ± 1.1	4.4 ± 0.1
C2E	25.0 ± 1.50	7.5 ± 0.8
C2F	21.1 ± 2.0	10 ± 0.2
C2ABC	15.4 ± 0.60	2.0 ± 0.1
C2DEF	14.7 ± 0.60	1.9 ± 0.8

Table 1.2: Fluorescence spectra [Ca2+]1/2 values for each C2 domain of otoferlin (modified from Colin Johnson et al., JCB, 2010)

Previous research on the auditory system has shown that otoferlin-deficient mice did not perform exocytosis in their cochlear hair cells (Beurg et al., 2008; Roux et al., 2006). The capacitance change of the cell membrane can indirectly measure the size of exocytosis. Presynaptic function of mice was examined by measuring cell membrane capacitance change (ΔC_m) following cell depolarization. As shown in Figure 1.21, when MET currents go into the IHCs, it depolarizes the IHC, causing outward K^+ currents and inward Ca^{2+} currents, triggering exocytosis. The fusion of neurotransmitter vesicles into cell membrane causes increase of cell surface area, which also increases the cell membrane capacitance, by measuring this capacitance change, it will give an indication of exocytosis at presynaptic active zones (Johnson et al., 2008).
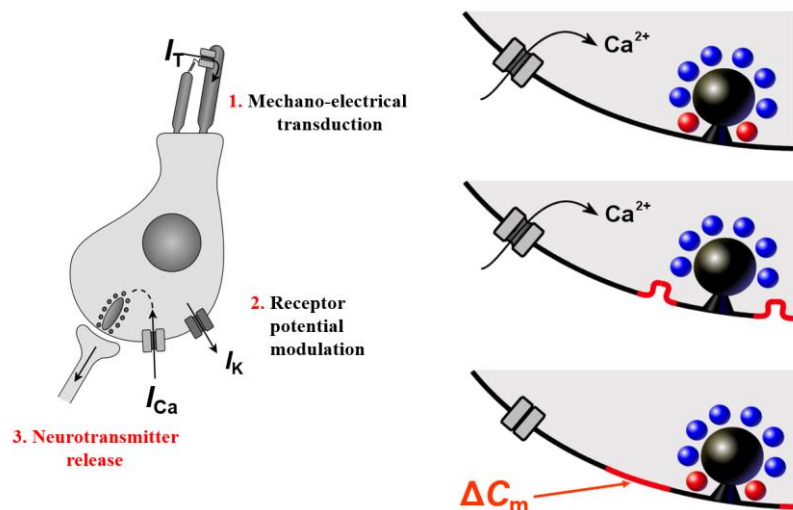
Figure 1.21:Vesicle fusion is estimated by measuring the change in cell membrane capacitance:

MET current causes cell depolarization, which then leads to receptor potential modulation of the hair cell. The modulation includes outward K^+ currents and inward Ca^{2+} currents. As mentioned before, inward Ca^{2+} current causes neurotransmitter release, which provide fused neurotransmitter vesicles to the cell membrane. The increase of cell surface area also increases the cell membrane capacitance. By measuring this capacitance difference, vesicle fusion can be indicated (Johnson et al., 2008).

As shown in Figure 1.22 previous research on the auditory system has shown that otoferlin-deficient mice did not perform exocytosis in their cochlear hair cells (Beurg et al., 2008; Roux et al., 2006). In P2-P3 immature murine OHCs, a linear relationship between exocytosis and calcium influx was observed in time-resolved patch-clamp capacitance measurements, but the calcium-evoked capacitance increases were gone in mutant $Otof^{-/-}$ mice (Figure 1.22), suggesting otoferlin plays an essential role in immature OHC exocytosis (Beurg et al., 2008).
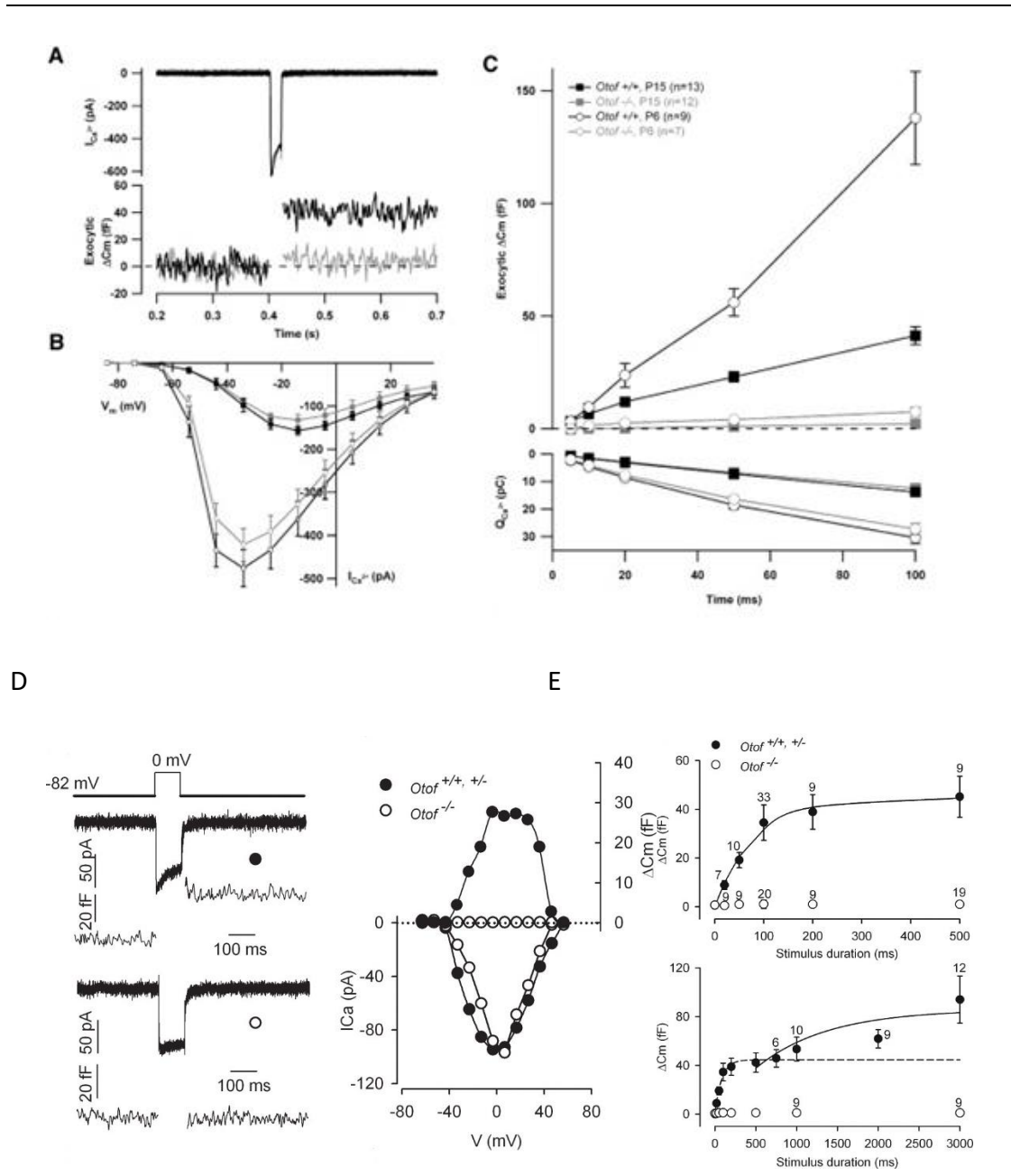
Figure 1.22:Capacitance measurement of otoferlin knockout hair cells

A, Typical recording of the capacitance measurement of P6 control and the otoferlin^{-/-} IHCs in response to 20ms depolarization stimulus. B, I-V curve of the control (black) and the otoferlin^{-/-} IHCs from P6 (circles) to P15 (squares) mice. C, Kinetics measurement D, ΔC_m measurement of immature (P2-P3) OHCs. The relationship of I_{Ca} against voltage is shown on the right. E, Immature OHCs kinetics. The upper graph defines the readily releasable pool(RRP) and the lower defines the secondary releasable pool (SRP)(modified from Beurg et al., 2008).

Current hypotheses of otoferlin function have been mainly on two directions: Ca^{2+} sensing and vesicle priming. The capability of otoferlin to interact with the SNARE proteins suggested that otoferlin might play like a Ca^{2+} sensor in a way similar to synaptotagmins. In previous research, otoferlin has been shown to have the ability to interact with the t-SNARE proteins syntaxin1 and SNAP25 in a Ca^{2+} dependent manner despite the fact that IHCs do not express neuronal SNAREs (Roux et al., 2006). When Ca^{2+} is present, otoferlin can also stimulate SNARE-mediated membrane fusion in vitro studies (Johnson et al., 2010). In one study, Syt1 expression in on $Otof^{-/-}$ mouse inner ear using viral gene transfer approach was performed to test the functional equivalence of otoferlin and Syt1 in exocytosis. With the high transduction rate and correct localization of Syt1, the IHC exocytosis was still missing in AAV treated IHCs (Reisinger et al., 2011).

Looking from a different point of view, otoferlin was suggested to play more like a vesicle replenishment priming factor. A mouse model called *Pachanga* carries C2F domain missense mutation. Its mutant IHCs showed that after short depolarizing voltage step stimulus (up to 10ms), there was no significant difference in size of Ca^{2+} inward current and corresponding exocytosis (Pangšrič et al., 2010). In comparison, when given longer stimulus (longer than 10ms) the rate of capacitance increase was slower in the mutant than in the heterozygotes, and such reduced sustained exocytosis can be increased by elevating extracellular Ca^{2+} concentration. The experiment testing exocytic response to Ca^{2+} uncaging and intrinsic Ca^{2+} dependence of exocytosis showed that the Ca^{2+}-triggered fusion mechanism was not affected by C2F domain mutation in *Pachanga* mice, but it does affect the replenishment rate of the RRP hence priming (Pangšrič et al., 2010). Further research is required to explain the discrepancies described above and the vesicle fusion machinery at IHC ribbon synapses is still waiting to be clarified.

In previous research, mature mice which carried otoferlin-C2C domain mutation (*Otof^{C2C/C2C}*) showed abnormal auditory nerve fiber responses: the ABR thresholds in *Otof^{C2C/C2C}* were higher than those in *Otof^{C2C/+}* and *Otof^{+/+}*. When the mice were one month old, the synchronous electrical response of primary afferent neurons were found much smaller in *Otof^{C2C/C2C}* when compared to *Otof^{C2C/+}* (Michalski et al., 2017). The capacitance measurements on mature *Otof^{C2C/C2C}* mice showed that when IHCs were stimulated by stepwise depolarization to -30mV and beyond (reflecting a high Ca^{2+} channel open probability), the ΔC_m was found to be significantly smaller than those in *Otof^{C2C/+}* mice. When plotting the ΔC_m against measured I_{Ca} to calculate the Ca^{2+} efficiency of readily releasable pool (RRP) release, the *Otof^{C2C/C2C}* mice showed a lower Ca^{2+} sensitivity of RRP vesicle fusion (Figure 1.23). In addition, the paired-pulse experiments showed that *Otof^{C2C/C2C}* had a smaller paired-pulse ratio of release compared to *Otof^{C2C/+}*. Such ratio is normally taken as a rough value for RRP replenishment, suggesting otoferlin is important for both vesicle priming stage and Ca^{2+} dependence of RRP replenishment of mature IHCs (Michalski et al., 2017).
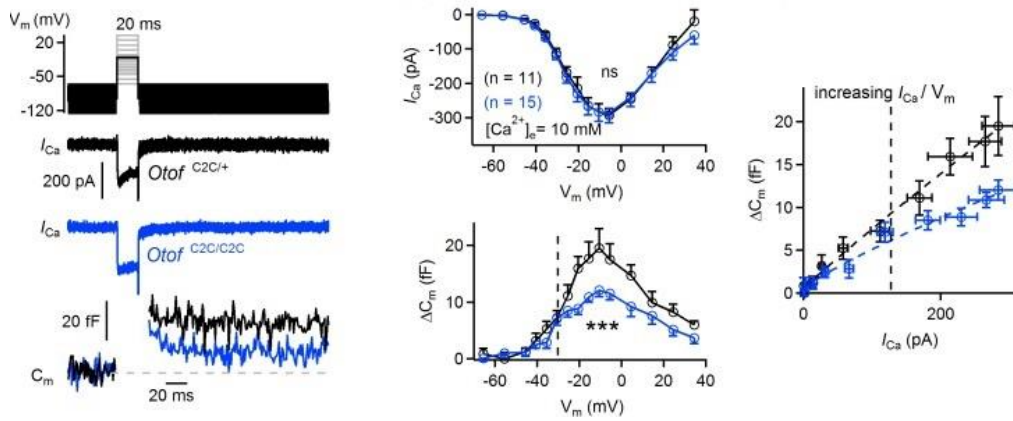
Figure 1.23: ΔCm measurement of mature (P15-P18) IHCs of control (Otof$^{C2C/+}$) and mutant (Otof$^{C2c/C2C}$) mice

The left graph contains example results of ΔC_m in response to inward I_{Ca} for 20ms voltage steps (from -95mV to +35mV). The relationship of I_{Ca} against voltage and ΔC_m against voltage are shown on the middle. There is no significant difference in inward I_{Ca} response between the controls and the mutant, but the ΔC_m of the mutant group was significantly smaller than control ΔC_m at around -10mV. Mean values of ΔC_m against inward I_{Ca} is plotted on the right, the I_{Ca}/Vm curve of both groups were fitted into power functions, the exponent of the control group was 0.94 and for the mutant group it was 0.83 (modified from Michalski et al., 2017).

In addition to contributing to exocytosis, otoferlin was found to play a role in endocytosis. The clathrin-mediated endocytosis (CME) helps to clear vesicles from active release sites (Hua et al., 2011). A critical part of the CME is called adaptor protein complex 2 (AP-2) (Hirst & Robinson, 1998). Coimmunoprecipitation assays revealed that AP-2 subunits act as otoferlin binding partners in mature murine IHCs. In previous research, a drug called dynasore, which causes the fission of clathrin-coated pits via AP-2 (Macia et al., 2006) and acts as an inhibitor of synaptic vesicle endocytosis (Newton et al., 2006) was used in real-time capacitance measurements of immature and mature mouse IHCs. The mouse IHCs were given a series of repetitive stimulus to deplete the RRP or secondary releasable pool (SRP). By measuring the ΔC_m, an indirect measurement of endocytosis would be achieved as it shows the rate of pool refilling. The real-time capacitance measurements of mature IHCs superfused with dynasore showed a larger depletion of the SRP compared to the control mice. Such difference was not observed in immature IHCs, indicating that mature mouse IHCs have CME to help with the vesicle recycling and otoferlin-AP-2 interaction might play an important role in it (Duncker et al., 2013).

In addition, otoferlin was found to be expressed in IHC Golgi-apparatus, colocalizing with Rab8b GTPase (Figure 1.24), a protein transport regulator, which is defective in a human autosomal recessive deafness form. The research indicated that otoferlin might be involved in Golgi-trafficking (Heidrych et al., 2008).
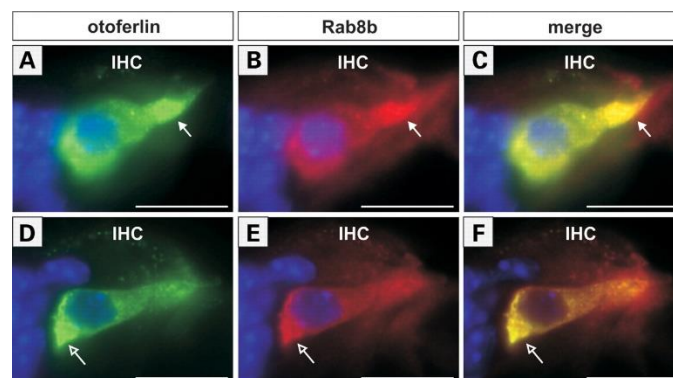
Figure 1.24: Immunohistochemistry result of co-localization of otoferlin and Rab8b in P7 mouse IHCs. (modified from Heidrych et al., 2008).

1.8.3 Synaptotagmins

In immature IHCs, the vesicle fusion at the presynaptic site is otoferlin independent until P6 (Safieddine et al., 2012), which suggested that there are some other Ca^{2+} sensors functioning at IHC ribbon synapses. Synaptotagmin is another type of Ca^{2+} sensor (Chapman, 2002). As mentioned above, the most investigated, Syt1, has two Ca^{2+} binding domains called C2A and C2B domain, and the binding of Ca^{2+} to the C2A loop 1 and loop 3 gives Syt1 the ability to form ionic bonds with the membrane surface (Chapman & Davis, 1998). Syt1 can also bind to Ca^{2+} with its C2B domain which is essential for vesicle fusion, but how cooperative the exocytosis can be with Ca^{2+} is determined by C2A Ca^{2+} binding (Shin et al., 2009).

Being different to Syt1 and Syt2, there was no detected Ca^{2+} binding to Syt4 (Dai et al., 2004). The binding of Syt4 C2A domains with negatively charged phospholipids such as phosphatidylserine (PS) and phosphatidylinositol (PI) showed lower cooperativity compared to that of Syt2 (Fukuda et al., 1996). In some rodent hippocampal neurons research, Syt4 was reported having no effect on synaptic transmission(Ting et al., 2006).

In other sensory systems, Syt4 is normally required for pituitary nerve terminal secretion by enhancing Ca^{2+}-induced-exocytosis when Ca^{2+} concentration is high (Zhang et al., 2009). Its C2A domain cannot bind to Ca^{2+} (Südhof, 2002), but our lab found that Syt4 establishes the linearity between the Ca^{2+} influx and the subsequent exocytosis and increases release efficiency in mature IHCs over the physiological Ca^{2+} concentration range (Johnson et al., 2010). As mentioned in the section of functional maturation of IHCs, the exocytotic Ca^{2+} dependence at IHCs can be defined as the relationship between Ca^{2+} entrance (I_{Ca}) and the rate of vesicle fusion (ΔC_m). This interaction can be displayed as a transfer function and in the wild type mature IHCs should present a linear transfer function as shown in the figure below (Figure 1.25, the line of Syt4 control). On the other hand, the Syt4 knock-out mice had far less linear exocytotic Ca^{2+} dependence (Figure 1.18, the line of Syt4 knockout), suggesting that

Syt4 linearize the exocytotic Ca^{2+} dependence of IHCs. The possibility of ribbon shape affecting and Ca^{2+} sensitivity was also ruled out using transmission electron microscopy (TEM). The ellipsoid shape (Sobkowicz et al., 1982) and number (Brandt et al., 2005) of synaptic ribbons in SytIV knock-outs were found not being different from wild-types (Johnson et al., 2010). Previous research mainly focused on Syt4 deficient mice; those results at the current cannot determine the real function of Syt4 in adult IHCs since the development was disrupted. To determine whether Syt4 is required for the function of mature IHCs, a conditional deletion of Syt4 in the mature cochlea would be needed.
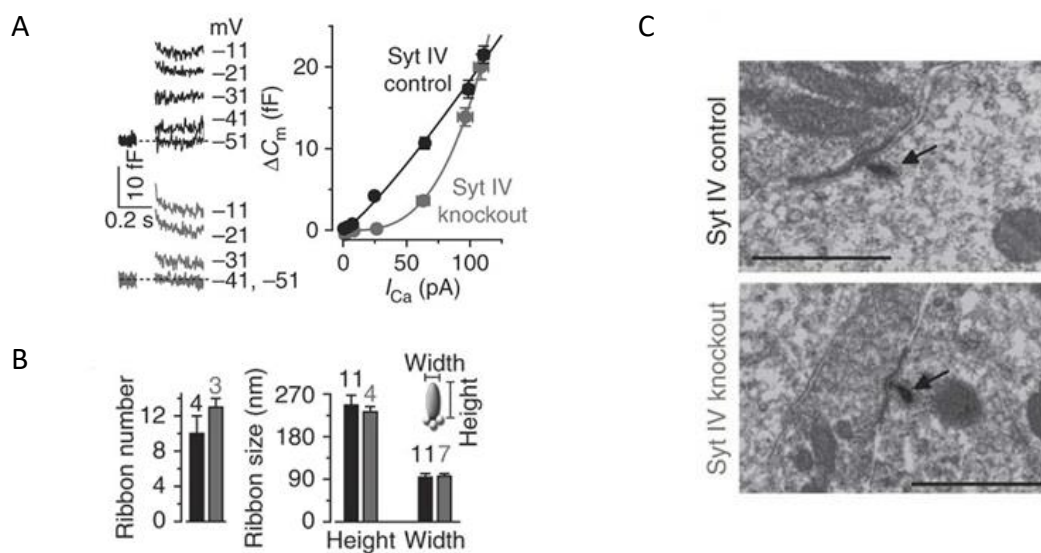
Figure 1.25:Syt4 knockout mice show non-linear Ca^{2+} dependence and normal ribbon synapse structure

A Syt4 knockout mice show less linear exocytotic Ca^{2+} dependence. The synaptic transfer curves of ΔC_m against I_{Ca} between −71 mV and −11 mV. Non-linear exocytotic Ca^{2+} dependence in Syt4 knockout IHCs and linear dependence in wild type. B TEM pictures show the cross-section structure of the ribbon synapses from Syt4-knock out mice and control mice. The scale bar represents 1 μm. C The quantity measurement of the ribbon synapses, showing no difference in shape between the mutants and the control mice (modified from Johnson *et al.*, 2010).

Being mentioned in the developmental part, the immature OHCs show a linear Ca^{2+} exocytotic dependence (Johnson et al., 2010). Such linear relationship can be also found in mature apical-coil IHCs responding to frequencies around or below about 3kHz (Johnson et al., 2005). In gerbils, due to a wider low-frequency hearing range (from less than 1kHz to 60kHz), the IHCs show a high-order Ca^{2+} dependence in the apical region and a linear relationship in basal region in the same cochlea (Johnson et al., 2008).The reverse transcription PCR of adult rat and guinea pig cochlea found the presence of Syt4 expression (Safieddine & Wenthold, 1999). Later research using immunostaining showed the presence of Syt4 in gerbil cochlea was correlated with the linear exocytotic Ca^{2+} dependence in gerbil cochlea. The *in situ* hybridization experiments of adult mouse cochlea also showed this correlation of Syt4 presence and linear exocytotic Ca^{2+}dependence (Johnson et al., 2010) (Figure 1.26).
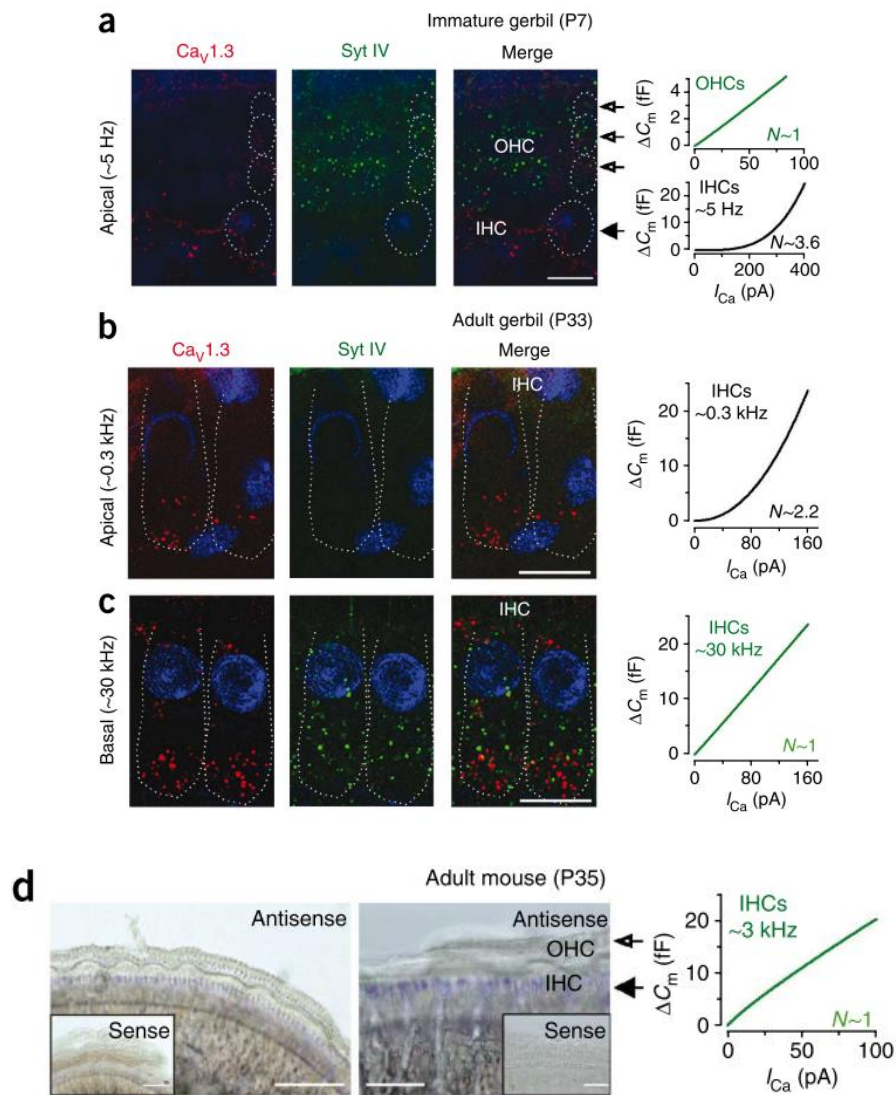
Figure 1.26:Immunostaining of CaV1.3 and Syt 4 proteins in immature and mature gerbil cochlea.

(a) Syt4 was found to be present in immature gerbil OHCs, not in IHCs. (b) Immunostaining of mature apical IHCs. (c) Immuno staining of mature basal IHCs. (d) In situ hybridization showing expression of Syt4 mRNA at the mature mouse IHCs. The right panel of (a)-(d) shows the relationship between the calcium current and capacitance change, indicating the Ca^{2+} exocytotic dependence. The scale bar in (a)-(c) represents 10μm, and in (d) it represent 200μm(left)and 50μm (right)respectively (modified from Johnson *et al.*, 2010).

1.9 Basigin Group Protein and hearing

1.9.1 Basigin Group protein

Basigin protein family consists of three members, Basigin (Bsg), Neuroplastin (Nptn) and Embigin (Emb). The gene *Bsg* and *Nptn* encode two isoforms of each kind of protein, Bsg1 and 2, and Np65 and 55 respectively, while gene *Emb* only encodes one product, Emb. Bsg1 and Np65 have one more extracellular Ig domain (Ig1, 2 and 3) than Bsg 2 and Np55 (Ig 2 and 3). For Emb, there are two Ig domains (Beesley et al., 2014)(Figure 1.27).
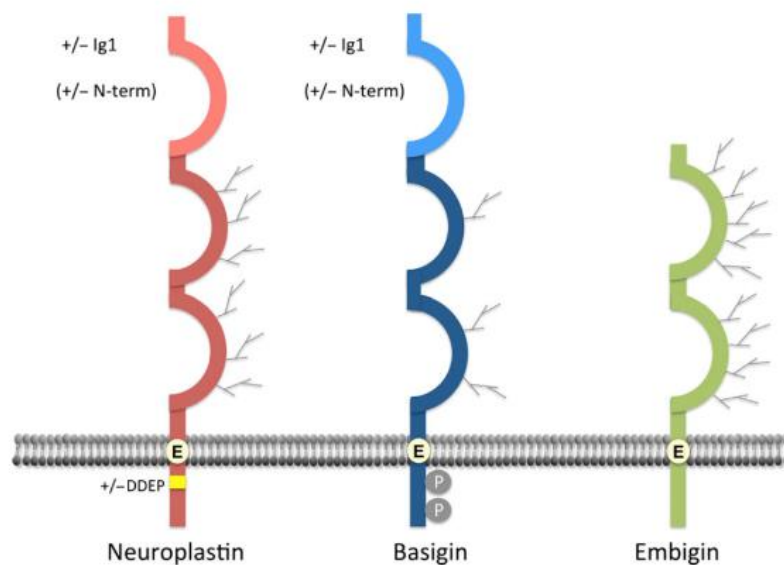
Figure 1.27:Structural features of the Basigin group proteins.

All three members have a transmembrane domain with a glutamate (E). In the cytoplasmic domain, Neuroplastins have alternative isoforms which contain a DDEP mini exon and Basigins have two phosphorylation sites. In extracellular parts, Neuroplastin and Basigin have isoforms which contain an extra Ig domain (± Ig1) while all three members contain two Ig domains (Ig 2 and 3)(modified from Beesley *et al.*, 2014).

It has been suggested that CAMs are involved in several cellular processes: formation, maturation, maintenance, and plasticity formation of synapses. Recently, it has been suggested that during synapse formation and stabilization, CAMs act as mediators to regulate the specificity between neural subtypes. Emb was shown to promote sprouting motor nerve terminals at the neuromuscular junction (Lain et al., 2009). The other member of the family, Bsg (Bsg1 and 2) was found to be involved in neuronal phoetal lymphocyte and extracellular matrix development in pathology research (Iacono et al., 2007). As for Neuroplastin, Np65 has been reported to be an important regulator of the number and function of excitatory or inhibitory hippocampal synapses (Herrera-Molin et al., 2014). The mediation of cell adhesion by Np-65 depends on homophilic trans-interaction between Ig1 domains. Previous research has shown Np-65 mediated neurite outgrowth *in vitro* and in the initial phase of rat spatial learning, suggesting a role of Np-65 in neural differentiation (Owczarek et al., 2011).

1.9.2 Neuroplastin 55 expression in mouse cochlea and its function in hearing

There have been some research investigating the function of Np55 and Np65 in hearing. Using *N*-ethyl-*N*-nitrosaurea (ENU) mutagenesis screen, researchers have been generating constitutional Np55 and Np65 knock-out mice.

In Np55 knock-out hearing research, scientists found that Np55 is expressed in the stereocilia of outer hair cells and required for normal outer hair cell function. The ENU induced mice were named as *audio-1*, which carry a T-to-A in the coding sequence of *Nptn* and the mutation is recessive as only the mutation is carried by both alleles were *audio-1* mice hearing impaired (Add Reference). The RT-PCR results of the research showed that in mRNA isolated from the organ of Corti, Np55 expression levels were much higher than which of Np65 from P7 to P28. Following *in situ* hybridization using Np55/65 probe and Np65-specific probe showed that at P4 the Np55/65 probe

detected strong expression in SGNs and the organ of Corti. However, the Np65-specific probe did not show signals in either hair cells, supporting cells or SGNs, indicating Np55 is the predominant *Nptn* isoform expressed in hair cells. Immunostaining experiments were used analysing the expression pattern of *Nptn* at protein level. In both histological section and whole-mount staining of organ of Corti at P7, expression of Np55/65 was observed (Figure 1.28 A and B). Interestingly, the signal can only be detected in the OHC stereocilia and it can be observed in all rows of stereocilia, and the signals are stronger towards the distal end and weaker at the base. Interestingly, although weak basolateral membrane expression can be observed, there is no expression of Np55/65 detected in IHCs. The *audito-1* mice did not show signals of Np55/65 expression (Figure 1.28 B and C). Immunogold staining of P7 and P60 OHCs and IHCs also showed Np55/65 expression at the OHC cell membrane surrounding the stereocilia not the IHCs (Zeng et al., 2016).
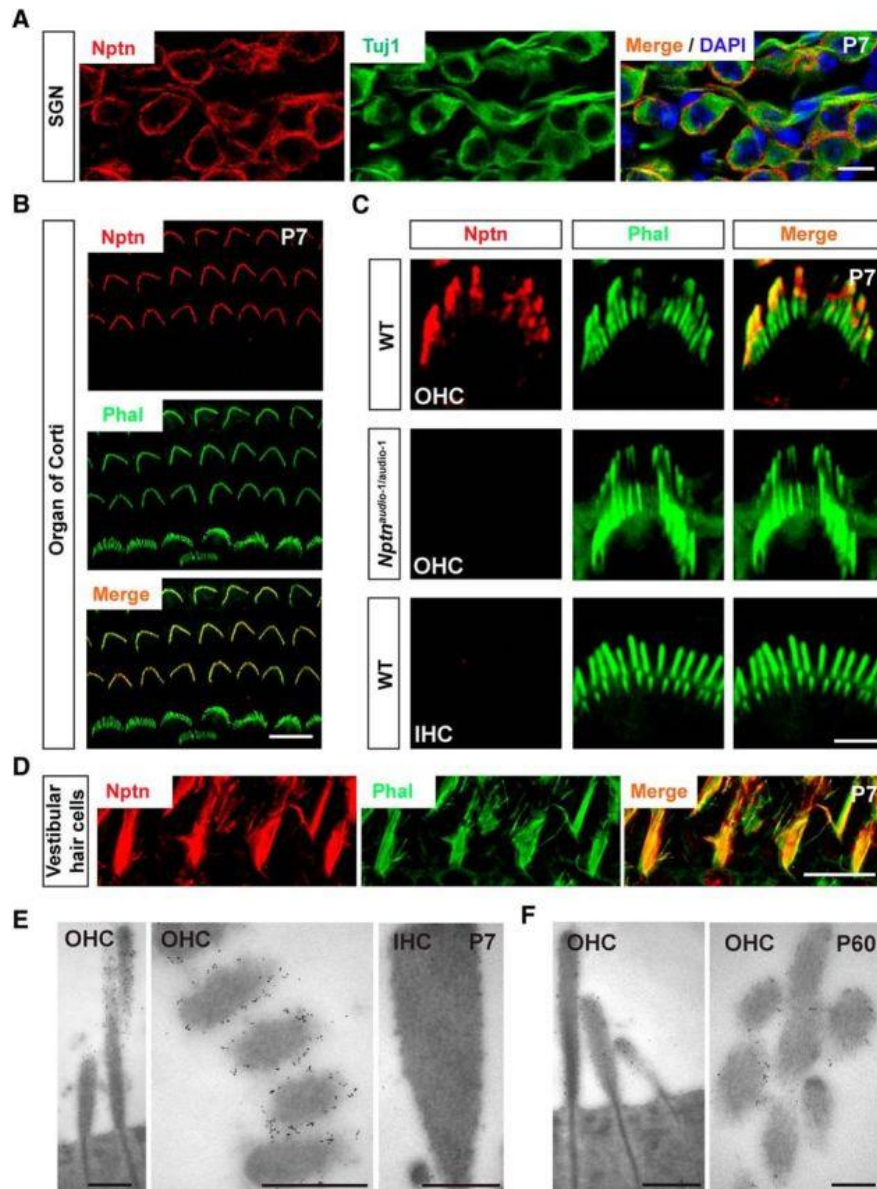
Figure 1.28: Immunostaining of audio-1 hair cells

A, Np55/65 (red) and Tuj1 (green SGN marker) labels localization of Np55/65 at the cell surface of SGN cell bodies. B, whole-mout cochlea staining of C57BL/6 mice at P7. Np55/65 (red) and phalloidin (green F-actin marker) showed Np55/65 staining on stereocilia of all three rows of OHCs. C, immunoreactivity near the distal ends of stereocilia, *audio-1* OHCs and WT IHCS did not show staining of Np55/65. D, vestibular hair cell expression of Np55/65. E,F, immunogold staining of *Nptn* at P7 and P60 stereocilia. A higher density of staining toward the upper part can be observed. Scale bars: A 10µm; B, 2µm; C,D, 10µm; E, 500nm (modified from Zeng et al., 2016).

The electron microscopy of *audio-1* mice showed that they had normal HC morphology between P14 and P40 along the whole cochlear duct (Figure 1.29A). Hair bundles' morphology starts to be altered when examined at P60 and became more obvious at P120. In P120 *audio-1* mice, there is about 25% hair bundle loss and the remaining hair bundles also show structural abnormalities (Figure 1.29B). In addition, scanning electron microscopy analysis on *audio-1* mice showed that the tectorial membrane in the mutant mice lack the coupling with the stereocilia hair bundles from P18, where the indentation that correspond to the stereocilia anchoring points is present in WT mice (Tsuprun & Santi, 1998).

The whole-cell mechanotransduction current tests on WT and *audio-1* showed that wild type OHCs had rapidly activating then adapted transducer currents (Xiong et al., 2012) and *audio-1* OHCs did not show significantly different saturated mechanotransduction current(Figure 1.29 C).
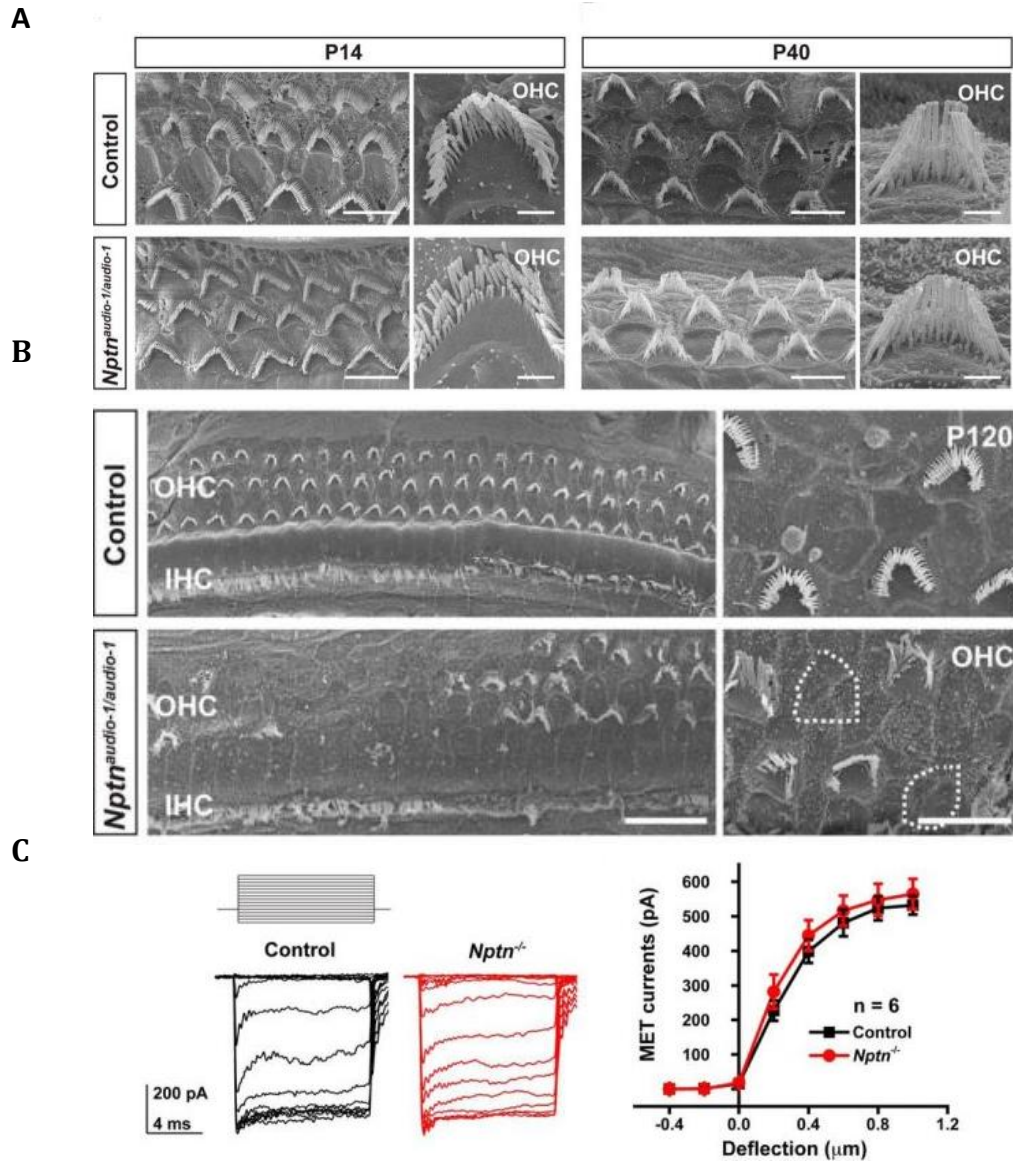
Figure 1.29:Electron microscopy and MET measurement of adult hair cells

A, Scanning electron microscopy of WT and *audio-1* mutant mice midapical cochlear hair bundles at P14 and P40. B, at P120, degeneration of OHCs found severe in homozygous *audio-1* mutant mice. C, Transduction currents of P7 WT and *Nptn-knock-out* mutant mice OHCs stimulated by stiff glass probe. The hair bundle deflection ranges from -400 to 1000nm (100nm steps), the holding potential was -70mV and each stimulation lasted 10ms. The current against displacement was plotted with mean ± SEM. The amplitudes of saturated mechanotransduction currents at maximal deflection are: WT 532 ± 27 pA, *Nptn* deficient 564 ± 44 pA (modified from Zeng et al., 2016).

Although the mechanotransduction of *audio-1* OHCs was normal, cochlear amplification was found to be affected. The method used is called *in vivo* volumetric optical coherence tomography vibrometry (VOCTV), which measures the displacement magnitudes and phases of BM and TM vibration (Lee et al., 2015). By normalizing the magnitude of BM and TM vibrations to those of the middle ear, a sensitivity ratio can be calculated to represent the cochlear amplification. For WT animals, there is a nonlinear amplification as increasing BM sensitivity correlates with decreasing stimulus levels (peak sensitivity move from 4-9kHz as the stimulus reduced). For *Nptn*-knock out mice, the peak BM sensitivity peak sensitivity stayed at nearly 4kHz regardless of the stimulus change (Figure 1.30A). Distortion product otoacoustic emission (DPOAE) measurements on P21 and P60 mice confirmed the lack of otoacoustic emissions. The DPOAEs present two primary tones (f1 and f2) to generate mechanical distortions in the inner ear. After OHCs amplifying the distortion, DPOAEs measure the amplified distortion that is propagate back through the middle ear and ear canal as the magnitude of sound emission (Ashmore, 2008). In *audio-1* homozygous mice at P21 and P60, all frequencies tested lacked DPOAEs, indicating the defected OHC function (Figure 1.30). In summary, previous research on Np55 concluded that it is expressed in the stereocilia of OHCs, and it is essential for OHC function.
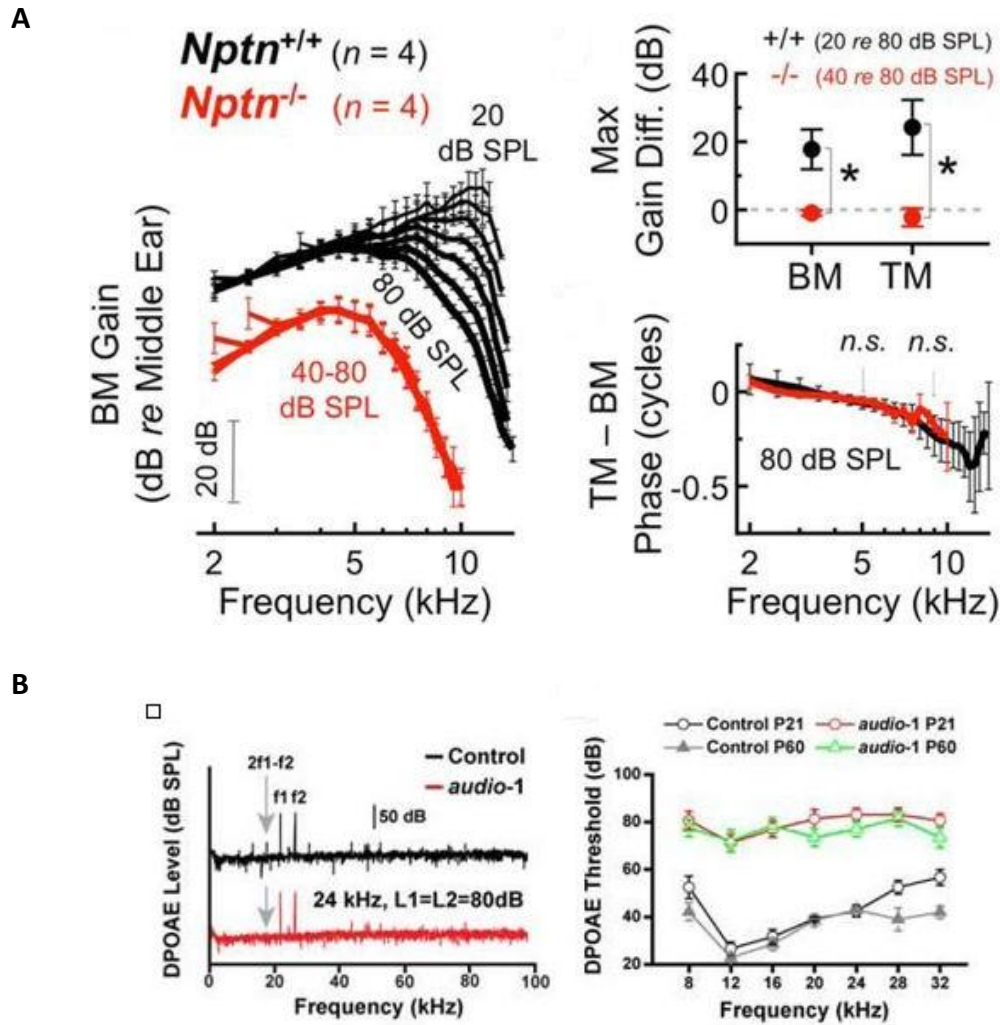
Figure 1.30:BM sensitivity and DPOAE measurement

A, Normalized BM displacement to middle ear displacement taken as BM sensitivity. WT OHC BM sensitivity increases with decreasing stimulus level, the tuning also became sharper. The *Nptn⁻/⁻* mice show a non-changing BM sensitivity to all stimulus level. The maximal cochlear gain at BM and TM are plotted, showing a significantly lower value from *Nptn⁻/⁻* mice. However, the phase of the TM relative to the BM was not significantly different. B, DPOAE response spectra from WT and homozygous *audio-1* mutant mice at a single stimulus condition. The grey arrow indicates the 2f1-f2 peak is missing in *audio-1* mutant mice. The DPOAE thresholds of P21 and P60 mice at different frequencies are plotted, *audio-1* mutant mice showed a much higher threshold, indicating lack of OHC function (modified from Zeng et al., 2016).

1.9.3 Neuroplastin 65 expression in mouse cochlea and its function in hearing

Recently, a mouse model of early-onset hearing loss, *pitch* was identified. The hearing loss was due to *Nptn* loss-of-function-mutation (*Nptn^pitch^*) as a result of N-ethyl-N-nitrosourea (ENU)-induced lesion and both *Nptn* encoded isoforms (NP65 and NP55) are affected. In WT whole cochleae qPCR analysis, it was found that the Np55 expression level remained stable between P4 and P27 while the Np65 expression increased about 7-fold at P12 compared with the level at P4 (Figure 1.31A). Using commercially available Np-65 antibodies, immunolabeling studies revealed the localization of Np65 proteins within the inner ear. The immunolabeling of P16 *Nptn^pitch/+^* mice showed that Np65 labeling was at the cuticular plate of the IHCs and OHCs as well as the basolateral region of the IHCs (Figure 1.31B). Wholemount immunolabeling of P16 *Nptn^+/+^* confirmed the IHC basolateral localization of Np65. *Nptn^pitch/pitch^* mice did not show Np65 immunolabeling (Figure 1.31C) and Np55 was not detected in P16 wild-type mice, indicating the absence of Np55 protein in P16 mice and absence of Np65 protein in the IHCs of pitch mutant mice.
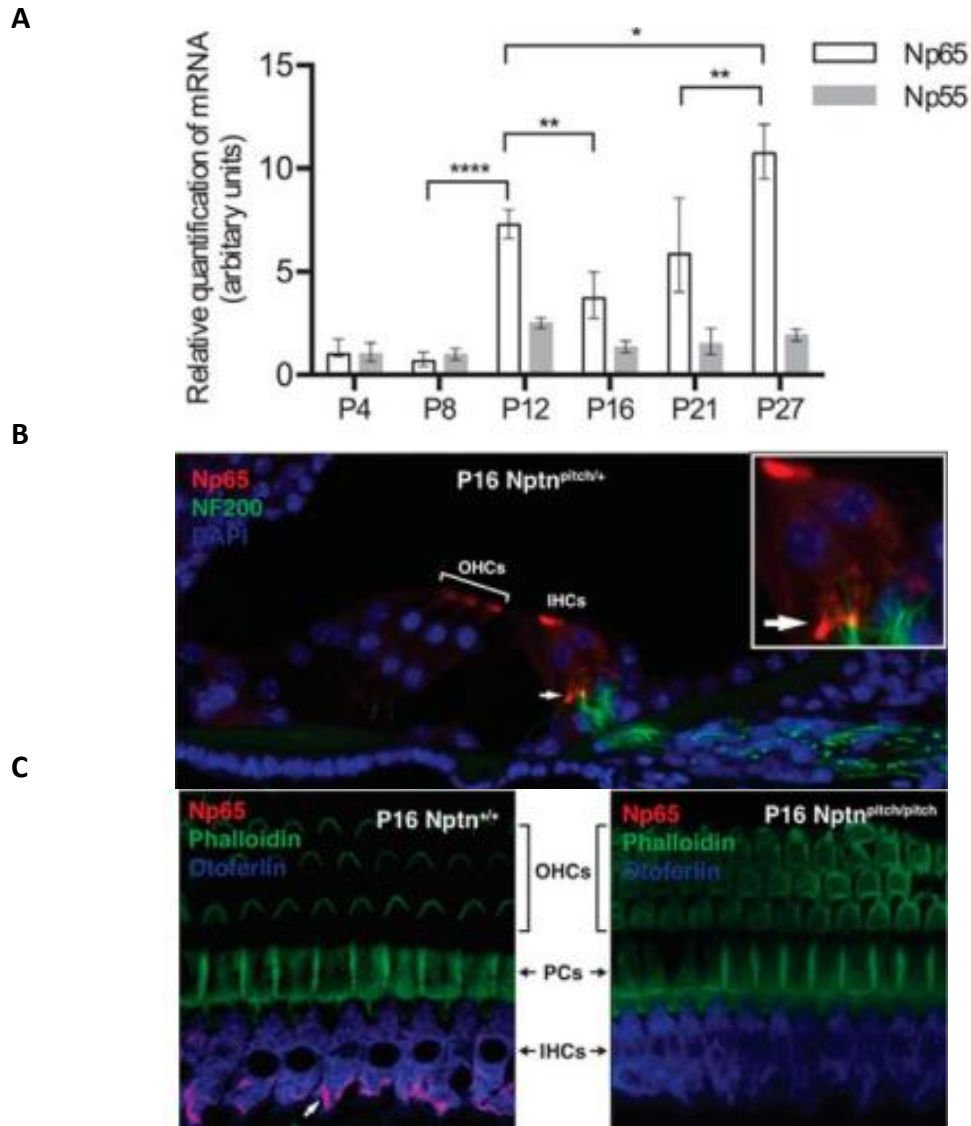
Figure 1.31:Checking Neruoplastin65 expression

A, mRNA level of Np55 and NP65 in from whole cochleae lysates at P8, P12, P21 and P27. The expression level at P4 was used as the reference. Np65 expression increases significantly (students' *t* test) from P8 to P12 and remains to be high until P27. B, mid-modiolar section of *Nptn^pitch/+*^ labelled with DAPI (blue), Np65 antibody(red) and anti-neurofilament-200 (green). Np65 staining was found at the cuticular plate of the IHCs and OHCs as well as basolateral region of the IHCs (arrow and inset). C, wholemount cochlear immunostaining, labelled with anti-Np65(red), anti-otoferlin(blue) and phalloidin (green). Np65 labeling was not found at the pillar cells (PCs) but only at the basolateral membrane of IHCs (modified from Carrott et al., 2016).

In terms of Np65's function in cochlea, previous research has been focusing on IHC synaptogenesis, MET function and exocytosis. MET current recordings on P6 OHCs did not show significant difference between the $Nptn^{pitch/pitch}$ and the WT OHCs. The ABR test on P16 and P27 mice showed that absence of Np65 affected hearing threshold of $Nptn^{pitch/pictch}$ mice. At both P16 and P27, $Nptn^{pitch/pictch}$ mice showed elevated hearing thresholds compared to the control groups ($\geqslant$70 dB SPL at P16 $\geqslant$85 dB SPL at P27, Figure 1.27A). As for synaptogenesis, the Neuroplastin deficient mice showed mismatching between IHC ribbons and the postsynaptic region of the SGNs. In the immunolabeling studies, anti-Ribeye (presynaptic IHC ribbon component, green) and anti-GluR2 antibody (an AMPA receptor that localized to the afferent postsynaptic density, red) were used to label the pre- and post-synaptic regions (Figure 1.32 A, B). The number of mismatched Ribeye and GluR2 puncta was significantly higher in $Nptn^{pitch/pictch}$ when compared to $Nptn^{+/+}$ mice (Figure 1.32 D, E)
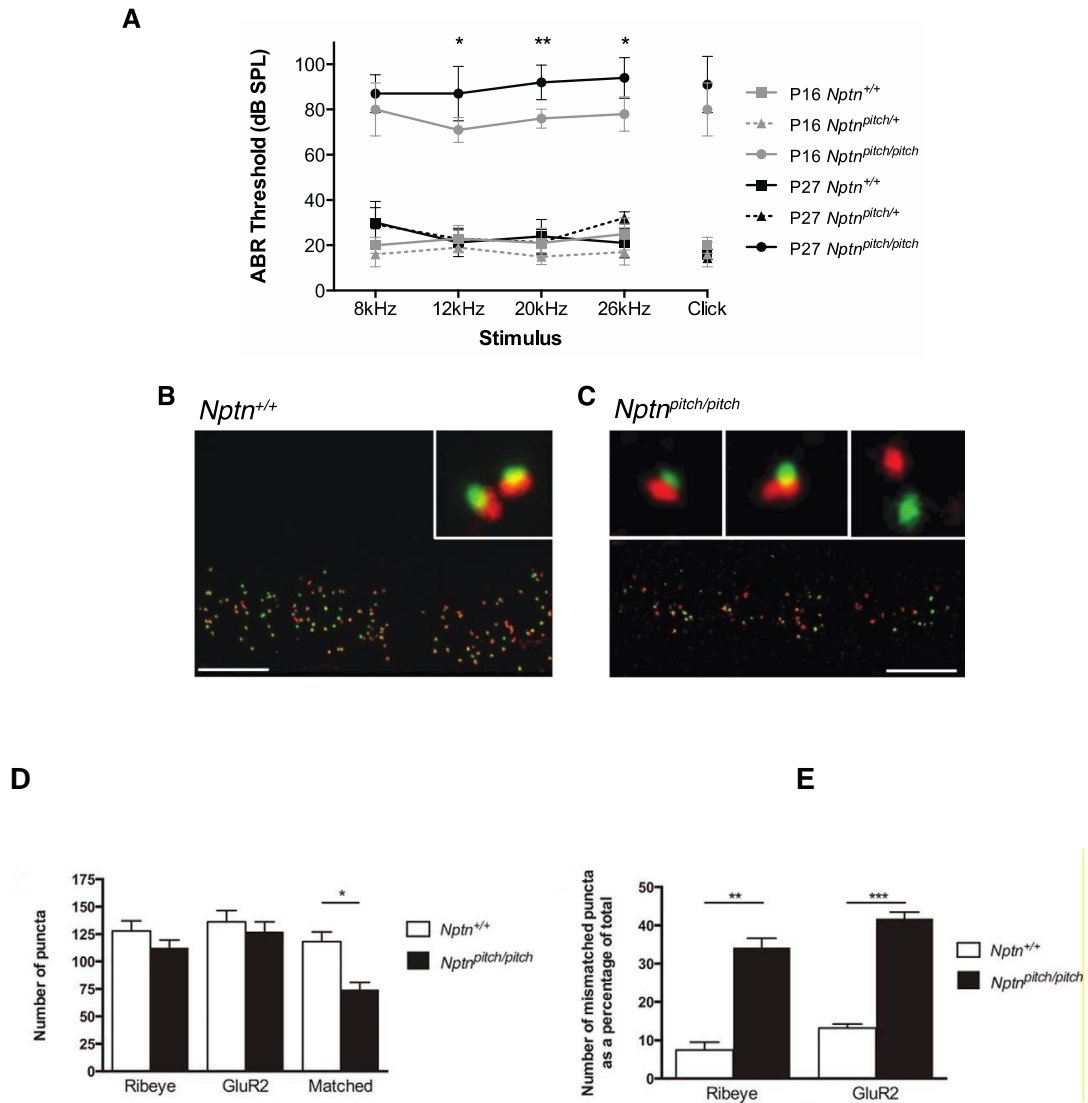
Figure 1.32:Nptn identified as a deafness gene.

(A) Loss of function of *Nptn* (*Nptn^pitch*) homozygotes (*Nptn^pitch/pitch*) showed hearing loss in P16 and P27 mice. (B) Juxtaposed pre-synaptic and post-synaptic markers (anti-Ribeye-green for pre-synaptic and anti-GluR2-red for post-synaptic) indicate normal IHC ribbon synapses in wild type mice (*Nptn^+/+*). (C) *Pitch* mice (*Nptn^pitch/pitch*) showed a decreased number of 'matched' synapses. (D): Quantification of the Ribeye-labeled and GluR2-labeled puncta as well as the matched puncta in wild type mice cochlea and *Nptn^pitch/pitch* cochlea. €: The percentage of mismatched Ribeye-labeled and GluR2-labeled puncta compared to the total number of Ribeye and GluR2 puncta*p<0.05, **p<0.01, ***p<0.001. Scale bar: 20μm (modified from Carrott *et al.*, 2016).

The capacitance measurement results also indicated that neuroplastin is required for exocytosis in adult IHCs. The protocol involved applying 50ms voltage steps to test readily releasable pool (RRP) (Johnson et al., 2008). ΔC_m of the control group ($Nptn^{+/pitch}$) and the mutant group ($Nptn^{Pitch/Pitch}$) were similar but the maximal I_{Ca} of the adult *pitch* mutant IHCs (n=9) was slightly higher than the control group (n=7, Figure 1.33 A-C, *p*<0.02). The change in ΔC_m as a function of I_{Ca} was plotted to indicate the exocytotic Ca^{2+} dependence. The synaptic transfer function measures the dependence (Johnson et al., 2010), the exponent of the fit in the mutant group was power of 3.2 ± 0.4 (*n* = 11), and the power of control IHCs was 1.1 ± 0.1 (*n* = 10, *p* < 0.0001, Figure 1.33D). Such results showed that mature *pitch* mouse IHCs' RRP are less sensitive towards Ca^{2+} influx to trigger Ca^{2+} dependant exocytosis (Carrott et al., 2016).

The Kinetics of Ca^{2+} dependant exocytosis was also measured. Figure 1.33E showed data of synaptic vesicle emptying rate under varying duration of -11mV depolarizing stimulus. During short stimuli (≤100 ms), the data represents the size of RRP, while the longer stimuli induce vesicle release from a SRP, which is located further away from Ca^{2+} channels(Johnson et al., 2008; Moser & Beutner, 2000; Von Gersdorff et al., 1996). According to Figure 1.33E, the RRP size of the two groups was similar but the *pitch* mouse IHCs had a much smaller SRP. The relative pool filling rates of SRP was examined using repetitive stimuli. The cells were given a train of 1s steps to -11mV from the holding potential. The cumulative ΔC_m results (Figure 1.33G) showed that the SRP release in *pitch* mouse IHCs was more easily saturated comparing to the control IHCs. The individual ΔC_m results also showed earlier depletion of the SRP in *pitch* IHCs(Figure 1.33H)(Carrott et al., 2016).
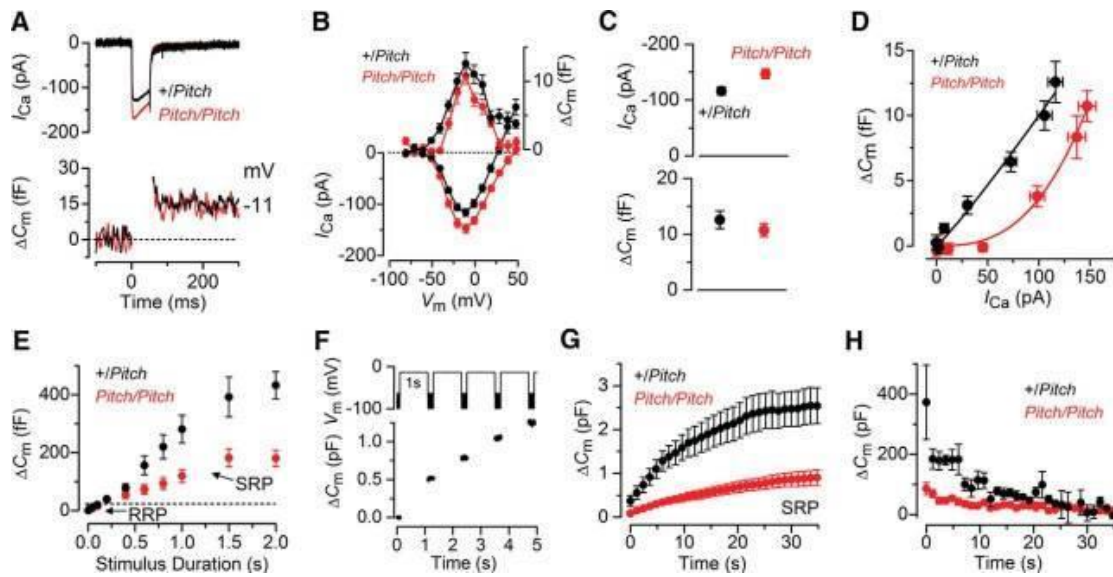
Figure 1.33: Δ Cm measurement of mature IHCs of pitch and control groups.

A, example results of I_{Ca} and corresponding ΔC_m under 50ms stimulus, only maximal response shown. B, I_{Ca} and ΔC_m plotted against V_m respectively. C, Maximal peak I_{Ca} and ΔC_m values for the control and *pitch* groups. D, Synaptic transfer curves, $\Delta C_m = cI_{Ca}^{N}$ where c is a scaling coefficient and the exponent N is the power. E, Average ΔC_m in response to varying voltage steps (2ms to 2s). F, ΔC_m measured from repetitive voltage steps to -11mV, eliciting SRP. G and H, cumulative and individual ΔC_m measured from trains of 1s stimuli protocol (modified from Carrott et al., 2016).

1.9.4 Aims and Objectives

Current findings on Neuroplastin focus on several aspects: As for expression, the expression of Np55 is mainly in OHC stereocilia while the Np65 are mainly found in cuticular plates of both IHCs and OHCs as well as basolateral part of IHCs. Functional wise, the function Np55 in cochlear hair cells are mainly about structural support of stereocilia and sound amplification. Np65 was found to be important in matching pre and post synaptic region of IHC and SGNs, as well as in exocytosis.

The findings furthered the understandings of Np55 and 65 but there are still gaps to fill in. As for expression, previous papers did not come to a common agreement of which isoform of neuroplastin is specifically expressed in which part of the hair cell. In terms of functional research, although Np65 was found being expressed in basolateral part of IHCs, there was no previous data investigating the basolateral current profile of the cochlear hair cells.

One aim of my PhD neuroplastin project was to check the expression of neuroplastin in cochlear hair cells using $Nptn^{tm1b/tm1b}$ mouse model to try to find better evidence of Np65 expression. The hearing tests and the molecular biology experiments were performed by Dr Newton, from our collaborative lab led by Dr Mike Bowl in MRC Harwell. The other aim of the neuroplastin project was to test basolateral functions of IHCs and OHCs using $Nptn^{tm1b/tm1b}$ mouse model. Patch clamping experiments testing basolateral K^+ current response as well as Ca^{2+}-evoked exocytosis of hair cells were performed.

As for Otoferlin, previous research has found that otoferlin is important for both types of hair cells' exocytosis using constitutive knock-out models. But there is an important question needs answering: are otoferlin just being important for development of hair cell exocytosis or it also plays a role in maintaining the exocytotic function of hair cells after maturation?

The Aim of otoferlin project during my PhD was to find a reliable conditional-knock-out mouse model, which can wait hair cells for their maturation before conditionally delete otoferlin to test exocytotic functions of mature IHCs. To achieve this, Otoferlin-tm1c line was crossed with different Cre lines for characterization.

2 General Methods

2.1 Ethics Statement

All the animal work was performed under the Animals (Scientific Procedures) Act 1986, the Home Office licensed, which is also approved by University of Sheffield Ethical Review Committee.

2.2 Animals

The animals used for the study were obtained from Mary Lyon Centre and MRC Harwell. The animals used for the Neuroplastin research were Neuroplastin-tm1b mice. The mice used for otoferlin research were Otoferlin-tm1c (flanking exon 10-11, generated by MRC Harwell from C57BL line) X Barhl1-Cre (Kolla et al., 2020) X Tdtomato, Otoferlin-tm1c X VGlut3-Cre (C. Li et al., 2018) X Tdtomato and Otoferlin-tm1c X Myo15-Cre (Jackson lab). All the mice were maintained at the university of Sheffield under a 12-hour light-dark cycle by the Home Office guidelines. The culling of the animals was performed using a Schedule1 method (cervical dislocation). Mice at the 1st to 5th postnatal week were used.

2.3 Tamoxifen Injection

Tamoxifen (T5648-1G, Sigma) was used to make a solution in Corn Oil (Sigma) at a final concentration 20µg/µl. The prepared tamoxifen solution was aliquoted in 2ml tubes and stored under -20°C, away from light exposure. When experimental mice grew big enough, normally above 9.0g, two doses of 0.2mg/g of tamoxifen with a gap of 48 hours were injected. As tamoxifen was toxic, during the preparation and injection, lab coat, face mask and double gloves were worn as protection. After the injection, the mice under procedure were carefully observed and weighed every day until they had reached their pre-injection weights. Humane end point was weight loss over 20%. The mice were kept until the day of the experiment.

2.4 Single-cell electrophysiology

2.4.1 Experimental stage and preparation

The set-up of the experiment is a combination of an upright microscope (Olympus BX51) and a custom-made rotating stage (connected to a thermocouple to control the recording temperature) affixed to it. The microscope is equipped with x60 water immersion objective (LUMPlanFL, Olympus) and x15 eyepieces and were placed on an anti-vibration table (TMC, USA) in a Faraday cage. The set-up then can be protected from electronic noise.

During the experiments, the cochlear spiral was placed in a chamber, which was mounted on the rotating stage, a continuous flow of extracellular solution was applied across the chamber at different speed (2-9ml/min), using a 65µF-capacitor-grounded pump (Cole-Parmer, USA).

A set of capillaries are placed to help with the experiments. The recording pipette was attached to the head-stage of the amplifier (Optopatch, Cairn Research Ltd, UK) and controlled by a micromanipulator (PatchStar, Scientifica, UK). A cleaning pipette, a grounding electrode and a thermal meter were also placed during the experiment (Figure 2.1A).

The patch-clamping experiments of membrane capacitance measurement is achieved by an integrated self-balancing lock-in amplifier (Optopatch, Cairn Research Ltd, UK). The traditional lock-in amplifier technique was firstly described by Neher and Marty (Marty and Neher, 1982). The way to measure the cell membrane capacitance change was to give a current into the cell via a patch pipette in whole-cell mode, compensating the electrode capacitance and then consider the system as a single capacitor being charged and discharged via the electrode series resistance (R_s). The lock-in amplifier has two detectors, and the two detectors had 90° shift from each other. During the recording, a sinusoidal command frequency is applied to the cell. When there was a small change in either the resistance or capacitance, a residual

sinusoidal current will appear, and the phase of which will differ by 90° according to which of these parameters has changed (Johnson et al., 2002).

The traditional lock-in amplifier is good at small capacitance changes where the output stays linear with the small capacitance change. However, for measurement of bigger changes with high time resolution, a modified method is needed. The later modified version, which was used in our experiments, had an integrated system, allowing the system to use the lock-in amplifier output signals compensating electronic adjustments of the resistance and capacitance control settings. The principle of the modified system is that, instead of using the signals from the two detectors, a negative-feedback loop is built in resistance and capacitance control settings. So in this mode, any change in resistance or capacitance will be automatically readjusted. The so called 'track-in' mode of the capacitance measurement provided linear and calibrated resistance and the capacitance measurement results came out with high sensitivity and significant time resolution(Johnson et al., 2002). The simplified circuit is illustrated in Figure 2B.

For current recordings, the recorded analogue signals were filtered at 2.5kHz or 5kHz with a Bessel low-pass filter to preserve the signals better across different frequencies. The current signals were then converted by Digidata 1440 A converter (Axon Instruments, USA) and sampled at 5 kHz or 10 kHz by the pClamp 10 software (Axon Instruments, USA), before being stored for off-line analysis.
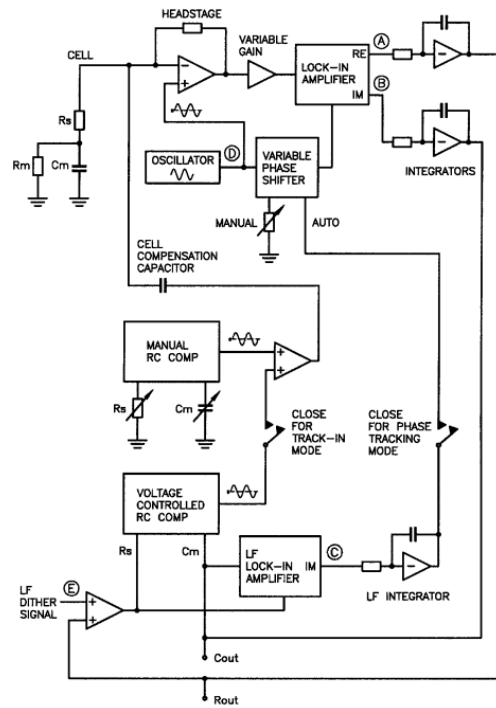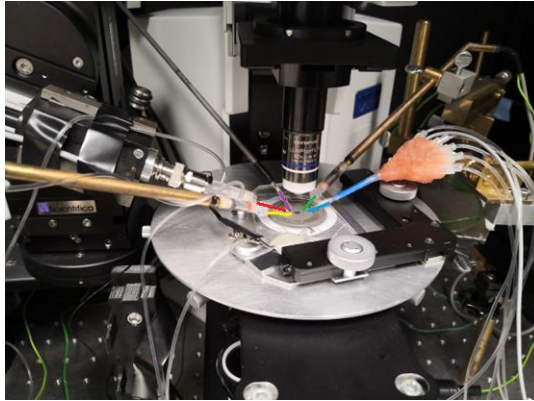
Figure 2.1: Set-up of the experiment stage and the concept of track-in amplifier system

A, Experiment stage set-up: red, patch-pipette, yellow, cleaning pipette, green: ground electrode, blue: perfusion tube, purple: thermocouple.

B, The 'track-in' system for membrane capacitance measurement. The system has two components, one is a traditional lock-in amplifier, which applies to membrane capacitance (C_m) and series resistance (R_s) measurement in whole-cell mode. The other component is an additional circuitry added in a side chain to form the 'track-in' amplifier system. The side circuitry can only be activated during capacitance measurement. In track-in mode, the output from the lock-in amplifier is integrated to adjust the compensation settings of the C_m and R_s, keeping the lock-in amplifier signals near zero, which makes the system self-balancing, leading to a linear response and a better capacitance measurement result without losing sensitivity or significant time resolution(Figure 2B modified from Johnson et al., 2002).

2.4.2 Experimental Solution

To keep the basolateral part of the hair cells under a near-physiological condition, the extracellular solution was used in the bath of the chamber, and it was continuously supplied through the pump. The extracellular solution also used 1X of Amino acids (11130-036, Gibco, USA) and vitamins (11120-037, Gibco, USA) as supplement. The composition of the extracellular solution is listed in Table 2.1. The pH of the solution was adjusted to 7.48 using 4M NaOH. The osmolality of the solution was around 308 mOsm/kg.

The recording pipettes were filled with intracellular solution, which was KCL or CsGlutamate-based. The KCL-based intracellular solution was used for total current and membrane potential recordings. The pH of the solution was adjusted to 7.28 with 1M KOH and the osmolality was around 293 mOsm/kg. For calcium current recordings and capacitance measurements, the intracellular solution was CsGlutamate-based, which was used to minimize the effect of potassium towards the recordings. The pH was adjusted to 7.28 with 1M CsOH and osmolality was also around 290 mOSM/kg. The detailed composition of the intracellular solutions is listed in Table 2.2

Table 2.1: Extracellular solution's composition

Component	Final concentration (mM)
NaCl	135
CaCl$_2$	1.3
KCl	5.8
MgCl$_2$	0.9
HEPES	10
Glucose	5.6
NaH$_2$PO$_4$	0.7
Na Pyruvate	2

Table 2.2: Intracellular solutions' composition

Component	Final concentration (mM)	
	KCl-based	Cs Glutamate-based
KCl	131.0	
CsCl		20
L-Glutamic Acid		110
EGTA-KOH	1.0	
EGTA-CSOH		1.0
GTP		0.3
$MgCl_2$	3.0	3.0
Na_2Phosphocreatine	10.0	10
Na_2ATP	5.0	5.0
HEPES	5.0	5.0

2.4.3 Pipettes

With a pipette puller (Narishige Instruments, Japan), pipettes for the experiments were pulled using different glass capillaries. The cleaning pipettes were pulled using borosilicate glass capillaries (30-0062, Harvard Apparatus, UK) and the tip diameter of which was around 2µm. Before experiments, the cleaning pipettes were filled with extracellular solution, connected to a syringe to apply negative or positive force towards the experimental cells. Patch pipettes were pulled from soda glass capillaries (1413027, Hilgenberg, Germany) To minimize the capacitance, the patch pipettes were coated with wax (Mr Zoggs SexWax, USA). The pipette resistance in extracellular solution was between 2-4 MΩ. When filled with KCl based solution, the patch pipette resistance for OHCs was between 3-4 MΩ and for IHCs it was 2-3 MΩ. When using CsGlutamate-based solution, the resistance for IHCs was 3-4 MΩ.

2.4.4 Tissue preparation

Cochleae of the experimental mice were removed from temporal bone and placed in ice-cold extracellular solution. Under a dissecting microscope (Leica, Germany). The dissection started with exposing cochlear spiral with the organ of Corti on the edge using tweezers. After removing stria vascularis, the apex of the cochlear spiral (including organs of Corti) was cut off from the modiolar part and then transferred to the chamber with extracellular solution, immobilized with nylon mesh attached to a steel ring. The transparent tectorial membrane covering the hair cells was removed in the chamber to expose hair cells (Figure 2.2).
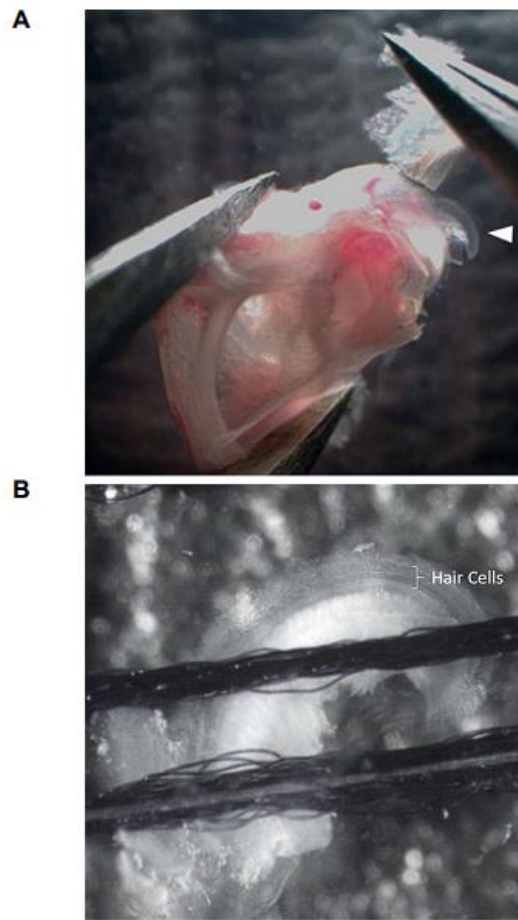
Figure 2.2：Tissue preparation for whole-cell patch clamping.

A, apical coil revealed by removing the bone from the top. B, The apical part of the organ of Corti placed under a nylon mesh in the experiment chamber.

2.4.5 Whole cell patch-clamp recordings

Using cleaning pipettes connected with syringes, positive or negative forces can be applied to remove the surrounding supporting cells of the hair cells. When the basal pole of the hair cells was exposed, the recording pipette was placed into the chamber and lowered to a close position towards the cell. During the process a continuous positive pressure was given by another syringe to prevent any blockage. At this stage, the offset of the recordings was adjusted. Then the patch pipette was placed onto the cell and then the positive pressure was turned into negative pressure to form a seal, the resistance can reach about 1GΩ. The holding potential of the cell was adjusted to -84mV. When the cells were charged, a transient current was generated, which can be calculated and compensated by the amplifier. During the process, a +10mV voltage was applied to the cell and the fast component of the transient was compensated using the amplifier. After the compensation, a sharp negative pressure was applied to break through the cell membrane, which led to a whole-cell patch-clamp configuration. The breaking through would be confirmed by a sharp reduction of resistance and then the cell capacitance can be calculated and measured by compensating slow component of the transient current.

For different purposes, the experiments were performed under different temperature. Basolateral current and voltage recordings were performed at room temperature (23–25 °C). Capacitance measurement and Calcium current recordings were performed at near body temperature (32–35 °C) to better activate the calcium channels. The recordings were acquired using pCLAMP software, during data acquisition, membrane potentials were corrected for the voltage drop based upon the series resistance (4-9MΩ) and 80% compensation was made using the amplifier.

2.4.6 Extracellular superfusion

During capacitance measurements, unaffected calcium current recordings were required, so a CsGlutamate-based intracellular solution containing potassium channel blockers was used. In addition, an extracellular solution containing potassium channel blockers were used. The channel blockers are a combination of tetraethylammonium chloride (TEACl, 86614, Sigma-Aldrich), linopirdine (1999, Tocris), 4-aminopyridine (4-AP, 275875, Sigma-Aldrich) and Apamine (1652, Tocris). During the experiment, the potassium blocker-containing extracellular solution was superfused using gravity flow. The composition of the solution was listed in Table 2.3. The osmolality of solution was 312 mOsm/kg.

Table 2.3: Superfusion solution's composition for capacitance measurement

Component	Final concentration (mM)
NaCl	110.0
KCl	5.8
$MgCl_2$	0.9
$CaCl_2$	1.3
NaH_2PO_4	0.7
HEPES	10.0
Glucose	5.6
TEACl	30
4-AP	15
Linopirdine	80µM (only when necessary)
Apamin	300nM (only when necessary)

2.5 Data analysis

The analysis of the recordings was based upon Clampfit software (Molecular Devices, USA) and OriginPro software (OriginLab, USA).

A liquid junction potential of -4mV and -11mV (measured between electrode and bath solution) were applied for chloride-based and glutamate-based intracellular solution, respectively, using Clampfit software. Leakage subtraction was also performed in Clampfit software when necessary. The leak conductance was calculated using Ohm's law:

$$V = R \times I = 1/G \times I,$$

In the equation, V is the voltage, R is the resistance, G is the conductance and I is the current. The resistance difference was calculated from current size at -70mV and -80mV, where no ion channel is activated.

The current analysis was performed in OriginPro software. Size of the steady current was measured between 145-165ms from the onset of the depolarizing voltage steps. Size of the fast potassium current was measured between 1.2-1.6ms. Calcium currents were measured at the peak. Current-voltage curves and capacitance-voltage curves were plotted using OriginPro software.

Statistical analysis was performed in Prism software (GraphPad Software, USA). T-test was used to compare between two groups (usually wild type and mutant group). For multiple dataset, one-way ANOVA or two-way ANOVA was used. The p-value for the statistical significance was set at 0.05.

2.6 Immunofluorescence

Cochleae were first fixed with 4% paraformaldehyde (PFA) in phosphate-buffered saline (PBS, pH 7.4) for 20 minutes at room temperature, then the organs of Corti were dissected in PBS. The PFA was washed off using PBS.

Blocking solution was made of PBST (0.5% Triton X-100 in PBS) with 5% normal goat (# 31873, Invitrogen) serum. After PBS wash, the organs of Corti were incubated in the blocking solution for 1 hour at room temperature.

Primary antibodies were diluted in PBST with 1% normal goat serum and then applied towards the organs of Corti for overnight incubation (37°C). For otoferlin experiments, the primary antibodies were mouse anti-otoferlin and rabbit anti-Myo7a (Table 2.5). In addition, the primary antibodies for neuroplastin and PMCA are also listed. The immunohistochemistry experiments for neuroplastin and PMCA is performed by Dr. Sherylanne Newton from Dr Michael R. Bowl group, MRC Harwell.

Secondary antibodies were diluted in 1:1000 in PBST with 1% normal goat serum. After overnight incubation in primary antibodies, the solution was washed off with PBS and organs of Corti were incubated in secondary antibodies for 1 hour incubation at 37°C. The secondary antibodies used were: goat anti-mouse IgG1 Alexa Fluor 568 (Invitrogen), Goat anti-rabbit IgG Alexa Fluor 405 and 488 (Invitrogen), goat anti-mouse IgG1 Alexa Fluor 405 and 488.

VECTASHIELD (H-1000, VECTOR Labs) was used to mount samples. A1 confocal microscope (Nikon Instruments, Japan) with 60x oil objective (CFI Plan Apo) was used to acquire confocal images with help of NIS-Elements software (Nikon Instruments, Japan). Photos were processed with Fiji ImageJ software and Zen software.

Primary antibody	Species-Isotype	Catalogue number	Company	Concentration
Otoferlin	Mouse-IgG1	Ab53233	Abcam	1:200
Myo7a	Rabbit-IgG	25-6790	Proteus Biosciences	1:500
Neuroplastin	Sheep anti-NP	AB2715517	R and D Systems	1:200
Np65	Goat anti-Np65	AB2155920	R and D Systems	1:100
PMCA	Mouse anti-PMCA 5F10	AB2061566	Thermo Fisher Scientific	1:200
PMCA1	Rabbit anti-PMCA1	AB2756567	Alomone Labs	1:200
PMCA2	Rabbit anti-PMCA2	AB303878	Abcam	1:200

Table 2.4: Primary antibody list

2.7 Genotyping by polymerase chain reaction (PCR)

Polymeric chain reaction (PCR) was used for amplification of the genomic DNA from all experimental mice. Tail samples were taken from experimental animals of all ages, while the ear clips were taken from mice which were older than P14. Tiny tail biopsy was performed on younger mice (from P2 to P12) for genotyping.

The DNA was extracted using lysis buffer that contains 25mM NaOH and 200µM EDTA under 98°C and the reaction was stopped by 40Mm TrisHCL (pH 5.5). PCR reactions were set up in 2X GoTaq mastermix. For each reaction, 1µl DNA was added to 19µl of master mix, which contains 10µl Gotaq mastermix, 1µl forward primer and 1µl reverse primer and 7µl water. The PCR programmes were differently designed for each kind of primers. The detailed list is shown in Table 2.5

Table 2.5: Primer list

Strain	Primer 5'-3'	Protocol	Expected bands
Nptn-tm1b Wt	WT F: TGGCCCTTGGTTTTCAGTAG WT R: AGAGGGCCAATTTCATACCC	95°C-5min,95°C-30sec,60°C-30sec,72°C-30sec(repeat 2-4 X35),72°C-5min	Wt~470bp,
Nptn-tm1b Mut	LacZ F: CCAGTTGGTCTGGTGTCA	95°C-5min,95°C-30sec,60°C-30sec,72°C-	Mut~450bp

	3armWTR: CCTAAACAGGGAGAGAGCT	30sec(repeat 2-4 X35),72°C-5min	
Otof-tm1c	5armWTF: TCCCAGGTAGCACTTGGTTT Crit WTR: GTGTAGAAGAACCCCGACCA	95°C-5min,95°C-30sec,60°C-30sec,72°C-30sec(repeat 2-4 X35),72°C-5min	Wt~230bp, Mut~350bp
Myo15-Cre	P1: AGGGACCTGACTCCACTTTGGG P2: TGGTGCACAGTCAGCAGGTTGG	95°C-5min,95°C-30sec,65°C-30sec,72°C-30sec(repeat 2-4 X35),72°C-5min	Myo15-Cre~500bp, band=Cre, no band =Wt
Barhl1-Cre	Cre F: CATTTGGGCCAGCTAAACAT Cre R: TAAGCAATCCCCAGAAATGC	95°C-5min,95°C-30sec,55°C-30sec,72°C-30sec(repeat 2-4 X35),72°C-5min	Barhl1-Cre~233bp, no band=Wt

Vglut3-Cre	Vglut3 F1: GCTGGTACACTACAGCGGAGTCATC Vglut3 F2: TGCAAGAACGTGGTGCCCCTCTATG Vglut3 R: TTAATCTCCCCCTTTCCCACGATTTGG	95°C-5min,95°C-30sec,60°C-30sec,72°C-30sec(repeat 2-4 X35),72°C-5min	Wt~407bp, Mut~310bp
Tdtomato Wt	TdtomatoFW: AAGGGAGCTGCAGTGGAGTA TdtomatoRV: CCGAAAATCTGTGGGAAGTC	95°C-5min,95°C-30sec,60°C-30sec,72°C-30sec(repeat 2-4 X35),72°C-5min	Wt~300bp,
Tdtomato Mut	TdmutFW: GGCATTAAAGCAGCGTATCC TdmutRV: CTGTTCCTGTACGGCATGG	95°C-5min,95°C-30sec,60°C-30sec,72°C-30sec(repeat 2-4 X35),72°C-5min	Mut~200bp

3 Results

3.1 Neuroplastin is essential for hair cell mechanotransduction, maturation and homeostasis

3.1.1 Introduction

In previous research focusing on central nervous system, neuroplastin was reported playing a role in keeping Ca^{2+} homeostasis (Bhattacharya et al., 2017) and also being important for delivery of plasma membrane Calcium ATPase (PMCA) to the cell surface membrane (Schmidt et al., 2017). Such findings raise a question whether neuroplastin also plays a similar role in cochlear hair cells.

Ca^{2+} homeostasis is one the important factors regulating cochlear physiology. Unlike the neurons in the central nervous system, the apical surface of the hair cells is exposed to the endolymph, which has a composition of ions resembles more like intracellular fluid (high in K^+, low in Ca^{2+} and Na^+) (Wangemann, 2006). As described in the introduction Chapter, the displacement of the hair bundles of HCs towards the exciting direction increases the MET channel open probability, which causes an inward depolarizing current flowing into HCs driven by a large electrical driving force for K^+ and also Ca^{2+} (Crawford, Evans, & Fettiplace, 1991). There are two main mechanisms for Ca^{2+} extrusion in cells: through PMCA or Na^+/Ca^{2+} exchanger. The Na^+/Ca^{2+} exchanger works in a way that 3 Na^+ ions moving down the electrochemical gradient across the membrane to exchange for 1 Ca^{2+} moving towards the opposite direction (DiPolo & Beaugé, 2006). However, due to the ionic composition of endolymph, the driving force for K^+ and Ca^{2+} is inward while for Na^+ it is outward (McPherson, 2018). Moreover, there is no sign of Na^+/Ca^{2+} exchanger in cochlear hair cells (Tucker & Fettiplace, 1995). In that sense, the only way for Ca^{2+} extrusion is through PMCA pumps.

PMCA is highly expressed in the hair bundle of cochlear OHCs, but it is also be detected in IHCs (Dumont et al., 2001). PMCA2, encoded by gene *ATP2b2*, is the isoform expressed in the stereocilia (Noben-Trauth et al., 1997) and ablation of *ATP2b2* gene causes deafness and balance disorders in mice (Kozel et al., 1998). One research focusing on immunostaining and hearing test showed that Np55 is expressed in the cell body of adult IHCs and at the stereocilia of OHCs (Lin et al., 2021). In addition, it was reported that the expression of neuroplastin is required for HC plasma membrane PMCA expression (Lin et al., 2021). These findings suggest that neuroplastin might affect cochlear hair cell homeostasis in a way related to PMCA expression.

As for other cellular functions, research focusing on the basolateral side of HCs showed that an absence of both Np55 and Np65 cause early-onset hearing loss, increased mis-matching between IHCs and afferent neurons of the auditory nerve, hence a failure in transmission of sound signals to the brain as well as decreased IHC exocytosis (Carrott et al., 2016).

Although a lot of research has been done on Neuroplastin-loss-of-function mutant mice, there are still more details waiting to be discovered from aspects of spatial (where exactly the neuroplastin expresses), temporal (at which timepoint neuroplastin plays an important role), and functional (what functions does neuroplastin play in different HCs) roles of Nptn in mouse hearing. This Chapter describes the results of a series of experiments including western blotting, immunostaining, ABR, DPOAEs and whole-cell patch-clamping, which were meant to test the expression and functional roles of neuroplastin on the basolateral potassium channel properties, MET and exocytosis of the constitutive knock-out *(Nptn^{tm1b/tm1b})* mice hair cells.

3.1.2 Both NP55 and 65 are expressed in mouse cochlea and absent in *Nptn^tm1b/tm1b* mice

As the project is in collaboration with MRC Harwell, Dr Sherylane Newton from MRC Harwell contributed to the molecular biology aspect of the project. To check for the expression of Np55 and Np65 in mouse cochlea, western blotting was performed. To detect both isoforms of Np, an anti-pan-NP antibody (1:200, R and D Systems Cat# AF7818, RRID:AB_2715517) was used. To detect Np65 expression, an anti-Np65-specific antibody was used (1:100, R and D Systems Cat# AF5360, RRID:AB_2155920). For western blotting, PNGase F was used to remove N-linked glycans in the lysates as neuroplastin is a highly glycosylated membrane protein (Beesley et al., 2014). After the enrichment of protein lysates, the whole cochlear membrane-enriched fraction was treated and anti-pan-NP antibody (1:1000, R and D Systems Cat# AF7818, RRID:AB_2715517) which detects both Np65 and Np55 in control mice, as well as a band shown by Np65-specific antibody((1:200, R and D Systems Cat# AF5360, RRID:AB_2155920)).

In *Nptn^tm1b/tm1b* cochlear membrane enriched lysates, neither the antibody bands were detected (Figure 3.1 A). Immunostaining of cochlear cryosection showed strong anti-pan-Np antibody at the stereocilia of the OHCs, IHC cell body and SGNs as well as the non-sensory cells lateral to OHCs (Figure 3.1C). Anti-Np65 antibody labelled the cell body of the IHCs as well as the basal region of non-sensory cells lateral to OHCs (Figure 3.1D). For *Nptn^tm1b/tm1b*, neither of the antibodies labelled the tissue at the same region (Figure 3C and D). The results confirmed the presence of both Np55 and Np65 protein isoforms in wild type HCs.

Auditory Brainstem Response (ABR) test was performed from 4-week-old control and the mutant mice. For *Nptn^tm1b/tm1b* mice, the hearing threshold was found to be higher than 70 dB SPL across all tested frequencies, while *Nptn^+/+* mice showed thresholds ranging from 20 to 55 dB SPL, which were within the normal range for each of the

frequencies tested. The results confirmed that $Nptn^{tm1b}$ allele is a null that causes hearing loss.

Heterozygous $Nptn^{+/tm1b}$ mice, interestingly, also showed a significantly higher ABR-thresholds for high frequency stimuli compared to wild-type mice ($\geq$ 18 kHz, P<0.001, one-way ANOVA, Figure 3.1E). Distortion-product otoacoustic emissions (DPOAEs) were also performed on 5-week-old mice to test *in vivo* OHC function. Like ABR tests, $Nptn^{tm1b/tm1b}$ mice showed significantly lower DPOAEs at all testing frequencies ($Nptn^{tm1b/tm1b}$, n=10, $Nptn^{+/+}$ n=7), $Nptn^{+/tm1b}$ mice' DPOAEs also significantly reduced in higher testing frequencies ($\geq$ 12 kHz, P<0.001, n=5, one-way ANOVA, Figure 3.1F). The important new finding of high-frequency hearing impairment in $Nptn^{+/tm1b}$ provides an impact on interpretation of heterozygous *Nptn* variants. If the case happened in human patient with hearing loss, it would provide a deeper insight of the mutation.
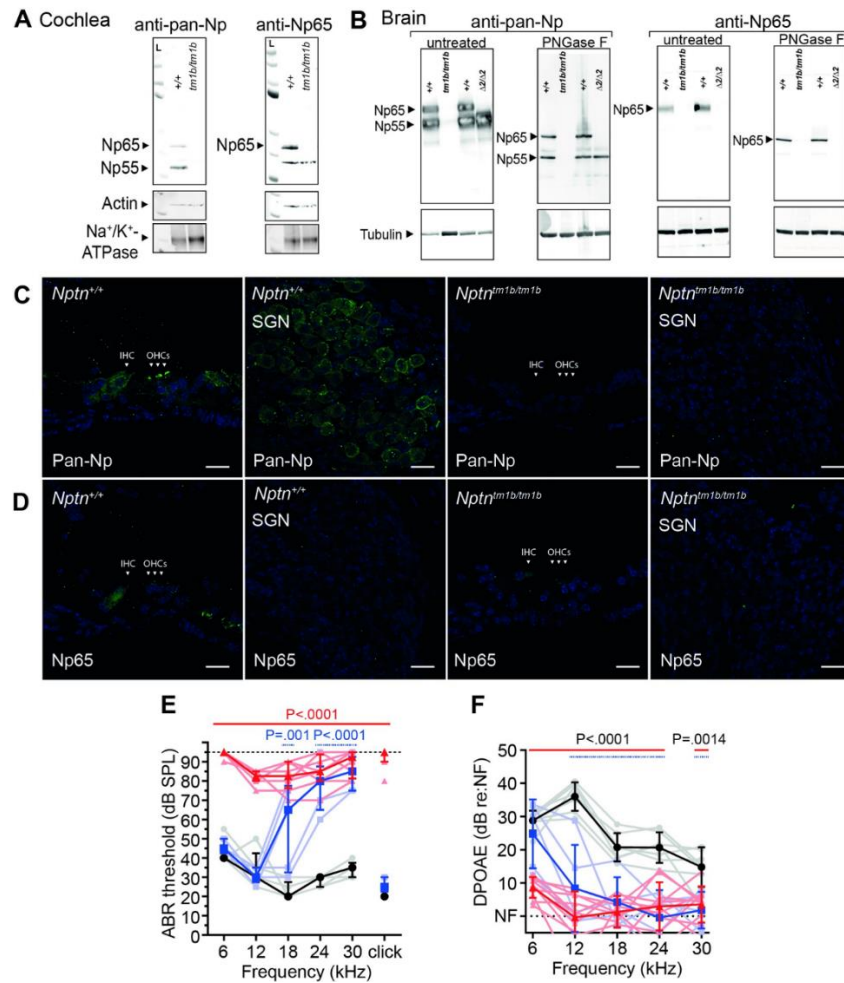
Figure 3.1: Np65 and Np55 are cochlear expressed

(A), Western blot of cochlear membrane-enriched fractions of *Nptn^{tm1b/tm1b}* and *Nptn^{+/+}* mice. Anti-pan-NP antibody detects native Np65 at 44.4kDa and Np55 at 31.3 kDa and the Np-65 specific antibody only detects Np65 in wild type mice. No specific band was detected in *Nptn^{tm1b/tm1b}* mouse cochleae. Na$^+$/K$^+$ ATPase was used as the membrane protein marker. (C) Immunostaining of cochlear cryosection using anti-pan-Np antibody, where IHC cell body, OHC hair bundle and supporting cells lateral to the hair cells as well as SGNs were detected in *Nptn^{+/+}* mice. Scale = 20 µm. (D) Immunostaining of cochlear cryosection using Np65-specific antibody, showing labelling of IHC cell body and supporting cells lateral to the hair cells, no labelling found in *Nptn^{tm1b/tm1b}* mouse cochlea, Scale = 20 µm. (E) ABR measurement of 4-week-old mice. *Nptn^{tm1b/tm1b}* mice showed significantly higher hearing threshold (red, n=8, modified from Newton et al., 2022). At all frequencies compared to *Nptn^{+/+}* mice (black, n=5). *Nptn^{+/tm1b}* mouse showed significant higher threshold at high frequencies (blue, n=5, ≥ 12 kHz, P<0.001, one-way ANOVA). (F) Average DPOAEs from 5-week-old mice. *Nptn^{tm1b/tm1b}* and *Nptn^{+/tm1b}* mice showed reduced response amplitudes (red, n=10, blue, n=5) than the control mice (black, n=7).   Data are mean ± SD with individual data points shown.

3.1.3 NPTN-tm1b mice failed to acquire mature functional profile

The immunolabelling data showed that Np55 is localised in OHC stereocilia bundles, so the very next question is to test whether the OHC activity can be affected by the absence of Neuroplsatin. The purpose of the experiments was to find out whether Nptn knock-out would affect response of the OHC to changes in membrane potentials. OHCs from postnatal day 7 to 16 (P7-P16) Nptn-tm1b mice (constitutive knock-out) were used for basolateral K^+ current recording by applying 170ms 10mV voltage steps from -140mV to 70mV. The Figure 3.2 A, B and C show a recording of a P7 wildtype ($Nptn^{+/+}$), a P7 heterozygote ($Nptn^{tm1b/+}$) and a P7 Nptn-knock-out ($Nptn^{tm1b/tm1b}$) OHC, respectively. As shown in Figure 3.2 A, B and C, the depolarizing voltage steps caused slowly activating currents (from the low slope of the currents in the first several milliseconds). There was also a small amount of inactivating outward currents which were voltage dependent. At hyperpolarizing voltage steps, very small inward rectifier currents were also recorded. The results are consistent with the previous research which demonstrated that during the first postnatal weeks, OHCs express a slow outward current $I_{K,neo}$. The very small inward rectifier currents are considered to be I_{K1} (Marcotti & Kros, 1999).

The steady-state current-voltage (I-V) relationship for the control current ($Nptn^{+/+}$ & $Nptn^{tm1b/+}$) and the mutant current ($Nptn^{tm1b/tm1b}$) is plotted based upon the collected data. As shown in Figure 3.2D, both control mice ($Nptn^{+/+}$ & $Nptn^{tm1b/+}$) and mutants ($Nptn^{tm1b/tm1b}$) showed very little K^+ currents at -120 mV and there was no significant difference in mean steady state K^+ currents (amplitude of I at 0mV) between the control ($Nptn^{+/+}$, 3.16 ± 1.0 nA, n = 5 $Nptn^{tm1b/+}$, 3.50 ± 0.9 nA, n = 7) and the mutant group ($Nptn^{tm1b/tm1b}$, 2.95 ± 0.5 nA, n = 6, P=0.5051, one-way ANOVA). As The results suggested that there is no phenotype observed in mutants, which suggested that the first postnatal week of OHC development was not affected by knock-out of Nptn.

Mouse OHCs matures around P8, at which point they express a negatively activated K^+ current through KCNQ4 channel, $I_{K,n}$ (Marcotti & Kros, 1999). $I_{K,n}$ is activated at -

124mV it can be seen in Figure (D) and (E), there were inward $I_{K,n}$ at -124mV and a quick deactivation. At positive voltages, there are also $I_{K,n}$ outward current observed in control OHCs (Figure 3.2E) but the size of the outward current in $Nptn^{tm1b/tm1b}$ OHCs was reduced. There is a significant decrease in size of $I_{K,n}$ of $Nptn^{tm1b/tm1b}$ OHCs r than which of $Nptn^{tm1b/+}$ OHCs ($Nptn^{tm1b/tm1b}$: 0.181 ± 0.086 nA and $Nptn^{+/+}$ & $Nptn^{tm1b/+}$: 0.701 ± 0.184 nA, p<0.0001, t-test, Figure 3.2G). The results suggest that the $Nptn^{tm1b/tm1b}$ OHCs' development is affected, and they do not mature properly.

A

B

C

D
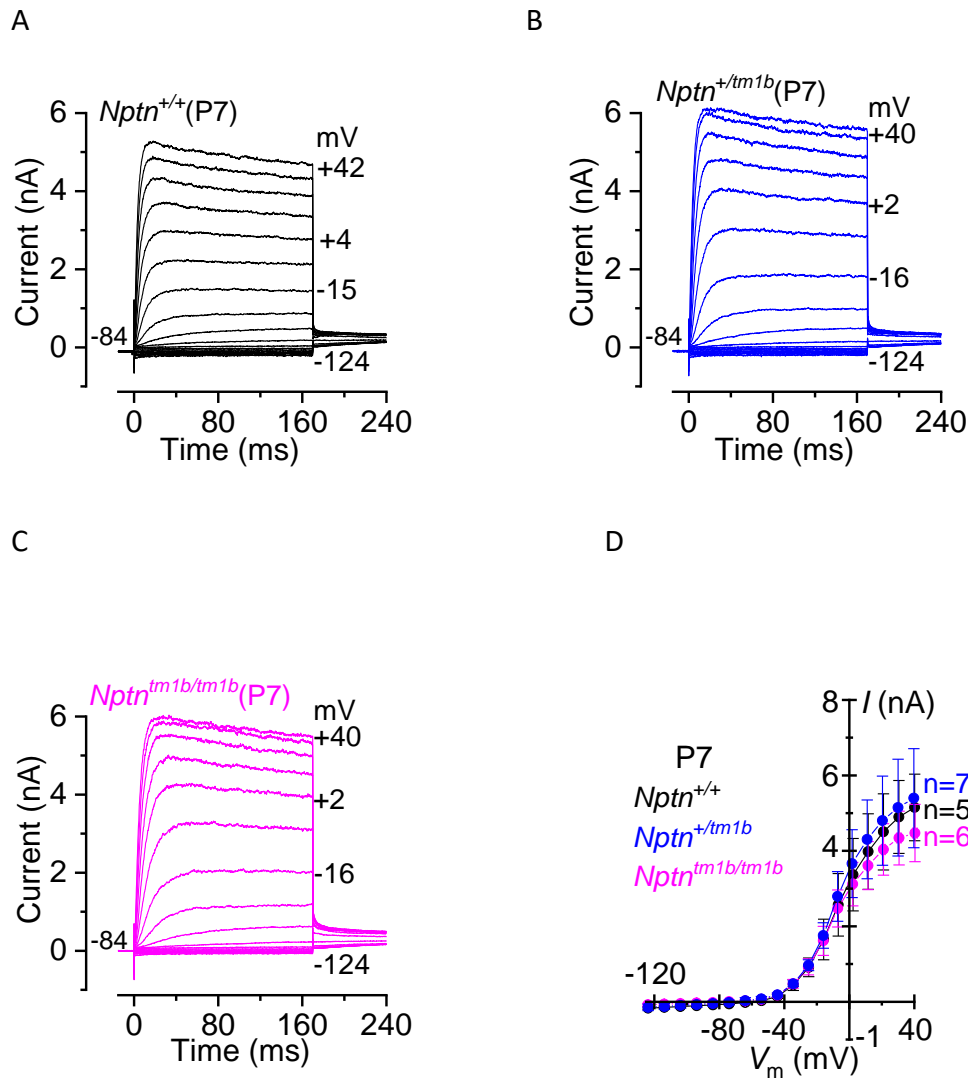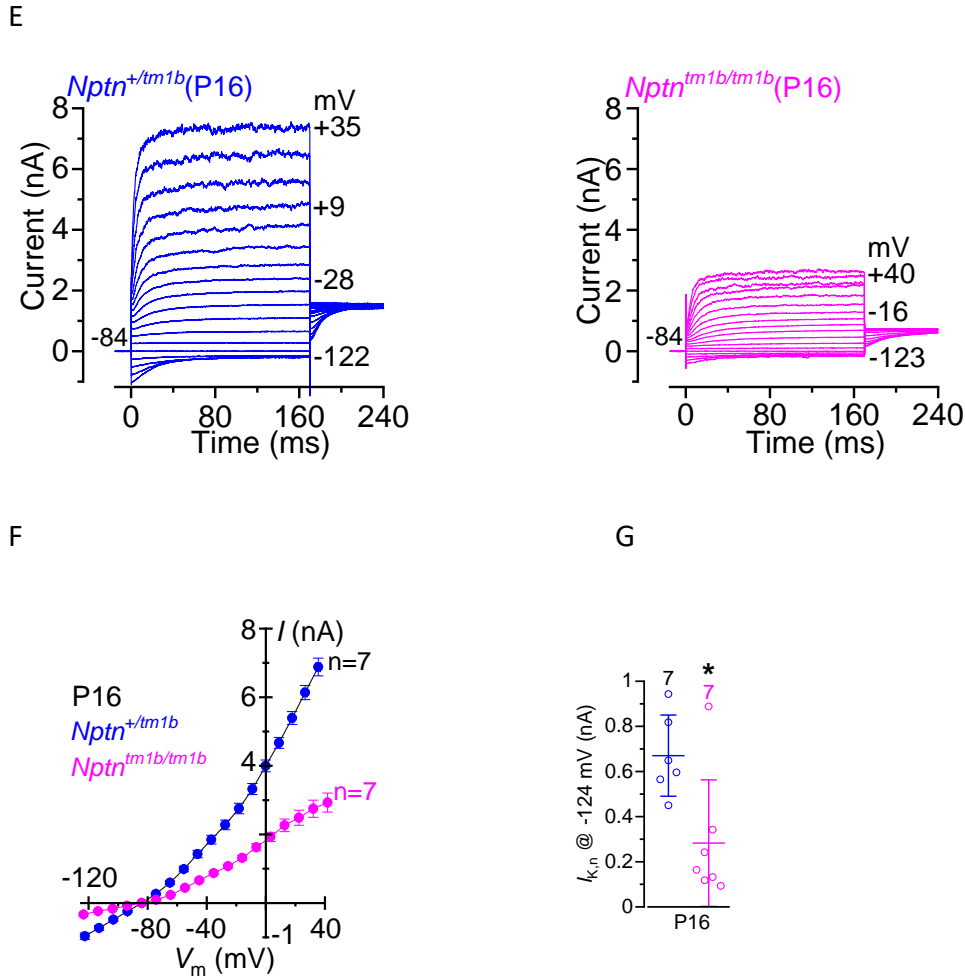
Figure 3.2: The development of OHCs is disrupted in *Nptn^tm1b/tm1b* mice.

(A-C) P7 K⁺ currents of one *Nptn^+/+* (A) OHC, one *Nptn^tm1b/+* (B) and one *Nptn^tm1b/tm1b* (C) OHC in response to 170ms 10mV voltage-steps from -140mV to 70mV. (D): Steady-state *I-V* curves with SD bars of the P7-P9 Nptn-tm1b control group (*Nptn^+/+* & *Nptn^tm1b/+*, n=5 and 7 respectively) and Mutant group (*Nptn^tm1b/tm1b*, n=6) OHCs. (E), P16 K⁺ currents of one *Nptn^tm1b/+* OHC one *Nptn^tm1b/tm1b* OHC in response to 170ms 10mv voltage-steps from -140mV to 70mV. (F): Steady-state *I-V* curves with SD bars of the P16 Nptn-tm1b control group (*Nptn^tm1b/+*, n=7) and Mutant group (*Nptn^tm1b/tm1b*, n=7) OHCs. (G): Individual plot of $I_{K,n}$ shows that there is a significant difference in mean $I_{K,n}$ currents between the two groups (*Nptn^tm1b/tm1b* : 0.181 ± 0.086 nA and *Nptn^tm1b/+* : 0.701 ± 0.184 nA, p<0.0001).

As for OHCs, mature IHCs respond to sound by opening MET channels at the top of the stereocilia (Fettiplace & Hackney, 2006). The inward depolarizing transducer currents are carried by K^+ and Ca^{2+}. The repolarizing currents are constituted by three components: fast-activating K^+ current ($I_{K,f}$)(Kros et al, 1998), slow-activating rectifier K^+ current ($I_{K,s}$)(Marcotti et al., 2003) and negatively activating K^+ current ($I_{K,n}$)(Marcotti et al., 2003; Oliver et al., 2003). When sound signal comes, the transducer currents and the repolarizing K^+ currents help to form the graded receptor potentials (RPs) of IHCs, which lead to glutamate release and activation of type I SGNs (Safieddine et al., 2012). Previous research showed that Nptn is required for IHC synaptogenesis, but the potassium current response to different membrane potentials was not checked. Potassium current recordings were performed on mature IHCs (P18-P25) by applying 170ms 10mV voltage steps from -140mV to 70mV.

Since Np55 is expressed at the OHC sterocilia, another important function of $Nptn^{tm1b}$ mouse OHC, MET, was tested. To test the function of immature and mature OHC MET functions, MET currents of P7 and P8 OHCs were elicited by a fluid jet from a pipette driven by a 25mm diameter piezoelectric disc (Kros et al., 1992). Sinusoidal force stimuli of 50Hz to the hair bundles were applied at -124mV and +96mV. When the OHCs were held at hyperpolarized potentials and the hair bundles displaced in the excitatory direction (towards the taller stereocilia), a large inward MET current was elicited in both control ($Nptn^{+/+}$ & $Nptn^{tm1b/+}$) and mutant ($Nptn^{tm1b/tm1b}$) in OHCs in both age groups (Figure 3.3 A and B showed one recording of P8 $Nptn^{tm1b/+}$ and one $Nptn^{tm1b/tm1b}$ P8 OHC saturating MET current). The movement of the bundles in the inhibitory direction, causing the reduced the resting current flowing through open MET channels (Figure 3.3 A and B, arrows). The MET current becomes outward when excitatory bundle displacements are applied when test voltage steps were positive to the reversal potential, which for a cation channel is around 0 mV. The size of resting current also increases due to an increased open probability of the MET channels(Crawford et al., 1989). (Figure 3.3 A-D). For P7 OHCs, there was no significant

difference in the maximal MET current at either -124 mV or +96 mV between the control ($Nptn^{+/+}$ & $Nptn^{tm1b/+}$) and the mutant ($Nptn^{tm1b/tm1b}$) group (-124 mV, P=0.7743, +96 mV, P=0.9537, one-way ANOVA, Figure 3.3 D, E and F). For P8 mice, the maximal MET current at -124 mV in control OHCs ($Nptn^{tm1b/+}$) was -1.622 ± 0.194 nA, n=14. The maximal MET current in mutant OHCs was 1.219 ± 0.138 nA, n=9. The size of the MET current in the mutant group was significantly smaller than the controls (P<0.0001, t-test, Figure 3.3 C and E). The maximal MET current at +96mV in P8 $Nptn^{tm1b/+}$ OHCs was also significantly higher than $Nptn^{tm1b/tm1b}$ at the same age (P<0.0001, t-test. Figure 3.3 C, F).

The results suggested that MET current is affected $Nptn^{tm1b}$ mouse OHCs. To further understand why the reduced MET current happens, we compared the resting open probability (P_{open}) of the MET channels. To start, the MET current at the rest is calculated by finding the difference between the current level before to the stimulus (dashed line) and the current level on the negative phase of the stimulus. Then the resting MET current is divided by the maximum peak-to-peak MET current. The mean P_{open} of the P7 $Nptn^{+/+}$ & $Nptn^{tm1b/+}$ OHCs at -124mV was not significantly different from P_{open} of the $Nptn^{tm1b/tm1b}$ OHCs (P=0.6316, one-way ANOVA, Figure 3.3G). There was also no significant difference found in P_{open} of P8 OHCs at -124mV (P = 0.5263, t-test, Figure 3.3G). The +96 mV P_{open} of P7 $Nptn^{+/+}$ & $Nptn^{tm1b/+}$ OHCs was significantly higher than P7 $Nptn^{tm1b/tm1b}$ OHCs (P=0.0201 one-way ANOVA, Figure 3.2H), The significant reduction of P_{open} was also found in P8 $Nptn^{tm1b/tm1b}$ OHCs (P=0.0006, t-test, Figure 3.3H).

Together with the MET current recording, the results suggested that the MET at both resting state as well as the responding period are reduced in size starting from P8. In previous research on central nervous system, Neuroplastin was found to be an auxiliary subunit of plasma membrane Ca^{2+}-ATPases (PMCA) to regulate Ca^{2+} clearance(Schmidt et al., 2017c). Absence of Neuroplastin in $Nptn^{tm1b/tm1b}$ OHCs might

have caused Ca^{2+} accumulation hence inhibited the opening of the MET channels due to a smaller Ca^{2+} driving force.

A

B

$Nptn^{+/tm1b}$(P8)

+96

−124

0.8nA

50 ms

±40V

$Nptn^{tm1b/tm1b}$(P8)

C

P7

$Nptn^{+/+}$

$Ntpn^{+/tm1b}$

$Ntpn^{tm1b/tm1b}$

n=3

n=6

n=5

-120   -40

40 80

V_m (mV)

1.8

1.2

0.6

-0.6

-1.2

-1.8

I (nA)

D

P8

$Ntpn^{+/tm1b}$

$Ntpn^{tm1b/tm1b}$

n=14

n=11

-120   -40

40 80

V_m (mV)

1.8

1.2

0.6

-0.6

-1.2

-1.8

I (nA)

E   F
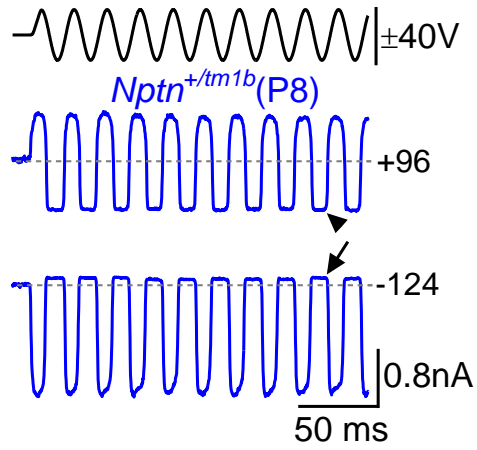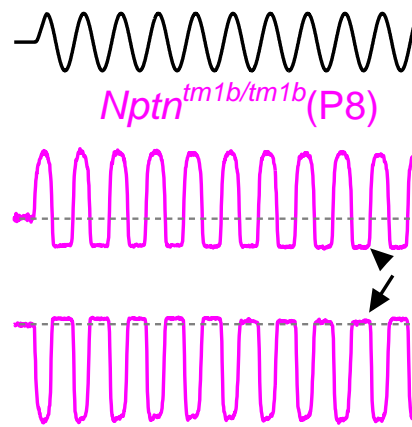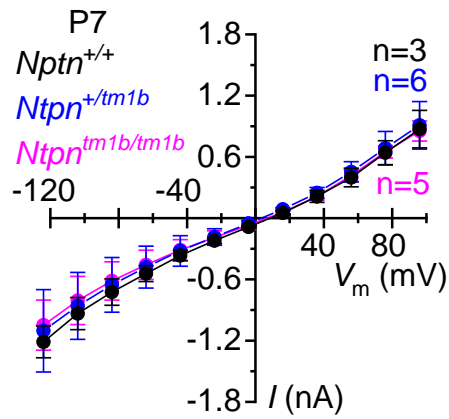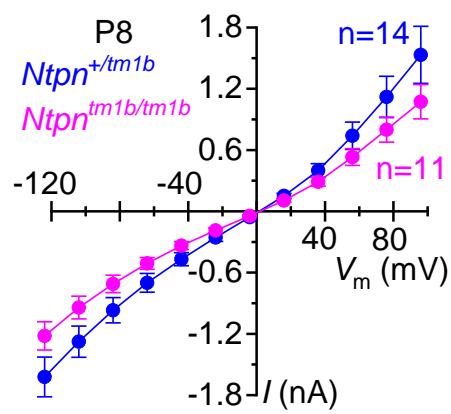
G   H
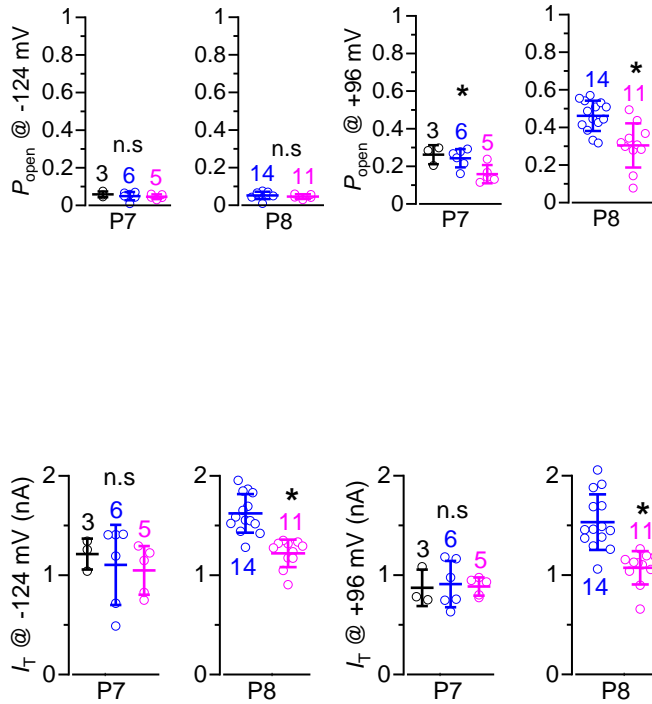
Figure 3.3：Mechanoelectrical transducer current is affected in *Nptn^{tm1b/tm1b}*

mice.

(A) and (B): Voltages steps from -124 mV to +96 mV were given to the OHCs and saturating MET currents recorded from a P8 *Nptn^{+/tm1b}*OHC (A) and a P8 *Nptn^{tm1b/tm1b}* OHC (B) are shown. For clarity, only the -124mV and +96mV recordings are shown. The frequency of the sinusoidal force stimulus was 50Hz, the arrows indicate the MET channel closure during hair bundles displacing in inhibitory direction. Dashed lines label the holding current at the holding potential -81mV. (C) and (D), Peak-to-Peak MET current of the control and the mutant OHCs of (C) P8 and (D) P7 groups plotted as an I-V curve. (E) and (F), maximal MET current recorded at (E) -124 mV and (F)+96 mV from OHCs at P7 and P8 of control and mutant groups. (G) and (H) Resting open probability (P_{open}) of the two groups was calculated and plotted. (G), P_{open} at -124mV. (H) P_{open} at +96 mV. MET current at the rest (the difference between the current level before to the stimulus and the current level on the negative phase of the stimulus) was divided by the maximum peak-to-peak MET current. Data are mean ± SD.

As shown in Figure 3.1, young-adult $Nptn^{tm1b/tm1b}$ mice showed significant hearing impairment, together with the finding of Np65 expression in basolateral region of the IHCs, the finding suggested that neuroplastin plays an important role in IHC basolateral function. To test development of IHCs in $Nptn^{tm1b/tm1b}$ mice, P18-P22 mature mice were first chosen to test the functional maturity. As shown in Figure 3.4 A and B, mature $Nptn^{tm1b/tm1b}$ IHCs showed a much slower activation of K^+ current (Figure 3.4B), while in IHCs from control mice, there were still fast components of K^+ current (Figure 3.4A). In Figure 3.2C, the first several milliseconds of the $I_{K,f}$ currents of the IHC from Figure 3.4A and 3.4B at about -10mV in are shown (labeled by the arrow) and it can be seen clearer that the $I_{K,f}$ component in $Nptn^{tm1b/tm1b}$ IHC is reduced. To quantify the observation, steady-state I-V curves were plotted based upon the data (Figure 3.4D) and the total K^+ currents at 0mV are plotted (Figure 3.4E). As shown in Figure3. 4E, there was a significant difference between the K^+ current of $Nptn^{tm1b/tm1b}$ IHCs and which of the $Nptn^{+/+}$ & $Nptn^{tm1b/+}$ IHCs at 0 mV P=0.0099, one-way ANOVA).

The $I_{K,f}$ and $I_{K,n}$ currents are also plotted (Figure 3.4F and 3.4G). It can be seen in Figure 3.4F, $Nptn^{tm1b/tm1b}$ IHCs had a smaller amplitude of $I_{K,f}$ 1ms after the stimulus at -25mV (Kros et al., 1998). The mean $I_{K,f}$ of $Nptn^{tm1b/tm1b}$ IHCs is 0.114 ± 0.100 nA, n=7, which is significantly smaller than the control group (P<0.0001, Figure 3.4F). As for $I_{K,n}$, individual current values at -124mV are plotted (where $I_{K,n}$ is activated). The mean $I_{K,n}$ value of $Nptn^{tm1b/tm1b}$ IHCs is 0.031±0.026nA, n=7, which is significantly reduced when compared to the control groups (P=0.0007, Figure 3.4G), $I_{K,f}$ is a key marker of mature IHCs. Around postnatal day 12, IHCs takes the final step of the development which turns immature IHCs from firing spontaneous action potentials to being able to fire high frequency graded potentials in response to sound stimulus. $I_{K,f}$ is a fast activating current which prevents the action potential generation of the IHCs (Corné J. Kros et al., 1998). Being similar to the current $I_{K,n}$ in OHCs, $I_{K,n}$ in IHCs also contributes to the maturation of IHCs to set the resting potentials and $I_{K,n}$ is about 65% active at resting potential to prevent depolarization (Marcotti, Johnson, Holley, et al., 2003b).

Significantly smaller $I_{K,f}$ and $I_{K,n}$ in P18-P25 IHCs indicates that the *Nptn*^{tm1b/tm1b} IHCs' development was affected and the maturation was not complete.

A

B

D
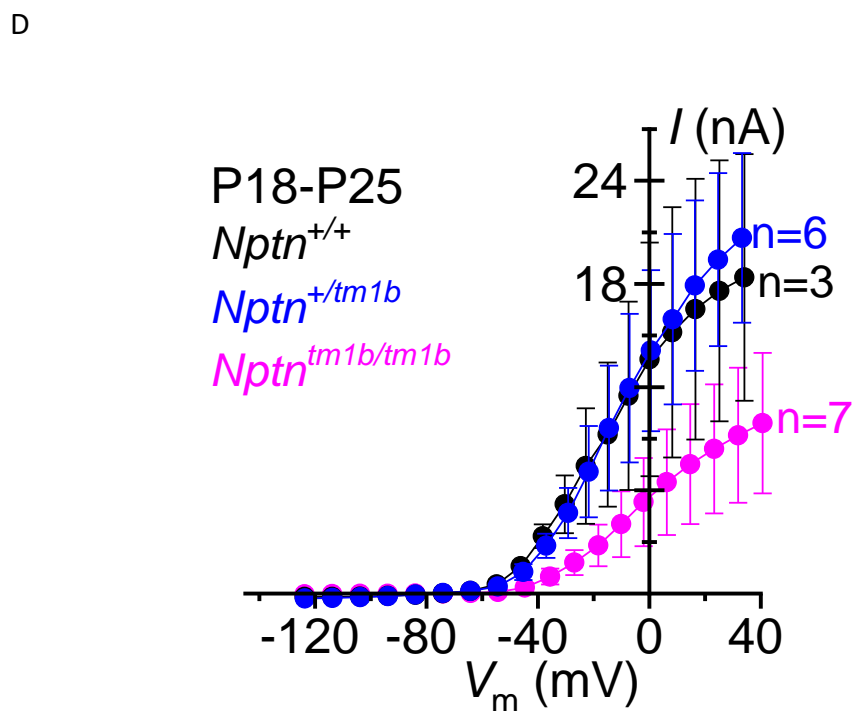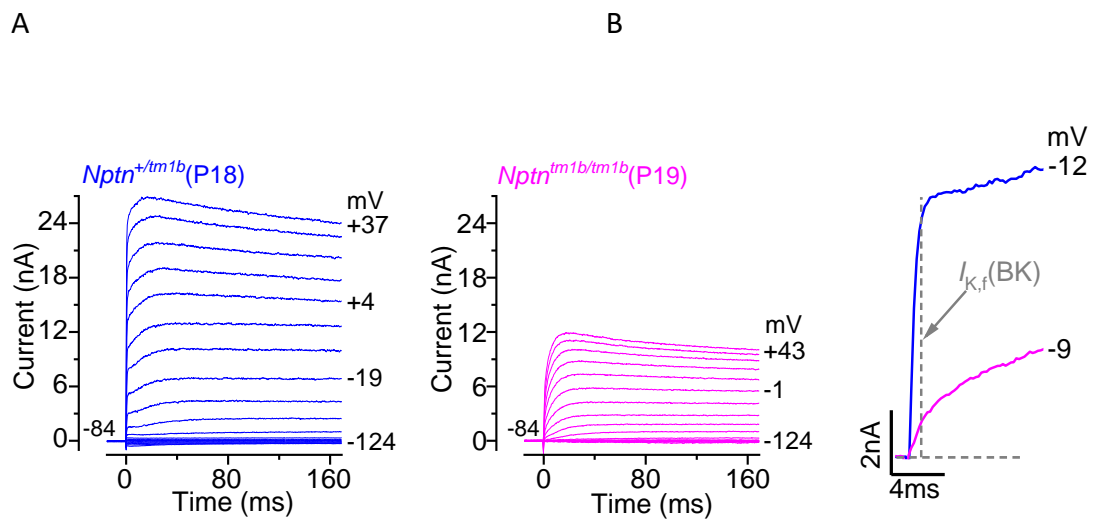
(more in next page)
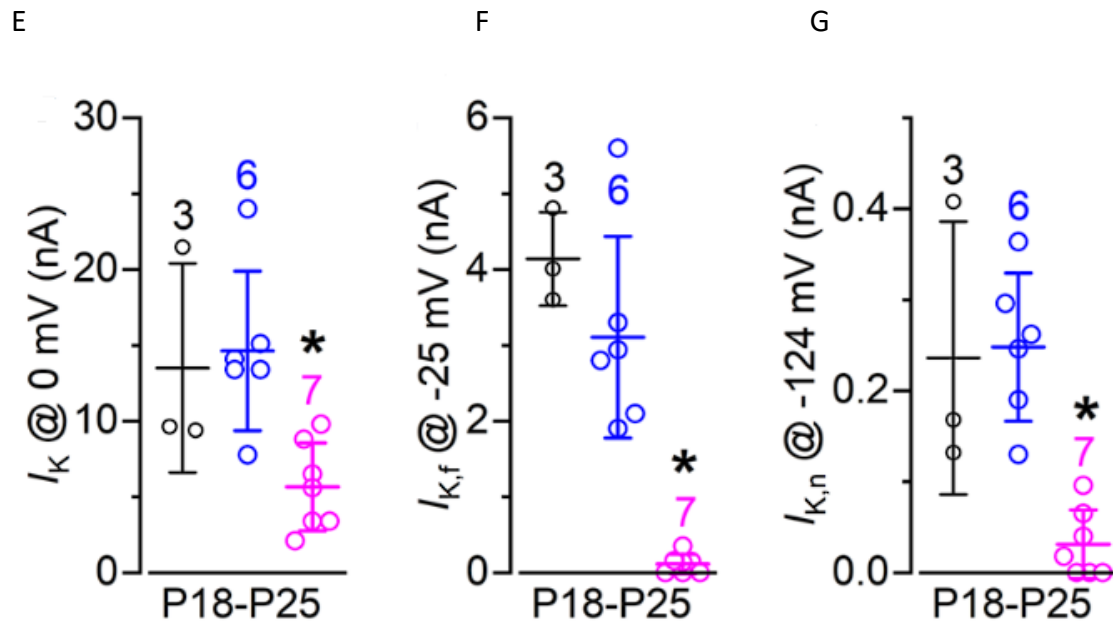
Figure 3.4: The development of OHCs is disrupted in *Nptn^tm1b/tm1b* mice

(A) and (B): a P18 *Nptn^tm1b/+* mouse IHC (A) and a P19 *Nptn^tm1b/tm1b* mouse (B) K$^+$ current recording in response to 170ms 10mV voltage-steps from -140mV to +70mV respectively. (C) $I_{K,f}$ at about -10mV of the IHCs in (A) and (B) in the first several milliseconds after the stimulus, labeled by the arrow. (D): Mean *I-V* curves of steady-state current of the control group (*Nptn^+/+* n=3 & *Nptn^tm1b/+* n=6) and the mutant group (*Nptn^tm1b/tm1b* n=7) IHCs respectively. The steady-state current is decided by amplitude of currents at 0 mV. (E) Inidividual steady-state current at 0mV of the two groups is plotted. The mean total I_K of *Nptn^tm1b/tm1b* IHC (5.657 ± 2.904 nA, n=7) is significantly smaller than which of the control IHCs (*P*=0.0099) (F) Individual $I_{K,f}$ which are decided by amplitude of currents at -25mV. The mean $I_{K,f}$ value of the   *Nptn^tm1b/tm1b* IHCs is 0.114 ± 0.100 nA, n=7 the mean values of the mutant group is significantly smaller than the control group, *P*<0.0001. (G): Inidividual $I_{K,n}$ values of the mutant and the control group, decided by the current value at -124mV (where it is activated). *Nptn^tm1b/tm1b* IHCs: 0.031 ± 0.026 nA, n=7.There is a significant difference between the two mean values, p=0.0007.

3.1.4 NPTN-tm1b mice showed normal exocytotic function

Previous research showed that *Nptn*-knockout mice showed significantly reduced exocytosis. To examine whether Nptn knock-out affected the presynaptic exocytosis, several protocols of capacitance measurements were performed on adult IHCs (most are P20 onwards). As shown in Figure 3.5 A-D, recordings of Ca^{2+} currents and capacitance changes of adult control (Figure3.5 A and C, P28) and mutant IHCs (Figure 3.5 B and D, P27) were obtained from 50ms of 10mV voltage steps from -81mV. The mean Ca^{2+} current responses (I_{Ca}) and voltages are plotted as an I-V curve (Figure 3.5E) and the corresponding mean cell membrane capacitance change (ΔC_m) is shown in Figure 3.5F. The data are plotted as mean data ± SEM. The statistical t-test of the maximal I_{Ca} shows that the mutant IHCs (*Nptn*$^{tm1b/tm1b}$, -193.95 ± 51.08 pA, n=5) had a slightly higher Ca^{2+} influx than the wild type (*Nptn*$^{+/+}$ & *Nptn*$^{tm1b/+}$, -130.33 ± 8.78 pA, n=5 IHCs from 5 mice. P=0.0337). However, there was no significant difference in corresponding maximal ΔC_m (*Nptn*$^{tm1b/tm1b}$, 9.16 ± 1.32 fF, n=5 IHCs from 5 mice. *Nptn*$^{+/+}$ & *Nptn*$^{tm1b/+}$, 16.52 ± 7.30 fF, n=5 IHCs from 5 mice. P=0.0865).

A

B

More in next page

C

D

E

F

G

H
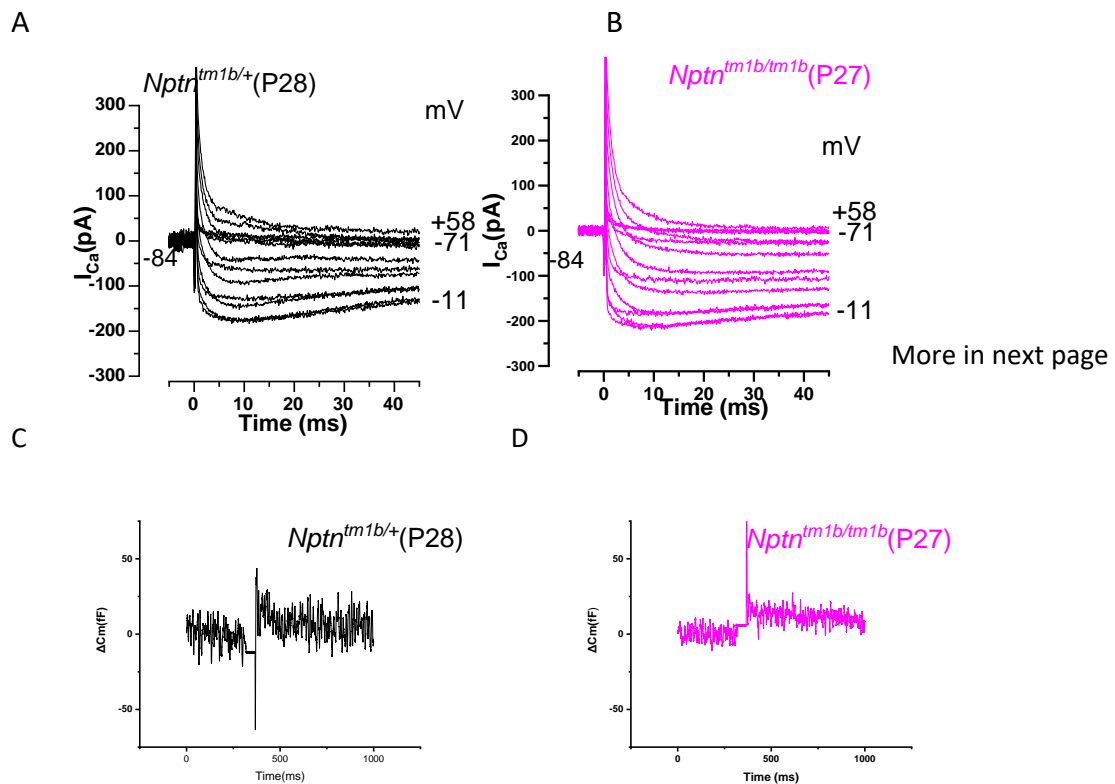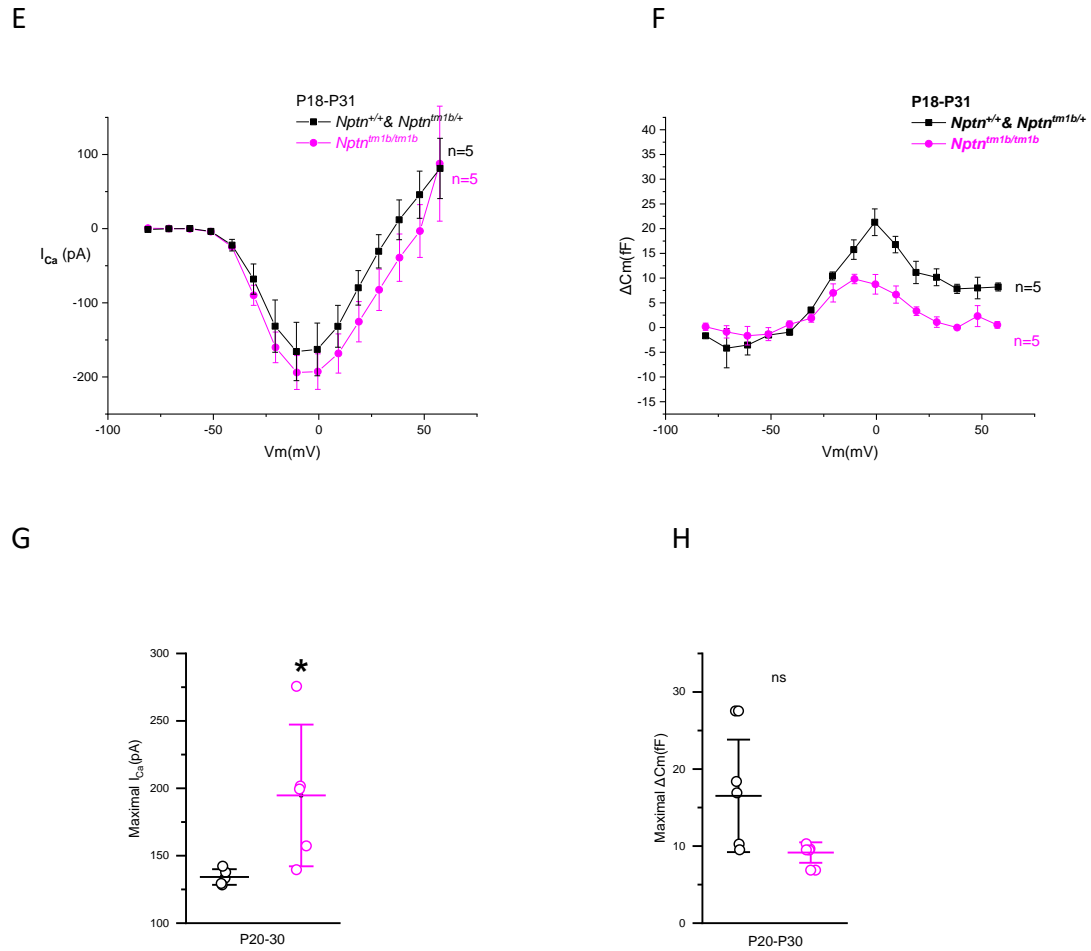
Figure 3.5: Adult Nptn$^{tm1b/+}$ IHC exocytosis is not affected

A and B: Current responses from IHCs of heterozygotes (*Nptn$^{tm1b/+}$*) and homozygotes (*Nptn$^{tm1b/tm1b}$*). C and D: Corresponding capacitance change (ΔC_m) from the heterozygous and homozygous mice (same IHCs as A and B). Recordings were obtained by applying 50ms voltage steps from -81 mV to +58 mV. E: I-V curve by plotting the maximal peak I_{Ca} against the voltage. F: Maximal ΔC_m against the voltage.

To test the neurotransmitter release rate, kinetic measurements, which were applying -11 mV voltage steps with different durations (2ms to 1.5s with at least 10s intervals) towards the adult IHCs. The approach gives an indication towards the emptying rate of readily releasable (RRP) and secondarily releasable pools (SRP). The experiments were performed using an extracellular solution contains 1.3 mM Ca^{2+} and at body temperature to better activate the vesicle release(Johnson et al., 2008). The vesicles which are docked at the active zones are defined as the RRP, which can be triggered and release the neurotransmitter in a shorter period ($\leq$100 ms). The SRP vesicles locate further away from the Ca^{2+} channels, which needs longer steps to induce the release(Johnson et al., 2008; Von Gersdorff et al., 1996). The average capacitance changes for *Nptn*$^{+/+}$ & *Nptn*$^{tm1b/+}$ with 100ms duration is 29.63 ± 7.06 fF n=6, for *Nptn*$^{tm1b/tm1b}$ it is 26.39 ± 11.08 fF, n=5. According to previous research, each IHC contains about 20 active zones (Roberts et al., 1990) at presynaptic region and each vesicle fusion contributes about 37aF towards the cell membrane capacitance change (Lenzi et al., 1999). So, the size of the RRP for *Nptn*$^{+/+}$ & *Nptn*$^{tm1b/+}$ mouse IHCs is on average about 800 vesicles, for *Nptn*$^{tm1b/tm1b}$, it is about 713 vesicles. There is no significant difference in RRP size(t-test).
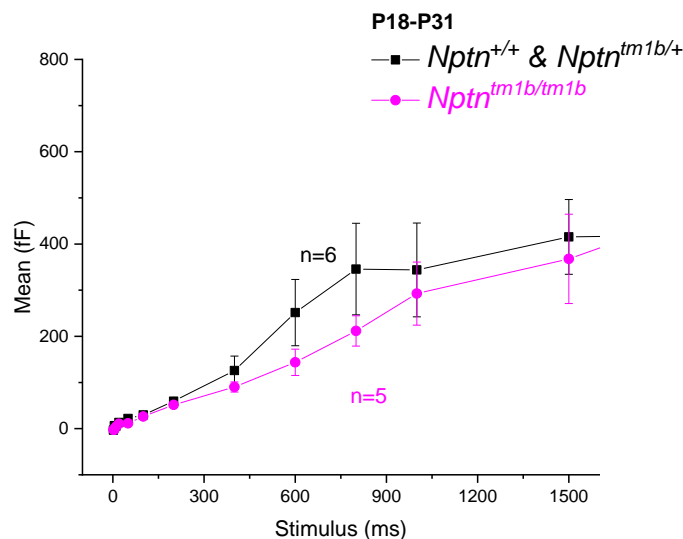
Figure 3.6: *Nptn*$^{tm1b/tm1b}$ mice showed normal RRP and SRP release.

To compare the Ca^{2+} dependence of exocytosis, the mean values of ΔC_m is plotted against the I_{Ca}. The change in ΔC_m was fitted as a function of I_{Ca} using the synaptic transfer function (Johnson et al., 2010). The equation is shown below, where c is a scaling coefficient, N is the power value that is from fits to the individual cells tested.

$$\Delta Cm = c I_{Ca}^{N}$$

The Nptn$^{+/+}$ & Nptn$^{tm1b/+}$ mouse IHCs showed an average p value of 1.76 ± 0.0834, n=6. For Nptn$^{tm1b/tm1b}$ IHCs p= 2.29 ± 0.41, n=5. Although the p value for the mutant is smaller than the wild type, there is no significant difference (t-test). Together with the kinetics measurement results, we did not find a significantly difference in exocytotic function between the wild type and Nptn$^{tm1b/tm1b}$ IHCs.
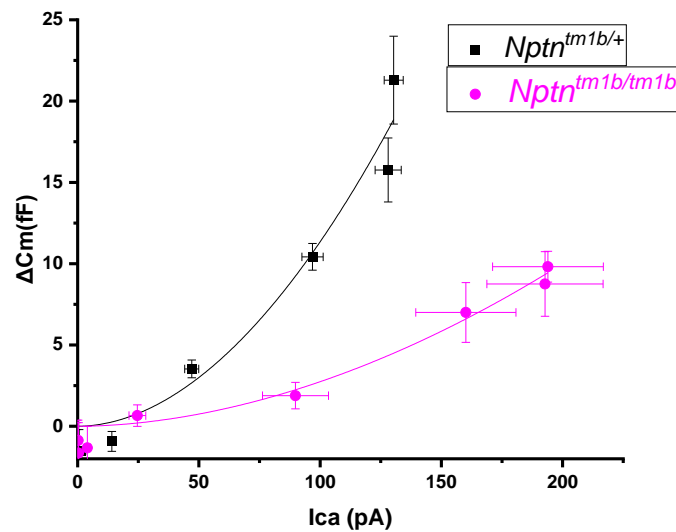
Figure 3.7: Nptn$^{tm1b/tm1b}$ mice showed similar exocytotic Ca^{2+} dependance.

ΔC_m plotted against the corresponding I_{Ca} between -71 mV and -11 mV (Johnson et al., 2010).

3.1.5 Neuroplastin in OHCs is required for PMCA2 stereocilia localisation

The findings of *Nptn^{tm1b/tm1b}* OHCs having affected MET function rose a question about which mechanism of the mutant OHCs is affected. To answer the question, we put our eyes on the Ca^{2+} homeostasis of OHCs. Cochlear HCs express Plasma Membrane Calcium ATPase (PMCA) proteins to extrude cytoplasmic Ca^{2+} into extracellular fluid. Previous research found that IHC basolateral membrane express mainly PMCA1, while OHC express abundant amount of another isoform PMCA2, in their stereocilia (Dumont et al., 2001b). As for Neuroplastin, *in vitro* studies found that Nptn transmembrane domain can lead to PMCA localization towards plasma membrane and Nptn is also essential for correct PMCA colocalization (Schmidt et al., 2017a). To test whether Neuroplastin is required for PMCA localization in HCs, immunostaining of PMCA1 and PMCA2 are performed on wild-type and *Nptn^{tm1b/tm1b}* mouse cochleae. From Figure 3.8 A, it is shown that PMCA1 is mainly found in basolateral membranes of both IHCs and OHCs as well as non-sensory cells. PMCA2 is found being localized mainly at stereocilia of OHCs. *Nptn^{tm1b/tm1b}* HCs showed remarkably reduced staining in IHCs, OHCs and non-sensory cells, indicating a reduction of expression of both PMCA isoforms (Figure 3.8 A and B). The staining of isoform specific Np65 knock-out mutant showed that there is no obvious reduction of PMCA immunoactivity in the cochlea (Figure 3.8 C, *Nptn^{Δexon2/Δexon2}*). The data confirms that neuroplastin is required for the correct localisation of PMCA proteins in OHCs, finding a link between the neuroplastin expression and PMCA provides a new direction of neuroplastin functional analysis in future studies.
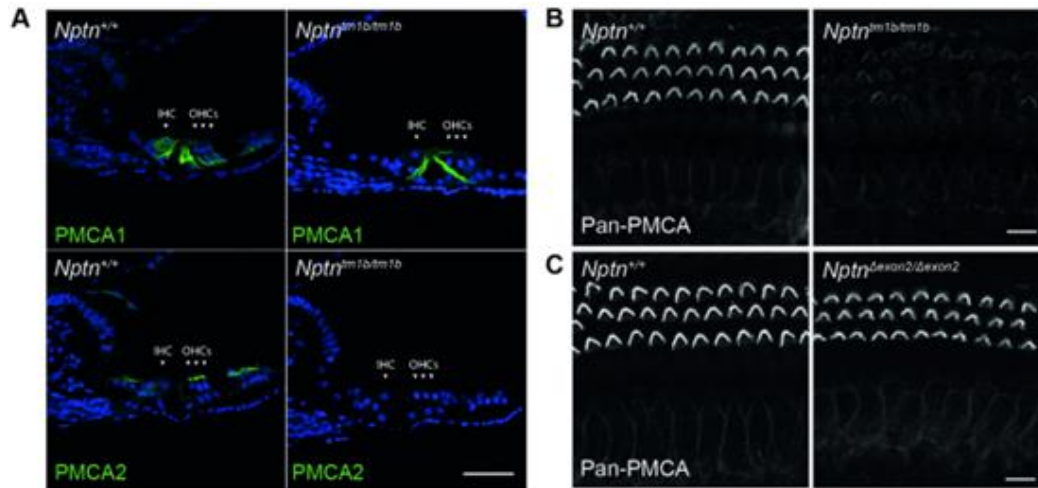
Figure 3.8 PMCA expression in OHC stereocilia depends on *Nptn* expression

A: Immunostaining of cochlear cryosections. Anti-PMCA1 and 2 staining showed that PMCA1 mainly localises at the membrane of both types of HCs, while PMCA2 is mainly expressed at the stereocilia of the OHCs. *Nptn^tm1b/tm1b* showed obvious reduction of both PMCA isoform staining. Scale bar: 20μm. B and C: Anti-pan-PMCA antibodies showed abundantly expressed PMCAs at wild type OHC stereocilia, and IHC membrane. The labelling is reduced in Nptn^tm1b/t1mb cochlea, but not in *Nptn^Δexon2/Δexon2* (Nptn-65 knock-out) cochleae. Scale bar: 10μm. *(modified from Newton et al., 2022).*

3.1.6 Discussion

3.1.6.1 Neuroplastin expression in hair cells is required for hearing

There have been different observations of neuroplastin expression in mammalian cochlea. Np55 expression was found in OHC stereocilia but not in IHCs (Zeng et al., 2016). Immunolabeling of cochlear sections showed Np65 expression at cuticular plates of both IHCs and OHCs as well as at basolateral part of IHCs(Carrott et al., 2016). In this study, using a pan-Np antibody, neuroplastin expression was found to be present in OHC stereocilia and IHC basolateral membrane. In non-sensory cells, immunolabeling results also showed Np signals in spiral ganglia and some lateral non-sensory cells (Figure 3.1). The results described in 3.1.2 generally agrees with the previous studies.

$Nptn^{tm1b/tm1b}$ mice showed significantly elevated hearing thresholds for stimuli at higher frequencies (≥18 kHz). The corresponding DPOAE responses (≥12 kHz) were also smaller (Figure 3.1 E and F). $Nptn^{tm1b/tm1b}$ mice showed elevated thresholds at about 70 dB, suggesting a reduction in OHC function due to neuroplastin knock-ou t(S. Newton et al., 2022).

3.1.6.2 Neuroplastin is essential for hair cell mechanotransduction, ion homeostasis and maturation

Previous research investigating OHC MET functions suggested that neuroplastin loss-of-function mutants showed normal OHC MET currents during immature age (≤P7). To further check the functional role of neuroplastin in OHCs, MET recordings were obtained from OHCs of P8 WT and $Nptn^{tm1b/tm1b}$ mice, which correspond to the onset of their mature function. The recordings showed that the maximal MET currents and

MET channel open probability at depolarized potentials were significantly reduced in $Nptn^{tm1b/tm1b}$ mice while no significant difference observed in P7 mice (Figure 3.3).

Ca^{2+} entry into the stereocilia drives adaptation of MET current. The reduced Ca^{2+} entry into the MET channel, for example near the Ca^{2+} equilibrium potential at positive voltage, leads to the removal of this adaptation and the increase open probability of MET channels(Corns, Johnson, et al., 2014). The reduced open probability of $Nptn^{tm1b/tm1b}$ MET channels at depolarized potentials suggests there is a Ca^{2+}-driven adaptation of the MET currents. Interestingly, as Figure 3.8 showed, the expression of PMCA at the OHC stereocilia of $Nptn^{tm1b/tm1b}$ mice is strongly reduced. When given repetitive bundle displacement stimulation, the reduced PMCA can very likely cause Ca^{2+} accumulation within OHCs near the MET channels, hence an adaptation and decreased open probability compared to the WT. The phenotype observed from $Nptn^{tm1b/tm1b}$ OHCs is in agreement with previous studies on new born mouse OHCs lacking Ca^{2+} pump (Ficarella et al., 2007).

On the basolateral side, $Nptn^{tm1b/tm1b}$ mouse HCs showed significantly reduced $I_{K,n}$ (Figure 3.2) and $Nptn^{tm1b/tm1b}$ IHCs showed much smaller $I_{K,f}$ (Figure 3.4), suggesting that the IHCs of the mutant mice fail to develop a mature basolateral current profile, possibly due to the disrupted MET function. In previous research, it was found that MET currents are responsible for depolarizing the HCs to cause spontaneous action potential firing activities in IHCs during development (Johnson et al., 2012) and such MET-driven spontaneous action potential firing is required for IHC maturation (Corns et al., 2018). As for OHCs, although the K^+ current size was smaller, the function of OHCs is still able to mature. Previous research focusing on mutations affecting MET showed different basolateral current profile. For example, Epidermal growth factor receptor pathway substrate 8 (Eps8) knock-out mice showed normal $I_{K,n}$ current (Zampini et al., 2011) while transmembrane protein TMC1 mutation showed reduced $I_{K,n}$ (Marcotti et al., 2006). So the exact link between the disrupted MET and reduced $I_{K,n}$ remains to be discovered.

3.1.6.3 Neuroplastin[tm1b/tm1b] shows normal function of exocytosis

Previous research using the *pitch* mouse model, an ENU-induced mutation in *Neuroplastin* gene, showed that the exocytosis of *Neuroplastin*[pitch/pitch] IHCs is severely impaired (Carrott et al., 2016). It showed that the vesicle release rate was reduced and the exocytotic dependence was significantly less linear than the wild type, suggesting Neuroplastin is required for exocytosis in adult IHCs. However, in this study, the *Neuroplastin*[tm1b/tm1b] mice showed no significant difference in either maximal ΔC_m or maximal I_Ca. The exocytotic dependence, defined by ΔC_m against corresponding I_Ca, was not found to be significantly different either. In addition, the measurement of kinetics, in purpose of checking the recruitment of RRP and SRP, did not show significant difference either. The capacitance measurement results of the study suggested that *Nptn*[tm1b/tm1b] mice had normal exocytotic function.

The *Nptn*[tm1b] knock-out allele was generated lacking exon 5 and 6, leading to Ig3 and transmembrane domain deletion, so both Np55 and Np65 were affected (S. Newton et al., 2022). In the *pitch* mutant, there is a nucleotide transversion at codon 315, altering WT sequence TGT (encoding cysteine) to a mutant sequence AGT (encoding serine). So, one possible explanation for the different observations is that the different protein structure of mutant neuroplastin lead to different functional effects. In addition, the sample size for capacitance measurement of the project is relatively small when comparing to previous research using capacitance measurements. Further experiments with a bigger sample size might reduce the variability of the results.

4 Characterization of Otoferlin conditional knock-out model

4.1 Introduction

After the investigation on the functional roles of neuroplastin, we moved on to investigate the Ca^{2+} sensors in mouse cochlear IHCs. As mentioned in chapter 1.1.7.2 the primary Ca^{2+} sensor in IHCs is otoferlin, a 6-C2-domain protein(C. P. Johnson & Chapman, 2010a). Otoferlin has been found to play an essential role in Ca^{2+}-dependent exocytosis(Roux et al., 2006) and endocytosis (Duncker et al., 2013). Previous research was performed on mouse models carrying otoferlin mutations. OHC capacitance measurements of $Otof^{-/-}$ mice suggested that otoferlin plays as the major Ca^{2+} sensor of exocytosis in immature P2-P3 mice (Beurg et al., 2008). IHC capacitance measurements showed that the Ca^{2+}-triggered exocytosis is almost abolished in otoferlin-knock-out P6 to P15 mice (Roux et al., 2006). Although a lot of research were focusing on otoferlin functional roles in mammalian cochlea, the experiments were mainly performed on otoferlin-knock-out mice before the onset of hearing. The mouse models used for otoferlin knock-out were all constitutive knock-out models, which means that otoferlin is never expressed in hair cells (Roux et al., 2006) and the results suggested that otoferlin plays an important role in cochlea HC function. However, there is still a gap in the knowledge of otoferlin function whether it is important for just the development of cochlear HC function or it also plays an important role in maintenance of the functions.

To answer the question whether otoferlin also plays an important role in maintenance of Ca^{2+}-dependent exocytotic function, conditional-knock-out mouse models which uses otoferlin-tm1c mouse crossed with Barhl1-Cre line or Vglut3-Cre line are used for postnatal conditional knock-out experiments. The Barhl1-Cre line was chosen as the Barhl1 gene is known as HC-specific transcription factors which can be detected as early as E14.5(S. Li et al., 2002). For a similar reason, Vglut3-Cre line was chosen as

Vglut3-Cre line was proved to be a reliable model in previous research and Vglut3-iCreER was found specifically labels cochlear IHCs at all postnatal ages(Li et al., 2018). In addition, to help with potential in vitro capacitance measurement experiments, a reporter protein, tdTomato was also involved. The conditional-knock-out is achieved by tamoxifen injection. After injection, translocation of Cre into nucleus removes stop codon before tdTomato coding sequences hence a permanent expression of tdTomato (Madisen et al., 2009).

The Aim of the experiments described in this chapter is to characterize the otoferlin conditional-knock-out model to decide whether it is a good tool for the further research. A cohort of tamoxifen injection and immunostaining experiments were performed.

4.2 Result

The first step of the project was trying to establish a reliable conditional-knockout model. The first set of experiments were performed on Otoferlin-tm1c X Barhl1-Cre X tdTomato mice. Two Tamoxifen injections were applied to each P20-P30 mice using different concentrations (50,100 and 200µg/g body weight) with 48-hour gap. Mice were left for 2-4 weeks before dissecting out the cochlea for immunostaining. The immunostaining showed that although tdTomato was expressed in the IHCs, suggesting the activation of Cre-recombinase, otoferlin signal was still present 4 weeks after injection (Figure 4.1).
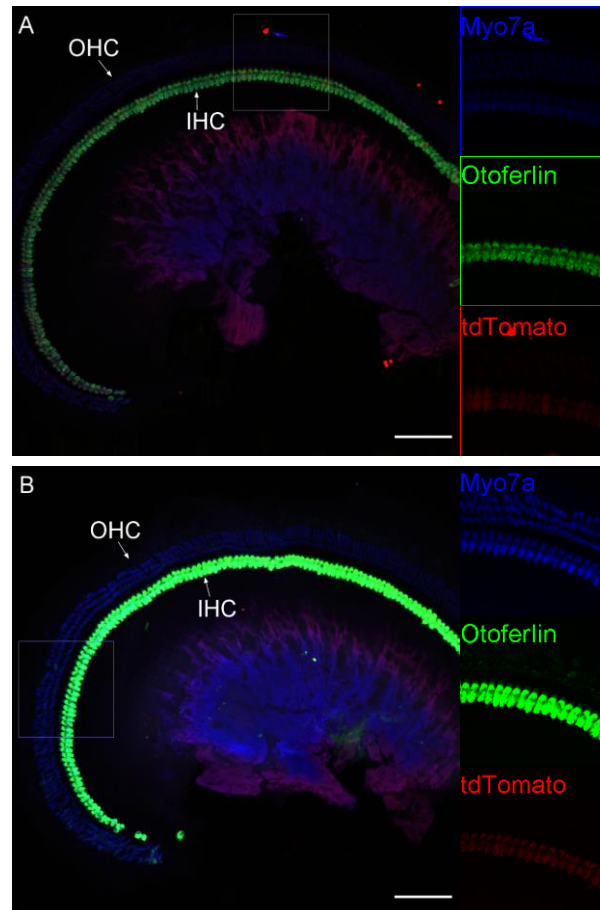
Figure 4.1:   P50 Barhl1-Cre line mice showed expression of otoferlin 4 weeks after treatment

Otoferlin$^{tm1c/tm1c}$ X Barhl1-Cre$^{+/-}$ X tdTomato$^{+/-}$ (A) and Otoferlin$^{tm1c/tm1c}$ X Barhl1-Cre$^{-/-}$ X tdTomato$^{+/-}$ (WT, B). Blue: Myo7a (cell marker), Green: Otoferlin, Red: tdTomato. Blue: Myo7a staining, cell marker. tdTomato emission. Scale bars represent 88µm.

The inconsistency between the tdTomato expression and otoferlin presence after 4 weeks rose a question about whether the Cre-activation was efficient to trigger otoferlin-knock-out. To increase the Cre-activation, a different model was generated using Otoferlin-tm1c X Vglut3-Cre X tdTomato. Vglut3-Cre line has been characterized as an efficient tamoxifen-inducible model in previous research(Li et al., 2018).

As previous experiments, 2 tamoxifen injections to achieve 200µg/g final concentration with 48-hour gap were applied to P20-P24 mice and the mice were left from 2-4 weeks before immunostaining experiments. As shown in Figure 4.2, although the transduction rate of tdTomato is high, there were only very few tdTomato-positive cells showed reduced signal of otoferlin staining.
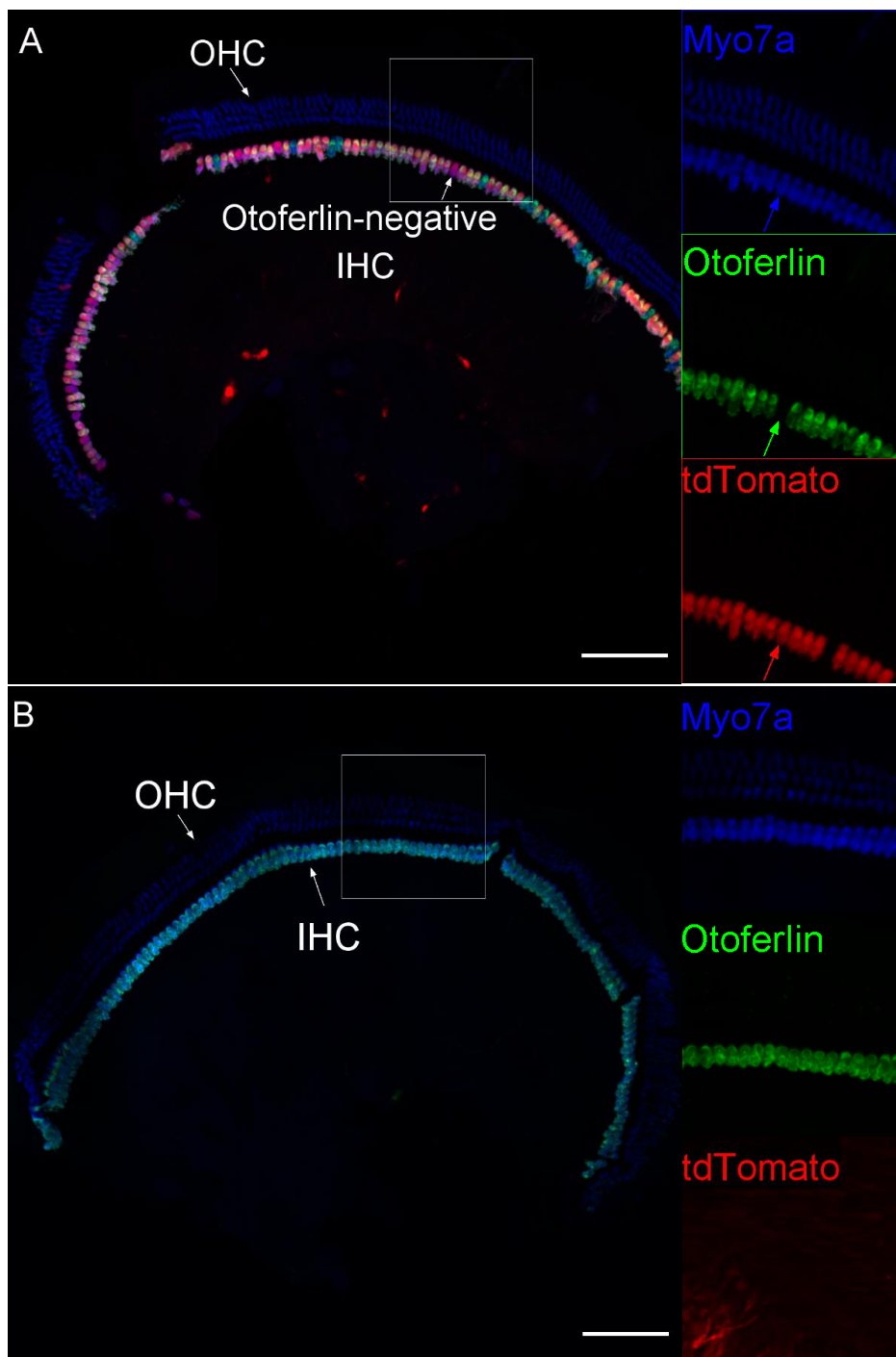
Figure 4.2: Several P50 Vglut3-Cre line mouse IHCs showed reduced otoferlin signal

Otoferlin[tm1c/tm1c] X Vglut3-Cre[+/-]X tdTomato^{+/-} (A) Otoferlin[tm1c/tm1c] X Vglut3-Cre^{-/-}X tdTomato^{+/-} (Wt,B). Blue: Myo7a (cell marker), Green: Otoferlin, Red: tdTomato. (B) does not include red channel as the staining was non-specific. Scale bars represent 88μm.

The same results of Vglut3-Cre line as Barhl1-Cre line suggested that the protocol of tamoxifen-inducing knock-out might need improvement. To find the key factor contributing towards the better knock-out, several factors were listed and changed, which include reducing the injection gap to 24 hours, using Cre-positive but tdTomato negative cells as internal controls, injecting younger mice (P10 to P14) and increasing tamoxifen dosage (for younger mice, the final concentration reached 200µg/g, which is twice as high as the suggested concentration). The P20-P24 mice injected with shorter gaps did not show different pattern of otoferlin-knock-out. TdTomato-negative but Cre-positive cells did not show much of otoferlin-knock-out either (data not shown). As shown in Figure 4.3, when P14 mice were injected high dosage of tamoxifen with 24h gap, after leaving for 4 weeks the signal of otoferlin staining was missing in several more IHCs of Otoferlin$^{tm1c/tm1c}$ X Vglut3-Cre$^{+/-}$X tdTomato$^{+/-}$ mice when compared to the P20-P24 mice. As for younger mice, P10 mice were injected with 24hour gap at a high dosage (200µg/g), the immunostaining experiments 4 weeks after injection showed that the number of IHCs otoferlin-positive decreased slightly when compared to the older mice (Figure 4.4).
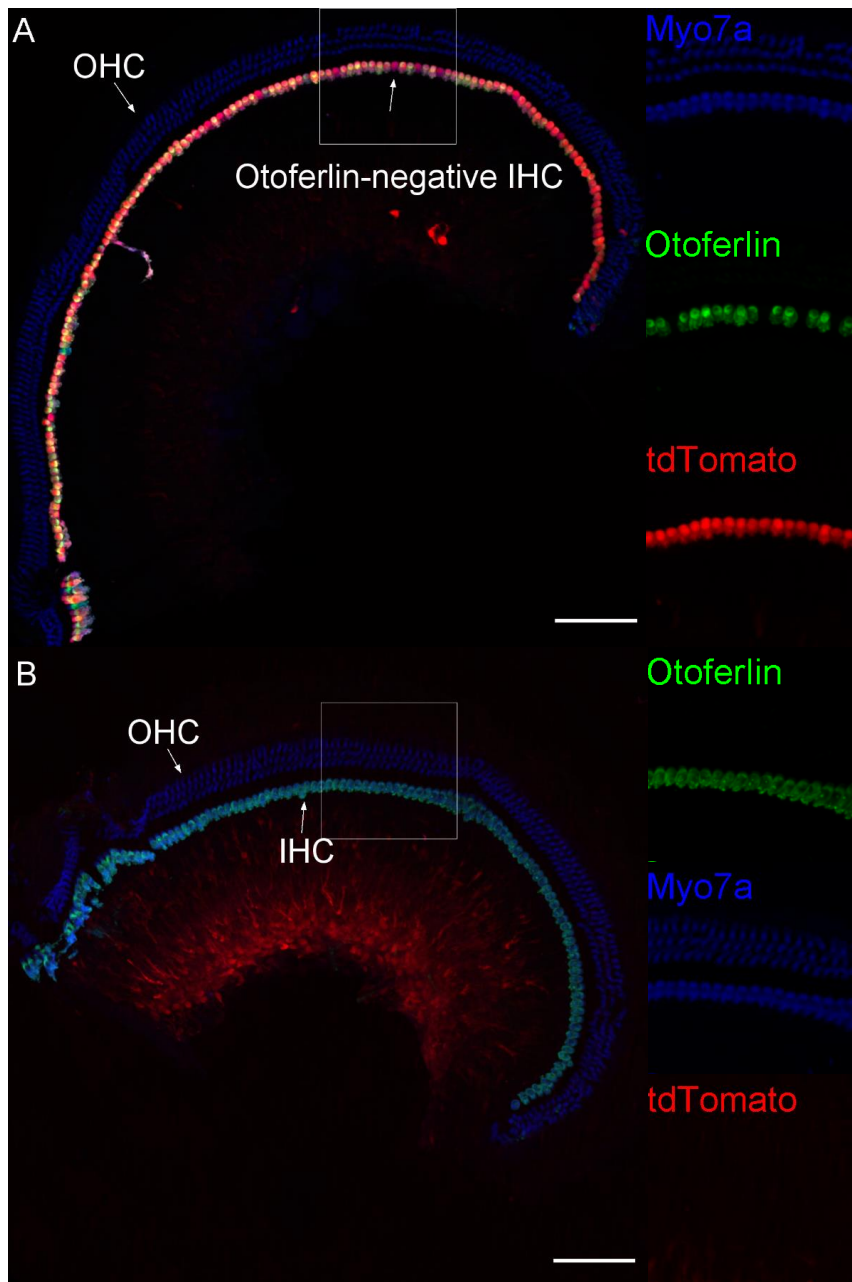
Figure 4.3: P42 Vglut3-Cre line mice showed reduced otoferlin signal

Otoferlin[tm1c/tm1c] X Vglut3-Cre^{+/-} X tdTomato^{+/-} (A) and Otoferlin[tm1c/tm1c] X Vglut3-Cre^{-/-} X tdTomato^{+/-} (Wt,B). Blue: Myo7a (cell marker), Green: Otoferlin, Red: tdTomato. Scale bars represent 88µm.
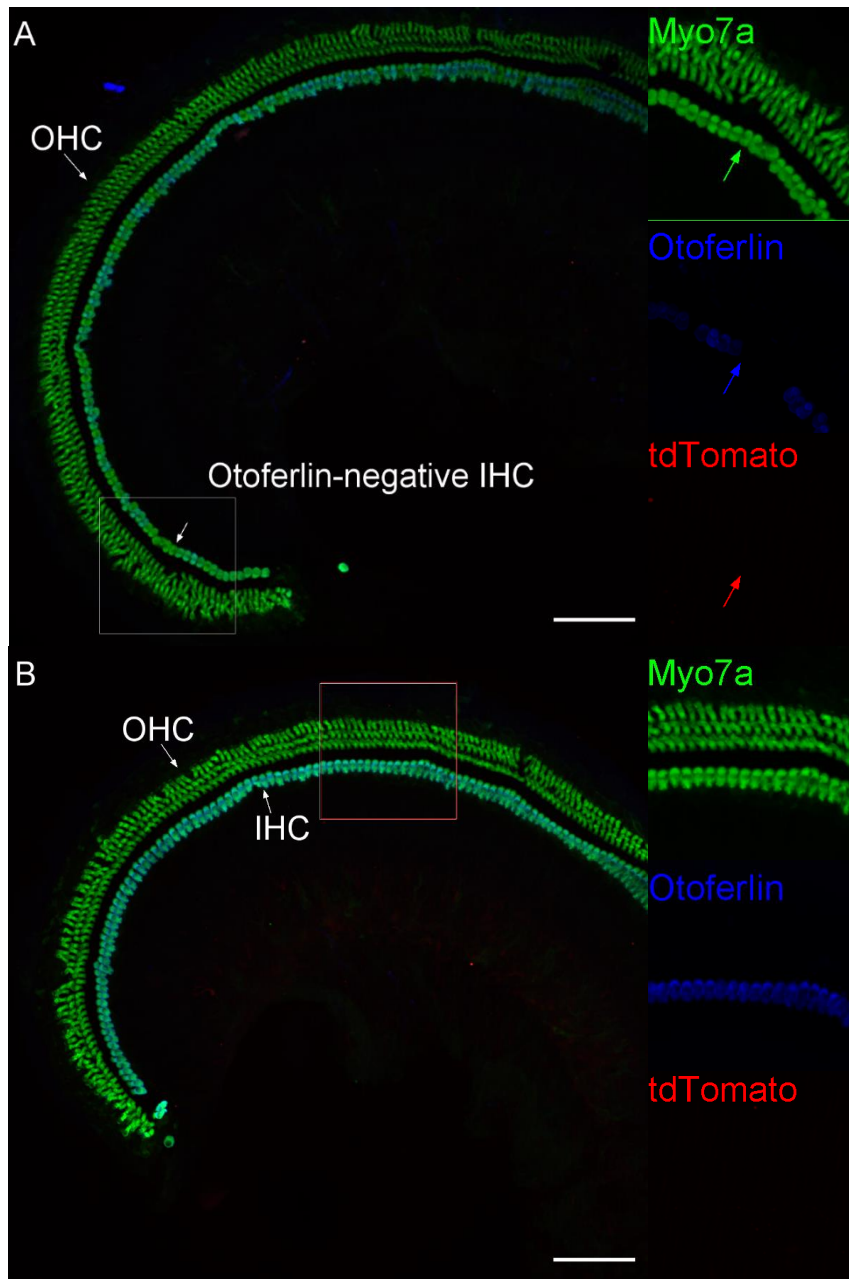
Figure 4.4: P38 Vglut3-Cre line mice showed reduced otoferlin signal

Otoferlin[tm1c/tm1c] X Vglut3-Cre^{+/-} X tdTomato^{+/-} (A) and Otoferlin[tm1c/tm1c] X Vglut3-Cre^{-/-} X tdTomato^{+/-} (Wt,B). Blue: Myo7a (cell marker), Green: Otoferlin, Red: tdTomato. Scale bars represent 88μm.

4.3 Discussion

Although the transduction rate of otoferlin-knock-out when younger mice (P10-P14) were injected with tamoxifen was higher, it was still much lower than that of tdTomato positive cells, leading to a problem of tdTomato not being a good marker of the otoferlin-knocked-out cell for further whole-cell patching experiments. The inconsistency between the tdTomato transduction and otoferlin-knock-out suggested different possibilities. One is that the sensitivity of tdTomato towards tamoxifen induced Cre-recombinase activation is higher than otoferlin. Another explanation of the results can be that the Cre-activation can not be triggered by the low concentration of tamoxifen within the system. The fact that higher dosage would kill the mice suggested that tamoxifen dosage can not be higher than the current concentration, making optimizing the protocol more difficult. There is also another possibility that otoferlin turnover at IHC synapses is very stable in adult mice, requiring a very long time to knockout otoferlin. To test this theory, a different model, Otoferlin-tm1c X Myo15-Cre, was introduced. The further details are described in the next chapter.

5 Otoferlin is required for maintenance of exocytosis in IHC ribbon synapses from late pre-mature age

5.1 Introduction

As described in chapter 4, the conditional-knock-out experiments focusing on mice after the 2nd postnatal week can not provide reliable samples for capacitance measurement. To resolve the problem, a more reliable model which can trigger conditional-knock-out at early stage is required using the Otoferlin-tm1c X Myo15-Cre mouse models. Myo15 is a gene that starts to express around postnatal day 1 (Anderson et al., 2000) and in this chapter we characterize the knock-out process of this model and did a series of electrophysiological recordings on the mutants to check whether there is an effect of the conditional knock-out on normal IHC function.

5.2 Results

To characterize the timeline of myo15-Cre expression-related otoferlin knock-out, a series of immunostaining experiments were performed on P7, P10 and P14 mouse cochlea. The time points were selected after considering that the half-life of the protein within the cells might keep the otoferlin function even after the myo15-Cre expression. On postnatal day 7 (P7), Otoferlin$^{tm1c/tm1c}$ X Myo15-Cre$^{-/-}$ (WT) IHCs and OHCs showed otoferlin staining (Red). As for Cre-positive IHCs, most of IHCs and OHCs still show otoferlin staining but the signal intensity started to decline in some IHCs, with the staining of otoferlin be more localized towards the apical side of the cell (Figure 5.1).

A Otoferlin$^{tm1c/tm1c}$ X Myo15-Cre$^{-/-}$
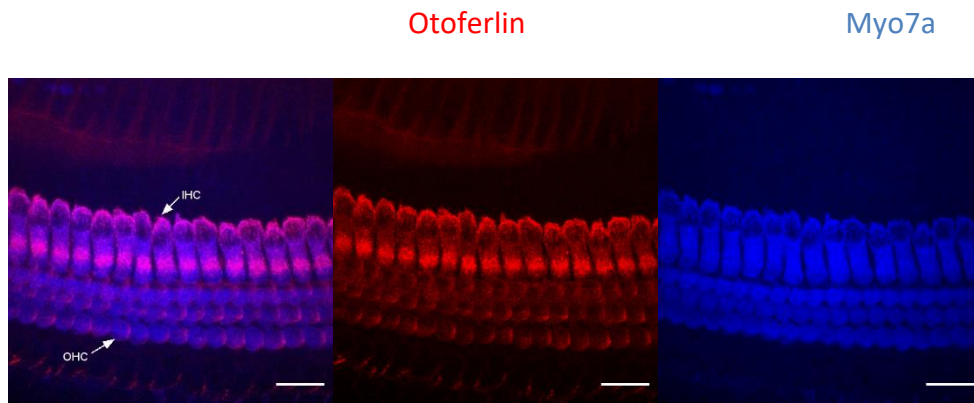
B Otoferlin$^{tm1c/tm1c}$ X Myo15-Cre$^{+/-}$
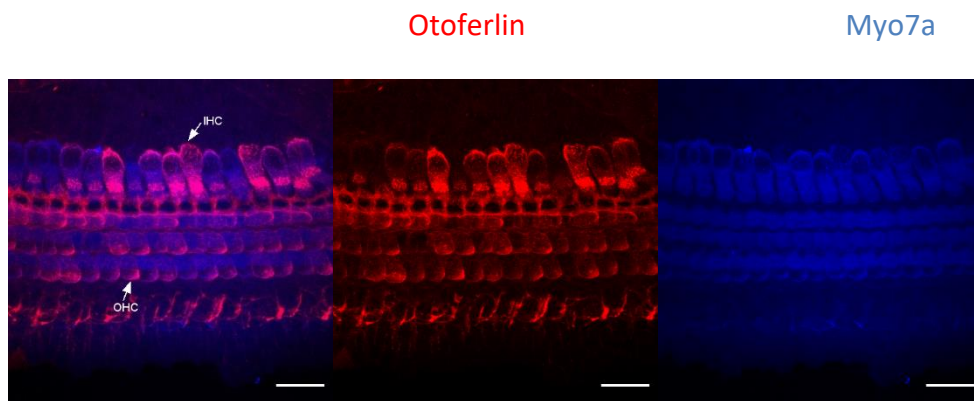
Figure 5.1: P7 Myo15-Cre line mouse IHCs start to show reduced otoferlin signal

Otoferlin$^{tm1c/tm1c}$ X Myo15-Cre$^{-/-}$ (A) and Otoferlin$^{tm1c/tm1c}$ X Myo15-Cre$^{+/-}$ mice (B). From the left are the composite, anti-otoferlin staining(red) and anti-myo7a(blue) staining. Scale bars represent 20µm.

At P10, Cre-positive IHCs showed a further reduction of otoferlin signal in immunostaining. Cell counting of otoferlin-positive and negative cells showed that about 70% of the cells in the imaging region did not show much of otoferlin signal (n=4, Figure 5.2).

A Otoferlin$^{tm1c/tm1c}$ X Myo15-Cre$^{+/-}$

Otoferlin   Myo7a

B Otoferlintm1c/tm1c X Myo15-Cre$^{-/-}$

Otoferlin   Myo7a
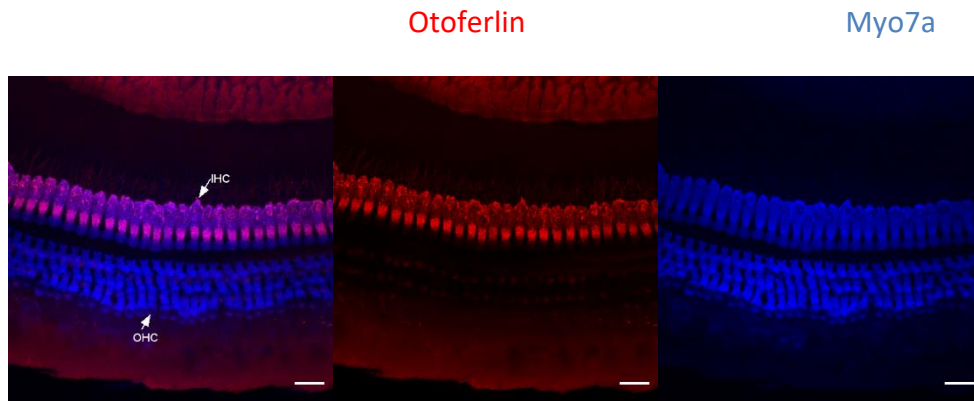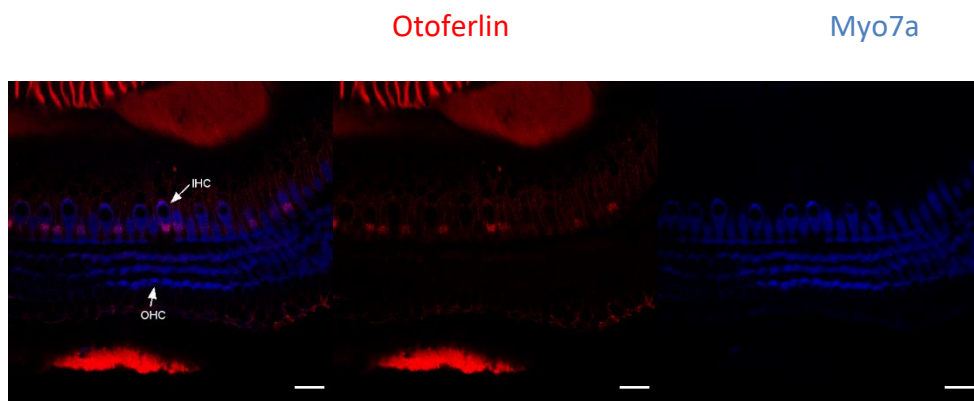
Figure 5.2： P10 Myo15-Cre line mouse IHCs showed strongly reduced otoferlin signal

Otoferlin$^{tm1c/tm1c}$ X Myo15-Cre$^{-/-}$ (A) and Otoferlin$^{tm1c/tm1c}$ X Myo15-Cre$^{+/-}$ mice (B). From the left to right are overlap, anti-otoferlin staining(red) and cell marker anti-myo7a (blue) staining. The otoferlin staining signal in P10 mutants are much more reduced and it is only present in about 30% of the IHCs observed. Scale bars represent 20μm.

After P14, the otoferlin staining signal is absent in all the IHCs (as well as OHCs), indicating that the otoferlin is fully degraded (Figure 5.3).

A Otoferlin$^{tm1c/tm1c}$ X Myo15-Cre$^{+/-}$
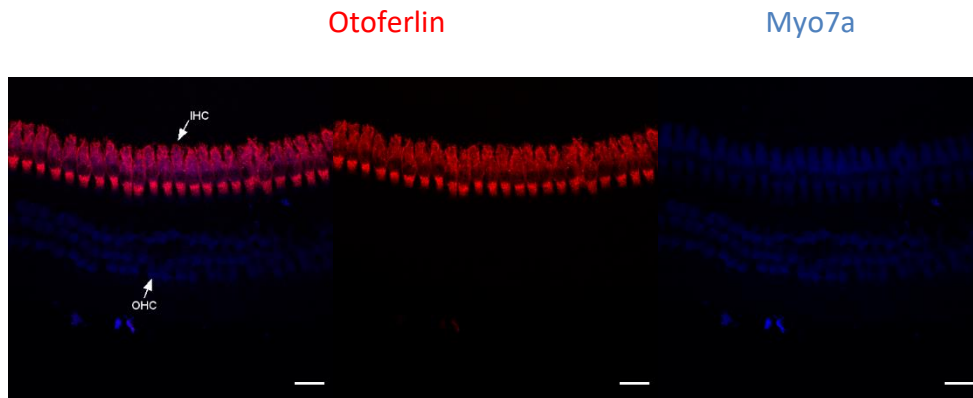
B Otoferlin$^{tm1c/tm1c}$ X Myo15-Cre$^{-/-}$
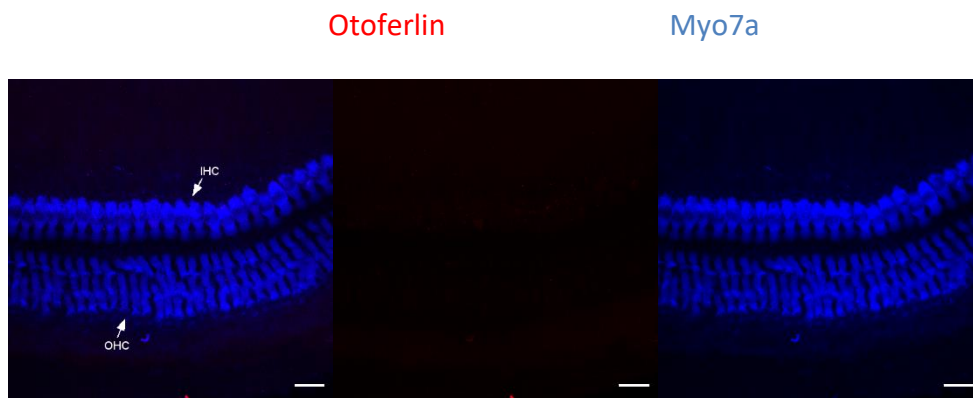
Figure 5.3：P14 Myo15-Cre line mouse IHCs showed no otoferlin staining,

Otoferlin$^{tm1c/tm1c}$ X Myo15-Cre$^{-/-}$ (A) and Otoferlin$^{tm1c/tm1c}$ X Myo15-Cre$^{+/-}$ mice (B). From the left to right are overlap, anti-otoferlin staining(red) and cell marker anti-myo7a(blue) staining. The otoferlin staining signal in P14 mutants are gone in all the IHCs observed. Scale bars represent 20μm.

The immunostaining experiment results established a timeline of the otoferlin knockout. The next questions is, whether the otoferlin degradation can lead to functional deficits. The functional test of otoferlin in Myo15-Cre-triggered knock-out model mainly involves different protocols of capacitance measurement. As in previous research, constitutive otoferlin$^{-/-}$ mice showed reduced Ca^{2+} evoked exocytosis(Beurg et al., 2008; Roux et al., 2006), the hypothesis is that Myo15-Cre positive cells would show reduced exocytosis. In combination with the immunostaining results, the reduction of exocytosis would be more significant from P10 onwards as there are more IHCs become otoferlin-negative.

At P7, IHCs were depolarized by applying 10mV voltage steps of 50ms duration from -81mV. The K$^+$ currents were blocked by TEA, 4-AP and Apamin to obtain better recordings of Ca^{2+} currents. As shown in Figure 5.4A, the I-V curve is plotted based upon mean voltage values and the correlated mean Ca^{2+} current (I_{Ca}). The data are plotted as mean data ± SEM. There is no significant difference between the mean maximal I_{Ca} value of the WT (Otoferlin$^{tm1c/tm1c}$ X Myo15-Cre$^{-/-}$: -477.40 ± 29.69 pA at

-11mV, n=11 IHCs from 8 mice) and knockout mice (Otoferlin$^{tm1c/tm1c}$ X Myo15-Cre$^{+/-}$: -395.40 ± 25.98 pA at -11mV, n=11 IHCs from 10 mice, p>0.05, unpaired t-test). In Figure 5.4B, it showed the mean capacitance change (ΔC_m) in response to the above voltage steps, there was no significant difference in mean ΔC_m between the two genotypes (Otoferlin$^{tm1c/tm1c}$ X Myo15-Cre$^{-/-}$: 22.17 ± 4.37 fF at -11mV, n=11 IHCs from 8 mice, Otoferlin$^{tm1c/tm1c}$ X Myo15-Cre$^{+/-}$ 14.30 ± 3.67 fF at -11mV, n=11 IHCs from 10 mice, p=0.1835, unpaired t-test). The results showed that at P7, although the otoferlin expression started to decrease, the size of exocytosis in Otoferlin$^{tm1c/tm1c}$ X Myo15-Cre$^{-/-}$ IHCs are still not significantly different from the control cells.
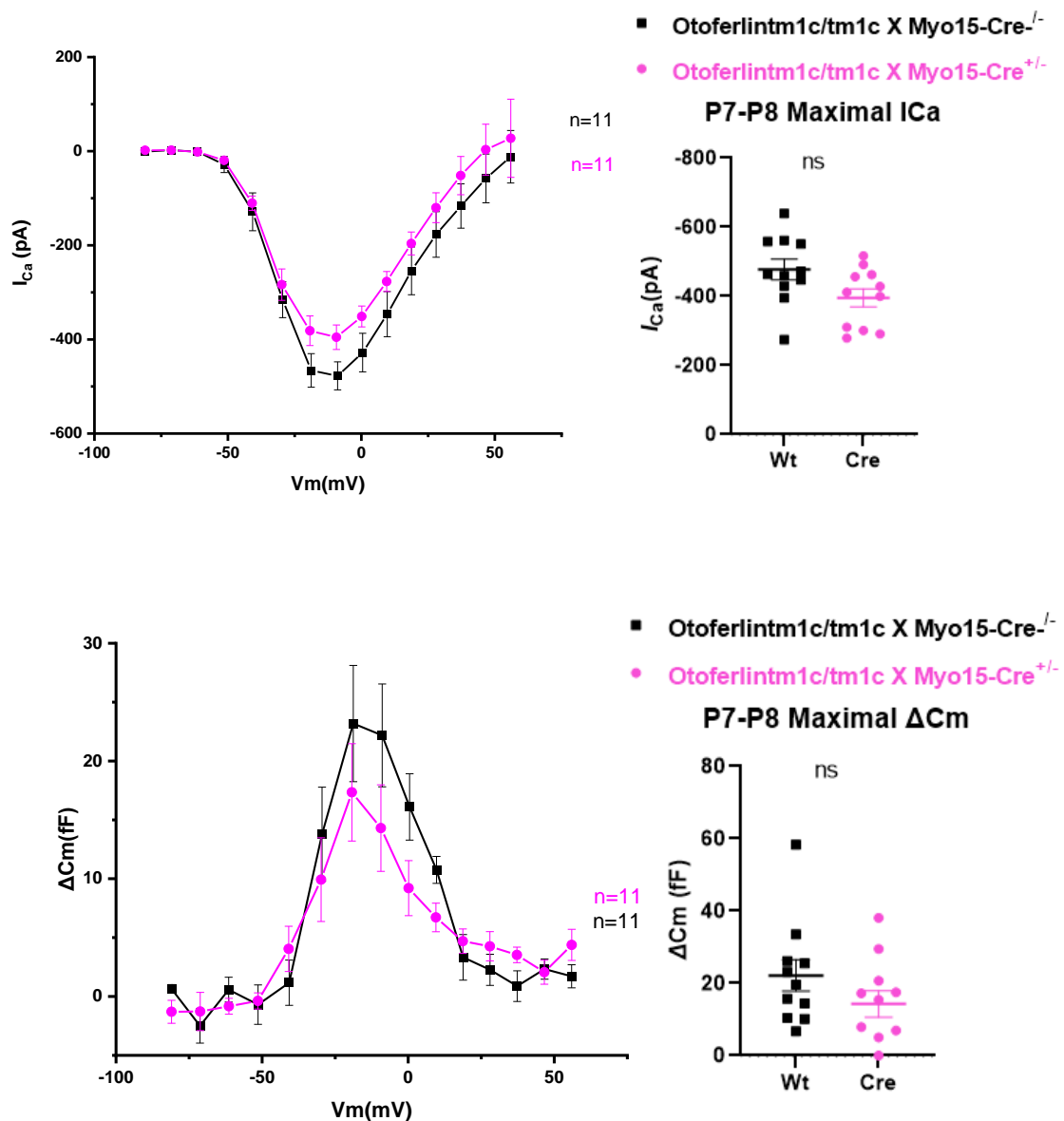
Figure 5.4: P7 Otoferlin^tm1c/tm1c X Myo15-Cre^-/- (WT) and Otoferlin^tm1c/tm1c X Myo15-Cre^+/- IHCs showed similar size of I_{Ca} and ΔC_m.

No significant difference in maximal I_{Ca} (at -11mV) and exocytosis (at -11mV) between P7 WT and Otoferlin^tm1c/tm1c X Myo15-Cre^+/- mice (Otoferlin^tm1c/tm1c X Myo15-Cre^-/-, n=11 IHCs from 8 mice, Otoferlin^tm1c/tm1c X Myo15-Cre^-/-, n=11 IHCs from 10 mice, p>0.05, unpaired t-tests). The data are plotted as mean data ± SEM.

To compare the sensitivity of the IHC exocytosis towards the inward Ca^{2+} current, the mean I_{Ca} value and the corresponding ΔC_m value was plotted and the line of best fit was drawn based on the following function:

$$\Delta Cm = cI_{Ca}^{N}$$

Where c is a scaling coefficient, N is the power value. The unpaired t-test showed that there was no significant difference in the power value (Otoferlin$^{tm1c/tm1c}$ X Myo15-Cre$^{-/-}$: 2.36 ± 0 .64, n=11 IHCs from 8 mice. Otoferlin$^{tm1c/tm1c}$ X Myo15-Cre$^{+/-}$: 2.97 ±0.95, n=11 IHCs from 10 mice, p>0.05, unpaired t-test). Indicating there was no difference in IHC exocytotic sensitivity towards the Ca^{2+}(Figure 5.5).
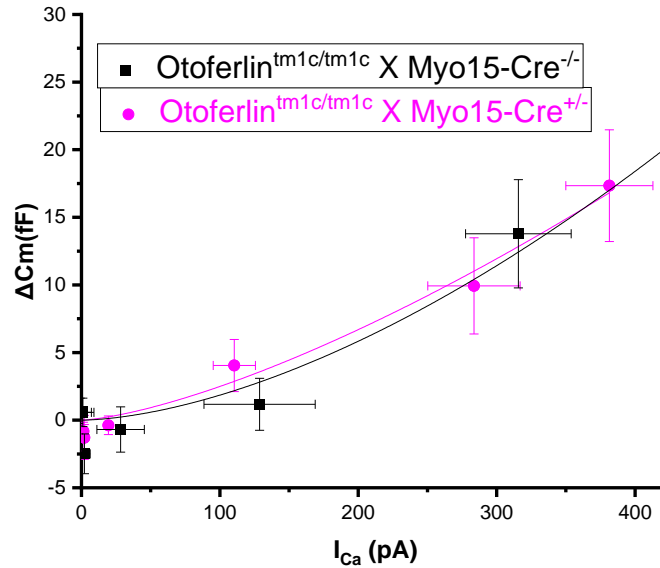
Figure 5.5： P7 Myo15-Cre line mouse IHC showed similar sensitivity of exocytosis compared to the WT.

Synaptic transfer curves are drawn by plotting ΔC_m against the corresponding I_{Ca} between -71mV and -11mV according to function $\Delta C_m = cI_{Ca}^{N}$, c is scaling coefficient and the N is the power value. Both the control and the mutant IHCs showed high-order exocytotic Ca^{2+} dependance (Otoferlin$^{tm1c/tm1c}$ X Myo15-Cre$^{-/-}$: 2.357 ± 0.64, n=11 IHCs from 8 mice, Otoferlin$^{tm1c/tm1c}$ X Myo15-Cre$^{+/-}$: 2.969 ± 0.95, n=11 IHCs from 10 mice, p>0.05, unpaired t-test). The data are plotted as mean data ± SEM.

The same protocol was applied to P10 IHCs and the I-V curve as well as ΔC_m-V curve is shown in Figure 5.6. Although there was no significant difference in the mean I_{Ca} values (Otoferlin[tm1c/tm1c] X Myo15-Cre^{-/-}: -472.43 ± 27.63 pA, n=9 IHCs from 8 mice, Otoferlin[tm1c/tm1c] X Myo15-Cre^{+/-}: -450.10 ± 20.65 pA, n=8 IHCs from 7 mice, p>0.05, unpaired t-test), the mean ΔC_m of the mutant IHCs start to become significantly smaller than the control (Otoferlin[tm1c/tm1c] X Myo15-Cre^{-/-}: 27.12 ± 2.01 fF at -11mV, n=9 IHCs from 8 mice, Otoferlin[tm1c/tm1c] X Myo15-Cre^{+/-} 13.82 ± 3.62 fF at -11mV, n=8 IHCs from 7 mice, p=0.048, unpaired t-test). The results showed that together with big decrease of otoferlin expression at P10, the size of exocytosis of Otoferlin[tm1c/tm1c] X Myo15-Cre^{-/-} IHCs started to be significantly lower than the control cells. In addition, the synaptic fit curve showed that there is no significant difference in the power value of the fit between the mean power values of the control and the mutant IHCs (p>0.05, unpaired t-test, Figure 5.7).
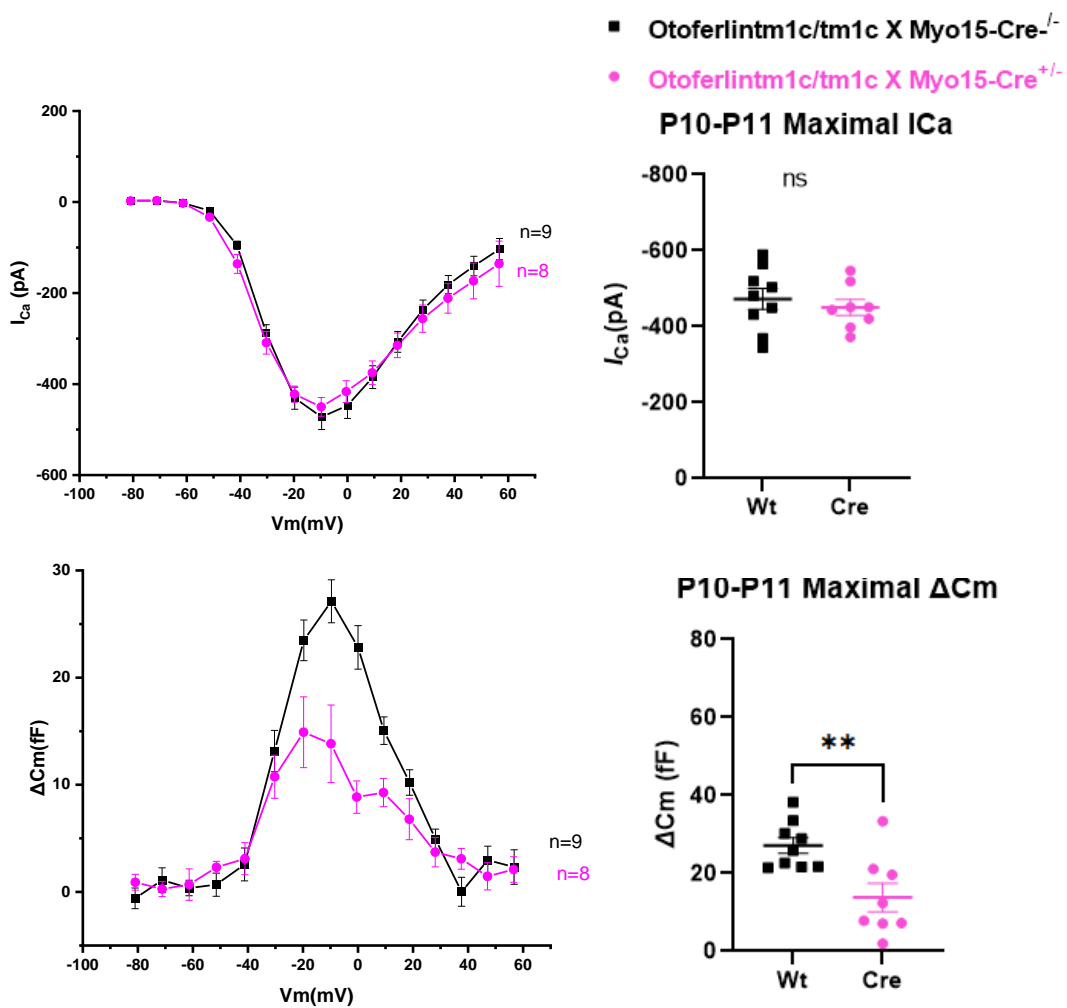
Figure 5.6: P10-P11 Otoferlin^{tm1c/tm1c} X Myo15-Cre^{+/-} IHCs showed significantly reduced ΔC_m and similar size of I_{Ca} compared with Otoferlin^{tm1c/tm1c} X Myo15-Cre^{-/-} (WT).

No significant difference in maximal I_{Ca} between P10-11 control and Otoferlin^{tm1c/tm1c} X Myo15-Cre^{+/-} mice (WT⁻: -472.43 ± 27.63 pA, n=9 IHCs from 8 mice, Otoferlin^{tm1c/tm1c} X Myo15-Cre^{+/-}: -450.10 ± 20.65 pA, n=8 IHCs from 7 mice, p>0.05, unpaired t-test). The maximal ΔC_m of Otoferlin^{tm1c/tm1c} X Myo15-Cre^{+/-} is significantly smaller than the WT IHCs (WT: 27.12±2.01 fF, n=9 IHCs from 8 mice Otoferlin^{tm1c/tm1c} X Myo15-Cre^{+/-} 13.82±3.62 fF, n=8 IHCs from 7 mice, p=0.048, unpaired t-test). The data are plotted as mean data ± SEM.
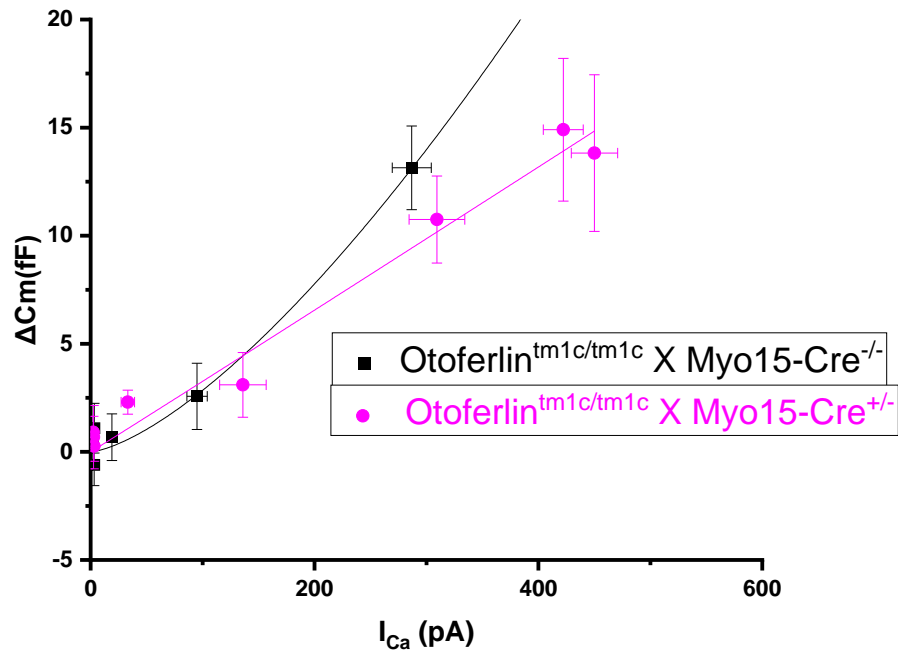
Figure 5.7：**P10-P11 Myo15-Cre line mouse IHC showed similar sensitivity of exocytosis compared to the WT.**

Synaptic transfer curves by plotting ΔC_m against the corresponding I_{Ca} between -71mV and -11mV according to function $\Delta C_m = cI_{Ca}^N$, c is scaling coefficient and the N is the power value. No significant difference between the mean power values of the control and the mutant IHCs. (n represents IHC number. p>0.05, unpaired t-test). The data are plotted as mean data ± SEM.

To further test the functional role of the Otoferlin$^{tm1c/tm1c}$ X Myo15-Cre$^{+/-}$ IHCs, kinetic measurements of capacitance change in response to voltage stimuli were used (2ms to 1s of stimulus at -11mV, at least 10s intervals). As shown in Figure 5.8, The kinetic measurements are an indicator of the size of the readily releasable pool (RRP) and the secondary releasable pool (SRP). During short stimuli (smaller than 100ms), the exocytosis are mainly due to neurotransmitter release docked at the active zones(Johnson et al., 2008). During longer steps, the vesicles are mainly recruited from the SRP, which are further away from Ca^{2+} channels (Johnson et al., 2008; Von Gersdorff et al., 1996). The two-way ANOVA analysis showed that the size of the Otoferlin$^{tm1c/tm1c}$ X Myo15-Cre$^{+/-}$IHC SRP is significantly smaller than the control IHCs (p=0.0073, two-way ANOVA).
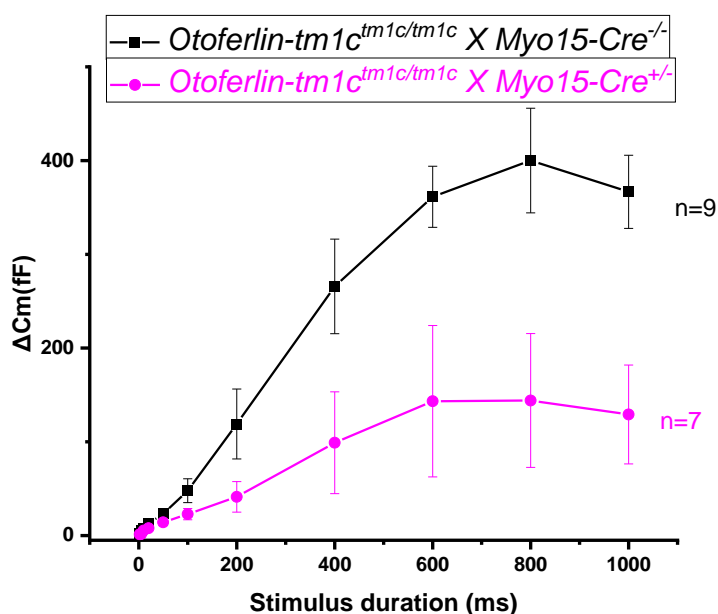
Figure 5.8: P10-P11 Otoferlin$^{tm1c/tm1c}$ X Myo15-Cre$^{+/-}$ IHCs has significantly reduced SRP size.

The size of SRP is significantly smaller in Otoferlin$^{tm1c/tm1c}$ X Myo15-Cre$^{+/-}$ mouse IHCs than the Otoferlin$^{tm1c/tm1c}$ X Myo15-Cre$^{-/-}$ (WT) mice (WT: n=9 IHCs from 9 mice, Otoferlin$^{tm1c/tm1c}$ X Myo15-Cre$^{+/-}$ n=7 IHCs from 6 mice, unpaired t-test, p=0.0073, two-way ANOVA). The data are plotted as mean data ± SEM.

Vesicle replenishment tests were performed on P10 IHCs to give an indication of how fast the IHCs can deplete the releasable pools. A train of 50ms stimulus at -11 mV were applied to the IHCs and the cumulative ΔC_m was recorded. As shown in Figure 5.9, Otoferlin[tm1c/tm1c] X Myo15-Cre^{+/-} IHCs showed a significantly smaller size of the cumulative ΔC_m, indicating that the mutant IHCs recruit vesicles slower than that in control mice (Otoferlin[tm1c/tm1c] X Myo15-Cre^{-/-}, n=4 IHCs, Otoferlin[tm1c/tm1c] X Myo15-Cre^{+/-}, n=5 IHCs, p=0.0315, two-way ANOVA).
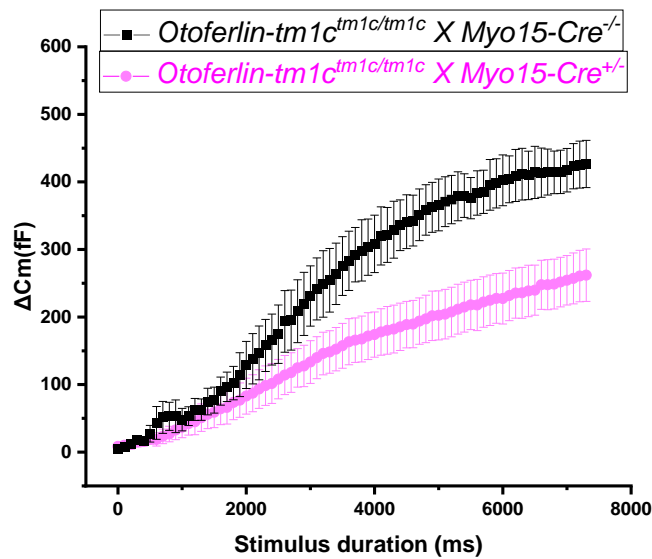
Figure 5.9: P10-11 Otoferlin[tm1c/tm1c] X Myo15-Cre^{+/-} IHCs showed significantly reduced vesicle replenishment rate

The vesicle replenishment is significantly slower in Otoferlin[tm1c/tm1c] X Myo15-Cre^{+/-} IHCs (WT, n=4 IHCs from 4 mice, Otoferlin[tm1c/tm1c] X Myo15-Cre^{+/-}, n=5 IHCs from 5 mice, p=0.0315, two-way ANOVA). The data are plotted as mean data ± SEM.

To further test whether correlation between the reduced otoferlin and the reduction in exocytosis, IHCs from post-hearing P12 to P13 mice were tested under the same protocols. Being different from immature IHCs, during the capacitance measurement, mature IHCs were perfused with linopirdine as well as TEA, 4-AP and Apamin. When given 50ms voltage steps from -81 mV to +55 mV, there was no significant difference in the mean value of maximal I_{Ca} (Otoferlin$^{tm1c/tm1c}$ X Myo15-Cre$^{-/-}$: -329.26 ± 34.52 pA at -1mV, n=11 IHCs from 11 mice, Otoferlin$^{tm1c/tm1c}$ X Myo15-Cre$^{+/-}$: -349.22±40.15pA at -1mV,n=6 IHCs from 6 mice, p>0.05, unpaired t-test), while the mutant IHCs showed significantly smaller size of maximal ΔC_m (Otoferlin$^{tm1c/tm1c}$ X Myo15-Cre$^{-/-}$: 15.94±2.98 fF at -1mV,n=11 IHCs from 11 mice,   Otoferlin$^{tm1c/tm1c}$ X Myo15-Cre$^{+/-}$ 8.65±1.64 fF at -1mV, n=6 IHCs from 6 mice, p=0.036, unpaired t-test, Figure 5.10). Being similar to P10 results, the size of exocytosis at Otoferlin$^{tm1c/tm1c}$ X Myo15-Cre$^{-/-}$ IHCs are significantly smaller than the wild type.
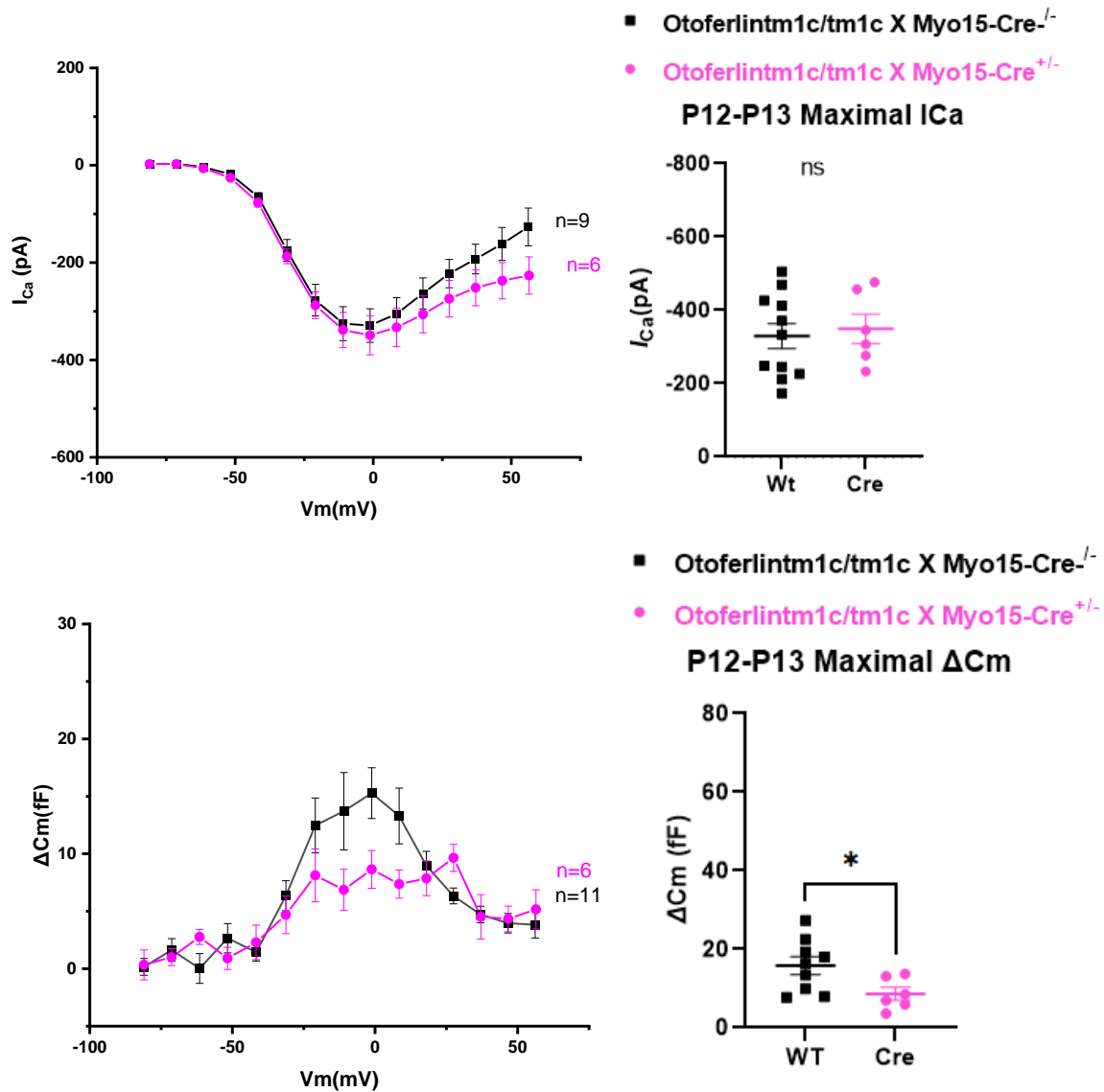
Figure 5.10: P12-P13 Otoferlin^tm1c/tm1c X Myo15-Cre^+/- IHCs showed significantly reduced ΔC_m and similar size of I_{Ca} compared with Otoferlin^tm1c/tm1c X Myo15-Cre^-/- (WT).

No significant difference in maximal I_{Ca} between P12-13 WT and Otoferlin^tm1c/tm1c X Myo15-Cre^+/- mice (WT: -329.26 ± 34.52 pA, n=11 IHCs, Otoferlin^tm1c/tm1c X Myo15-Cre^+/-: -349.22±40.15 pA, n=6 IHCs, p>0.05, unpaired t-test). The maximal $ΔC_m$ of Otoferlin^tm1c/tm1c X Myo15-Cre^+/- is significantly smaller than the WT IHCs (WT: 15.94 ±2.98 fF, n=11 IHCs, Otoferlin^tm1c/tm1c X Myo15-Cre^+/- 8.65±1.64 fF, n=6 IHCs, p=0.036, unpaired t-test). The data are plotted as mean data ± SEM.

ΔC_m against I_{Ca} (Figure 5.11) shows the best fit for both the control and the mutant IHCs showed no significant difference in exocytotic Ca^{2+} dependance (Otoferlin[tm1c/tm1c] X Myo15-Cre^{-/-}: N power=1.205±0.17, n=9 IHCs from 8 mice, Otoferlin[tm1c/tm1c] X Myo15-Cre^{+/-}: N power=0.74±0.18, n=6 IHCs from 6 mice, p>0.05, unpaired t-test).
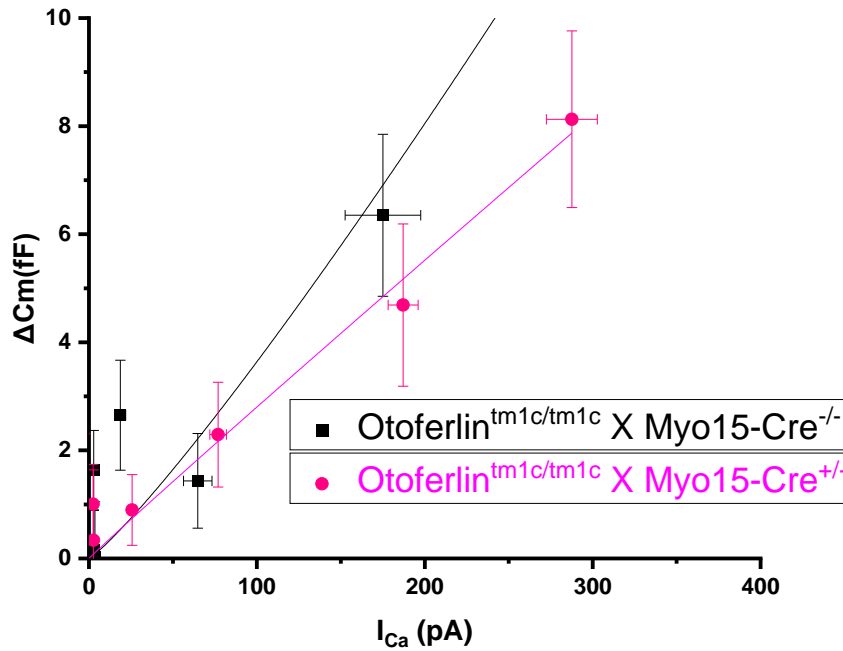
Figure 5.11: P12-P13 Myo15-Cre line mouse IHC showed similar sensitivity of exocytosis compared to the WT.

Synaptic transfer curves by plotting ΔC_m against the corresponding I_{Ca} between -71mV and -11mV according to function $\Delta C_m = cI_{Ca}{}^N$, c is scaling coefficient and the N is the power value. No significant difference between the mean power values of the control and the mutant IHCs (Otoferlin[tm1c/tm1c] X Myo15-Cre^{-/-}: 1.205±0.17, n=9 IHCs from 8 mice, Otoferlin[tm1c/tm1c] X Myo15-Cre^{+/-}: 0.74±0.18, n=6 IHCs from 6 mice, p>0.05, unpaired t-test). The data are plotted as mean data ± SEM.

To further test the size of the RRP and SRP, kinetics measurement of the capacitance changes of the P12-P13 mouse IHCs were performed. As shown in Figure 5.9, there was a significant reduction in SRP size of Otoferlin[tm1c/tm1c] X Myo15-Cre[+/-]IHCs (p<0.0001, two-way ANOVA).
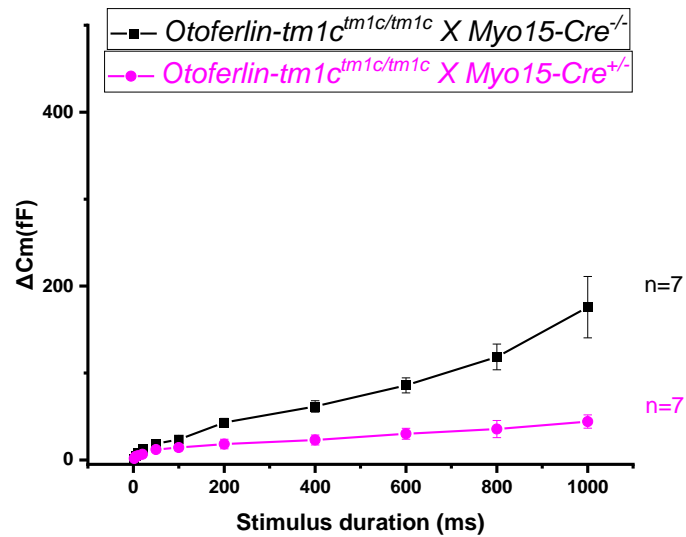
Figure 5.12: P12-P13 Otoferlin[tm1c/tm1c] X Myo15-Cre^{+/-} IHCs has significantly reduced SRP size.

The size of SRP is significantly smaller in Otoferlin[tm1c/tm1c] X Myo15-Cre^{+/-} mouse IHCs (Otoferlin[tm1c/tm1c] X Myo15-Cre^{-/-}: n=7 IHCs from 7 mice, Otoferlin[tm1c/tm1c] X Myo15-Cre^{+/-}: n=7 IHCs from 7 mice, p>0.05, unpaired t-test p<0.0001, two-way ANOVA). The data are plotted as mean data ± SEM.

Vesicle replenishment tests showed similar results towards the P10-P11 IHCs. The Otoferlin[tm1c/tm1c] X Myo15-Cre^{+/-} IHCs showed significant reduction of the cumulative ΔC_m when compared to the WT (Otoferlin[tm1c/tm1c] X Myo15-Cre^{-/-}, n=5 IHCs from 5 mice, Otoferlin[tm1c/tm1c] X Myo15-Cre^{+/-} n=7 IHCs from 5 mice, p<0.0001, two-way ANOVA).
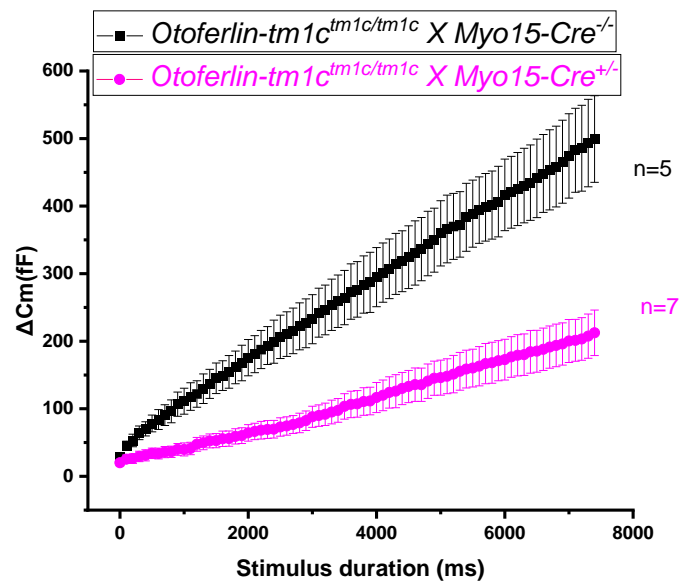
Figure 5.13: P12-P13 Otoferlin[tm1c/tm1c] X Myo15-Cre^{+/-} IHCs showed significantly reduced vesicle replenishment rate

The vesicle replenishment is significantly slower in Otoferlin[tm1c/tm1c] X Myo15-Cre^{+/-} IHCs (Otoferlin[tm1c/tm1c] X Myo15-Cre^{-/-}, n=5 IHCs from 5 mice, Otoferlin[tm1c/tm1c] X Myo15-Cre^{+/-} n=7 IHCs, p<0.0001, two-way ANOVA). The data are plotted as mean data ± SEM.

As shown in Figure 5.3, from P14 onwards, otoferlin signals were not detected in all the Otoferlin$^{tm1c/tm1c}$ X Myo15-Cre$^{+/-}$ IHCs. It was interesting to test whether there are still any Ca^{2+}-activated exocytotic behavior in those cells. 50ms of 10mV voltage steps from -81mV to +55mV (K$^+$ currents blocked by TEA, 4-AP and Linopirdine) showed that the maximal I_{Ca} was still similar between the control and the Otoferlin$^{tm1c/tm1c}$ X Myo15-Cre$^{+/-}$ IHCs (Otoferlin$^{tm1c/tm1c}$ X Myo15-Cre$^{-/-}$: -200.52 ± 12.96 pA at -11mV, n=9 IHCs from 9 mice, Otoferlin$^{tm1c/tm1c}$ X Myo15-Cre$^{+/-}$: -170.74±13.40 pA at +11mV, n=4 IHCs from 4 mice, p=0.1625, unpaired t-test). The mutant IHCs showed significantly smaller ΔC_m (Otoferlin$^{tm1c/tm1c}$ X Myo15-Cre$^{-/-}$: 14.07±2.03 fF at -11mV, n=6 IHCs from 6 mice   Otoferlin$^{tm1c/tm1c}$ X Myo15-Cre$^{+/-}$ 2.53±1.55 fF at +11mV, n=4 IHCs from 4 mice, p=0.0035, unpaired t-test). Interestingly, the maximal I_{Ca} of Otoferlin$^{tm1c/tm1c}$ X Myo15-Cre$^{+/-}$ IHCs are shifted towards more depolarized voltage (from -11mV to 11mV, Figure 5.14).
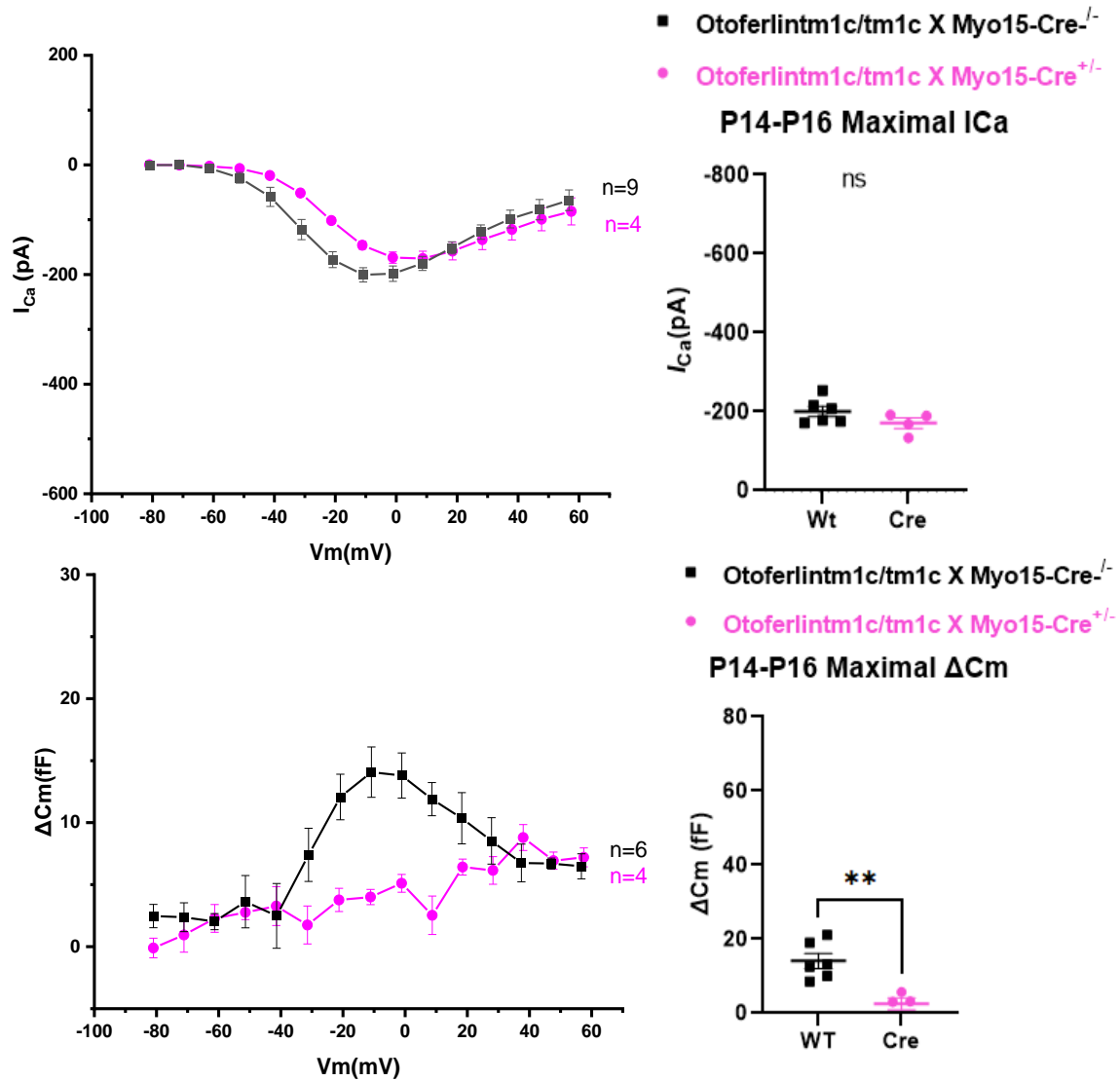
Figure 5.14: P14-P16 Otoferlin^tm1c/tm1c X Myo15-Cre^+/- IHCs showed significantly reduced ΔC_m and similar size of *I_Ca* compared with Otoferlin^tm1c/tm1c X Myo15-Cre^-/- (WT).

No significant difference in maximal I_{Ca} between P14-16 WT and Otoferlin^tm1c/tm1c X Myo15-Cre^+/- mice (WT^-: -200.52±12.96 pA at -11mV, n=9 IHCs from 9 mice, Otoferlin^tm1c/tm1c X Myo15-Cre^+/-: -170.74±13.40 pA at +11mV, n=4 IHCs from 4 mice, p=0.1625, unpaired t-test). The maximal ΔC_m of Otoferlin^tm1c/tm1c X Myo15-Cre^+/- is significantly smaller than the WT IHCs (WT: 14.07±2.03 fF at -11mV, n=6 IHCs from 6 mice, Otoferlin^tm1c/tm1c X Myo15-Cre^+/- 2.53±1.55 fF at +11mV, n=4 IHCs from 4 mice, p=0.0035, unpaired t-test). The data are plotted as mean data ± SEM.

Using power fit to examine the relationship between the I_{Ca} and the corresponding ΔC_m in the mutant IHCs become difficult as there was barely any exocytosis in the mutant IHCs. The WT IHCs showed linear exocytotic Ca^{2+} dependence as expected (Otoferlin$^{tm1c/tm1c}$ X Myo15-Cre$^{-/-}$: 1.104±0.27, n=6 IHCs from 6 mice. Otoferlin$^{tm1c/tm1c}$ X Myo15-Cre$^{+/-}$: 0.21±0.09, n=4 IHCs from 4 mice, p=0.0211, unpaired t-test, Figure 5.15).
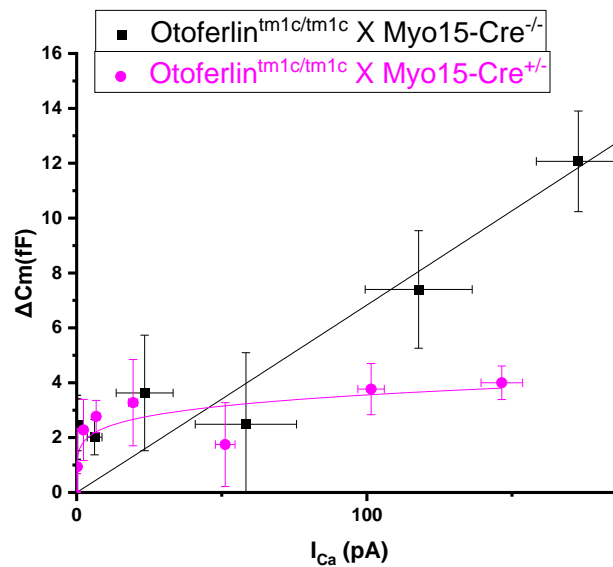
Figure 5.15: P14-P16 Myo15-Cre line mouse IHC showed disrupted exocytotic dependency of Ca^{2+}

Synaptic transfer curves by plotting ΔC_m against the corresponding I_{Ca} between -71mV and -11mV according to function $\Delta C_m = cI_{Ca}^{N}$, c is scaling coefficient and the N is the power value. The difference in power value is big (Otoferlin$^{tm1c/tm1c}$ X Myo15-Cre$^{-/-}$: 1.104±0.27, n=6 IHCs from 6 mice, Otoferlin$^{tm1c/tm1c}$ X Myo15-Cre$^{+/-}$: 0.21±0.09, n=4 IHCs from 4 mice, p=0.0211, unpaired t-test). The data are plotted as mean data ± SEM.

Kinetics measurement of the capacitance changes of the P14-P6 mouse IHCs showed that the SRP size of Otoferlin[tm1c/tm1c] X Myo15-Cre^{+/-} IHCs at -11mV stimulus are almost none (Otoferlin[tm1c/tm1c] X Myo15-Cre^{-/-}, n=7 IHCs from 7 mice, Otoferlin[tm1c/tm1c] X Myo15-Cre^{+/-} n=8 IHCs from 8 mice, p<0.0001, two-way ANOVA, Figure 5.16).
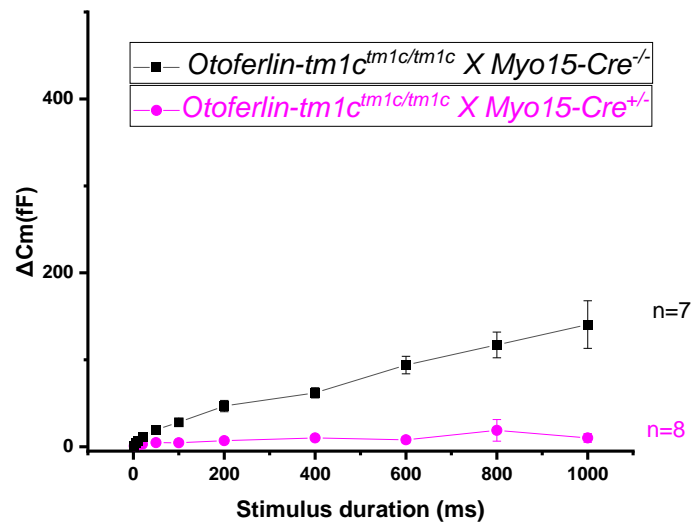
Figure 5.16: P14-P16 Otoferlin[tm1c/tm1c] X Myo15-Cre^{+/-} IHCs has significantly reduced SRP size.

The size of SRP is significantly smaller in Otoferlin[tm1c/tm1c] X Myo15-Cre^{+/-} mouse IHCs (Otoferlin[tm1c/tm1c] X Myo15-Cre^{-/-}, n=7 IHCs from 7 mice, Otoferlin[tm1c/tm1c] X Myo15-Cre^{+/-} n=8 IHCs from 8 mice, p<0.0001, two-way ANOVA). The data are plotted as mean data ± SEM.

Vesicle replenishment tests showed that mutant IHCs showed very little size of cumulative ΔC_m when compared to the control (Otoferlin[tm1c/tm1c] X Myo15-Cre^{-/-}, n=4 IHCs from 4 mice, Otoferlin[tm1c/tm1c] X Myo15-Cre^{+/-} n=6 IHCs from 5 mice, p<0.0001, two-way ANOVA, Figure 5.17).
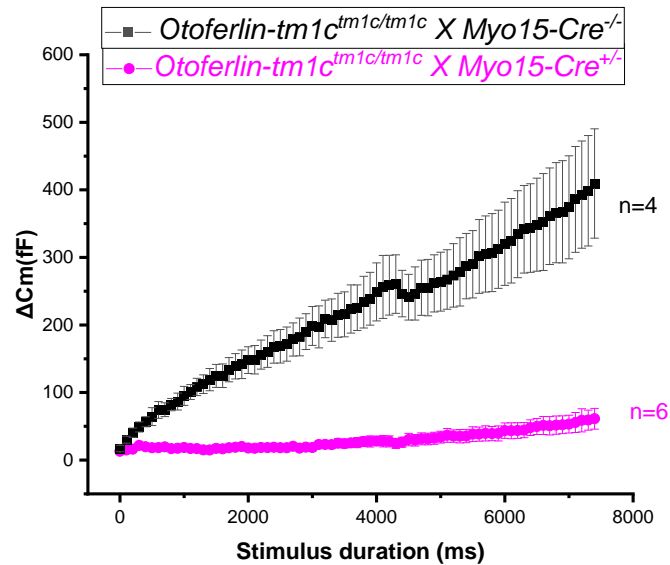
Figure 5.17: P14-P16 Otoferlin[tm1c/tm1c] X Myo15-Cre^{+/-} IHCs showed significantly reduced vesicle replenishment rate

The vesicle replenishment is significantly slower in Otoferlin[tm1c/tm1c] X Myo15-Cre^{+/-} IHCs (Otoferlin[tm1c/tm1c] X Myo15-Cre^{-/-}, n=4 IHCs from 4 mice, Otoferlin[tm1c/tm1c] X Myo15-Cre^{+/-} n=6 IHCs from 5 mice, p<0.0001, two-way ANOVA). The data are plotted as mean data ± SEM.

It was shown that the exocytosis of P14 Otoferlin$^{tm1c/tm1c}$ X Myo15-Cre$^{+/-}$ is significantly reduced and it is necessary to check whether the reduction is consistent at later ages. So, capacitance measurements were performed on P20-P30 mice. Being consistent with the previous results, there was no significant difference in mean value of I_{Ca} between the Otoferlin$^{tm1c/tm1c}$ X Myo15-Cre$^{-/-}$ and Otoferlin$^{tm1c/tm1c}$ X Myo15-Cre$^{+/-}$ mice (Otoferlin$^{tm1c/tm1c}$ X Myo15-Cre$^{-/-}$: -205.23 ± 38.22 pA at -11mV, n=6 IHCs from 5 mice Otoferlin$^{tm1c/tm1c}$ X Myo15-Cre$^{+/-}$: -145.24±25.57 pA at -1mV, n=7 IHCs from 7 mice, p>0.05, unpaired t-test). Interestingly, being similar to P14 mice, the maximal I_{Ca} of Otoferlin$^{tm1c/tm1c}$ X Myo15-Cre$^{+/-}$ IHCs showing a shift towards more depolarized potential when compared to the wild type (from about -11mV to -1 mV Figure 5.15). From perspective of capacitance change, Otoferlin$^{tm1c/tm1c}$ X Myo15-Cre$^{+/-}$ IHCs showed significant smaller size of maximal ΔC_m (4.60 ±1.19 fF at -1mV, n=6 IHCs from 6 mice) than the wild type (11.87±1.81 fF at -11mV, n=6 IHCs from 5 mice, p=0.0072, unpaired t-test Figure 5.15)
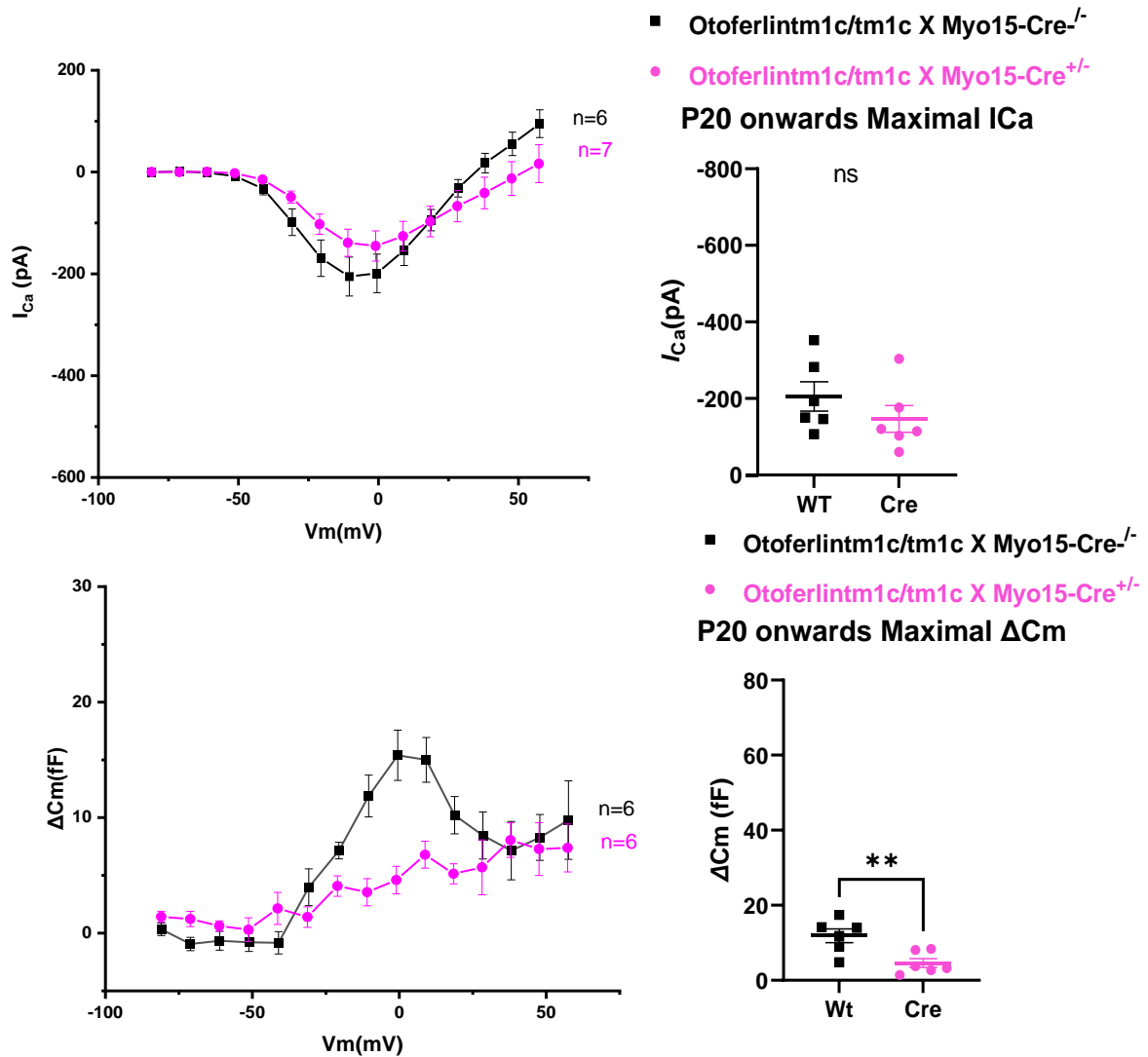
Figure 5.18: Mature (P20 onwards) Otoferlin^tm1c/tm1c X Myo15-Cre^+/- IHCs showed significantly reduced ΔC_m and similar size of *I_Ca* compared with Otoferlin^tm1c/tm1c X Myo15-Cre^-/- (WT).

No significant difference in maximal I_{Ca} between P14-16 WT and Otoferlin^tm1c/tm1c X Myo15-Cre^+/- mice WT: -205.23±38.22 Pa at -11mV, n=6 IHCs from 5 mice, Otoferlin^tm1c/tm1c X Myo15-Cre^+/-: -145.24±25.57 pA at -1mV, n=7 IHCs from 7 mice, p>0.05, unpaired t-test). The maximal ΔC_m of Otoferlin^tm1c/tm1c X Myo15-Cre^+/- is significantly smaller than the wt IHCs (WT^-: 4.596±1.19 fF at -11mV, n=6 IHCs from 5 mice, Otoferlin^tm1c/tm1c X Myo15-Cre^+/- 11.87±1.81 fF at -1mV, n=6 IHCs from 6 mice, p=0.0072, unpaired t-test). The data are plotted as mean data ± SEM.

The kinetics measurement showed that the SRP size of Otoferlin$^{tm1c/tm1c}$ X Myo15-Cre$^{+/-}$ was significantly smaller than the control (Otoferlin$^{tm1c/tm1c}$ X Myo15-Cre$^{-/-}$, n=5 IHCs from 5 mice, Otoferlin$^{tm1c/tm1c}$ X Myo15-Cre$^{+/-}$ n=5 IHCs from 5 mice, p=0.0025, two-way ANOVA). To better compare the size of the RRP recorded by the protocol, ΔC_m from individual IHCs were plotted against the time of stimulus (up to 100ms) and the simple exponential fit using the equation y = A1*exp(-x/t1) + y0, where y0 represents the size of the value. The unpaired t-test showed that the RRP size of the control are significantly bigger than the mutant IHCs (Otoferlin$^{tm1c/tm1c}$ X Myo15-Cre$^{-/-}$: 24.03±3.95, n=4 IHCs from 4 mice Otoferlintm$^{1c/tm1c}$ X Myo15-Cre$^{+/-}$ 4.77±0.67fF, n=5 IHCs from 5 mice, p=0.015, unpaired t-test, Figure 5.19 A). As for vesicle replenishment, unfortunately there was no data for the Wt IHCs. As shown in Figure 5.19B The cumulative ΔC_m recorded from Otoferlin$^{tm1c/tm1c}$ X Myo15-Cre$^{+/-}$ IHCs (n=4 IHCs from 3 mice) are very small.
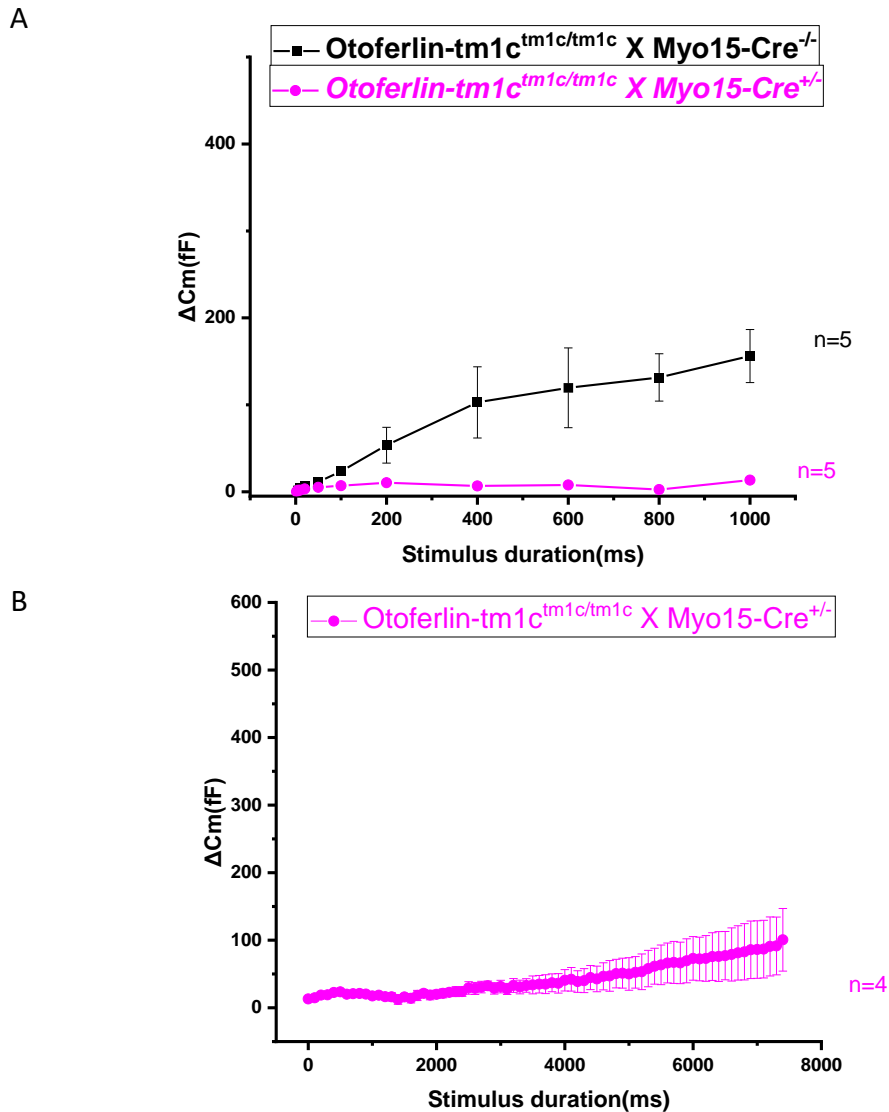
Figure 5.19: Mature (P20 onwards) Otoferlin$^{tm1c/tm1c}$ X Myo15-Cre$^{+/-}$ IHCs has significantly reduced SRP size and the vesicle replenishment rate is not high

A. Average ΔC_m of IHCs from mice older than P20 in response to voltage steps from 2ms to 1s of -11mV voltage stimulus, indicating RRP and SRP size. The size of SRP is significantly smaller in Otoferlin$^{tm1c/tm1c}$ X Myo15-Cre$^{+/-}$ mouse IHCs (Otoferlin$^{tm1c/tm1c}$ X Myo15-Cre$^{-/-}$, n=5 IHCs from 5 mice, Otoferlin$^{tm1c/tm1c}$ X Myo15-Cre$^{+/-}$ n=5 IHCs from 5 mice, p=0.0025, two-way ANOVA). B. Average cumulative ΔC_m of the Otoferlin$^{tm1c/tm1c}$ X Myo15-Cre$^{+/-}$ IHCs from mice older than P20 in response to a train of 50ms stimuli to -11 mV (Otoferlin$^{tm1c/tm1c}$ X Myo15-Cre$^{+/-}$ n=4 IHCs from 3 mice). The data are plotted as mean data ± SEM.

5.3 Discussion

5.3.1 Otoferlin[tm1c/tm1c] X Myo15-Cre^{+/-} mouse HCs show decreased otoferlin expression starting from the second postnatal week

Otoferlin[tm1c/tm1c] X Myo15-Cre^{+/-} mouse HCs show decreased otoferlin expression starting from second postnatal week.

The first sets of experiments described in this chapter was to characterize the timeline of otoferlin conditional knock-out. Although myo15 expression starts at around P1-P2(Anderson et al., 2000), the actual effect of Cre is not clear. From immunostaining, we observed that the Otoferlin[tm1c/tm1c] X Myo15-Cre^{+/-} IHCs showed decreased expression of otoferlin from P7 and the reduction becomes more obvious from P10 onwards. The results indicate that in Otoferlin[tm1c/tm1c] X Myo15-Cre^{+/-} model, it needs about a week to have the full effect of Cre-induced knock-out.

5.3.2 Otoferlin is not essential for hair cell morphology

There have been several research about effect of otoferlin knock-out on morphology of cochlear hair cells. Our results of immunostaining provided evidence that the Otoferlin[tm1c/tm1c] X Myo15-Cre^{+/-} mice showed similar cell body shape of IHCs and OHCs in comparison with the wild type, which is in agreement with the previous results(Johnson et al., 2005). Although there have been observations about hair cell shape and morphology, more details of ribbon synapse formation are yet to be discovered. In previous research, *Otof^{-/-}* mice were observed a decreased number of ribbon synapses and floating ribbons were found in some abnormal synapses(Roux et al., 2006). In this sense, whether the abnormal synapses are the secondary effect of synaptic dysfunction is yet to be discovered. More electron-microscopy checking details of hair cell morphology is yet to be performed.

5.3.3 Otoferlin is essential for maintenance of IHC exocytotic function from the second postnatal week

Although the Ca^{2+} currents were not affected, the Ca^{2+}-triggered exocytosis of the Otoferlin$^{tm1c/tm1c}$ X Myo15-Cre$^{+/-}$ IHCs from P10 onwards becomes significantly reduced and reached to the bottom around P14. The older recordings showed that there is no sign of recovery from P20 to P30. The results agreed with the previous experiment results on immature and early mature IHCs(Roux et al., 2006), indicating that otoferlin acts as the major Ca^{2+} sensor in hair cells and the function of otoferlin is required for maintenance of normal hair cell exocytotic function from late pre-mature age to mature age.

The results of Ca^{2+}-dependent exocytotic sensitivity showed that there was no significant difference between the Otoferlin$^{tm1c/tm1c}$ X Myo15-Cre$^{+/-}$ IHCs and the WT throughout the experimental age. More experiments using a variation of extracellular Ca^{2+} concentrations for capacitance measurement can potentially discover more details about the Ca^{2+} sensitivity in otoferlin-negative IHCs.

The kinetics measurements indicate that not only the RRP, the SRP of the Otoferlin$^{tm1c/tm1c}$ X Myo15-Cre$^{+/-}$ IHCs were affected. In Otoferlin$^{tm1c/tm1c}$ X Myo15-Cre$^{+/-}$ IHCs, the size of the SRP starts to decrease from P10 and saturation of SRP depletion became more obvious from P14 onwards. The vesicle replenishment results also indicate that the rate of release was affected in otoferlin-knocked-out IHCs, from P10 onwards, it became slower and slower from P10 onwards. The results suggested that otoferlin acts as a vesicle replenishment priming factor and otoferlin is required for the maintenance of the function from late pre-mature age to mature age.

In the future, some more details of the cause of the defects of the exocytotic functions in otoferlin-negative IHCs can be potentially tested. For example, checking whether the distribution and morphology of vesicles in ribbon synapses can provide more information about whether the reduced vesicle replenishment was due to the

decreased number of vesicles. Potentially, a more delayed conditional knock-out model (after proper maturation) can give a better insight of the maintenance role of otoferlin for proper exocytotic functions.

6 General Discussion

Morphological and functional development of cochlear hair cell is a delicate process which requires precise changes at the right timing (chapter 1.1.6 and 1.1.7), failing to do so might lead to disruption of proper hair cell function. Two important functions of cochlear hair cells, mechanoelectrical transduction (chapter 1.1.2.2) and synaptic machinery (chapter 1.1.8), are the most well investigated. Although there have been a lot of research in last several decades, more knowledge about functional roles of specific proteins is needed. Here, we have investigated two proteins, neuroplastin and otoferlin, which both were hypothesized that playing essential roles in cochlear hair cell.

6.1 Neuroplastin research

6.1.1 The role of Neuroplastin in cochlear hair cells

Neuroplastin is a cell adhesion molecule that belongs to Basigin protein family. The two isoforms, Neuroplastin 65 (3 Ig domains) and 55 (2 IG domains) were found to be expressed in cochlear hair cells (Carrott et al., 2016; Zeng et al., 2016). Previous results suggested that Np65 plays an essential role in synaptogenesis and cochlear exocytotic function(Carrott et al., 2016), while Np55 was found to be important for normal OHC function, which include maintenance of hair bundles and cochlear amplification(Zeng et al., 2016). However, there are still gaps in knowledge of the spatial and functional roles of neuroplastin in mouse hearing (chapter 1.1.8). In the project related to neuroplastin, the hypothesis was that neuroplastin has important roles in development of basolateral cell properties, MET and exocytosis.

It was debatable where two isoforms of Nptn are expressed in cochlear hair cells. To provide a better understanding, the first steps of the project was to check the expression of Np55 and Np65 in HCs and to test whether the $Nptn^{tm1b/tm1b}$ mice show impaired hearing function. Agreeing with previous research (Carrott et al., 2016; Zeng et al., 2016), neuroplastin expression was found in OHC stereocilia, IHC basolateral membrane, spiral ganglia and some non-sensory hair cells (Figure 3.1). As expected, $Nptn^{tm1b/tm1b}$ showed significantly reduced hearing (Figure 3.1 E and F).

6.1.2 The role of neuroplastin in mechanoelectrical transduction apparatus

From the DPOAE experiments (Figure 3.1 F), we found a reduction of OHC function in $Nptn^{tm1b/tm1b}$ mice. The next step was to check which particular part of the OHC function was affected. In previous research, P7 $Nptn$-knock-out mouse OHCs showed normal MET function (Carrott et al., 2016), but it lacks mature OHC MET recordings. In addition, $Nptn$ expression is required for a HC plasma membrane protein, PMCA expression(Lin et al., 2021). PMCA, as the major Ca^{2+} pump in the hair cells, helps to extrude Ca^{2+} ions from the hair bundles (Dumont et al., 2001b). We tested P7 and P8 OHC MET currents of both WT and $Nptn^{tm1b/tm1b}$ mice, the $Nptn^{tm1b/tm1b}$ OHC recordings showed that there was a reduced open probability of MET channels, suggesting a Ca^{2+}-driven adaptation of the MET currents (Figure 3.3). In addition, we also found that there was a strong reduction of PMCA expression in $Nptn^{tm1b/tm1b}$ OHC stereocilia, suggesting the Ca^{2+} accumulation in OHCs due to lack of PMCA.

6.1.3 The role of neuroplastin in acquiring basolateral K$^+$ channel profile

Previous research showed that neuroplastin-negative hair cells show lack of functions from many perspectives of view. Here, we want to have a better understanding of cochlear hair cell maturation in neuroplastin knock-out mice. Our results showed that in $Nptn^{tm1b/tm1b}$ mice, both IHCs and OHCs showed strongly reduced I$_{K,n}$ (Figure 3.2) and there was a significantly reduced size of I$_{K,f}$ (Figure 3.4). The results mean that $Nptn^{tm1b/tm1b}$ IHCs fail to mature properly. The cause of the IHC immature basolateral current profile might be due to disrupted MET functions. MET currents were found to be important for IHC spontaneous action potential firing, which is an important factor for IHC development (Johnson et al., 2012). As for OHCs, the cause of the reduced K$^+$ current is unclear as according to previous research, disruptions in MET might lead to different phenotypes(Marcotti et al., 2006; Zampini et al., 2011).

6.1.4 The role of neuroplastin in exocytosis

In previous research, neuroplastin-knock-out IHC showed severely impaired exocytosis(Carrott et al., 2016). In this study, recordings of IHC maximal ΔC_m or maximal I$_{Ca}$ in response to 50ms voltage steps showed no significant difference between the WT and the $Nptn^{tm1b/tm1b}$ mice. Kinectics measurement also showed similar response towards different duration of stimulus. The cause of the different observation is still unclear, and the sample size of the experiments is smaller when compared with previous studies. So, potentially, more recordings under the same protocol might give a better understanding of the problem.

6.2 Otoferlin research

6.2.1 Characterizing otoferlin-conditional knock-out models

Another protein we investigated is otoferlin, the primary Ca^{2+} sensor in cochlear hair cell (Roux et al., 2006). After depolarization caused by MET currents, Ca^{2+} sensors in cochlear HCs binds to the Ca^{2+} from the influx, triggering synaptic vesicle fusion process(Chapman, 2002). Previous research has been focusing on testing two perspectives of otoferlin functions. For Ca^{2+} sensing, otoferlin was found to be capable of binding SNARE proteins despite the fact that HCs do not express neuronal SNAREs, indicating it might sense Ca^{2+} in synaptotagmin-like ways(Roux et al., 2006). Functional equivalence tests showed that Syt1 can not compensate the effect of otoferlin knock-out (Reisinger et al., 2011). For vesicle replenishment priming, otoferlin C2F domain mutation was found showing normal Ca^{2+} currents and corresponding exocytosis but a slower rate of capacitance increase after longer stimulus (Pangšrič et al., 2010). A lot of research focusing just on constitutive knock-out models rose a question: is otoferlin just important for development of normal exocytotic function, or it is also needed for maintenance? To answer this question, we have put some effort generating and characterizing otoferlin-conditional knock-out models.

The first sets of attempts were made using tamoxifen sensitive Cre mouse lines. The aim of the experiments was to generate a mouse line that can develop normally throughout the first two postnatal weeks and then otoferlin can be conditionally knocked-out with tamoxifen injection. Two Cre lines, Barhl1-Cre and Vglut3-Cre were chosen as Barhl1 being a HC-specific transcription factor start to express before otoferlin expression(S. Li et al., 2002), and Vglut3-Cre line was found to be a reliable model focusing on cochlear IHCs at all postnatal ages(C. Li et al., 2018). TdTomato, the marker protein to show the Cre transduction was also involved for potential whole cell patch-clamping experiments(Madisen et al., 2009). The results showed that after hair cell maturation, the transduction rate of otoferlin-knock-out is less good than

tdTomato transduction (Figure 4.1-4.3). Tamoxifen injection into younger mice (P10) showed a slightly increased proportion of otoferlin-negative IHCs but the inconsistency between the tdTomato expression and the otoferlin-knock-out lead to a problem with potential future examining of IHC exocytotic functions (Figure 4.4). To avoid tamoxifen-related conditional-knock-out problem, we used an auto conditional Cre line, Myo15-Cre, as Myo15 is expressed in cochlear HC as early as P1-P2 (Anderson et al., 2000), it avoided the problem due to the older age. The immunostaining results of *otoferlin$^{tm1c/tm1c}$* X *Myo15-Cre$^{+/-}$* showed that otoferlin expression starts to decrease at the beginning of the second postnatal week (Figure 5.1 and 5.2) while at P14 the otoferlin is fully knocked-out (Figure 5.3). The several days of otoferlin conditional knock-out gave us a good model for characterization of otoferlin function from P7 to mature age.

6.2.2 The role of otoferlin in cochlear hair cells

From observation of immunostaining samples, otoferlin-knock-out HCs showed similar body shapes incomparison with the WT, which is in agreement with the previous findings(Johnson et al., 2005). Functional tests of otoferlin conditional knock-out using capacitance measurement gave us a better insight of roles of otoferlin in Ca^{2+} sensing and exocytosis.

Capacitance measurements using 50ms voltage steps showed that although Otoferlin$^{tm1c/tm1c}$ X Myo15-Cre$^{+/-}$ IHCs showed smilar maximal I$_{Ca}$ throughout the experimental age (P7 to P20 onwards) to the WT, the corresponding maximal ΔC_m starts to be significantly smaller from P10 onwards. After P14, the ΔC_m in response to Ca^{2+} currents are almost abolished (Figure 5.4, 5.5, 5.8 and 5.11). The findings agrees with the previous research(Roux et al., 2006), suggesting the Ca^{2+} sensing role of otoferlin not just important for early hair cell exocytosis, but also in late pre-mature to mature age.

Kinetics measurements using different durations of maximal ΔC_m triggering voltage stimulus (-11mV) showed that Otoferlin[tm1c/tm1c] X Myo15-Cre^{+/-} IHCs also had a significantly smaller size of SRP from P10. The SRP depletion is more obvious from P14 onwards (Figure 5.6, 5.9, 5.13 and 5.16). Vesicle replenishments indicate that after first post-natal week, otoferlin is still required for maintenance of the vesicle replenishment priming (Figure 5.7, 5.10, 5.14 and 5.16).

6.3 Conclusion and future work

In summary, we have gone through detailed analysis of one cell adhesion molecule, neuroplastin and one Ca^{2+} sensor otoferlin. Neuroplastin was found to be playing a role in HC mature basolateral current profile acquirement as well as OHC Ca^{2+} homeostasis. For the future, there are two more family members of the basigin family, basigin and embigin. Testing the functional roles of those proteins can give us a better insight of the functional roles of cell adhesion molecules in cochlear hair cells.

As for otoferlin, the conditional-knock-out model characterization indicated the otoferlin is required for maintenance of proper exocytotic function from late pre-mature to mature age and it provided a good tool analyzing functional roles of the protein during the experimental age. In the future, generation of a better inducible conditional knock out mouse model can further dissect the functional roles of otoferlin along the timeline, giving us a better understanding of otoferlin functions not just during development, but also after maturation.

References

Abe, T., Kakehata, S., Kitani, R., Maruya, S. I., Navaratnam, D., Santos-Sacchi, J., & Shinkawa, H. (2007). Developmental expression of the outer hair cell motor prestin in the mouse. *Journal of Membrane Biology*, *215*(1), 49–56. https://doi.org/10.1007/s00232-007-9004-5

Alsina, B., Abelló, G., Ulloa, E., Henrique, D., Pujades, C., & Giraldez, F. (2004). FGF signaling is required for determination of otic neuroblasts in the chick embryo. *Developmental Biology*, *267*(1), 119–134. https://doi.org/10.1016/j.ydbio.2003.11.012

Anderson, D. W., Probst, F. J., Belyantseva, I. A., Fridell, R. A., Beyer, L., Martin, D. M., Wu, D., Kachar, B., Friedman, T. B., Raphael, Y., & Camper, S. A. (2000). The motor and tail regions of myosin XV are critical for normal structure and function of auditory and vestibular hair cells. *Human Molecular Genetics*, *9*(12), 1729–1738. https://doi.org/10.1093/HMG/9.12.1729

Anniko, M. (1983). Postnatal maturation of cochlear sensory hairs in the mouse. *Anatomy and Embryology*, *166*(3), 355–368. https://doi.org/10.1007/BF00305923

Ashmore, J. (2008). Cochlear Outer Hair Cell Motility. *Physiological Reviews*, *88*(1), 173–210. https://doi.org/10.1152/physrev.00044.2006

Atkinson, P. J., Najarro, E. H., Sayyid, Z. N., & Cheng, A. G. (2015). Sensory hair cell development and regeneration: Similarities and differences. *Development (Cambridge)*, *142*(9), 1561–1571. https://doi.org/10.1242/dev.114926

Augustine, G. J. (2001). *How does calcium trigger neurotransmitter release ? G eorge J Augustine*. 320–326.

Barclay, M., Ryan, A. F., & Housley, G. D. (2011). Type I vs type II spiral ganglion neurons exhibit differential survival and neuritogenesis during cochlear development. *Neural Development*, *6*(1), 33. https://doi.org/10.1186/1749-8104-6-33

Basch, M. L., Brown, R. M., Jen, H. I., & Groves, A. K. (2016). Where hearing starts: The development of the mammalian cochlea. *Journal of Anatomy*, *228*(2), 233–254. https://doi.org/10.1111/joa.12314

Becker, L., Schnee, M. E., Niwa, M., Sun, W., Maxeiner, S., Talaei, S., Kachar, B., Rutherford, M. A., & Ricci, A. J. (2018). The presynaptic ribbon maintains vesicle populations at the hair cell afferent fiber synapse. *ELife*, *7*. https://doi.org/10.7554/eLife.30241

Beesley, P. W., Herrera-Molina, R., Smalla, K. H., & Seidenbecher, C. (2014). The Neuroplastin adhesion molecules: Key regulators of neuronal plasticity and synaptic function. *Journal of Neurochemistry*, *131*(3), 268–283. https://doi.org/10.1111/jnc.12816

Békésy., G. von. (1961). Experiments in hearing. *Journal of Chronic Diseases*, *13*(1), 86–87. https://doi.org/10.1017/CBO9781107415324.004

Belyantseva, I. A., Boger, E. T., Naz, S., Frolenkov, G. I., Sellers, J. R., Ahmed, Z. M., Griffith, A. J., & Friedman, T. B. (2005). Myosin-XVa is required for tip localization of whirlin and differential elongation of hair-cell stereocilia. *Nature Cell Biology*, *7*(2), 148–156. https://doi.org/10.1038/ncb1219

Berglund, A. M., & Ryugo, D. K. (1987). Hair cell innervation by spiral ganglion neurons in the mouse. *Journal of Comparative Neurology*, *255*(4), 560–570. https://doi.org/10.1002/cne.902550408

Beurg, M., Safieddine, S., Roux, I., Bouleau, Y., Petit, C., & Dulon, D. (2008). Calcium- and Otoferlin-Dependent Exocytosis by Immature Outer Hair Cells. *Journal of Neuroscience*, *28*(8), 1798–1803. https://doi.org/10.1523/JNEUROSCI.4653-07.2008

Beutner, D., & Moser, T. (2001). The presynaptic function of mouse cochlear inner hair cells during development of hearing. *Journal of Neuroscience*, *21*(13), 4593–4599. https://doi.org/10.1523/JNEUROSCI.21-13-04593.2001

Beutner, D., Voets, T., Neher, E., & Moser, T. (2001). Calcium dependence of exocytosis and

endocytosis at the cochlear inner hair cell afferent synapse. *Neuron*, *29*(3), 681–690.

https://doi.org/10.1016/S0896-6273(01)00243-4

Bhattacharya, S., Herrera-Molina, R., Sabanov, V., Ahmed, T., Iscru, E., Stöber, F., Richter, K.,

Fischer, K. D., Angenstein, F., Goldschmidt, J., Beesley, P. W., Balschun, D., Smalla, K. H.,

Gundelfinger, E. D., & Montag, D. (2017). Genetically Induced Retrograde Amnesia of

Associative Memories After Neuroplastin Ablation. *Biological Psychiatry*, *81*(2), 124–

135. https://doi.org/10.1016/J.BIOPSYCH.2016.03.2107/ATTACHMENT/AC77CAC8-

AC31-4BEA-9D59-CA9CA6A66D48/MMC1.PDF

Bissonnette, J. P., & Fekete, D. M. (1996). Standard atlas of the gross anatomy of the

developing inner ear of the chicken. *Journal of Comparative Neurology*, *368*(4), 620–

630. https://doi.org/10.1002/(SICI)1096-9861(19960513)368:4<620::AID-

CNE12>3.0.CO;2-L

Bok, J., Bronner-Fraser, M., & Wu, D. K. (2005). Role of the hindbrain in dorsoventral but not

anteroposterior axial specification of the inner ear. *Development*, *132*(9), 2115–2124.

https://doi.org/10.1242/dev.01796

Bok, J., Raft, S., Kong, K. A., Koo, S. K., Dräger, U. C., & Wu, D. K. (2011). Transient retinoic

acid signaling confers anterior-posterior polarity to the inner ear. *Proceedings of the

National Academy of Sciences of the United States of America*, *108*(1), 161–166.

https://doi.org/10.1073/pnas.1010547108

Boron and Boulpaep. (2012). *Medical Physiology, 2e Updated Edition*. Saunders Elsevier.

https://www.dawsonera.com/readonline/9781455711819

Brandt, A., Khimich, D., & Moser, T. (2005). Few CaV1.3 channels regulate the exocytosis of a

synaptic vesicle at the hair cell ribbon synapse. *Journal of Neuroscience*, *25*(50), 11577–

11585. https://doi.org/10.1523/JNEUROSCI.3411-05.2005

Brandt, A., Striessnig, J., & Moser, T. (2003). Cav1.3 channels are essential for development and presynaptic activity of Cochlear inner hair cells. *The Journal of Neuroscience*, *23*(PART 3), 10832–10840. https://doi.org/10.1007/978-3-662-44845-8_26

Brooker, R., Hozumi, K., & Lewis, J. (2006). Notch ligands with contrasting function: Jagged1 and Delta1 in the mouse inner ear. *Development*, *133*(7), 1277–1286. https://doi.org/10.1242/dev.02284

Brown, M. C. (1994). Antidromic responses of single units from the spiral ganglion. *Journal of Neurophysiology*, *71*(5), 1835–1847. https://doi.org/10.1152/jn.1994.71.5.1835

Brownell, W. E., Bader, C. R., Bertrand, D., & Ribaupierre, Y. De. (1985). Evoked Mechanical Responses of Isolated Cochlear Outer Hair Cells Published by : American Association for the Advancement of Science Stable URL : http://www.jstor.org/stable/1695058 . *Science*, *227*(4683), 194–196.

Butola, T., Wichmann, C., & Moser, T. (2017). Piccolo promotes vesicle replenishment at a fast central auditory synapse. *Frontiers in Synaptic Neuroscience*, *9*(OCT). https://doi.org/10.3389/fnsyn.2017.00014

Cai, T., Seymour, M. L., Zhang, H., Pereira, F. A., & Groves, A. K. (2013). Conditional deletion of Atoh1 reveals distinct critical periods for survival and function of hair cells in the organ of Corti. *Journal of Neuroscience*, *33*(24), 10110–10122. https://doi.org/10.1523/JNEUROSCI.5606-12.2013

Carrott, L., Bowl, M. R., Aguilar, C., Johnson, S. L., Chessum, L., West, M., Morse, S., Dorning, J., Smart, E., Hardisty-Hughes, R., Ball, G., Parker, A., Barnard, A. R., MacLaren, R. E., Wells, S., Marcotti, W., & Brown, S. D. M. (2016). Absence of Neuroplastin-65 Affects Synaptogenesis in Mouse Inner Hair Cells and Causes Profound Hearing Loss. *Journal of Neuroscience*, *36*(1), 222–234. https://doi.org/10.1523/JNEUROSCI.1808-15.2016

Chapman, E. R. (2002). Synaptotagmin: A Ca2+sensor that triggers exocytosis? *Nature Reviews Molecular Cell Biology*, *3*(7), 498–508. https://doi.org/10.1038/nrm855

Chapman, E. R., & Davis, A. F. (1998). Direct interaction of a Ca2+-binding loop of synaptotagmin with lipid bilayers. *Journal of Biological Chemistry*, *273*(22), 13995–14001. https://doi.org/10.1074/jbc.273.22.13995

Chen, P., & Segil, N. (1999). p27(Kip1) links cell proliferation to morphogenesis in the developing organ of Corti. *Development*, *126*(8), 1581–1590.

Cooper, N. P., & Guinan, J. J. (2006). Efferent-mediated control of basilar membrane motion. *Journal of Physiology*, *576*(1), 49–54. https://doi.org/10.1113/jphysiol.2006.114991

Corns, L. F., Bardhan, T., Houston, O., Olt, J., Holley, M. C., Masetto, S., Johnson, S. L., & Marcotti, W. (2014). Functional Development of Hair Cells in the Mammalian Inner Ear. In *Development of Auditory and Vestibular Systems: Fourth Edition* (pp. 155–188). Elsevier Inc. https://doi.org/10.1016/B978-0-12-408088-1.00006-3

Corns, L. F., Johnson, S. L., Kros, C. J., & Marcotti, W. (2014). *Calcium entry into stereocilia drives adaptation of the mechanoelectrical transducer current of mammalian cochlear hair cells*. 1–6. https://doi.org/10.1073/pnas.1409920111

Corns, L. F., Johnson, S. L., Roberts, T., Ranatunga, K. M., Hendry, A., Ceriani, F., Safieddine, S., Steel, K. P., Forge, A., Petit, C., Furness, D. N., Kros, C. J., & Marcotti, W. (2018). Mechanotransduction is required for establishing and maintaining mature inner hair cells and regulating efferent innervation. *Nature Communications*, *9*(1). https://doi.org/10.1038/S41467-018-06307-W

Crawford, A. C., Evans, M. G., & Fettiplace, R. (1989). Activation and adaptation of transducer currents in turtle hair cells. *The Journal of Physiology*, *419*(1), 405–434. https://doi.org/10.1113/jphysiol.1989.sp017878

Crawford, A. C., Evans, M. G., & Fettiplace, R. (1991). The actions of calcium on the mechano-electrical transducer current of turtle hair cells. *The Journal of Physiology*, *434*(1), 369–398. https://doi.org/10.1113/jphysiol.1991.sp018475

Crawford, A. C., Evans, M. G., Fettiplacet$, R., Evans, M. C., & Fettiplace, R. (1991). THE ACTIONS OF CALCIUM ON THE MECHANO-ELECTRICAL TRANSDUCER CURRENT OF TURTLE HAIR CELLS $ Names printed in alphabetical order. MS 8682. *Journal of Physiology*, *434*, 369–398. https://www.ncbi.nlm.nih.gov/pmc/articles/PMC1181423/pdf/jphysiol00449-0370.pdf

Dai, H., Shin, O. H., Machius, M., Tomchick, D. R., Südhof, T. C., & Rizo, J. (2004). Structural basis for the evolutionary inactivation of Ca2+ binding to synaptotagmin 4. *Nature Structural and Molecular Biology*, *11*(9), 844–849. https://doi.org/10.1038/nsmb817

Darrow, K. N., Maison, S. F., & Liberman, M. C. (2006). Cochlear efferent feedback balances interaural sensitivity. *Nature Neuroscience*, *9*(12), 1474–1476. https://doi.org/10.1038/nn1807

Daudet, N., & Lebart, M. C. (2002). Transient expression of the T-isoform of plastins/fimbrin in the stereocilia of developing auditory hair cells. *Cell Motility and the Cytoskeleton*, *53*(4), 326–336. https://doi.org/10.1002/cm.10092

Denoble P & Chimiak J (n.d.). (n.d.). *Anatomy of the Ear | Ears & Diving - DAN Health & Diving*. Retrieved June 22, 2020, from https://www.diversalertnetwork.org/health/ears/anatomy-of-the-ear

DEOL, M. S. (1964). the Abnormalities of the Inner Ear in Kreisler Mice. *Journal of Embryology and Experimental Morphology*, *12*(September), 475–490.

DiPolo, R., & Beaugé, L. (2006). Sodium/calcium exchanger: Influence of metabolic regulation on ion carrier interactions. *Physiological Reviews*, *86*(1), 155–203. https://doi.org/10.1152/PHYSREV.00018.2005/ASSET/IMAGES/LARGE/Z9J0010623880 036.JPEG

Driver, E. C., Sillers, L., Coate, T. M., Rose, M. F., & Kelley, M. W. (2013). The Atoh1-lineage gives rise to hair cells and supporting cells within the mammalian cochlea. *Developmental Biology*, *376*(1), 86–98. https://doi.org/10.1016/j.ydbio.2013.01.005

Dumont, R. A., Lins, U., Filoteo, A. G., Penniston, J. T., Kachar, B., & Gillespie, P. G. (2001a). Plasma Membrane Ca2+-ATPase Isoform 2a Is the PMCA of Hair Bundles. *The Journal of Neuroscience*, *21*(14), 5066. https://doi.org/10.1523/JNEUROSCI.21-14-05066.2001

Dumont, R. A., Lins, U., Filoteo, A. G., Penniston, J. T., Kachar, B., & Gillespie, P. G. (2001b). Plasma Membrane Ca2+-ATPase Isoform 2a Is the PMCA of Hair Bundles. *The Journal of Neuroscience*, *21*(14), 5066. https://doi.org/10.1523/JNEUROSCI.21-14-05066.2001

Duncker, S. V., Franz, C., Kuhn, S., Schulte, U., Campanelli, D., Brandt, N., Hirt, B., Fakler, B., Blin, N., Ruth, P., Engel, J., Marcotti, W., Zimmermann, U., & Knipper, M. (2013). Otoferlin Couples to Clathrin-Mediated Endocytosis in Mature Cochlear Inner Hair Cells. *Journal of Neuroscience*, *33*(22), 9508–9519. https://doi.org/10.1523/JNEUROSCI.5689-12.2013

Ehret, G. (1976). Development of absolute auditory thresholds in the house mouse (Mus musculus). *Journal of the American Audiology Society*, *1*(5), 179–184.

Elliott, S. J., & Shera, C. A. (2012). The cochlea as a smart structure. *Smart Materials and Structures*, *21*(6). https://doi.org/10.1088/0964-1726/21/6/064001

Evans, R. (2020). *Cross-links between stereocilia in the human organ of Corti*. *99*(January 1985), 11–19.

Fariñas, I., Jones, K. R., Tessarollo, L., Vigers, A. J., Huang, E., Kirstein, M., De Caprona, D. C., Coppola, V., Backus, C., Reichardt, L. F., & Fritzsch, B. (2001). Spatial shaping of cochlear innervation by temporally regulated neurotrophin expression. *Journal of Neuroscience*, *21*(16), 6170–6180. https://doi.org/10.1523/jneurosci.21-16-06170.2001

Fernández-Chacón, R., Königstorfer, A., Gerber, S. H., García, J., Matos, M. F., Stevens, C. F., Brose, N., Rizo, J., Rosenmund, C., & Südhof, T. C. (2001). Synaptotagmin I functions as a calcium regulator of release probability. *Nature*, *410*(6824), 41–49. https://doi.org/10.1038/35065004

Fernandez, I., Araç, D., Ubach, J., Gerber, S. H., Shin, O. H., Gao, Y., Anderson, R. G. W., Südhof, T. C., & Rizo, J. (2001). Three-dimensional structure of the synaptotagmin 1 C2B-domain: Synaptotagmin 1 as a phospholipid binding machine. *Neuron*, *32*(6), 1057–1069. https://doi.org/10.1016/S0896-6273(01)00548-7

Fettiplace, R., & Hackney, C. M. (2006). The sensory and motor roles of auditory hair cells. *Nature Reviews Neuroscience*, *7*(1), 19–29. https://doi.org/10.1038/nrn1828

Ficarella, R., Di Leva, F., Bortolozzi, M., Ortolano, S., Donaudy, F., Petrillo, M., Melchionda, S., Lelli, A., Domi, T., Fedrizzi, L., Lim, D., Shull, G. E., Gasparini, P., Brini, M., Mammano, F., & Carafoli, E. (2007). A functional study of plasma-membrane calcium-pump isoform 2 mutants causing digenic deafness. *Proceedings of the National Academy of Sciences of the United States of America*, *104*(5), 1516. https://doi.org/10.1073/PNAS.0609775104

Friedman, H. V., Bresler, T., Garner, C. C., & Ziv, N. E. (2000). *Assembly of New Individual Excitatory Synapses: Time Course and Temporal Order of Synaptic Molecule Recruitment*. *27*, 57–69.

Fritzsch, B. (1996). Development of the Labyrinthine Efferent Systema. *Annals of the New York Academy of Sciences*, *781*(1), 21–33. https://doi.org/10.1111/J.1749-6632.1996.TB15690.X

Froud, K. E., Wong, A. C. Y., Cederholm, J. M. E., Klugmann, M., Sandow, S. L., Julien, J. P., Ryan, A. F., & Housley, G. D. (2015). Type II spiral ganglion afferent neurons drive medial olivocochlear reflex suppression of the cochlear amplifier. *Nature Communications*, *6*(May), 1–9. https://doi.org/10.1038/ncomms8115

Fuchs, P. A. (1996). Synaptic transmission at vertebrate hair cells. *Current Opinion in Neurobiology*, *6*(4), 514–519. https://doi.org/10.1016/S0959-4388(96)80058-4

Fukuda, M., Kojima, T., & Mikoshiba, K. (1996). Phospholipid composition dependence of Ca2+-dependent phospholipid binding to the C2A domain of synaptotagmin IV. *Journal of Biological Chemistry*, *271*(14), 8430–8434. https://doi.org/10.1074/jbc.271.14.8430

Furness, D. N., Richardson, G. P., & Russell, I. J. (1989). Stereociliary bundle morphology in organotypic cultures of the mouse cochlea. *Hearing Research*, *38*(1–2), 95–109. https://doi.org/10.1016/0378-5955(89)90131-7

Gil-Loyzaga, P., & Pujol, R. (1988). Synaptophysin in the developing cochlea. *International Journal of Developmental Neuroscience*, *6*(2), 155–160. https://doi.org/10.1016/0736-5748(88)90040-8

Goodyear, R. J., Marcotti, W., Kros, C. J., & Richardson, G. P. (2005). Development and properties of stereociliary link types in hair cells of the mouse cochlea. *Journal of Comparative Neurology*, *485*(1), 75–85. https://doi.org/10.1002/cne.20513

Goutman, J. D., & Glowatzki, E. (2007). Time course and calcium dependence of transmitter release at a single ribbon synapse. *Proceedings of the National Academy of Sciences of the United States of America*, *104*(41), 16341–16346. https://doi.org/10.1073/pnas.0705756104

Guinan, J. J. (2006). Olivocochlear efferents: Anatomy, physiology, function, and the measurement of efferent effects in humans. In *Ear and Hearing* (Vol. 27, Issue 6, pp. 589–607). Ear Hear. https://doi.org/10.1097/01.aud.0000240507.83072.e7

H. Spoendlin. (1973). The innervation of the cochlear receptor. *A.R. Moller (Ed.), Mechanisms in Hearing, Academic Press, New York*, 185–229. https://books.google.com/books?hl=en&lr=&id=P5FrDzCFiwsC&oi=fnd&pg=PA185&ots=EFzjqf3Pvu&sig=1dMFxh9AhHZuNMp67bfzlFnfRZU

Hallworth, R., & Nichols, M. G. (2012). Prestin in HEK cells is an obligate tetramer. *Journal of Neurophysiology*, *107*(1), 5–11. https://doi.org/10.1152/jn.00728.2011

Heidrych, P., Zimmermann, U., Breß, A., Pusch, C. M., Ruth, P., Pfister, M., Knipper, M., & Blin, N. (2008). Rab8b GTPase, a protein transport regulator, is an interacting partner of otoferlin, defective in a human autosomal recessive deafness form. *Human Molecular Genetics*, *17*(23), 3814–3821. https://doi.org/10.1093/HMG/DDN279

Helyer, R., Cacciabue-Rivolta, D., Davies, D., Rivolta, M. N., Kros, C. J., & Holley, M. C. (2007). A model for mammalian cochlear hair cell differentiation in vitro: Effects of retinoic acid on cytoskeletal proteins and potassium conductances. *European Journal of Neuroscience*, *25*(4), 957–973. https://doi.org/10.1111/j.1460-9568.2007.05338.x

Helyer, R. J., Kennedy, H. J., Davies, D., Holley, M. C., & Kros, C. J. (2005). Development of outward potassium currents in inner and outer hair cells from the embryonic mouse cochlea. *Audiology and Neuro-Otology*, *10*(1), 22–34. https://doi.org/10.1159/000081545

Herrera-Molin, R., Sarto-Jackson, I., Montenegro-Venegas, C., Heine, M., Smalla, K. H., Seidenbecher, C. I., Beesley, P. W., Gundelfinger, E. D., & Montag, D. (2014). Structure of excitatory synapses and GABA$_a$ receptor localization at inhibitory synapses are regulated by neuroplastin-65. *Journal of Biological Chemistry*, *289*(13), 8973–8988. https://doi.org/10.1074/jbc.M113.514992

Hibino, H., Pironkova, R., Onwumere, O., Vologodskaia, M., Hudspeth, A. J., & Lesage, F. (2002). RIM binding proteins (RBPs) couple Rab3-interacting molecules (RIMs) to voltage-gated Ca2+ channels. *Neuron*, *34*(3), 411–423. https://doi.org/10.1016/S0896-6273(02)00667-0

Hirst, J., & Robinson, M. S. (1998). Clathrin and adaptors. *Biochimica et Biophysica Acta - Molecular Cell Research*, *1404*(1–2), 173–193. https://doi.org/10.1016/S0167-4889(98)00056-1

Hua, Y., Sinha, R., Thiel, C. S., Schmidt, R., Hüve, J., Martens, H., Hell, S. W., Egner, A., & Klingauf, J. (2011). A readily retrievable pool of synaptic vesicles. *Nature Neuroscience*, *14*(7), 833–839. https://doi.org/10.1038/nn.2838

Huang, L. C., Barclay, M., Lee, K., Peter, S., Housley, G. D., Thorne, P. R., & Montgomery, J. M. (2012). Synaptic profiles during neurite extension, refinement and retraction in the developing cochlea. *Neural Development*, *7*(1). https://doi.org/10.1186/1749-8104-7-38

Huang, L. C., Thorne, P. R., Housley, G. D., & Montgomery, J. M. (2007a). Spatiotemporal definition of neurite outgrowth, refinement and retraction in the developing mouse cochlea. *Development*, *134*(16), 2925–2933. https://doi.org/10.1242/dev.001925

Huang, L. C., Thorne, P. R., Housley, G. D., & Montgomery, J. M. (2007b). Spatiotemporal definition of neurite outgrowth, refinement and retraction in the developing mouse cochlea. *Development*, *134*(16), 2925–2933. https://doi.org/10.1242/dev.001925

Hudspeth, A. J. (2014). Integrating the active process of hair cells with cochlear function. *Nature Reviews Neuroscience*, *15*(9), 600–614. https://doi.org/10.1038/nrn3786

Hudspeth, A. J., & Corey, D. P. (1977). Sensitivity, polarity, and conductance change in the response of vertebrate hair cells to controlled mechanical stimuli. *Proceedings of the National Academy of Sciences of the United States of America*, *74*(6), 2407–2411. https://doi.org/10.1073/pnas.74.6.2407

Iacono, K. T., Brown, A. L., Greene, M. I., & Saouaf, S. J. (2007). CD147 immunoglobulin superfamily receptor function and role in pathology. *Experimental and Molecular Pathology*, *83*(3), 283–295. https://doi.org/10.1016/j.yexmp.2007.08.014

Jahn, R., Schiebler, W., Ouimet, C., & Greengard, P. (1985). A 38,000-dalton membrane protein (p38) present in synaptic vesicles. *PNAS*, *82*(June), 4137–4141.

Jarman, A. P., Grau, Y., Jan, L. Y., & Jan, Y. N. (1993). atonal is a proneural gene that directs chordotonal organ formation in the Drosophila peripheral nervous system. *Cell*, *73*(7), 1307–1321. https://doi.org/10.1016/0092-8674(93)90358-W

Jean, P., de la Morena, D. L., Michanski, S., Tobón, L. M. J., Chakrabarti, R., Picher, M. M., Neef, J., Jung, S. Y., Gültas, M., Maxeiner, S., Neef, A., Wichmann, C., Strenzke, N., Grabner, C., & Moser, T. (2018). The synaptic ribbon is critical for sound encoding at high rates and with temporal precision. *ELife*, *7*. https://doi.org/10.7554/eLife.29275

Johnson, C. P., & Chapman, E. R. (2010a). Otoferlin is a calcium sensor that directly regulates SNARE-mediated membrane fusion. *Journal of Cell Biology*, *191*(1), 187–197. https://doi.org/10.1083/jcb.201002089

Johnson, C. P., & Chapman, E. R. (2010b). Otoferlin is a calcium sensor that directly regulates SNARE-mediated membrane fusion. *Journal of Cell Biology*, *191*(1), 187–197. https://doi.org/10.1083/JCB.201002089

Johnson, S. L., Forge, A., Knipper, M., Munkner, S., & Marcotti, W. (2008). Tonotopic Variation in the Calcium Dependence of Neurotransmitter Release and Vesicle Pool Replenishment at Mammalian Auditory Ribbon Synapses. *Journal of Neuroscience*, *28*(30), 7670–7678. https://doi.org/10.1523/JNEUROSCI.0785-08.2008

Johnson, S. L., Kennedy, H. J., Holley, M. C., Fettiplace, R., & Marcotti, W. (2012). The Resting Transducer Current Drives Spontaneous Activity in Prehearing Mammalian Cochlear Inner Hair Cells. *Journal of Neuroscience*, *32*(31), 10479–10483. https://doi.org/10.1523/JNEUROSCI.0803-12.2012

Johnson, Stuart L., Eckrich, T., Kuhn, S., Zampini, V., Franz, C., Ranatunga, K. M., Roberts, T. P., Masetto, S., Knipper, M., Kros, C. J., & Marcotti, W. (2011). Position-dependent patterning of spontaneous action potentials in immature cochlear inner hair cells. *Nature Neuroscience*, *14*(6), 711–717. https://doi.org/10.1038/nn.2803

Johnson, Stuart L., Forge, A., Knipper, M., Münkner, S., & Marcotti, W. (2008). Tonotopic variation in the calcium dependence of neurotransmitter release and vesicle pool replenishment at mammalian auditory ribbon synapses. *Journal of Neuroscience*, *28*(30), 7670–7678. https://doi.org/10.1523/JNEUROSCI.0785-08.2008

Johnson, Stuart L., Franz, C., Kuhn, S., Furness, D. N., Rüttiger, L., Münkner, S., Rivolta, M. N., Seward, E. P., Herschman, H. R., Engel, J., Knipper, M., & Marcotti, W. (2010). Synaptotagmin IV determines the linear Ca 2+ dependence of vesicle fusion at auditory ribbon synapses. *Nature Neuroscience*, *13*(1), 45–52. https://doi.org/10.1038/nn.2456

Johnson, Stuart L., Kennedy, H. J., Holley, M. C., Fettiplace, R., & Marcotti, W. (2012). The Resting Transducer Current Drives Spontaneous Activity in Prehearing Mammalian Cochlear Inner Hair Cells. *The Journal of Neuroscience*, *32*(31), 10479. https://doi.org/10.1523/JNEUROSCI.0803-12.2012

Johnson, Stuart L., Marcotti, W., & Kros, C. J. (2005). Increase in efficiency and reduction in Ca2+ dependence of exocytosis during development of mouse inner hair cells. *Journal of Physiology*, *563*(1), 177–191. https://doi.org/10.1113/jphysiol.2004.074740

Johnson, Stuart L, Beurg, M., Marcotti, W., & Fettiplace, R. (2011). Article Prestin-Driven Cochlear Amplification Is Not Limited by the Outer Hair Cell Membrane Time Constant. *Neuron*, *70*(6), 1143–1154. https://doi.org/10.1016/j.neuron.2011.04.024

Johnson, Stuart L, & Marcotti, W. (2008). *Biophysical properties of Ca V 1 . 3 calcium channels in gerbil inner hair cells*. *4*, 1029–1042. https://doi.org/10.1113/jphysiol.2007.145219

Johnson, Stuart L, Thomas, M. V, & Kros, C. J. (2002). *Membrane capacitance measurement using patch clamp with integrated self-balancing lock-in amplifier*. 653–663. https://doi.org/10.1007/s00424-001-0763-z

Jung, S., Oshima-Takago, T., Chakrabarti, R., Wong, A. B., Jing, Z., Yamanbaeva, G., Picher, M. M., Wojcik, S. M., Göttfert, F., Predoehl, F., Michel, K., Hell, S. W., Schoch, S., Strenzke, N., Wichmann, C., & Moser, T. (2015). Rab3-interacting molecules 2α and 2β promote the abundance of voltage-gated CaV1.3 Ca2+ channels at hair cell active zones. *Proceedings of the National Academy of Sciences of the United States of America*, *112*(24), E3141–E3149. https://doi.org/10.1073/pnas.1417207112

Kaltenbach, J. A., & Falzarano, P. R. (1994). Postnatal development of the hamster coclea. I. Growth of hair cells and the organ of Corti. *The Journal of Comparative Neurology*, *340*(1), 87–97. https://doi.org/10.1002/cne.903400107

Kandel. (2000). *Principles of Neural Science, Fourth Edition | AccessNeurology | McGraw-Hill Medical*. https://neurology.mhmedical.com/book.aspx?bookID=1049

Kandler, K., Clause, A., & Noh, J. (2009). Tonotopic reorganization of developing auditory brainstem circuits. In *Nature Neuroscience* (Vol. 12, Issue 6, pp. 711–717). NIH Public Access. https://doi.org/10.1038/nn.2332

Karis, A., Pata, I., Hikke Van Doorninck, J., Grosveld, F., De Zeeuw, C. I., De Caprona, D., & Fritzsch, B. (2001). Transcription Factor GATA-3 Alters Pathway Selection of Olivocochlear Neurons and Affects Morphogenesis of the Ear Indexing terms: ear development; inner ear efferents; cochlear efferents; cochlear formation. *J. Comp. Neurol*, *429*, 615–630.

Khimich, D., Nouvtan, R., Pujol, R., Diesk, S. T., Egner, A., Gundelfinger, E. D., & Moser, T. (2005). Hair cell synaptic ribbons are essential for synchronous auditory signalling. *Nature*, *434*(7035), 889–894. https://doi.org/10.1038/nature03418

Kiang, N., … M. L.-C., & 1984, undefined. (n.d.). Afferent innervation of the mammalian cochlea. *Cambridge University Press …*.

Kiyokawa, H., Kineman, R. D., Manova-Todorova, K. O., Soares, V. C., Huffman, E. S., Ono, M., Khanam, D., Hayday, A. C., Frohman, L. A., & Koff, A. (1996). Enhanced growth of mice lacking the cyclin-dependent kinase inhibitor function of P27Kip1. *Cell*, *85*(5), 721–732. https://doi.org/10.1016/S0092-8674(00)81238-6

Klenchin, V. A., & Martin, T. F. J. (2000). Priming in exocytosis: Attaining fusion-competence after vesicle docking. *Biochimie*, *82*(5), 399–407. https://doi.org/10.1016/S0300-9084(00)00208-X

Kloosterman, W. P., & Plasterk, R. H. A. (2006). The Diverse Functions of MicroRNAs in Animal Development and Disease. In *Developmental Cell* (Vol. 11, Issue 4, pp. 441–450). Dev Cell. https://doi.org/10.1016/j.devcel.2006.09.009

Kolla, L., Kelly, M. C., Mann, Z. F., Anaya-Rocha, A., Ellis, K., Lemons, A., Palermo, A. T., So, K. S., Mays, J. C., Orvis, J., Burns, J. C., Hertzano, R., Driver, E. C., & Kelley, M. W. (2020). Characterization of the development of the mouse cochlear epithelium at the single cell level. *Nature Communications 2020 11:1*, *11*(1), 1–16. https://doi.org/10.1038/s41467-020-16113-y

Kozel, P. J., Friedman, R. A., Erway, L. C., Yamoah, E. N., Liu, L. H., Riddle, T., Duffy, J. J., Doetschman, T., Miller, M. L., Cardell, E. Lou, & Shull, G. E. (1998). Balance and Hearing Deficits in Mice with a Null Mutation in the Gene Encoding Plasma Membrane Ca2+-ATPase Isoform 2 *. *Journal of Biological Chemistry*, *273*(30), 18693–18696. https://doi.org/10.1074/JBC.273.30.18693

Kros, C. J., Rusch, A., & Richardson, G. P. (1992). Mechano-electrical transducer currents in hair cells of the cultured neonatal mouse cochlea. *Proceedings of the Royal Society B: Biological Sciences*, *249*(1325), 185–193. https://doi.org/10.1098/rspb.1992.0102

Kros C.J., Ruppersberg J.P., R. A. (1998). Expression of a potassium current in inner hair cells during development of hearing in mice. *Nature*, *4*(1997), 281–284.

Kros, Corné J., Ruppersberg, J. P., & Rüsch, A. (1998). Expression of a potassium current inner hair cells during development of hearing in mice. *Nature*, *394*(6690), 281–284. https://doi.org/10.1038/28401

Kuhn, S., Johnson, S. L., Furness, D. N., Chen, J., Ingham, N., Hilton, J. M., Steffes, G., Lewis, M. A., Zampini, V., Hackney, C. M., Masetto, S., Holley, M. C., Steel, K. P., & Marcotti, W. (2011). miR-96 regulates the progression of differentiation in mammalian cochlear inner and outer hair cells. *Proceedings of the National Academy of Sciences of the United States of America*, *108*(6), 2355–2360. https://doi.org/10.1073/pnas.1016646108

Lain, E., Carnejac, S., Escher, P., Wilson, M. C., Lømo, T., Gajendran, N., & Brenner, H. R. (2009). A novel role for embigin to promote sprouting of motor nerve terminals at the

neuromuscular junction. *Journal of Biological Chemistry*, *284*(13), 8930–8939. https://doi.org/10.1074/jbc.M809491200

Lee, H. Y., Raphael, P. D., Park, J., Ellerbee, A. K., Applegate, B. E., & Oghalai, J. S. (2015). Noninvasive in vivo imaging reveals differences between tectorial membrane and basilar membrane traveling waves in the mouse cochlea. *Proceedings of the National Academy of Sciences of the United States of America*, *112*(10), 3128–3133. https://doi.org/10.1073/pnas.1500038112

Lee, Y. S., Liu, F., & Segil, N. (2006). A morphogenetic wave of p27Kip1 transcription directs cell cycle exit during organ of Corti development. *Development*, *133*(15), 2817–2826. https://doi.org/10.1242/dev.02453

Lenzi, D., Runyeon, J. W., Crum, J., Ellisman, M. H., & Roberts, W. M. (1999). Synaptic Vesicle Populations in Saccular Hair Cells Reconstructed by Electron Tomography. *The Journal of Neuroscience*, *19*(1), 119. https://doi.org/10.1523/JNEUROSCI.19-01-00119.1999

Leube, R. E., Kaiser, P., Seiter, A., Zimbelmann, R., Franke, W. W., Rehm, H., Knaus, P., Prior, P., Betz, H., & Reinke, H. (1987). Synaptophysin: molecular organization and mRNA expression as determined from cloned cDNA. *The EMBO Journal*, *6*(11), 3261–3268. https://doi.org/10.1002/j.1460-2075.1987.tb02644.x

Lewis, B. P., Burge, C. B., & Bartel, D. P. (2005). Conserved seed pairing, often flanked by adenosines, indicates that thousands of human genes are microRNA targets. In *Cell* (Vol. 120, Issue 1, pp. 15–20). Cell Press. https://doi.org/10.1016/j.cell.2004.12.035

Li, C., Shu, Y., Wang, G., Zhang, H., Lu, Y., Li, X., Li, G., Song, L., & Liu, Z. (2018). Characterizing a novel vGlut3-P2A-iCreER knockin mouse strain in cochlea. *Hearing Research*, *364*, 12–24. https://doi.org/10.1016/J.HEARES.2018.04.006

Li, C. W., Van De Water, T. R., & Ruben, R. J. (1978). The fate mapping of the eleventh and twelfth day mouse otocyst: An in vitro study of the sites of origin of the embryonic

inner ear sensory structures. *Journal of Morphology*, *157*(3), 249–267. https://doi.org/10.1002/jmor.1051570302

Li, H., Liu, H., Balt, S., Mann, S., Corrales, C. E., & Heller, S. (2004). Correlation of Expression of the Actin Filament-Bundling Protein Espin with Stereociliary Bundle Formation in the Developing Inner Ear. *Journal of Comparative Neurology*, *468*(1), 125–134. https://doi.org/10.1002/cne.10944

Li, S., Price, S. M., Cahill, H., Ryugo, D. K., Shen, M. M., & Xiang, M. (2002). Hearing loss caused by progressive degeneration of cochlear hair cells in mice deficient for the Barhl1 homeobox gene. *Development*, *129*(14), 3523–3532. https://doi.org/10.1242/DEV.129.14.3523

Liberman, M. C. (1980). Morphological differences among radial afferent fibers in the cat cochlea: An electron-microscopic study of serial sections. *Hearing Research*, *3*(1), 45–63. https://doi.org/10.1016/0378-5955(80)90007-6

Liberman, M. C. (1982). Single-neuron labeling in the cat auditory nerve. *Science*, *216*(4551), 1239–1241. https://doi.org/10.1126/science.7079757

Liberman, M. C., & Brown, M. C. (1986). Physiology and anatomy of single olivocochlear neurons in the cat. *Hearing Research*, *24*(1), 17–36. https://doi.org/10.1016/0378-5955(86)90003-1

Liberman, M. Charles, Dodds, L. W., & Pierce, S. (1990). Afferent and efferent innervation of the cat cochlea: Quantitative analysis with light and electron microscopy. *Journal of Comparative Neurology*, *301*(3), 443–460. https://doi.org/10.1002/cne.903010309

Lim, D. J., & Anniko, M. (1985). Developmental morphology of the mouse inner ear: A scanning electron microscopic observation. *Acta Oto-Laryngologica*, *99*(S422), 5–69. https://doi.org/10.3109/00016488509121766

Lin, X., Brunk, M. G. K., Yuanxiang, P., Curran, A. W., Zhang, E., Stöber, F., Goldschmidt, J., Gundelfinger, E. D., Vollmer, M., Happel, M. F. K., Herrera-Molina, R., & Montag, D.

(2021). Neuroplastin expression is essential for hearing and hair cell PMCA expression.
Brain Structure and Function 2021 226:5, *226*(5), 1533–1551.
https://doi.org/10.1007/S00429-021-02269-W

Macia, E., Ehrlich, M., Massol, R., Boucrot, E., Brunner, C., & Kirchhausen, T. (2006).
Dynasore, a Cell-Permeable Inhibitor of Dynamin. *Developmental Cell*, *10*(6), 839–850.
https://doi.org/10.1016/j.devcel.2006.04.002

Madisen, L., Zwingman, T. A., Sunkin, S. M., Oh, S. W., Zariwala, H. A., Gu, H., Ng, L. L.,
Palmiter, R. D., Hawrylycz, M. J., Jones, A. R., Lein, E. S., & Zeng, H. (2009). A robust and
high-throughput Cre reporting and characterization system for the whole mouse brain.
Nature Neuroscience 2009 13:1, *13*(1), 133–140. https://doi.org/10.1038/nn.2467

Maison, S. F., Pyott, S. J., Meredith, A. L., & Liberman, M. C. (2013). Olivocochlear
suppression of outer hair cells in vivo: Evidence for combined action of BK and SK2
channels throughout the cochlea. *Journal of Neurophysiology*, *109*(6), 1525–1534.
https://doi.org/10.1152/jn.00924.2012

Marcotti, W. (2012). Functional assembly of mammalian cochlear hair cells. *Experimental
Physiology*, *97*(4), 438–451. https://doi.org/10.1113/expphysiol.2011.059303

Marcotti, W., Erven, A., Johnson, S. L., Steel, K. P., & Kros, C. J. (2006). Tmc1 is necessary for
normal functional maturation and survival of inner and outer hair cells in the mouse
cochlea. *Journal of Physiology*, *574*(3), 677–698.
https://doi.org/10.1113/jphysiol.2005.095661

Marcotti, W., Géléoc, G. S. G., Lennan, G. W. T., & Kros, C. J. (1999). Transient expression of
an inwardly rectifying potassium conductance in developing inner and outer hair cells
along the mouse cochlea. *Pflugers Archiv European Journal of Physiology*, *439*(1–2),
113–122. https://doi.org/10.1007/s004240051134

Marcotti, W., Johnson, S. L., Holley, M. C., & Kros, C. J. (2003a). Developmental changes in
the expression of potassium currents of embryonic , neonatal and mature mouse inner

hair cells. *Journal of Physiology*, *14*, 383–400.
https://doi.org/10.1113/jphysiol.2002.034801

Marcotti, W., Johnson, S. L., Holley, M. C., & Kros, C. J. (2003b). *Developmental changes in the expression of potassium currents of embryonic , neonatal and mature mouse inner hair cells*. *14*, 383–400. https://doi.org/10.1113/jphysiol.2002.034801

Marcotti, W., Johnson, S. L., Holley, M. C., & Kros, C. J. (2003c). Developmental changes in the expression of potassium currents of embryonic, neonatal and mature mouse inner hair cells. *The Journal of Physiology*, *548*(2), 383–400. https://doi.org/10.1111/j.1469-7793.2003.00383.x

Marcotti, W., Johnson, S. L., & Kros, C. J. (2004). A transiently expressed SK current sustains and modulates action potential activity in immature mouse inner hair cells. *Journal of Physiology*, *560*(3), 691–708. https://doi.org/10.1113/jphysiol.2004.072868

Marcotti, W., Johnson, S. L., Rüsch, A., & Kros, C. J. (2003). Sodium and calcium currents shape action potentials in immature mouse inner hair cells. *Journal of Physiology*, *552*(3), 743–761. https://doi.org/10.1113/jphysiol.2003.043612

Marcotti, W., & Kros, C. J. (1999). Developmental expression of the potassium current I(K,n) contributes to maturation of mouse outer hair cells. *Journal of Physiology*, *520*(3), 653–660. https://doi.org/10.1111/j.1469-7793.1999.00653.x

Marty and Neher. (1982). Discrete changes of cell membrane capacitance observed under conditions of enhanced secretion in bovine adrenal chromaffin cells. *Proceedings of the National Academy of Sciences of the United States of America*, *79*(21), 6712. https://doi.org/10.1073/PNAS.79.21.6712

Matsubara, A., Laake, J. H., Davanger, S., Usami, S. I., & Ottersen, O. P. (1996). Organization of AMPA receptor subunits at a glutamate synapse: A quantitative immunogold analysis of hair cell synapses in the rat organ of corti. *Journal of Neuroscience*, *16*(14), 4457–4467. https://doi.org/10.1523/jneurosci.16-14-04457.1996

McGrath, J., Roy, P., & Perrin, B. J. (2017). Stereocilia morphogenesis and maintenance through regulation of actin stability. In *Seminars in Cell and Developmental Biology* (Vol. 65, pp. 88–95). Academic Press. https://doi.org/10.1016/j.semcdb.2016.08.017

McNeil, P. L., & Kirchhausen, T. (2005). An emergency response team for membrane repair. *Nature Reviews. Molecular Cell Biology*, *6*(6), 499–505. https://doi.org/10.1038/NRM1665

McPherson, D. R. (2018). Sensory Hair Cells: An Introduction to Structure and Physiology. *Integrative and Comparative Biology*, *58*(2), 282–300. https://doi.org/10.1093/ICB/ICY064

Michalski, N., Goutman, J. D., Auclair, S. M., de Monvel, J. B., Tertrais, M., Emptoz, A., Parrin, A., Nouaille, S., Guillon, M., Sachse, M., Ciric, D., Bahloul, A., Hardelin, J. P., Sutton, R. B., Avan, P., Krishnakumar, S. S., Rothman, J. E., Dulon, D., Safieddine, S., & Petit, C. (2017). Otoferlin acts as a Ca2+sensor for vesicle fusion and vesicle pool replenishment at auditory hair cell ribbon synapses. *ELife*, *6*, 1–34. https://doi.org/10.7554/eLife.31013

Michalski, N., Michel, V., Bahloul, A., Lefèvre, G., Barral, J., Yagi, H., Chardenoux, S., Weil, D., Martin, P., Hardelin, J. P., Sato, M., & Petit, C. (2007). Molecular characterization of the ankle-link complex in cochlear hair cells and its role in the hair bundle functioning. *Journal of Neuroscience*, *27*(24), 6478–6488. https://doi.org/10.1523/JNEUROSCI.0342-07.2007

Michel, V., Goodyear, R. J., Weil, D., Marcotti, W., Perfettini, I., Wolfrum, U., Kros, C. J., Richardson, G. P., & Petit, C. (2005). Cadherin 23 is a component of the transient lateral links in the developing hair bundles of cochlear sensory cells. *Developmental Biology*, *280*(2), 281–294. https://doi.org/10.1016/j.ydbio.2005.01.014

Morsli, H., Tuorto, F., Choo, D., Postiglione, M. P., Simeone, A., & Wu, D. K. (1999). Otx1 and Otx2 activities are required for the normal development of the mouse inner ear. *Development*, *126*(11), 2335–2343.

Moser, T., & Beutner, D. (2000). Kinetics of exocytosis and endocytosis at the cochlear inner hair cell afferent synapse of the mouse. *Proceedings of the National Academy of Sciences of the United States of America*, *97*(2), 883–888. https://doi.org/10.1073/PNAS.97.2.883

Mukherjee, K., Yang, X., Gerber, S. H., Kwon, H. B., Ho, A., Castillo, P. E., Liu, X., & Südhof, T. C. (2010). Piccolo and bassoon maintain synaptic vesicle clustering without directly participating in vesicle exocytosis. *Proceedings of the National Academy of Sciences of the United States of America*, *107*(14), 6504–6509. https://doi.org/10.1073/pnas.1002307107

Newton, A. J., Kirchhausen, T., & Murthy, V. M. (2006). Inhibition of dynamin completely blocks compensatory synaptic vesicle endocytosis. *Proceedings of the National Academy of Sciences of the United States of America*, *103*(47), 17955–17960. https://doi.org/10.1073/pnas.0606212103

Newton, S., Kong, F., Carlton, A. J., Aguilar, C., Parker, A., Codner, G. F., Teboul, L., Id, S. W., Brown, S. D. M., Marcotti Id, W., & Bowl Id, M. R. (2022). Neuroplastin genetically interacts with Cadherin 23 and the encoded isoform Np55 is sufficient for cochlear hair cell function and hearing. *PLOS Genetics*, *18*(1), e1009937. https://doi.org/10.1371/JOURNAL.PGEN.1009937

Ni, W., Lin, C., Guo, L., Wu, J., Chen, Y., Chai, R., Li, W., & Li, H. (2016). Extensive supporting cell proliferation and mitotic hair cell generation by in vivo genetic reprogramming in the neonatal mouse Cochlea. *Journal of Neuroscience*, *36*(33), 8734–8745. https://doi.org/10.1523/JNEUROSCI.0060-16.2016

Nishida, Y., Rivolta, M. N., & Holley, M. C. (1998). Timed markers for the differentiation of the cuticular plate and stereocilia in hair cells from the mouse inner ear. *Journal of Comparative Neurology*, *395*(1), 18–28. https://doi.org/10.1002/(SICI)1096-9861(19980525)395:1<18::AID-CNE2>3.0.CO;2-K

Noben-Trauth, K., Zheng, Q. Y., Johnson, K. R., & Nishina, P. M. (1997). mdfw:A Deafness

Susceptibility Locus That Interacts with Deaf Waddler (dfw). *Genomics*, *44*(3), 266–272.

https://doi.org/10.1006/GENO.1997.4869

Nouvian, R., Beutner, D., Parsons, T. D., & Moser, T. (2006). Structure and function of the

hair cell ribbon synapse. *Journal of Membrane Biology*, *209*(2–3), 153–165.

https://doi.org/10.1007/s00232-005-0854-4

Nouvian, Régis, Neef, J., Bulankina, A. V., Reisinger, E., Pangršié, T., Frank, T., Sikorra, S.,

Brose, N., Binz, T., & Moser, T. (2011). Exocytosis at the hair cell ribbon synapse

apparently operates without neuronal SNARE proteins. *Nature Neuroscience*, *14*(4),

411–413. https://doi.org/10.1038/nn.2774

Okoruwa, O. E., Weston, M. D., Sanjeevi, D. C., Millemon, A. R., Fritzsch, B., Hallworth, R., &

Beisel, K. W. (2008). Evolutionary insights into the unique electromotility motor of

mammalian outer hair cells. *Evolution and Development*, *10*(3), 300–315.

https://doi.org/10.1111/j.1525-142X.2008.00239.x

Oliver, D., Knipper, M., Derst, C., & Fakler, B. (2003). Resting Potential and Submembrane

Calcium Concentration of Inner Hair Cells in the Isolated Mouse Cochlea Are Set by

KCNQ-Type Potassium Channels. *The Journal of Neuroscience*, *23*(6), 2141–2149.

Olson, E. S., Duifhuis, H., & Steele, C. R. (2012). Von Békésy and cochlear mechanics. *Hearing

Research*, *293*(1–2), 31–43. https://doi.org/10.1016/j.heares.2012.04.017

Ota, C. Y., & Kimura, R. S. (1980). Ultrastructural study of the human spiral ganglion. *Acta

Oto-Laryngologica*, *89*(1–2), 53–62. https://doi.org/10.3109/00016488009127108

Owczarek, S., Soroka, V., Kiryushko, D., Larsen, M. H., Yuan, Q., Sandi, C., Berezin, V., & Bock,

E. (2011). Neuroplastin-65 and a mimetic peptide derived from its homophilic binding

site modulate neuritogenesis and neuronal plasticity. *Journal of Neurochemistry*,

117(6), 984–994. https://doi.org/10.1111/j.1471-4159.2011.07269.x

Palmer, A. R., & Russell, I. J. (1986). Phase-locking in the cochlear nerve of the guinea-pig and its relation to the receptor potential of inner hair-cells. *Hearing Research*, *24*(1), 1–15. https://doi.org/10.1016/0378-5955(86)90002-X

Palmgren, S., Ojala, P. J., Wear, M. A., Cooper, J. A., & Lappalainen, P. (2001). Interactions with PIP2, ADP-actin monomers, and capping protein regulate the activity and localization of yeast twinfilin. *Journal of Cell Biology*, *155*(2), 251–260. https://doi.org/10.1083/jcb.200106157

PangrŠič, T., Reisinger, E., & Moser, T. (2012). Otoferlin: A multi-C 2 domain protein essential for hearing. *Trends in Neurosciences*, *35*(11), 671–680. https://doi.org/10.1016/j.tins.2012.08.002

Pangrsic, T., & Vogl, C. (2018). Balancing presynaptic release and endocytic membrane retrieval at hair cell ribbon synapses. *FEBS Letters*, *592*(21), 3633–3650. https://doi.org/10.1002/1873-3468.13258

Pangšrič, T., Lasarow, L., Reuter, K., Takago, H., Schwander, M., Riedel, D., Frank, T., Tarantino, L. M., Bailey, J. S., Strenzke, N., Brose, N., Müller, U., Reisinger, E., & Moser, T. (2010). Hearing requires otoferlin-dependent efficient replenishment of synaptic vesicles in hair cells. *Nature Neuroscience 2010 13:7*, *13*(7), 869–876. https://doi.org/10.1038/nn.2578

Parsons, T. D., Lenzi, D., Almers, W., & Roberts, W. M. (1994). Calcium-triggered exocytosis and endocytosis in an isolated presynaptic cell: Capacitance measurements in saccular hair cells. *Neuron*, *13*(4), 875–883. https://doi.org/10.1016/0896-6273(94)90253-4

Pauley, S., Wright, T. J., Pirvola, U., Ornitz, D., Beisel, K., & Fritzsch, B. (2003). Expression and function of FGF10 in mammalian inner ear development. *Developmental Dynamics*, *227*(2), 203–215. https://doi.org/10.1002/dvdy.10297

Peng, A. W., Belyantseva, I. A., Hsu, P. D., Friedman, T. B., & Heller, S. (2009). Twinfilin 2 regulates actin filament lengths in cochlear stereocilia. *Journal of Neuroscience*, *29*(48), 15083–15088. https://doi.org/10.1523/JNEUROSCI.2782-09.2009

Perin, M. S., Brose, N., Jahn, R., & Sudhof, T. C. (1991). Domain structure of synaptotagmin (p65). *Journal of Biological Chemistry*, *266*(1), 623–629.

Pickles, J. O., Comis, S. D., & Osborne, M. P. (1984). Cross-links between stereocilia in the guinea pig organ of Corti, and their possible relation to sensory transduction. *Hearing Research*, *15*(2), 103–112. https://doi.org/10.1016/0378-5955(84)90041-8

Pirvola, U., Ylikoski, J., Palgi, J., Lehtonen, E., Arumae, U., & Saarma, M. (1992). Brain-derived neurotrophic factor and neurotrophin 3 mRNAs in the peripheral target fields of developing inner ear ganglia. *Proceedings of the National Academy of Sciences of the United States of America*, *89*(20), 9915–9919. https://doi.org/10.1073/pnas.89.20.9915

Platzer, J., Engel, J., Schrott-fischer, A., Stephan, K., Bova, S., Chen, H., Zheng, H., Pharmakologie, B., & Farmacologia, D. (2000). *Congenital Deafness and Sinoatrial Node Dysfunction in Mice Lacking Class D L-Type Ca 2 ⍰ Channels*. *102*, 89–97.

Prosser, H. M., Rzadzinska, A. K., Steel, K. P., & Bradley, A. (2008). Mosaic Complementation Demonstrates a Regulatory Role for Myosin VIIa in Actin Dynamics of Stereocilia. *Molecular and Cellular Biology*, *28*(5), 1702–1712. https://doi.org/10.1128/mcb.01282-07

Pujol, R., Lavigne-Rebillard, M., & Lenoir, M. (1998). *Development of Sensory and Neural Structures in the Mammalian Cochlea* (pp. 146–192). Springer, New York, NY. https://doi.org/10.1007/978-1-4612-2186-9_4

Pujol, Remy, Eybalin, M., & Puel, J.-L. (1995). Recent advances in cochlear neurotransmission: physiology and pathophysiology. *Physiology*, *10*(4), 178–183.

Raphael, Y., & Altschuler, R. A. (2003). Structure and innervation of the cochlea. *Brain Research Bulletin*, *60*(5–6), 397–422. https://doi.org/10.1016/S0361-9230(03)00047-9

Reisinger, E., Bresee, C., Neef, J., Nair, R., Reuter, K., Bulankina, A., Nouvian, R., Koch, M.,

Bückers, J., Kastrup, L., Roux, I., Petit, C., Hell, S. W., Brose, N., Rhee, J. S., Kügler, S.,

Brigande, J. V., & Moser, T. (2011). Probing the Functional Equivalence of Otoferlin and

Synaptotagmin 1 in Exocytosis. *Journal of Neuroscience*, *31*(13), 4886–4895.

https://doi.org/10.1523/JNEUROSCI.5122-10.2011

Roberts, W. M., Jacobs, R. A., & Hudspeth, A. J. (1990). Colocalization of ion channels

involved in frequency selectivity and synaptic transmission at presynaptic active zones

of hair cells. *The Journal of Neuroscience*, *10*(11), 3664.

https://doi.org/10.1523/JNEUROSCI.10-11-03664.1990

Roux, I., Hosie, S., Johnson, S. L., Bahloul, A., Cayet, N., Nouaille, S., Kros, C. J., Petit, C., &

Safieddine, S. (2009). Myosin VI is required for the proper maturation and function of

inner hair cell ribbon synapses. *Human Molecular Genetics*, *18*(23), 4615–4628.

https://doi.org/10.1093/hmg/ddp429

Roux, I., Safieddine, S., Nouvian, R., Grati, M., Simmler, M. C., Bahloul, A., Perfettini, I., Le

Gall, M., Rostaing, P., Hamard, G., Triller, A., Avan, P., Moser, T., & Petit, C. (2006).

Otoferlin, Defective in a Human Deafness Form, Is Essential for Exocytosis at the

Auditory Ribbon Synapse. *Cell*, *127*(2), 277–289.

https://doi.org/10.1016/j.cell.2006.08.040

Roux, I., Wersinger, E., McIntosh, J. M., Fuchs, P. A., & Glowatzki, E. (2011). Onset of

cholinergic efferent synaptic function in sensory hair cells of the rat cochlea. *Journal of

Neuroscience*, *31*(42), 15092–15101. https://doi.org/10.1523/JNEUROSCI.2743-11.2011

RUBEN, & J., R. (1967). Development of the inner ear of the mouse : a radioautographic

study of terminal mitoses. *Acta Otolaryngol. (Stockh.)*, *220*, 1–44.

https://ci.nii.ac.jp/naid/10029379665

Rüttiger, L., Zimmermann, U., & Knipper, M. (2017). Biomarkers for Hearing Dysfunction:

Facts and Outlook. *Orl*, *79*(1–2), 93–111. https://doi.org/10.1159/000455705

Rzadzinska, A. K., Schneider, M. E., Davies, C., Riordan, G. P., & Kachar, B. (2004). An actin molecular treadmill and myosins maintain stereocilia functional architecture and self-renewal. *Journal of Cell Biology*, *164*(6), 887–897. https://doi.org/10.1083/jcb.200310055

Safieddine, S., & Wenthold, R. J. (1999). SNARE complex at the ribbon synapses of cochlear hair cells: Analysis of synaptic vesicle- and synaptic membrane-associated proteins. *European Journal of Neuroscience*, *11*(3), 803–812. https://doi.org/10.1046/j.1460-9568.1999.00487.x

Safieddine, Saaid, El-Amraoui, A., & Petit, C. (2012). The Auditory Hair Cell Ribbon Synapse: From Assembly to Function. *Annual Review of Neuroscience*, *35*(1), 509–528. https://doi.org/10.1146/annurev-neuro-061010-113705

Safieddine, Saaid, & Wenthold, R. J. (1997). The glutamate receptor subunit δ1 is highly expressed in hair cells of the auditory and vestibular systems. *Journal of Neuroscience*, *17*(19), 7523–7531. https://doi.org/10.1523/JNEUROSCI.17-19-07523.1997

Sakaguchi, H., Tokita, J., Naoz, M., Bowen-Pope, D., Gov, N. S., & Kachar, B. (2008). Dynamic compartmentalization of protein tyrosine phosphatase receptor Q at the proximal end of stereocilia: Implication of myosin Vi-based transport. *Cell Motility and the Cytoskeleton*, *65*(7), 528–538. https://doi.org/10.1002/cm.20275

Sanchez-Calderon, H., Milo, M., Leon, Y., & Varela-nieto, I. (2007). A network of growth and transcription factors controls neuronal differentation and survival in the developing ear. *The International Journal of Developmental Biology*, *51*(6–7), 557–570. https://doi.org/10.1387/ijdb.072373hs

Saunders, J. C., & Garfinkle, T. J. (1981). The morphology of inner hair cell stereocilia in the mouse. *The Journal of the Acoustical Society of America*, *70*(S1), S7–S8. https://doi.org/10.1121/1.2019056

Schmidt, N., Kollewe, A., Constantin, C. E., Henrich, S., Ritzau-Jost, A., Bildl, W., Saalbach, A., Hallermann, S., Kulik, A., Fakler, B., & Schulte, U. (2017a). Neuroplastin and Basigin Are Essential Auxiliary Subunits of Plasma Membrane Ca2+-ATPases and Key Regulators of Ca2+Clearance. *Neuron*, *96*(4), 827-838.e9. https://doi.org/10.1016/j.neuron.2017.09.038

Schmidt, N., Kollewe, A., Constantin, C. E., Henrich, S., Ritzau-Jost, A., Bildl, W., Saalbach, A., Hallermann, S., Kulik, A., Fakler, B., & Schulte, U. (2017b). Neuroplastin and Basigin Are Essential Auxiliary Subunits of Plasma Membrane Ca 2+-ATPases and Key Regulators of Ca 2+ Clearance. *Neuron*, *96*(4), 827-838.e9. https://doi.org/10.1016/J.NEURON.2017.09.038

Schmidt, N., Kollewe, A., Constantin, C. E., Henrich, S., Ritzau-Jost, A., Bildl, W., Saalbach, A., Hallermann, S., Kulik, A., Fakler, B., & Schulte, U. (2017c). Neuroplastin and Basigin Are Essential Auxiliary Subunits of Plasma Membrane Ca2+-ATPases and Key Regulators of Ca2+ Clearance. *Neuron*, *96*(4), 827-838.e9. https://doi.org/10.1016/j.neuron.2017.09.038

Schwander, M., Kachar, B., & Müller, U. (2010). The cell biology of hearing. In *Journal of Cell Biology* (Vol. 190, Issue 1, pp. 9–20). The Rockefeller University Press. https://doi.org/10.1083/jcb.201001138

Shao, X., Davletov, B. A., Sutton, R. B., Südhof, T. C., & Rizo, J. (1996). Bipartite Ca2+-binding motif in C2 domains of synaptotagmin and protein kinase C. *Science*, *273*(5272), 248–251. https://doi.org/10.1126/science.273.5272.248

Sherr, C. J., & Roberts, J. M. (1999). CDK inhibitors: Positive and negative regulators of G1-phase progression. *Genes and Development*, *13*(12), 1501–1512. https://doi.org/10.1101/gad.13.12.1501

Shi, F., Cheng, Y. F., Wang, X. L., & Edge, A. S. B. (2010). β-Catenin up-regulates Atoh1 expression in neural progenitor cells by interaction with an Atoh1 3' enhancer. *Journal of Biological Chemistry*, *285*(1), 392–400. https://doi.org/10.1074/jbc.M109.059055

Shi, F., Hu, L., Jacques, B. E., Mulvaney, J. F., Dabdoub, A., & Edge, A. S. B. (2014). β-catenin is required for hair-cell differentiation in the cochlea. *Journal of Neuroscience*, *34*(19), 6470–6479. https://doi.org/10.1523/JNEUROSCI.4305-13.2014

Shin, O.-H., Xu, J., Rizo, J., & Sudhof, T. C. (2009). Differential but convergent functions of Ca2+ binding to synaptotagmin-1 C2 domains mediate neurotransmitter release. *Proceedings of the National Academy of Sciences*, *106*(38), 16469–16474. https://doi.org/10.1073/pnas.0908798106

Shotwell, S. L., Jacobs, R., & Hudspeth, A. J. (1981). Directional Sensitivity of Individual Vertebrate Hair Cells To Controlled Deflection of Their Hair Bundles. *Annals of the New York Academy of Sciences*, *374*(1), 1–10. https://doi.org/10.1111/j.1749-6632.1981.tb30854.x

Siemens, J., Lillo, C., Dumont, R. A., Reynolds, A., Williams, D. S., Gillespie, P. G., & Müller, U. (2004). Cadherin 23 Is a component of the tip link in hair-cell stereocilla. *Nature*, *428*(6986), 950–955. https://doi.org/10.1038/nature02483

Simmons, D. D. (2002). Development of the inner ear efferent system across vertebrate species. In *Journal of Neurobiology* (Vol. 53, Issue 2, pp. 228–250). John Wiley & Sons, Ltd. https://doi.org/10.1002/neu.10130

Smith, C. A., & Sjöstrand, F. S. (1961). Structure of the nerve endings on the external hair cells of the guinea pig cochlea as studied by serial sections. *Journal of Ultrasructure Research*, *5*(6), 523–556. https://doi.org/10.1016/S0022-5320(61)80025-7

Sobkowicz, H. M., Rose, J. E., Scott, G. E., & Slapnick, S. M. (1982). Ribbon synapses in the developing intact and cultured organ of corti in the mouse. *Journal of Neuroscience*, *2*(7), 942–957. https://doi.org/10.1523/jneurosci.02-07-00942.1982

Sobkowicz, H. M., Rose, J. E., Scott, G. L., & Levenick, C. V. (1986). Distribution of synaptic ribbons in the developing organ of Corti. *Journal of Neurocytology*, *15*(6), 693–714. https://doi.org/10.1007/BF01625188

Sollner, T., Whiteheart, S. W., Brunner, M., Erdjument-bromage, H., Geromanos, S., Tempst,

P., & Rothman, J. E. (1993). SNAP receptors implicated in vesicle targeting and fusion.

Nature, *362*(March), 318–324.

Spiegel, M. F., & Watson, C. S. (1984). Performance On Frequency-discrimination Tasks By

Musicians And Nonmusicians. *Journal of the Acoustical Society of America*, *76*(6), 1690–

1695. https://doi.org/10.1121/1.391605

Spoendlin, H. (1971). Degeneration behaviour of the cochlear nerve. *Archiv Für Klinische Und*

Experimentelle Ohren- Nasen- Und Kehlkopfheilkunde, *200*(4), 275–291.

https://doi.org/10.1007/BF00373310

Spoendlin, H. (1981). Differentiation of cochlear afferent neurons. *Acta Oto-Laryngologica*,

91(1–6), 451–456. https://doi.org/10.3109/00016488109138527

Strutz, J. (1981). Efferent innervation of the cochlea. *Annals of Otology, Rhinology &*

Laryngology, *90*(2), 158–160. https://doi.org/10.1177/000348948109000212

Südhof, T. C. (2002). Synaptotagmins: Why so many? *Journal of Biological Chemistry*,

277(10), 7629–7632. https://doi.org/10.1074/jbc.R100052200

Südhof, T. C., Czernik, A. J., Kao, H. T., Takei, K., Johnston, P. A., Horiuchi, A., Kanazir, S. D.,

Wagner, M. A., Perin, M. S., De Camilli, P., & Greengard, P. (1989). Synapsins: Mosaics

of shared and individual domains in a family of synaptic vesicle phosphoproteins.

Science, *245*(4925), 1474–1480. https://doi.org/10.1126/science.2506642

Takei, K., & Haucke, V. (2001). Clathrin-mediated endocytosis: Membrane factors pull the

trigger. *Trends in Cell Biology*, *11*(9), 385–391. https://doi.org/10.1016/S0962-

8924(01)02082-7

Takenawa, T., & Itoh, T. (2001). Phosphoinositides, key molecules for regulation of actin

cytoskeletal organization and membrane traffic from the plasma membrane. In

Biochimica et Biophysica Acta - Molecular and Cell Biology of Lipids (Vol. 1533, Issue 3,

pp. 190–206). Biochim Biophys Acta. https://doi.org/10.1016/S1388-1981(01)00165-2

Teudt, I. U., & Richter, C. P. (2014). Basilar membrane and tectorial membrane stiffness in the CBA/CaJ mouse. *JARO - Journal of the Association for Research in Otolaryngology*, *15*(5), 675–694. https://doi.org/10.1007/s10162-014-0463-y

Thiers, F. A., Nadol, J. B., & Liberman, M. C. (2008). Reciprocal synapses between outer hair cells and their afferent terminals: Evidence for a local neural network in the mammalian cochlea. *JARO - Journal of the Association for Research in Otolaryngology*, *9*(4), 477–489. https://doi.org/10.1007/s10162-008-0135-x

Thomsen, E. (1967). The ultrastructuhe of the spiral ganglion in the Guinea pig. *Acta Oto-Laryngologica*, *63*(S224), 442–448. https://doi.org/10.3109/00016486709123621

Tilney, L. G., Tilney, M. S., & DeRosier, D. J. (1992). Actin filaments, stereocilia, and hair cells: How cells count and measure. In *Annual Review of Cell Biology* (Vol. 8, pp. 257–274). Annu Rev Cell Biol. https://doi.org/10.1146/annurev.cb.08.110192.001353

Ting, J. T., Kelley, B. G., & Sullivan, J. M. (2006). Synaptotagmin IV does not alter excitatory fast synaptic transmission or fusion pore kinetics in mammalian CNS neurons. *Journal of Neuroscience*, *26*(2), 372–380. https://doi.org/10.1523/JNEUROSCI.3997-05.2006

Tritsch, N. X., Yi, E., Gale, J. E., Glowatzki, E., & Bergles, D. E. (2007). The origin of spontaneous activity in the developing auditory system. *Nature*, *450*(7166), 50–55. https://doi.org/10.1038/nature06233

Tsuprun, V., & Santi, P. (1998). Structure of outer hair cell stereocilia links in the chinchilla. *Journal of Neurocytology*, *27*(7), 517–528. https://doi.org/10.1023/A:1006903926571

Tucker, T., & Fettiplace, R. (1995). Confocal imaging of calcium microdomains and calcium extrusion in turtle hair cells. *Neuron*, *15*(6), 1323–1335. https://doi.org/10.1016/0896-6273(95)90011-X

Ubach, J., Zhang, X., Shao, X., Südhof, T. C., & Rizo, J. (1998). Ca2+ binding to synaptotagmin: How many Ca2+ ions bind to the tip of a C2-domain? *EMBO Journal*, *17*(14), 3921–3930. https://doi.org/10.1093/emboj/17.14.3921

Úlehlová, L., Voldřich, L., & Janisch, R. (1987). Correlative study of sensory cell density and cochlear length in humans. *Hearing Research*, *28*(2–3), 149–151. https://doi.org/10.1016/0378-5955(87)90045-1

Verpy, E., Leibovici, M., Zwaenepoel, I., Liu, X. Z., Gal, A., Salem, N., Mansour, A., Blanchard, S., Kobayashi, I., Keats, B. J. B., Slim, R., & Petit, C. (2000). A defect in harmonin, a PDZ domain-containing protein expressed in the inner ear sensory hair cells, underlies Usher syndrome type 1C. *Nature Genetics*, *26*(1), 51–55. https://doi.org/10.1038/79171

Von Gersdorff, H., Vardi, E., Matthews, G., & Sterling, P. (1996). Evidence that vesicles on the synaptic ribbon of retinal bipolar neurons can be rapidly released. *Neuron*, *16*(6), 1221–1227. https://doi.org/10.1016/S0896-6273(00)80148-8

Wangemann, P. (2006). Supporting sensory transduction: Cochlear fluid homeostasis and the endocochlear potential. *Journal of Physiology*, *576*(1), 11–21. https://doi.org/10.1113/jphysiol.2006.112888

Wedemeyer, C., Martín, J. Z. de S., Ballestero, J., Gómez-Casati, M. E., Torbidoni, A. V., Fuchs, P. A., Bettler, B., Elgoyhen, A. B., & Katz, E. (2013). Activation of presynaptic GABAb(1a,2) receptors inhibits synaptic transmission at mammalian inhibitory cholinergic olivocochlear-hair cell synapses. *Journal of Neuroscience*, *33*(39), 15477–15487. https://doi.org/10.1523/JNEUROSCI.2554-13.2013

Weisstaub, N., Vetter, D. E., Belén Elgoyhen, A., & Katz, E. (2002). The α9α10 nicotinic acetylcholine receptor is permeable to and is modulated by divalent cations. *Hearing Research*, *167*(1–2), 122–135. https://doi.org/10.1016/S0378-5955(02)00380-5

Weston, M. D., Pierce, M. L., Rocha-Sanchez, S., Beisel, K. W., & Soukup, G. A. (2006). MicroRNA gene expression in the mouse inner ear. *Brain Research*, *1111*(1), 95–104. https://doi.org/10.1016/j.brainres.2006.07.006

Wong, A. B., Rutherford, M. A., Gabrielaitis, M., Pangr, T., Frank, T., Michanski, S., Hell, S., Wolf, F., & Wichmann, C. (2014). *Developmental refinement of hair cell synapses tightens the coupling of Ca 2 + influx to exocytosis*. *33*(3), 247–264.

Wright, A. (1984). Dimensions of the cochlear stereocilia in man and the guinea pig. *Hearing Research*, *13*(1), 89–98. https://doi.org/10.1016/0378-5955(84)90099-6

Wu, D. K., Nunes, F. D., & Choo, D. (1998). Axial specification for sensory organs versus non-sensory structures of the chicken inner ear. *Development*, *125*(1).

Xiong, W., Grillet, N., Elledge, H. M., Wagner, T. F. J., Zhao, B., Johnson, K. R., Kazmierczak, P., & Müller, U. (2012). TMHS is an integral component of the mechanotransduction machinery of cochlear hair cells. *Cell*, *151*(6), 1283–1295. https://doi.org/10.1016/j.cell.2012.10.041

Zampini, V., Rüttiger, L., Johnson, S. L., Franz, C., Furness, D. N., Waldhaus, J., Xiong, H., Hackney, C. M., Holley, M. C., Offenhauser, N., Fiore, P. P., Knipper, M., Masetto, S., & Marcotti, W. (2011). Eps8 Regulates Hair Bundle Length and Functional Maturation of Mammalian Auditory Hair Cells. *PLoS Biology*, *9*(4), 1001048. https://doi.org/10.1371/JOURNAL.PBIO.1001048

Zeng, W.-Z., Grillet, N., Dewey, J. B., Trouillet, A., Krey, J. F., Barr-Gillespie, P. G., Oghalai, J. S., & Muller, U. (2016). Neuroplastin Isoform Np55 Is Expressed in the Stereocilia of Outer Hair Cells and Required for Normal Outer Hair Cell Function. *Journal of Neuroscience*, *36*(35), 9201–9216. https://doi.org/10.1523/JNEUROSCI.0093-16.2016

Zenisek, D., Horst, N. K., Merrifield, C., Sterling, P., & Matthews, G. (2004). Visualizing synaptic ribbons in the living cell. *Journal of Neuroscience*, *24*(44), 9752–9759. https://doi.org/10.1523/JNEUROSCI.2886-04.2004

Zhang, Z., Bhalla, A., Dean, C., Chapman, E. R., & Jackson, M. B. (2009). Synaptotagmin IV: A multifunctional regulator of peptidergic nerve terminals. *Nature Neuroscience*, *12*(2), 163–171. https://doi.org/10.1038/nn.2252